

# Absolute Flux Density Measurement and Associated Instrumentation for Radio Astronomy below 100 MHz

Richard Henry Tillman

Dissertation submitted to the Faculty of the  
Virginia Polytechnic Institute and State University  
in partial fulfillment of the requirements for the degree of

Doctor of Philosophy  
in  
Electrical Engineering

Steven W. Ellingson, Chair

Gary S. Brown

John M. Ruohoniemi

Richard M. Buehrer

Nahum Arav

August 9, 2016

Blacksburg, Virginia

Keywords: Radio Astronomy, Radiometry, Receiver Design

Copyright 2016, Richard Henry Tillman

# Absolute Flux Density Measurement and Associated Instrumentation for Radio Astronomy below 100 MHz

Richard Henry Tillman

(ABSTRACT)

This dissertation reports new measurements of the absolute flux densities of the brightest astrophysical sources visible from the northern hemisphere with  $\mathcal{O}[10\%]$  accuracy between 30–78 MHz. These measurements provide additional confidence in the existing understanding of the flux density spectra of these sources in this frequency range. This dissertation also reports new measurements of the antenna temperature due to the diffuse Galactic background between 30–78 MHz, addressing a paucity of existing measurements in this band. These measurements are relevant especially in the context of contemporary interest in radio astronomy and 21 cm cosmology in this frequency range.

A new active antenna system and measurement technique were developed to facilitate these measurements. The antennas are simple, thin dipoles, allowing for accurate characterization. Amplification is preceded by notch filters to mitigate interference induced non-linearity. Previous efforts have used well matched antennas. The narrowband antennas and notch filters on the front end create large, frequency varying impedance mismatch that must be accounted for, and we demonstrate how this can be done. We present a novel *in situ* technique that uses the antenna temperature measurements to improve the calibration of the antennas and internal noise sources.

*To Muzzie*

# Acknowledgments

This work was supported in part by the Virginia Tech Bradley Foundation, and in part by the National Science Foundation through Grants AST-1105949 and AST-1139963.

I owe an unimaginable amount of gratitude to my advisor, Dr. S.W. Ellingson, for the opportunity to pursue my Ph.D. with him. Under his tutelage, I have grown by unfathomable bounds as an engineer, scientist, and professional.

I am also grateful to my committee members Drs. G. Brown, J.M. Ruohoniemi, R.M. Buehrer, and N. Arav for their time and effort participating in my Ph.D. process.

A very special thank you to Dr. G. Taylor at the University of New Mexico (UNM) for providing the location for collecting the data necessary for this research. Additionally, I would like to thank Drs. J. Dowell, and F. Schinzel, currently of UNM, and Dr. J. Craig, and Mr. O. Leone, formerly of UNM, for their helpful assistance and conversations regarding this research.

My thanks to my MPRG colleagues. In particular, thanks to Mr. J. Brendler for two years of assistance in several aspect of this research. Thanks to Mr. X. Gomez for help during the many long, insect infested nights at Kelly Flats during the Summer and Fall of 2015 portions of the data collection campaign. Additionally, thanks to Ms. J. Dsouza, Mr. A. Yellu, Mr. N. Hu, and Mr. J. Cadena for assisting in various aspects of this research and the data collection.

A huge thank you to the MPRG staff, in particular Ms. Hilda Reynolds and Ms. Nancy Goad.

I cannot thank Hilda enough for the countless orders and reorders of parts and equipment. The work presented in this dissertation was greatly facilitated by the lab space and freedom Nancy allowed.

Thanks to my friends and family (Josie, Aaron, Ben, Jordan, Rob, Ellis, and Justin) for reminding me that sometimes getting away from the lab is a viable step in solving a problem. In particular, thanks to my partner Jen, for reasons uncountable.

Finally, all of this would not be possible without the ever present support of my parents, Fred and Mary. While they may not have understood my research, that never stopped them from asking about it, sometimes incessantly. I love you, Mom and Dad.

# Contents

<b>1</b>	<b>Introduction</b>	<b>1</b>
1.1	Existing State of the Art for Low Frequency Flux Density Calibration . . . . .	4
1.2	Contributions Reported in this Dissertation . . . . .	10
1.2.1	New Flux Density Measurements . . . . .	10
1.2.2	Measurement of the Diffuse Sky Emission in 30–78 MHz . . . . .	10
1.2.3	Improved Instrumentation and Techniques . . . . .	12
1.2.4	Determination of Practical Limits in the Sensitivity-Linearity Tradeoff in Front End Design . . . . .	13
1.3	Organization of this Dissertation . . . . .	13
<b>2</b>	<b>Methodology</b>	<b>14</b>
2.1	Characterization of Sources . . . . .	14
2.2	Characterization of the Galactic Background Noise . . . . .	17
2.3	Comprehensive System Model (CSM) . . . . .	18
2.4	Isolation of the Source Flux Density (Fringe Rate Processing) . . . . .	23
2.4.1	Theory . . . . .	24

2.4.2	Example of the Source Isolation . . . . .	28
2.5	Antenna Temperature Model (ATM) . . . . .	32
2.5.1	<i>In Situ</i> Calibration of the Receiver Gain . . . . .	32
2.5.2	Estimation of the Galactic Background Noise . . . . .	37
2.6	<i>In Situ</i> Calibration of Antenna Impedance and Internal Noise Source . . . . .	39
2.6.1	Revised Antenna Model . . . . .	39
2.6.2	Internal Noise Source . . . . .	40
2.6.3	Joint Determination of $C_s$ , $C_p$ , and $\Delta T_{cal}$ . . . . .	41
2.7	Coherent Interferometry Model (CIM) . . . . .	42
2.7.1	Derivation of the CIM Measurement Equation . . . . .	42
2.7.2	Determination of $H^{(m)}$ . . . . .	43
2.8	Summary of Methodology . . . . .	44
<b>3</b>	<b>Instrumentation</b> . . . . .	<b>47</b>
3.1	Antennas . . . . .	49
3.1.1	Mechanical Design . . . . .	50
3.1.2	Effective Length: IT/PEC . . . . .	52
3.1.3	Effective Length: MoM . . . . .	53
3.1.4	Antenna Impedance . . . . .	56
3.1.5	Ground Loss . . . . .	62
3.2	Front End Electronics (FEE) . . . . .	64
3.2.1	FEE Design . . . . .	65

3.2.2	FEE Performance . . . . .	66
3.2.3	FEE Input Impedance . . . . .	68
3.3	Cables . . . . .	71
3.4	Analog Receiver (ARX) . . . . .	73
3.5	Anti-Aliasing Filters (AAF) . . . . .	74
3.6	Summary of the Analog System Response . . . . .	75
3.7	System Sensitivity . . . . .	81
3.8	Digital Receiver (DRX) . . . . .	84
3.9	Bias and Control Circuits . . . . .	87
3.10	System Commissioning . . . . .	88
3.11	RFI Mitigation . . . . .	96
3.11.1	Time Domain RFI Mitigation . . . . .	97
3.11.2	Joint Time-Frequency Domain RFI Mitigation . . . . .	99
<b>4</b>	<b>Measurement Campaign</b>	<b>102</b>
4.1	VLA North Arm Site . . . . .	102
4.2	Kelly Flats . . . . .	105
4.3	Available Data for Each Source . . . . .	106
<b>5</b>	<b>Data Reduction</b>	<b>116</b>
5.1	ATM Phase of the Data Reduction . . . . .	119
5.1.1	Estimation of $G_R(Z'_A)$ . . . . .	119

5.1.2	Estimation of $T_{sky}$ . . . . .	120
5.2	Joint Optimization of $C_p$ , $C_s$ , and $\Delta T_{cal}$ . . . . .	122
5.3	Isolation of the Source Flux . . . . .	125
5.4	CIM Phase of the Data Reduction . . . . .	130
<b>6</b>	<b>Results</b>	<b>133</b>
6.1	Evaluation of Effective Length Models . . . . .	133
6.2	The Flux Density Estimates . . . . .	137
6.2.1	Cyg A . . . . .	137
6.2.2	Cas A . . . . .	140
6.2.3	Tau A . . . . .	142
6.2.4	Vir A . . . . .	142
6.2.5	Summary of the Flux Density Estimates . . . . .	144
6.3	Measurements of the Diffuse Sky Emission in 30–78 MHz . . . . .	147
<b>7</b>	<b>Summary and Future Work</b>	<b>152</b>
7.1	Findings . . . . .	152
7.2	Suggested Future Work . . . . .	154
7.2.1	Improved Flux Density Measurements of the A-Team Sources . . . . .	154
7.2.2	Other Applications of this Work . . . . .	156
<b>A</b>	<b>A Note on the Galactic Background</b>	<b>158</b>
<b>B</b>	<b>Conversion from Celestial Equatorial Coordinates to Local Azimuth and</b>	

Elevation	161
<b>C Taylor Series Approximation of the Geometric Delay</b>	<b>163</b>
<b>D Derivation of Equations Used in the Receiver Calibration</b>	<b>166</b>
D.1 Available Gain of the Parasitic Impedance . . . . .	166
D.2 Recalculation of Transducer Power Gain for Different Source Impedances . . .	167
D.3 Recalculation of Receiver Noise Temperature for a Different Source Impedance	169
<b>E Noise Diode Characterization</b>	<b>171</b>
<b>F The Radiometric Interferometry Model (RIM)</b>	<b>180</b>
<b>G Instrumentation Design Details</b>	<b>183</b>
G.1 FEE Design Details . . . . .	183
G.2 Anti-Aliasing Filter Design Details . . . . .	188
G.3 Bias and Control Design Details . . . . .	188
<b>H GNL Analysis</b>	<b>197</b>
<b>I Measurement of Baselines</b>	<b>199</b>
<b>List of Symbols</b>	<b>201</b>
<b>References</b>	<b>207</b>

# List of Figures

1.1	Flux density estimates and associated error, epoch 1965, used in the Baars <i>et al.</i> flux scale (see text). The power law fit to the measurements is also shown.	3
1.2	Antennas used in (top left to right) LWA1, LOFAR, SKA-Lowband Array (artist representation), and (bottom) MWA.	5
1.3	The 50 MHz radio sky above at a latitude of $+34^\circ$ at 20:00 LST, corresponding to Cyg A's transit. The zenith is at the origin, and the horizon is the perimeter of the circle. GC is the Galactic center.	7
1.4	Same as Fig. 1.3, but at 08:00 LST.	7
1.5	Simplified schematic of a two-element interferometer.	8
1.6	Flux density for Tau A and associated error, using the current best available absolute flux density measurements.	10
1.7	The new flux density measurements reported in this dissertation. Measurements from this work are denoted by an "o", and the measurements shown in Fig. 1.1 are denoted by an "x". The dashed line is the Baars flux scale.	11
2.1	Source tracks for the A-Team sources at a latitude of $+34^\circ$ , approximately that of the VLA. The angle is $\phi$ (east at $\phi = 0^\circ$ , north at $\phi = 90^\circ$ ), and the radius is $\cos\theta$ , where $\theta$ is the zenith angle.	16

2.2	Contribution of the Galactic synchrotron background to the antenna temperature of a dipole-type antenna isolated from ground loss according to Eq. (2.2). The center curve is the daily mean value whereas the upper and lower curves represent the typical limits due to diurnal variation at about $+34^\circ$ latitude. . . . .	18
2.3	Diagram for the two-element interferometer system model. . . . .	20
2.4	Antenna model. The superscripts have been suppressed for clarity. . . . .	22
2.5	Receiver model; see Section 2.3 for notation. The superscripts have been suppressed for clarity. $A_R(Z'_A)$ is related, but not equivalent, to $G_R(Z'_A)$ defined in Section 2.5.1. . . . .	22
2.6	Signal processing procedure. . . . .	24
2.7	Fringes at 42 MHz for the simulation described in Section 2.4.2. $\Delta\nu = 63$ kHz, $\Delta t = 60$ s. . . . .	29
2.8	Cross-correlation for the simulation described in Section 2.4.2. $\Delta\nu = 63$ kHz, $\Delta t = 60$ s. . . . .	30
2.9	Magnitude of the per-channel FFT of the cross-correlation shown in Fig. 2.8. The bottom panel is a narrowband cut from the upper panel at $\nu = 42$ MHz. $\Delta\nu = 63$ kHz, $\Delta t = 60$ s. . . . .	31
2.10	Magnitude of the per-channel FFT of the cross-correlation shown in Fig. 2.8 after delay stopping for Cyg A. The bottom panel is a narrowband cut from the upper panel at $\nu = 42$ MHz. $\Delta\nu = 63$ kHz, $\Delta t = 60$ s. . . . .	33
2.11	Estimate of the flux of Cyg A. . . . .	34
2.12	Block diagram of the three-state switching receiver. . . . .	35
2.13	Equivalent circuit of the revised antenna impedance discussed in Section 2.6.1. . . . .	40
2.14	Equivalent circuit model to determine $S_A$ . . . . .	44

2.15	Overview of the methodology presented in this chapter. . . . .	45
3.1	Block diagram of the two-element interferometer. . . . .	48
3.2	Deployed antenna, with the ground screen outlined. See Fig. 3.4 for dimensions.	49
3.3	The back end, shown in its portable enclosure. (a) Front of the back end. (b) Back of the back end. . . . .	50
3.4	Mechanical diagram of the antenna, drawn to scale. All dimensions are in centimeters. Only one leg of each mast is shown; there are two other identical legs mutually separated by $120^\circ$ to the pictured leg. Polypropylene guy wires (not shown, see e.g. Fig. 3.4) stabilize the masts. . . . .	51
3.5	Mechanical diagram of the antenna feed, drawn to scale. Dimensions are inches.	51
3.6	IT/PEC model of the projected effective length of the antenna at 47 MHz (left) and 74 MHz (right). Co-polarized components are shown. . . . .	54
3.7	MoM calculations of projected effective length of the antenna at 47 MHz (left) and 74 MHz (right). Co-polarized components are shown. . . . .	56
3.8	Comparison of $Z_A$ over an infinite PEC ground and over a real ground (medium and very dry) with the ground screen. Note the difference in $Z_A$ for the medium and very dry ground is negligible, such that the two curves are iden- tical. . . . .	57
3.9	The antenna terminals and the surrounding features. See Fig. 3.5 for dimensions.	58
3.10	Resulting $Z_A$ from full wave simulations including a detailed model of the feed.	59
3.11	Measured reflection coefficient at the antenna terminals. The different curves are for the two antenna; solid for Antenna A, dashed for Antenna B. . . . .	60
3.12	Impedance of the antenna. . . . .	60

3.13	Estimate of $R_{loss}$ . . . . .	62
3.14	Same as Fig. 3.12 but including estimated $C_p$ and $C_s$ determined in Section 5.2. . . . .	63
3.15	Ground loss efficiency for various ground conditions. . . . .	65
3.16	A fabricated FEE within its enclosure, with the cover removed. . . . .	67
3.17	Block diagram of the FEE. . . . .	67
3.18	Measured (solid) and predicted (dashed) gain and noise temperature of the FEE. . . . .	69
3.19	The parasitic impedance $Z_p$ . . . . .	70
3.20	The FEE input impedance $Z_{in}$ . . . . .	70
3.21	The receiver input impedance $Z_R$ . The nominal value is determined from the schematic (see Fig. G.1), assuming a constant $75 \Omega$ input impedance for the HELA-10. . . . .	71
3.22	Diagram of the cables connecting the FEE to the back end. . . . .	72
3.23	Measured and expected (from datasheet values) gain of the cable assemblies. . . . .	72
3.24	The ETA receiver within its enclosure. . . . .	74
3.25	Schematic diagram of the AAFs. . . . .	76
3.26	The fabricated AAFs. Note the AAF3 board also contains the dual high-pass version of AAF3, selectable with a switch, which was never used. . . . .	77
3.27	Measured gain of two AAFs in cascade. $Z_0 = 50\Omega$ . . . . .	77
3.28	Aliasing rejection of each AAF. . . . .	78
3.29	Measured cascade gain of the receiver, from the antenna terminals on the FEE to the input of the DRX. . . . .	79

3.30 (Left): Contributions to the apparent $T_{sys}$ . (Right): $T_{sky}$ relative to other sources of noise. . . . .	82
3.31 (Top): SEFD for each antenna. (Bottom): Resulting noise in the cross correlation. . . . .	83
3.32 Frequency band identification. The shaded regions indicate regions within 30–78 MHz in which data was not collected. . . . .	85
3.33 Block diagram of the Control Board. . . . .	88
3.34 A fabricated Control Board. . . . .	89
3.35 Block diagram of the Bias Board. . . . .	89
3.36 A fabricated Bias Board. . . . .	89
3.37 Normalized histogram of DRX output samples in each FEE calibration state.	91
3.38 Measured PSD at the output of the ARX in each state, for each antenna. $\Delta\nu = 1$ MHz, $\Delta t = 3.3$ ms. . . . .	92
3.39 Power spectrum from the observation considered in this section. The left pane is the time-average of each frequency bin. The bottom pane is the continuum power. $\Delta\nu = 65$ kHz, $\Delta t = 20$ s, 42 MHz center frequency. . . . .	93
3.40 Magnitude of the cross correlation. $\Delta\nu = 65$ kHz, $\Delta t = 20$ s, 42 MHz center frequency. . . . .	94
3.41 Phase of the cross correlation. $\Delta\nu = 65$ kHz, $\Delta t = 20$ s, 42 MHz center frequency. . . . .	95
3.42 Measured (solid) and modeled (dashed) fringes from Cas A ( $f_g \approx 1.3$ mHz). $\Delta\nu = 65$ kHz, $\Delta t = 20$ s, 42 MHz center frequency, 23:30-01:30 LST. Amplitude has been normalized for a unit RMS amplitude; i.e. this is not gain calibrated. . . . .	96

3.43	Power spectrum for an observation exhibiting significant RFI, indicated by the dashed outline boxes. $\Delta\nu = 65$ kHz, $\Delta t = 20$ s, 42 MHz center frequency.	97
3.44	Magnitude of the cross correlation for an observation exhibiting significant RFI. $\Delta\nu = 65$ kHz, $\Delta t = 20$ s, 42 MHz center frequency. . . . .	98
3.45	Same as Fig. 3.44, but in the cold state. $\Delta\nu = 65$ kHz, $\Delta t = 20$ s, 42 MHz center frequency. . . . .	98
3.46	Raw voltage samples before mitigation. $\Delta\nu = 8.33$ MHz, $\Delta t = 12$ $\mu$ s, 42 MHz center frequency. . . . .	99
3.47	Power spectrum for an observation after excising RFI. 0.38% of pixels excised. $\Delta\nu = 65$ kHz, $\Delta t = 20$ s, 42 MHz center frequency . . . . .	100
3.48	Magnitude of the cross correlation after excising RFI. 0.43% of pixels excised. $\Delta\nu = 65$ kHz, $\Delta t = 20$ s, 42 MHz center frequency . . . . .	101
4.1	Location of VLA-NA relative to the core of the VLA. The VLA-NA is in the boxed region, and is shown in Fig. 4.2. . . . .	103
4.2	Google Maps screen shot of the VLA-NA measurement site. The site's fence is indicated by the black square. Each side of the fence is 120 m. . . . .	104
4.3	Baselines used at the VLA-NA site. The site's fence is indicated by the square. $+x$ is East and $+y$ is North. The origin is at the Northwest corner of the fence, located at latitude, longitude $+34.2475^\circ$ , $-107.6416^\circ$ . . . . .	105
4.4	Google Maps screen shot of the Kelly Flats measurement site. . . . .	108
4.5	Source tracks of each source during the Cyg A measurements. Points are for every hour between 16:00-22:00 LST. (see Fig. 2.1 and associated text for interpretation.) . . . . .	110

4.6	Source tracks of each source during the Cas A measurements. Points are for every hour between 23:00-02:00 LST. . . . .	114
4.7	Source tracks of each source during the Vir A measurements. Points are for every hour between 11:00-14:00 LST. . . . .	114
4.8	Source tracks of each source during the Tau A measurements. Points are for every hour between 04:00-08:00 LST. . . . .	115
5.1	PSD ( $S_{out,i}$ ) in each state ( $i = 1, 2, 3$ ). $\Delta\nu = 65.1$ kHz, $\Delta t = 20$ s. . . . .	117
5.2	Cross correlation ( $\rho_{mn}$ ) in each state. $\Delta\nu = 65.1$ kHz, $\Delta t = 20$ s. . . . .	118
5.3	Measured PSD in each state, from each antenna. This is the same as the first time index in each state shown in Fig. 5.1. $\Delta\nu = 65.1$ kHz, $\Delta t = 20$ s. . . . .	120
5.4	Estimate of the receiver gain (top) and noise temperature (bottom) for each antenna, for the first iteration of the ATM phase of data reduction. . . . .	121
5.5	Estimate of $T_A$ from the first iteration of the ATM phase of data reduction. $\Delta\nu = 65.1$ kHz, $\Delta t = 20$ s. . . . .	122
5.6	Estimate of $T_{sky}$ from the first iteration of the ATM phase of data reduction. X-pol, $\Delta\nu = 65.1$ kHz, $\Delta t = 20$ s. . . . .	123
5.7	Same as Fig. 5.6, but now for all available observations and polarizations, and bias tails excluded. . . . .	124
5.8	Estimate of $T_{sky}$ after determining $C_p$ , $C_s$ , and $\Delta T_{cal}$ . . . . .	126
5.9	Cross correlation shown in Fig. 5.2 after transformation to the fringe rate domain. . . . .	127
5.10	Comparison of the estimated fringe rate to the expected fringe rate (top) at 42 MHz, and (bottom) at LST=20:00. . . . .	128

5.11	Same as Fig. 5.9, but after delay stopping using the estimated fringe rate shown in Fig. 5.10. . . . .	129
5.12	Cross correlation spectrum after fringe rate processing to isolate Cyg A. . .	130
5.13	Product of the transfer functions of the two receivers. . . . .	131
5.14	The projected effective length. . . . .	131
5.15	Flux density estimate of Cyg A from the OBS2 measurement. The dashed lines are the Baars flux scale and its associated error. . . . .	132
6.1	Flux density of Cyg A, estimated with the effective length computed by (left) MoM and (right) IT/PEC. Only data taken when Cyg A is greater than 70° above the horizon are included. The dashed lines represent the Baars flux scale and associated error. . . . .	134
6.2	Flux density of Cas A, estimated with the effective length computed by (left) MoM and (right) IT/PEC. The dashed lines represent the Baars flux scale and associated error. . . . .	135
6.3	Flux density of Vir A, estimated with the effective length computed by (left) MoM and (right) IT/PEC. The dashed lines represent the Baars flux scale and associated error. . . . .	136
6.4	Flux density of Tau A, estimated with the effective length computed by (left) MoM and (right) IT/PEC. The dashed lines represent the Baars flux scale and associated error. . . . .	136
6.5	Flux density estimate for every available each observation of Cyg A. The text above each frequency band lists the polarization, baseline, and $\theta$ in degrees at the middle of each observation. The dashed lines represent the Baars flux scale and its associated error. . . . .	138

6.6	Average of the observations shown in Fig. 6.5. Per-band power law fits are shown as dashed lines. The dashed lines represent the Baars flux scale and its associated error. . . . .	139
6.7	Final flux density of Cyg A. The circles indicate the nominal values; the error bars indicate the $1\sigma$ uncertainty. The dashed lines represent the Baars flux scale and its associated error. . . . .	139
6.8	Same as Fig. 6.5, but now for Cas A. . . . .	141
6.9	Same as Fig. 6.6, but now for Cas A. . . . .	141
6.10	Same as Fig. 6.7, but now for Cas A. . . . .	142
6.11	Same as Fig. 6.5, but now for Tau A. . . . .	143
6.12	Same as Fig. 6.6, but now for Tau A. . . . .	143
6.13	Same as Fig. 6.7, but now for Tau A. . . . .	144
6.14	Same as Fig. 6.5, but now for Vir A. . . . .	145
6.15	Same as Fig. 6.6, but now for Vir A. . . . .	145
6.16	Same as Fig. 6.7, but now for Vir A. . . . .	146
6.17	Estimate of $T_{sky}$ for each observation at 19:00 LST. $\Delta\nu = 65.1$ kHz, $\Delta t = 20$ s.	148
6.18	Average of the observations shown in Fig. 6.17. $\Delta\nu = 65.1$ kHz, $\Delta t = 20$ s. . . . .	148
6.19	Final estimate of $T_{sky}$ at 19:00 LST. $\Delta\nu = 65.1$ kHz, $\Delta t = 20$ s. . . . .	149
6.20	Final estimate of $T_{sky}$ for 23:30 LST. $\Delta\nu = 65.1$ kHz, $\Delta t = 20$ s. . . . .	149
6.21	Final estimate of $T_{sky}$ for 04:30 LST. $\Delta\nu = 65.1$ kHz, $\Delta t = 20$ s. . . . .	150
6.22	Final estimate of $T_{sky}$ for 11:30 LST. $\Delta\nu = 65.1$ kHz, $\Delta t = 20$ s. . . . .	150

A.1	Contribution of the Galactic background radiation to the cross correlation. The dashed line is Eq. (A.8). The solid line is the result of the numerical integration of Eq. (A.1) using the realistic (non-uniform) sky temperature distribution discussed in Section 2.2. . . . .	160
D.1	Model defining $T_R(Z_{cal})$ . . . . .	170
D.2	Modification of Fig. D.1 used to determine $T_R(Z'_A)$ . . . . .	170
E.1	Equivalent circuit of the calibration circuit. . . . .	172
E.2	Equivalent circuit of the calibration circuit for the noise diode calibration measurement. See text for explanation of the notation. . . . .	174
E.3	Block diagram of the test jig used in the $T_{cal}$ measurement. The displayed gain and noise figure (NF) are at the closest frequency to 50 MHz that is reported by the manufacturer. . . . .	174
E.4	Measured impedances used in the noise diode calibration measurement procedure. . . . .	175
E.5	Measured $Z_{cal}$ . . . . .	176
E.6	Measured gain and input-referred noise temperature of the test jig. The dots show the measured $G_{jig}(Z_0)$ , while the dashed line is the fit to the measurement. . . . .	176
E.7	Measured $G_{ATTN}$ . . . . .	177
E.8	PSD measured by the spectrum analyzer for the noise diode calibration measurement for the two FEEs. . . . .	177
E.9	Estimated PSD available to the test jig ( $S_1$ ) and available from the noise diode ( $S_D$ ). . . . .	178
E.10	Estimate of $T_{cal}$ . . . . .	178

E.11	Same as Fig. E.10, but with the modification $\Delta T_{cal}$ determined in Section 5.2.	179
G.1	Schematic of the FEE. “Feed1” and “Feed2” are the antenna terminals.	184
G.2	Bias and control circuit on the FEE PCB.	186
G.3	Layout of FEE. From top to bottom, the layers are top copper, ground plane, power plane, and bottom copper. The top silk screen layer is shown on all layers for reference.	187
G.4	Block diagram of the control circuit on the FEE PCB.	188
G.5	Schematic of the control board.	189
G.6	PCB layout of the control board. From top to bottom, the layers are top copper, ground plane, power plane, and bottom copper.	190
G.7	Schematic of the bias board.	191
G.8	PCB layout of the bias board. The top and bottom layers are top and bottom copper, respectively.	192
G.9	Schematic of the I/V Monitor board.	193
G.10	PCB layout of the I/V Monitor board. The top and bottom layers are top and bottom copper, respectively.	194
G.11	The fabricated I/V Monitor board.	195
H.1	Block diagram of a general receiver.	198
I.1	Coordinate distances and notation used to estimate the baselines used in the VLA-NA campaign.	200

# List of Tables

1.1	Summary of low frequency flux density information. . . . .	6
1.2	Summary of the instruments used in the absolute flux density measurements listed in Table 1.1. . . . .	9
2.1	Astronomical data for the A-Team sources. Flux density values are for 81 MHz, from the Baars flux scale [13]. Cas A has been further scaled by $-0.75\%/year$ per [4], to the current (2016) epoch. . . . .	15
2.2	Nominal observing times for each source, assuming 2 hr observations (see text).	17
2.3	Priors required for the absolute flux density and Galactic background noise measurements, and where they are determined in this dissertation. . . . .	46
3.1	Comparison of the new FEE to those of other contemporary radio telescopes.	68
3.2	GNL analysis of the ETA receiver. These values are approximately independent of frequency over 30–78 MHz. . . . .	80
3.3	GNL stage-cascade analysis of the receiving system used in the two-element interferometer at 42 MHz, the center of band 2 (see Section 3.8). . . . .	81

4.1	Components of the baseline vectors used at the VLA-NA. $+x$ is East and $+y$ is North. Antenna A is taken as the origin for each baseline. The uncertainty of each coordinate is $<10$ m. . . . .	106
4.2	Observations collected during the VLA-NA measurement campaign. Missing observations (e.g. OBS3, OBS6-9) were planned, but were not performed due to time constraints. . . . .	107
4.3	Observations collected during the Kelly Flats measurement campaign. The asterisks indicate datasets that were not used in the results presented in this work (see text). . . . .	108
4.4	Data used in the flux density estimates of Cyg A. Horizontal spaces demarcate the frequency bands. . . . .	109
4.5	Data used in the flux density estimates of Cas A. Horizontal spaces demarcate the frequency bands. . . . .	111
4.6	Data used in the flux density estimates of Vir A. Horizontal spaces demarcate the frequency bands. . . . .	112
4.7	Data used in the flux density estimates of Tau A. Horizontal spaces demarcate the frequency bands. . . . .	113
5.1	Prior measurements required to estimate $G_R(Z'_A)$ . . . . .	119
5.2	Additional priors required to estimate $T_R(Z'_A)$ and $T_{sky}$ . . . . .	121
5.3	Modifications to the priors used by the ATM. See text for details. . . . .	125
6.1	Summary of new flux density estimates for the A-Team sources. . . . .	146
6.2	Summary of the measurements of $T_{sky}$ . $T_{ref}$ is given for $\nu_{ref} = 58$ MHz. . . . .	151
6.3	Comparison between $T_{sky}$ determined by this work to the model (GSM+IT/PEC)	151

G.1	Bill of materials for the FEE, including the enclosure, mechanical parts, and temperature sensors. The different sections, demarcated by the double lines, indicate parts procured from different distributors; from top to bottom, these distributors are Digikey, Lowe's, Mouser, Mini-Circuits, Mercury, OnSet, and ExpressPCB. Total cost is for 4 FEEs, and includes spare parts. . . . .	185
G.2	DC voltages on which the FEE changes its calibration state. . . . .	186
G.3	Bill of materials for each AAF. Nyquist zone and corner frequency ( $\nu_c$ ) are indicated for each filter. Digikey is the distributor for all parts. . . . .	196
I.1	Measured distance between the antenna locations and the VLA-NA fence posts.	200
I.2	GPS coordinates for the antennas during the Kelly Flats measurement campaign.	200

# Chapter 1

## Introduction

Low frequency ( $\sim 300$  MHz and below) radio astronomy has seen an increase in attention over the last two decades. This renewed interest is due in part to the development of techniques for mitigating the phase error introduced by the ionosphere, which allows for imaging at resolutions comparable to that achieved at higher frequencies; and in part to the emergence of wideband digital beamforming arrays, which now provide sufficient collecting area for useful sensitivity. Some prominent examples of new arrays include the first station of the Long Wavelength Array<sup>1</sup> (LWA1) in New Mexico [1], the LOw Frequency ARray<sup>2</sup> (LOFAR) in the Netherlands [2], the Murchison Widefield Array<sup>3</sup> (MWA) in Australia [3], and the “Phase I Low Frequency” component of the Square Kilometer Array<sup>4</sup> (SKA) planned for construction in Australia.

Science topics motivating the use of low frequencies in astrophysics include:

- Studies of astrophysical objects such as supernova remnants (e.g. [4]) and pulsars (e.g. [5, 6]).

---

<sup>1</sup><http://lwa.unm.edu/>

<sup>2</sup><http://www.lofar.org/>

<sup>3</sup><http://www.mwatelescope.org/>

<sup>4</sup><http://www.skatelescope.org/>

- Studies of the ionosphere (e.g. [7, 8, 9]).
- Studies of cosmic rays (e.g. [10, 11]).
- Cosmology, including the Epoch of Reionization and “Cosmic Dawn” (see e.g. [12]).

The new arrays identified above have recently begun to produce their first science results. A recurring issue brought to light in these results is a lack of accurate flux density<sup>5</sup> calibration. Flux density calibration is typically performed by first measuring the power received from an unresolved (angular dimension much smaller than the array’s half-power beamwidth) source of known flux density, and then solving for and subsequently calibrating out the system response from the measurement. Figure 1.1 shows the flux density spectra from the widely-used Baars *et al.* (1977) flux scale [13] for the “A-Team” sources. These are Cygnus A (Cyg A), Cassiopeia A (Cas A), Taurus A (Tau A), and Virgo A (Vir A); the brightest sources visible from the northern hemisphere. At frequencies above  $\sim 400$  MHz, the absolute flux densities of these and other sources are accurately known and well-modeled by a power law in frequency (see Section 1.1), which allows for accurate extrapolation to other frequencies. At lower frequencies, however, the flux densities are not accurately known. This is due in part to a lack of measurements, and in part to limited accuracy of the existing measurements. The inaccuracy of existing measurements is due to the difficulty of separating the source flux from the bright background noise, as will be explained in Section 1.1. Complicating the situation further is the fact that the flux density spectrum “turns over” in this frequency regime [14].<sup>6</sup>

This dissertation reports new estimates of the flux densities of the A-Team sources between 30–78 MHz. The uncertainty on these measurements is  $\mathcal{O}[10\%]$  at frequencies with no other comparable measurement, validating the existing flux density models in this frequency range.<sup>7</sup> The new estimates are summarized in Section 1.2.1, and are documented in Chap-

---

<sup>5</sup>Flux density is power per unit area per unit bandwidth. Flux density is typically reported in janskys (Jy) where  $1 \text{ Jy} = 10^{-26} \text{ W m}^{-2} \text{ Hz}^{-1}$ .

<sup>6</sup>“Turn over” refers to a change in slope from positive to negative with increasing frequency.

<sup>7</sup>All reported errors in this dissertation represent  $1\sigma$  uncertainty with respect to the mean, unless otherwise

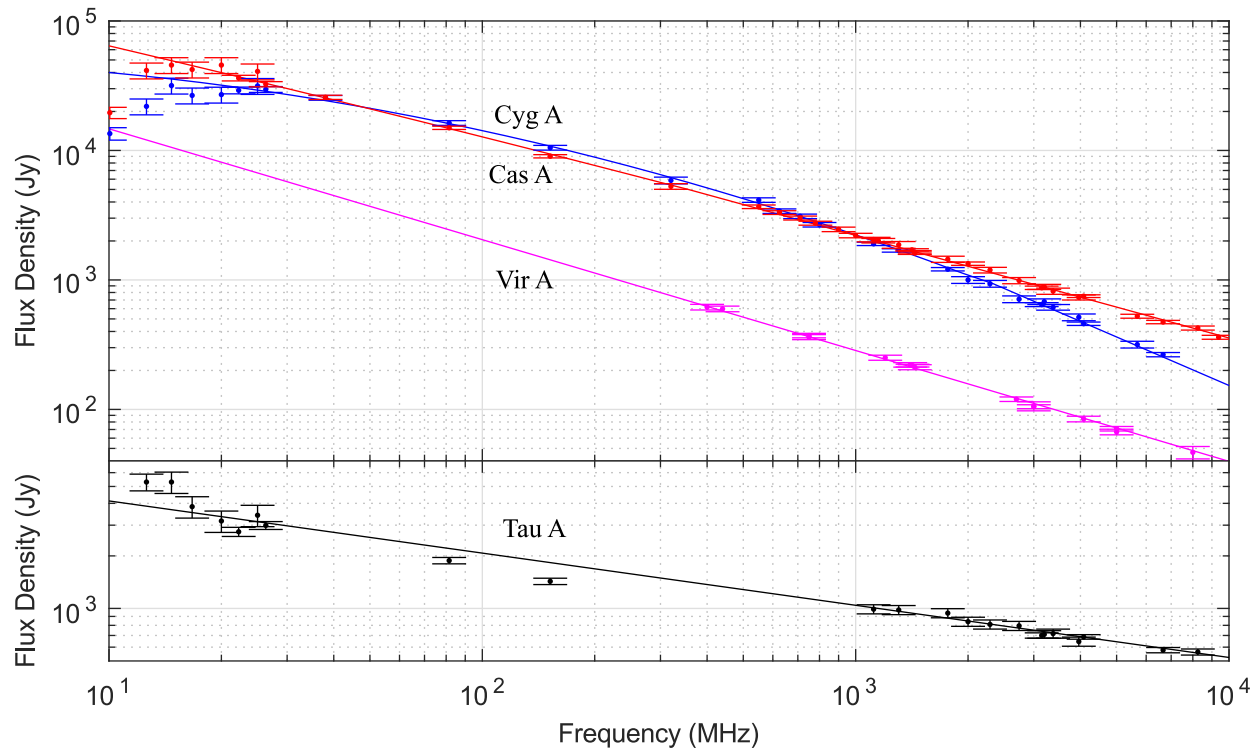


Figure 1.1: Flux density estimates and associated error, epoch 1965, used in the Baars *et al.* flux scale (see text). The power law fit to the measurements is also shown.

ter 6. The techniques used to obtain these estimates are summarized in Section 1.2.3 and documented in Chapters 2 and 3.

The rest of this chapter is organized as follows. The state of the art in flux density measurements is reviewed in Section 1.1. Section 1.2 summarizes the contributions of this research. Finally, Section 1.3 provides the organization of this dissertation.

---

stated.

## 1.1 Existing State of the Art for Low Frequency Flux Density Calibration

Several new instruments have accompanied the re-emergence of low frequency radio astronomy, as discussed previously. These new instruments are arrays consisting of tens to thousands of dual-polarized dipole-type antennas combined using digital signal processing to act as a beamforming array and/or imaging interferometer.

Flux density calibration of these instruments is desirable or necessary for most science applications. However, the new instruments themselves are ill-suited to perform absolute flux density measurements. The reason for this is twofold. First, these systems use relatively complex antennas (see examples in Fig. 1.2) with the result that the antenna response is difficult to accurately predict or measure; and therefore difficult to calibrate out of the measurement. The antenna response is further complicated due to strong mutual coupling associated with the close spacing between antennas in the arrays which these antennas are located. Second, these instruments have no internal gain or noise calibration, due to the cost and complexity associated with fitting every antenna with this capability. (The use of internal calibration in absolute flux density measurements is discussed in Chapter 2.)

To accurately measure the absolute flux densities of astrophysical sources in the project reported in this dissertation, new instrumentation was developed. The new instrument, documented in Chapter 3, uses the simplest possible antennas, separated by 10s of wavelengths to mitigate against coupling, and with internal gain and noise calibration.

Table 1.1 provides a summary of the best available flux density measurements at low frequencies. Note the errors are on the order of 10s of percent. The relative flux density measurements and the flux scales are derived from, and are therefore limited by the accuracy of, the absolute flux density measurements. Flux scales are models of the flux density derived from the absolute and relative measurements, which allows for interpolation/extrapolation to other frequencies. The most commonly-used flux scale is that of Baars *et al.* (1977), which

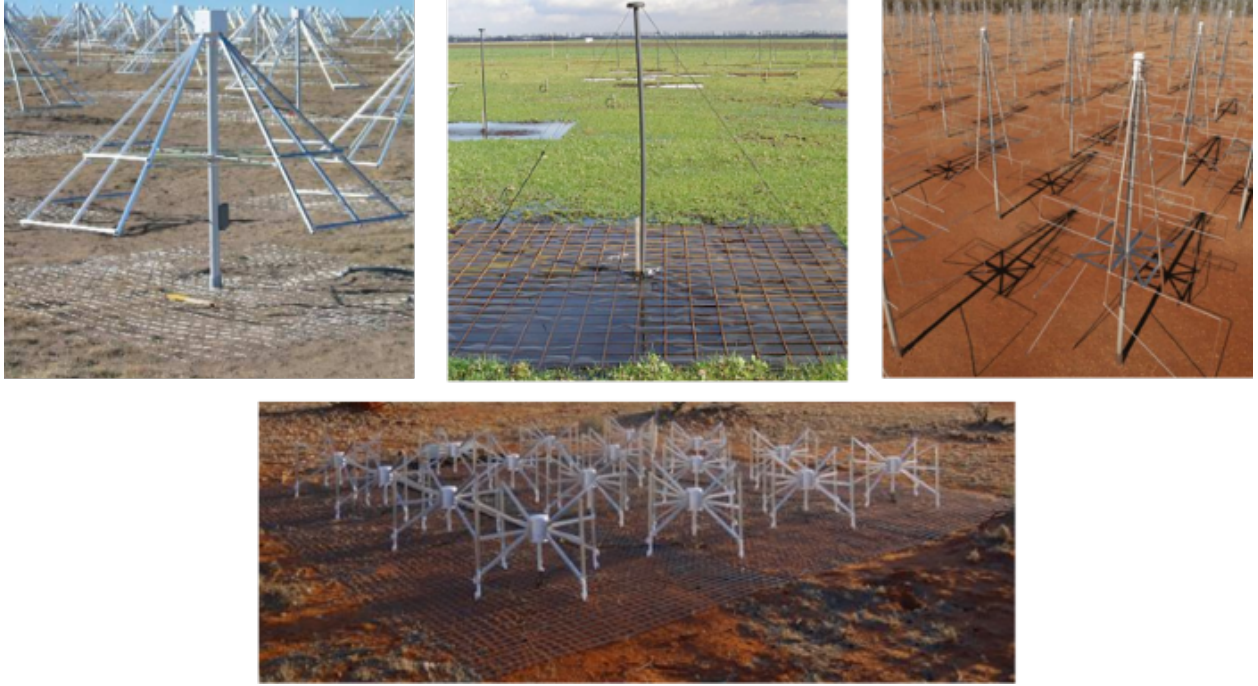


Figure 1.2: Antennas used in (top left to right) LWA1, LOFAR, SKA-Lowband Array (artist representation), and (bottom) MWA.

uses the model

$$\log_{10} S_{\nu}^{src} = a + b \log_{10} \nu_{\text{MHz}} + c \log_{10}^2 \nu_{\text{MHz}} \quad (1.1)$$

where  $S_{\nu}^{cal}$  is the flux density of the source,  $\nu_{\text{MHz}}$  is frequency in MHz, and the constants  $a$ ,  $b$ , and  $c$  are chosen to fit the model to the available measurements [13]. For many sources  $c$  is negligible, such that the flux scale model may be represented in the form

$$\begin{aligned} S_{\nu}^{src} &= 10^{a+b \log_{10} \nu_{\text{MHz}}} \\ &= S_{\nu}^{ref} \left( \frac{\nu_{\text{MHz}}}{\nu_{ref}} \right)^{\alpha} \end{aligned} \quad (1.2)$$

where

$$S_{\nu}^{ref} = 10^a \nu_{ref}^{\alpha} \quad (1.3)$$

is the flux density of the source at a frequency  $\nu_{ref}$ , and  $\alpha = b$  is referred to as the “spectral index”.

Table 1.1: Summary of low frequency flux density information.

Reference	Sources	$\nu$ MHz	% Error
<i>Absolute Flux Density Measurements</i>			
Wells 1958 [15]	Cas A & Cyg A	18.5, 27, 50, 87, 108	$\sim 20$
Braude <i>et al.</i> 1962 [16]	Cas A	19.5, 20.5, 22, 24, 25, 28, 29.5, & 31	$\sim 20$
Bridle 1967 [17]	Cas A & Cyg A	10.05	$\sim 10$
Parker 1968 [18]	A-Team (except Vir A)	38, 81.5, & 152	$\sim 5$
Braude <i>et al.</i> 1969 [19]	80 sources	12.6, 14.7, 16.7, 20, & 25	$\sim 20$
Viner 1975 [20]	A-Team	26.3	$\sim 10$
<i>Relative Flux Density Measurements</i>			
Roger <i>et al.</i> 1969 [21]	200 sources	22.25	$\sim 10$
Viner & Erickson 1975 [22]	471 sources	26.3	$\sim 15$
Kassim 1988 [23]	702 sources	30.9	$\sim 20$
Jacobs <i>et al.</i> 2011 [24]	480 sources (south. hem.)	145	$\sim 20$
<i>Flux Scales</i>			
Baars 1977 <i>et al.</i> [13]	A-Team & 13 others	400-15000	$\sim 5$
Helmboldt 2008 <i>et al.</i> [25]	388 sources	74	$\sim 1$
Scaife and Heald 2012 [26]	6 sources	30-300	$\sim 20$
Jacobs <i>et al.</i> 2013 [27]	32 sources (south. hem.)	100-200	$\sim 5$

At low frequencies, the emission from the Galactic synchrotron radiation results in bright background noise present everywhere in the sky. Figures 1.3 and 1.4 show the sky background at two representative local sidereal times (LST) from the popular Global Sky Model (GSM) of de Oliveira-Costa *et al.* [28]. This illustrates why dish antennas and phased arrays are impractical for flux density measurements at low frequencies: A large, unknown amount of flux will enter the main beam (since the sources have angular dimensions which are typically less than a beamwidth) and sidelobes from the background.

Single dipole antennas acting as an interferometer are better suited for flux density measurement of discrete sources in this frequency regime. Figure 1.5 shows a simple diagram of a two-element interferometer that may be used to isolate the source flux density from the background. The signal from the source arrives at one antenna at a delay  $\tau_g$  relative to the second antenna. This delay results in a phase shift in the recorded output of the correlator  $\rho_{12}$ . The delay changes as the Earth rotates, giving rise to a time-varying rotation in the

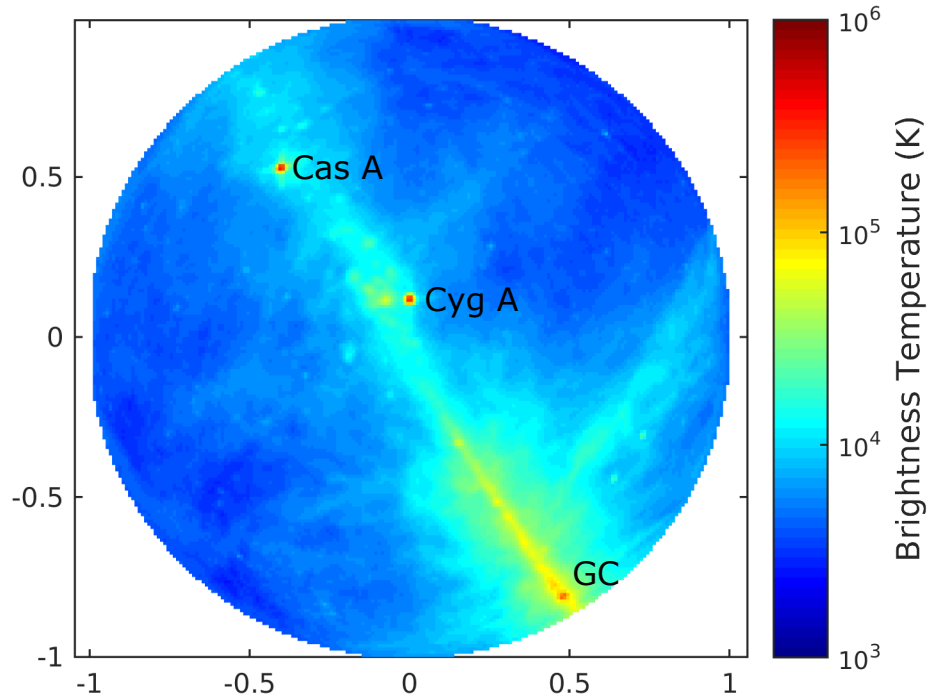


Figure 1.3: The 50 MHz radio sky above at a latitude of  $+34^\circ$  at 20:00 LST, corresponding to Cyg A's transit. The zenith is at the origin, and the horizon is the perimeter of the circle. GC is the Galactic center.

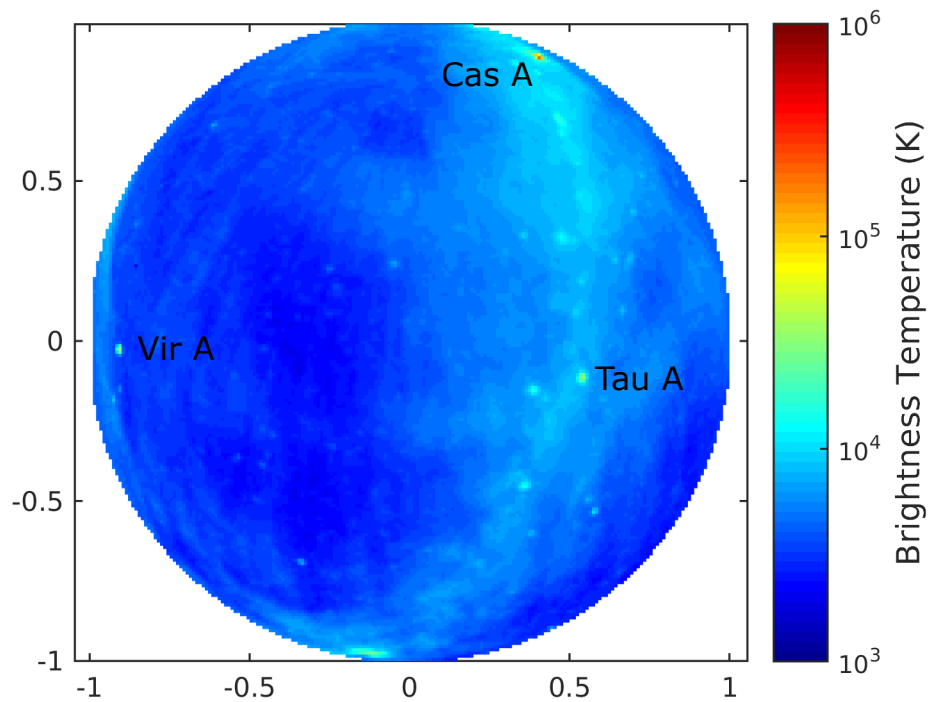


Figure 1.4: Same as Fig. 1.3, but at 08:00 LST.

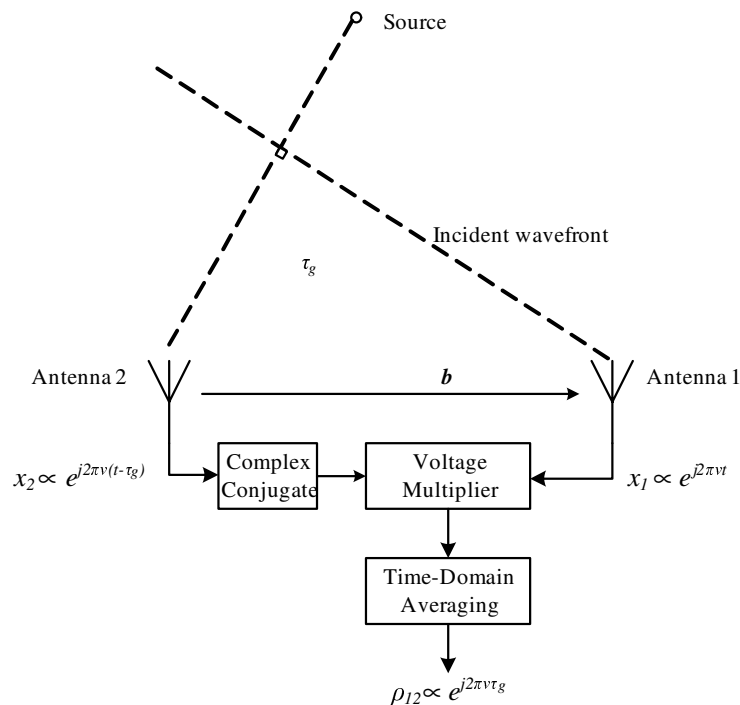


Figure 1.5: Simplified schematic of a two-element interferometer.

phase of  $\rho_{12}$ . On the other hand, the background noise is ever-present, and de-correlates for sufficiently separated antennas (see Appendix A). The individual spatial contributions to  $\rho_{12}$  may be identified using Fourier analysis, as described in Section 2.4.

Table 1.2 summarizes the systems used in each of the absolute flux density measurements identified in Table 1.1. With only two exceptions (noted), each system is a two-element interferometer oriented along an East-West (E-W) baseline.<sup>8</sup> Use of simple dipole antennas facilitates accurate estimation of the antenna response,<sup>9</sup> and the large antenna separation makes mutual coupling negligible, along with the associated error in the calculated antenna response. Gain calibration was performed using a model of the system path, while noise calibration was performed through the use of a calibrated noise source.

<sup>8</sup>An E-W baseline is used as this maximizes the fringe rate (see Section 2.4).

<sup>9</sup> While true in principle, the uncertainty of the antenna response dominates the uncertainty of the flux density measurements reported in this work. Similarly, uncertainty of the antenna response is likely the primary limitation of the previous measurements summarized in Table 1.1.

Table 1.2: Summary of the instruments used in the absolute flux density measurements listed in Table 1.1.

Reference	Antenna	Baseline	$\nu_{\text{MHz}}$
Wells 1958	Folded dipoles over ground screen	30-150 m	18.5, 27, 50, 87, & 108
Braude <i>et al.</i> 1962	$4 \times 6$ cophased dipoles	150 m	19.5, 20.5, 22, 24, 25, 28, 29.5, & 31
Bridle 1967	Cophased $\lambda/2$ dipoles	900 m	10.05
Parker 1968	$\lambda/2$ dipoles over ground screen	280 m	38, 81.5, & 152
Braude <i>et al.</i> 1969	$\lambda/2$ dipoles in a T-shaped phased array	†	12.6, 14.7, 16.7, 20, & 25
Viner 1975	$\lambda$ dipoles in a grating array with a $\lambda/2$ outrigger	†	26.3

†Not an interferometer.

Limitations of the measurements in Table 1.1 that impact modern radio astronomy are the  $\mathcal{O}[10\%]$  errors and the large spacing between measurements above  $\sim 25$  MHz. Figure 1.6 demonstrates this impact. In this example, Tau A is used to calibrate observations of the Crab Pulsar (B0531+21), which is embedded within Tau A.<sup>10</sup> Combining the best-available data at 22 MHz (6% error) [21] and 81 MHz (4.2% error) [18] with the best available spectral index estimate ( $\alpha = -0.27 \pm 0.08$ ) derived from candidate power laws, the true flux density may be anywhere within the shaded region. Improvement requires more-accurate source flux density values, and at a sufficient number of frequencies to allow for the derivation of accurate frequency scaling models. Such measurements are reported in this dissertation, constituting the primary contribution of this work.

<sup>10</sup>This example is adapted from a problem in flux calibration reported in [29].

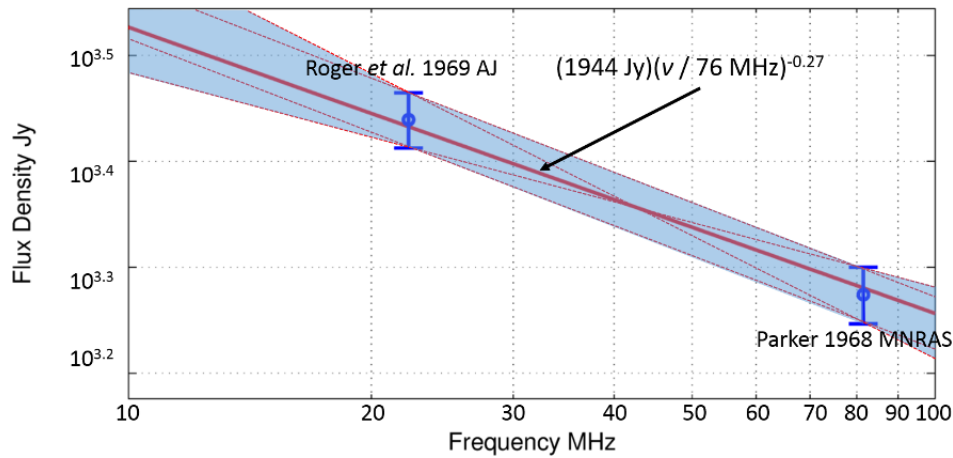


Figure 1.6: Flux density for Tau A and associated error, using the current best available absolute flux density measurements.

## 1.2 Contributions Reported in this Dissertation

### 1.2.1 New Flux Density Measurements

Figure 1.7 summarizes the results of the new measurements, compared to the Baars flux scale and the measurements therein. The objective is not yet to modify or replace this flux scale, but simply to generate new measurements (and techniques for making such measurements) that might be used for this purpose in the future. The measurements span the frequency range between 30–78 MHz. An interpretation of these results is presented Section 6.2

### 1.2.2 Measurement of the Diffuse Sky Emission in 30–78 MHz

The new source flux density measurements require accurate measurement of the system gain, noise, and antenna impedance. A side product of this work is an accurate measurement of the diffuse Galactic synchrotron radiation. This in itself has applications in cosmology [30, 31], ionospheric studies (e.g. [32]), and riometry (e.g. [33]). The new measurements are presented in Section 6.3. The measured spectral index ranges from  $-2.15$  to  $-2.65$  depending on LST and antenna orientation. This is in good agreement with the measurements at higher

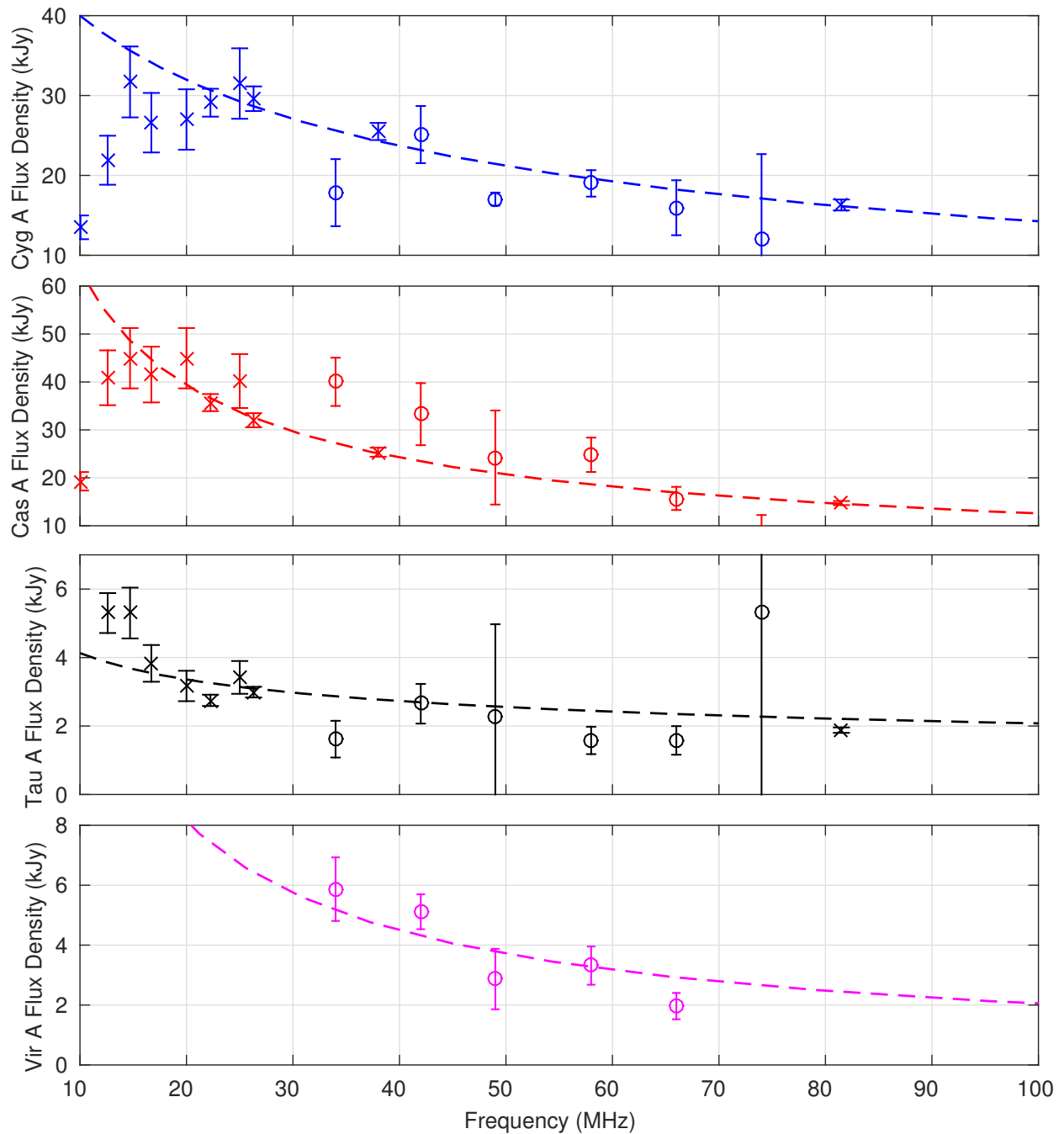


Figure 1.7: The new flux density measurements reported in this dissertation. Measurements from this work are denoted by an “o”, and the measurements shown in Fig. 1.1 are denoted by an “x”. The dashed line is the Baars flux scale.

frequencies, which predict a spectral index of about  $-2.5$ .

### 1.2.3 Improved Instrumentation and Techniques

The new source flux density measurements were facilitated by improved instrumentation and techniques. The instrument is based on a new active antenna system employing highly-linear front ends (also reported in [34]), which facilitate measurements at locations with significant radio frequency interference (RFI); and internal gain and noise calibration. Two active antennas are operated as a two-element interferometer, similar to several of the instruments detailed in Table 1.2. However, the voltages from each antenna are recorded ( $x_1$  and  $x_2$  in Fig. 1.5), as opposed to the output of a correlator ( $\rho_{12}$  in Fig. 1.5). This allows for improved RFI mitigation; RFI is excised before the signals are correlated. Furthermore, measurements were made on multiple baselines, as opposed to an East-West baseline alone, as a means to mitigate systematics and thereby reduce measurement uncertainty. Chapter 3 provides further details of the instrumentation, and Chapter 4 provides further details of the measurement setup.

The measurements summarized in Tables 1.1 and 1.2 are narrowband and used antennas that are well-matched to the receiver over the narrow bandwidth. Additionally, precise measurements of the diffuse sky emission have previously been reported which used antennas that are well matched to the receiver over a wide bandwidth [35]. This work, in contrast, presents precise interferometric and radiometric measurements using narrowband dipoles, which exhibit large impedance mismatch over the majority of the frequency band. This is achieved by precisely accounting for the effect of the mismatch on the receiver, and by employing the measurement of the diffuse Galactic emission as an aid in the calibration. The technique is described in Chapter 2, and summarized in Fig. 2.15.

### 1.2.4 Determination of Practical Limits in the Sensitivity-Linearity Tradeoff in Front End Design

One challenge in the design of instrumentation for modern low frequency radio astronomy is achieving the required sensitivity with sufficient linearity. High linearity is important due to the presence of strong RFI at these frequencies. In the process of designing the instrumentation for the absolute flux density measurements, new design principles were developed that apply to a broad range of applications. A survey of commercially-available monolithic microwave integrated circuit (MMIC) amplifiers appropriate for use in radio astronomy and other applications was performed to characterize the sensitivity-linearity tradeoff. Additionally, this work quantified the benefits of combining amplifiers in (1) balanced configurations and in (2) parallel configurations of balanced amplifiers as a means of improving the linearity of front ends. This work resulted in a journal paper [34], elements of which appear throughout this dissertation.

## 1.3 Organization of this Dissertation

This dissertation is organized as follows. Chapter 2 (“Methodology”) describes the methodology used to obtain the absolute flux density measurements. Chapter 3 (“Instrumentation”) documents the new instrumentation developed to perform the absolute flux density measurements. Chapter 4 (“Measurement Campaign”) documents the campaign to collect the data for the flux density measurements, which was carried out between May 2015 and January 2016. Chapter 5 (“Data Reduction”) documents the data reduction and absolute calibration used to obtain estimates of the flux densities for the A-Team sources from the data collected during the measurement campaign. The culmination of the work in Chapters 2-5, the new flux density estimates, is presented in Chapter 6 (“Results”). Finally, conclusions and suggestions for future work are discussed in Chapter 7 (“Summary and Future Work”).

# Chapter 2

## Methodology

This chapter documents the methodology used to perform absolute flux density measurements in this work. Sections 2.1 and 2.2 describe the characterization of the sources and the Galactic background, respectively. Section 2.3 describes the system model of the interferometer used for the measurement. Section 2.4 presents the signal processing techniques used to isolate the signal of interest in the interferometric data. Section 2.5 presents the “Antenna Temperature Model” (ATM), an alternative model used to determine system parameters required to calibrate the measurement. Section 2.6 describes how the prior measurements and parameters (priors) required in the calibration are determined *in situ* using the ATM. Section 2.7 presents the “Coherent Interferometry Model” (CIM), a special case of the model described in Section 2.3, which is used to estimate the source flux densities. Finally, Section 2.8 (in particular Fig. 2.15) summarizes the methodology.

### 2.1 Characterization of Sources

Table 2.1 shows relevant astronomical parameters for the A-Team sources. The ideal source for flux density calibration of a low frequency telescope is unresolved (i.e. much smaller in

Table 2.1: Astronomical data for the A-Team sources. Flux density values are for 81 MHz, from the Baars flux scale [13]. Cas A has been further scaled by  $-0.75\%/year$  per [4], to the current (2016) epoch.

Source	3C ID	Type	Right Ascension [hr:min:sec]	Declination [ $^{\circ}$ ,',"]	$S_{81}^{src}$ [Jy]	Size [arcmin]
Cyg A	3C405	Galaxy	19:59:28	40:44:02	$16200 \pm 680$	3.5
Cas A	3C461	Supernova	23:23:28	58:48:42	$14600 \pm 800$	5.5
Vir A	3C274	Galaxy	12:30:49	12:23:28	$2500 \pm 125^{\dagger}$	7.4
Tau A	3C144	Supernova	5:34:32	22:00:52	$1880 \pm 79$	6

$\dagger$ There are no absolute flux density measurements of Vir A at this frequency. The value reported here is obtained by extrapolation using the Baars flux scale.

angular dimension than the telescope’s half-power beamwidth), bright enough to be easily distinguishable over the bright sky background (see e.g. Figs. 1.3 and 1.4), and essentially invariant over long (decades) time scales. The time-invariance criterion makes bright radio galaxies, such as Cyg A and Vir A, attractive sources. Supernova remnants such as Cas A and Tau A are bright, but have flux density values which exhibit a gradual decrease on the order of fractions of a percent per year [4, 36]. This decrease may need to be accounted for when using supernova remnants as flux density calibration sources.

It is necessary to know where each source is located in the sky during the absolute flux density measurement. Appendix B presents the relationship between the equatorial coordinates of the sources, as given in Table 2.1, to local spherical coordinates. Figure 2.1 shows the tracks traced out by the A-Team sources when observed over a sidereal day at a latitude of  $+34^{\circ}$ , roughly that of the VLA, where most of the measurements reported in this work were made (see Chapter 4).

The antennas used in the absolute flux density measurements are horizontal dipoles, nominally having maximum gain near zenith (see Section 3.1.2). Therefore, the sources are best observed near transit (i.e. when crossing the prime meridian, the vertical axis in Fig. 2.1) to maximize the signal-to-noise ratio. With this in mind, Table 2.2 lists the nominal observing

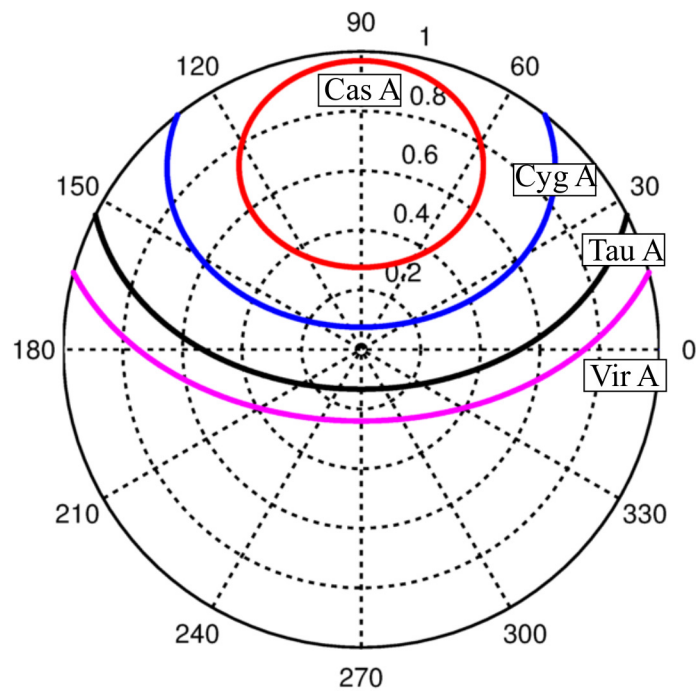


Figure 2.1: Source tracks for the A-Team sources at a latitude of  $+34^\circ$ , approximately that of the VLA. The angle is  $\phi$  (east at  $\phi = 0^\circ$ , north at  $\phi = 90^\circ$ ), and the radius is  $\cos\theta$ , where  $\theta$  is the zenith angle.

Table 2.2: Nominal observing times for each source, assuming 2 hr observations (see text).

Source	Start LST HH:MM	Stop LST HH:MM
Tau A	04:34	06:34
Vir A	11:31	13:31
Cyg A	18:59	20:59
Cas A	23:23	01:23

times for each source. The times are given in Local Sidereal Time (LST), defined here as the right ascension at the intersection of the prime meridian and the southern horizon. Observations are scheduled such that the source transits in the middle of the observation, with the exception of Cas A. Cas A observations begin at the transit of Cas A to better isolate from Cyg A (more on this in Section 2.4).

## 2.2 Characterization of the Galactic Background Noise

At the low frequencies considered in this work, natural noise is dominated by the Galactic synchrotron background radiation, resultant from charged particles accelerated to relativistic speeds in the interstellar medium. Contributions from other sources, such as the  $\approx 2.7$  K cosmic microwave background, are negligible by comparison.

The sky noise's contribution to antenna temperature is given by (see e.g. [37])

$$T_{sky} = \frac{1}{\Omega_A} \iint_{\theta, \phi} T(\theta, \phi) P(\theta, \phi) d\Omega \quad (2.1)$$

where  $\Omega_A$  is the antenna's beam solid angle,  $P(\theta, \phi)$  is the antenna's normalized power pattern,  $T(\theta, \phi)$  is the sky noise distribution (e.g. Figs. 1.3 and 1.4), and  $d\Omega$  is the differential element of solid angle. Using the popular Global Sky Model (GSM) of de Oliveira-Costa *et al.* [28] and a model for the antenna pattern, Eq. (2.1) may be used to compute  $T_{sky}$  as a function of frequency and LST.

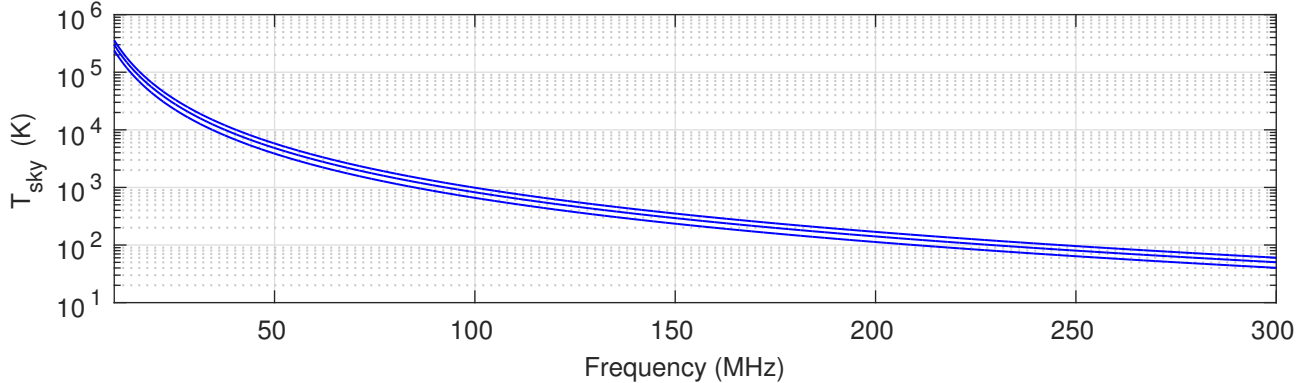


Figure 2.2: Contribution of the Galactic synchrotron background to the antenna temperature of a dipole-type antenna isolated from ground loss according to Eq. (2.2). The center curve is the daily mean value whereas the upper and lower curves represent the typical limits due to diurnal variation at about  $+34^\circ$  latitude.

For a low-gain antenna,  $T_{sky}$  is well-modeled by the power law

$$T_{sky} \approx T_{ref} \left( \frac{\nu}{\nu_{ref}} \right)^\alpha \quad (2.2)$$

where  $\nu$  is frequency,  $T_{ref}$  is the value of  $T_{sky}$  at the reference frequency  $\nu_{ref}$ , and  $\alpha$  is the spectral index. As an example, Fig. 2.2 shows Eq. (2.2) with  $T_{ref} = 9120$  K at  $\nu_{ref} = 39$  MHz, and  $\alpha = -2.55$  (these parameters were derived in Appendix I of [38]). The diurnal variation of about  $\pm 20\%$  is indicated in Fig. 2.2, with the maximum corresponding to the transit of the Galactic center ( $\sim 17:00$  LST). The value of this particular model in the present work is as a “sanity check” of the measured antenna temperature, which is an intermediate product on the way to source flux density estimation.<sup>1</sup>

## 2.3 Comprehensive System Model (CSM)

This section presents the “Comprehensive System Model” (CSM) for a two-element interferometer. The CSM is used to identify the system parameters that must be characterized

<sup>1</sup>To emphasize this point, we do not expect the difference between a measurement of  $T_{sky}$  and Eq. (2.2) to be a metric of the error in the measurement.

for the absolute flux density measurements, and to facilitate the discussion in Section 2.4 regarding isolation of the source from the Galactic background noise.

Consider the problem shown in Fig. 2.3. The source is modeled by a monochromatic plane wave  $\mathbf{E}^{src}(\mathbf{r}, t)$  having units of  $\text{V m}^{-1} \text{ Hz}^{-1/2}$ , at frequency  $\nu$ , from a direction  $\hat{\mathbf{s}}$  with flux density  $S_\nu^{src}$ . The vector  $\mathbf{r}$  denotes the point in space where the field is sampled. For an unpolarized wave, the flux density represented by  $\mathbf{E}^{src}(\mathbf{r}, t)$  is divided equally between any two unit vectors that are mutually orthogonal to  $\hat{\mathbf{s}}$  (see e.g. [39, Chapter 5]). Thus, the electric field from the source may be written as

$$\mathbf{E}^{src}(\mathbf{r}, t) = (\hat{\boldsymbol{\theta}}c_\theta(t) + \hat{\boldsymbol{\phi}}c_\phi(t)) \frac{E_\nu^{src}}{\sqrt{2}} e^{j\beta\hat{\mathbf{s}}\cdot\mathbf{r}} \quad (2.3)$$

where  $c_\theta(t)$  and  $c_\phi(t)$  are independent, complex-valued, zero-mean, unit-variance, Gaussian-distributed random variables,  $E_\nu^{src}$  is the root-mean-square (RMS) electric field amplitude, and  $\beta$  is the wavenumber. The flux density is related to the field intensity by

$$\begin{aligned} S_\nu^{src} &= \frac{\langle |\mathbf{E}^{src}(\mathbf{r}, t)|^2 \rangle}{\eta} \\ &= \frac{|E_\nu^{src}|^2}{\eta} \end{aligned} \quad (2.4)$$

where  $\langle \cdot \rangle$  represents time-domain averaging, and  $\eta \approx 376.7 \Omega$  is the wave impedance of free space.

In addition to the plane wave incident from the source, the antenna also receives signals from other celestial sources, the Galactic background noise, and RFI. RFI is assumed to have been mitigated, and will not be considered here; mitigation of RFI is discussed in Section 3.11.

As already stated, the Galactic background noise may be described by a temperature distribution  $T(\psi)$ , where  $\psi$  denotes a point  $(\theta, \phi)$  on the sky. For the frequency range considered in this work, the flux density from a direction  $\psi$  is well approximated by the Rayleigh-Jeans

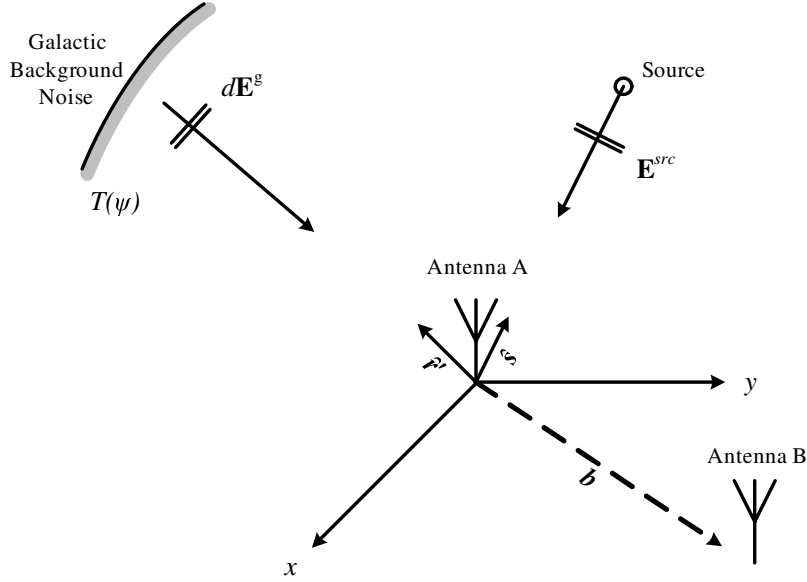


Figure 2.3: Diagram for the two-element interferometer system model.

law (see e.g. [14])

$$dS^g(\psi) \cong \frac{2k}{\lambda^2} T(\psi) d\Omega \quad (2.5)$$

Since the radiation from the Galactic synchrotron noise and other astrophysical sources is unpolarized at the spatial resolutions considered in this work, we can again make the assumption that the flux density is divided equally between the two basis vectors  $\hat{\boldsymbol{\theta}}$  and  $\hat{\boldsymbol{\phi}}$ . The contribution to the electric field from the portion of the sky in the  $\hat{\mathbf{r}}'(\psi)$  direction is then

$$d\mathbf{E}^g(\mathbf{r}, \psi, t) = (\hat{\boldsymbol{\theta}}g_{\theta}(\psi, t) + \hat{\boldsymbol{\phi}}g_{\phi}(\psi, t)) \sqrt{\frac{2\eta k}{\lambda^2}} e^{j\beta\hat{\mathbf{r}}'(\psi)\cdot\mathbf{r}} \sqrt{T(\psi)d\Omega} \quad (2.6)$$

where  $g_{\theta}(\psi, t)$  and  $g_{\phi}(\psi, t)$ , similar to  $c_{\theta}(t)$  and  $c_{\phi}(t)$ , are independent, complex-valued, zero-mean, unit-variance, Gaussian-distributed random variables.

This electric field induces an open-circuit voltage  $v_A^{(m)}(t)$  on the terminals of antenna  $m$ . This voltage is related to the incident electric field from direction  $\hat{\mathbf{s}}$  through the antenna's

vector electric length (VEL), denoted  $\mathbf{l}_e^{(m)}(\hat{\mathbf{s}})$ , having units of meters, such that

$$v_A^{(m)}(t) = v_{src}^{(m)}(t) + v_g^{(m)}(t) \quad (2.7)$$

where

$$v_{src}^{(m)}(t) = \mathbf{l}_e^{(m)}(\hat{\mathbf{s}}) \cdot \mathbf{E}^{src}(\mathbf{r}^{(m)}, t) \quad (2.8)$$

and<sup>2</sup>

$$v_g^{(m)}(t) = \iint_{\Omega} \mathbf{l}_e^{(m)}(\psi) \cdot d\mathbf{E}^g(\mathbf{r}^{(m)}, t) \quad (2.9)$$

In our coordinate system, Antenna A is at the origin, such that  $\mathbf{r}^{(A)} = \mathbf{0}$ , and Antenna B is at the end of the baseline, such that  $\mathbf{r}^{(B)} = \mathbf{b}$ .

The antenna is modeled as a Thévenin equivalent circuit consisting of voltages in series with the antenna impedance, as shown in Fig. 2.4. The antenna impedance is given by

$$Z_A^{(m)} = R_{rad}^{(m)} + R_{loss}^{(m)} + jX_A^{(m)} \quad (2.10)$$

where  $R_{rad}^{(m)}$  and  $R_{loss}^{(m)}$  are the contributions of radiation and ohmic loss, respectively, to the real part of  $Z_A$ . The mean-square magnitude (i.e. variance) of the antenna voltage spectral density  $v_A$  is given by

$$\langle |v_A^{(m)}|^2 \rangle = 4kT_A^{(m)} R_{rad}^{(m)} \quad (2.11)$$

where  $T_A^{(m)}$  is the antenna temperature.  $T_A^{(m)}$  is defined as the power spectral density (PSD; W Hz<sup>-1</sup>) that the antenna would deliver to a conjugate-matched load  $Z_A^{(m)*}$ , divided by  $k$ .

The voltage  $v_{int}^{(m)}(t)$  represents noise due to ohmic loss in the antenna, and has mean-square

---

<sup>2</sup>It is noted that the  $v_g^{(m)}(t)$  integral contains a radical of a differential (e.g.  $\sqrt{d\Omega}$ ). We will never evaluate this integral directly, but will instead evaluate the product of two similar integrals (i.e.  $v_g^{(m)}(t) \left( v_g^{(n)}(t) \right)^*$ ). By invoking the limit definition of the integral, and assuming the integrand is well-behaved, it can be shown that the product of two such integrals can be written as a single integral with respect to the radican (e.g.  $d\Omega$ ).

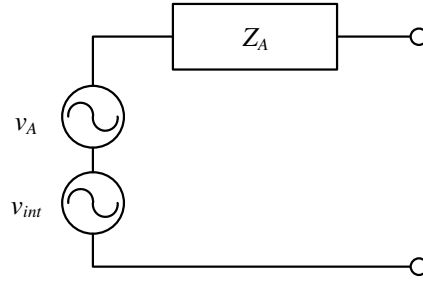


Figure 2.4: Antenna model. The superscripts have been suppressed for clarity.

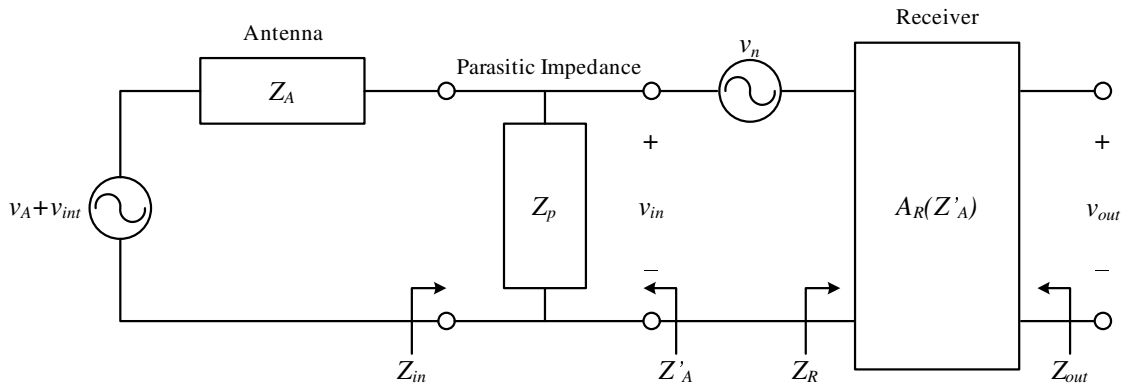


Figure 2.5: Receiver model; see Section 2.3 for notation. The superscripts have been suppressed for clarity.  $A_R(Z'_A)$  is related, but not equivalent, to  $G_R(Z'_A)$  defined in Section 2.5.1.

magnitude

$$\left\langle \left| v_{int}^{(m)}(t) \right|^2 \right\rangle = 4kT_{amb}R_{loss} \quad (2.12)$$

where  $T_{amb}$  is the ambient physical temperature.  $R_{loss}$  is determined in Section 3.1.4.

The receiver model is shown in Fig. 2.5. Note the parallel impedance  $Z_p$ . This represents a significant parasitic impedance associated with the interface between the antenna and the receiver. Section 3.2.3 provides further detail about how this comes about in the instrument developed in this work.

The receiver is characterized by its voltage gain

$$A_R^{(m)}(Z_A^{(m)}) \triangleq v_{out}^{(m)} / v_{in}^{(m)} \quad (2.13)$$

where  $Z_A^{(m)} = Z_A^{(m)} || Z_p$ , “||” denotes two impedances in parallel, and equivalent noise voltage spectral density<sup>3</sup>

$$v_n^{(m)}(t) = n^{(m)}(t) \sqrt{4kT_R^{(m)} R_n^{(m)}} \quad (2.14)$$

where  $n^{(m)}(t)$  is another independent, complex-valued, zero-mean, unit-variance, Gaussian-distributed random variable, and  $T_R^{(m)}$  is the input-referred equivalent noise temperature of the receiver. It will not be necessary to know  $R_n$  in this work.

The sampled voltage is therefore

$$v_{out}^{(m)}(t) = H^{(m)} v_A^{(m)}(t) + G^{(m)} v_n^{(m)}(t) \quad (2.15)$$

where

$$H^{(m)} = \frac{Z_{in}^{(m)}}{Z_{in}^{(m)} + Z_A^{(m)}} A_R^{(m)}(Z_A^{(m)}) \quad (2.16)$$

and

$$G^{(m)} = \frac{Z_A^{(m)}}{Z_A^{(m)} + Z_R^{(m)}} A_R^{(m)}(Z_A^{(m)}) \quad (2.17)$$

## 2.4 Isolation of the Source Flux Density (Fringe Rate Processing)

This section describes the signal processing used to isolate the source flux density from the sampled voltages  $v_{out}^{(m)}(t)$ , which include the relatively bright Galactic background noise as well as other sources. Figure 2.6 summarizes the signal processing algorithm. The signals from the two antennas are cross-correlated using a “FX” correlation scheme [40]. In a “FX” correlator, each time-domain signal is first decomposed into frequency channels using a short-time Fourier transform (the “F” in FX). Then, for each frequency channel, the narrow-

---

<sup>3</sup>Traditionally a noise current is placed in parallel with the noise voltage. This is done to account for the fact that noise power appears at the output of the receiver when the input of the receiver is left as an open circuit. Since this receiver will never have an open circuit at the input during the measurements, a single noise voltage is sufficient to characterize the receiver noise.

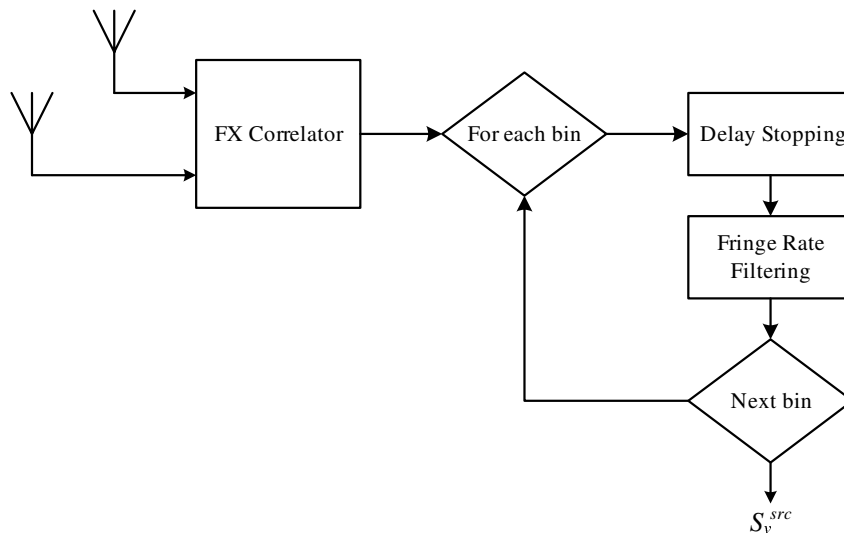


Figure 2.6: Signal processing procedure.

band signal from one antenna is multiplied with the complex conjugate of the narrowband signal from the other antenna (the “X”), and the product is averaged.

The rest of this section is organized as follows. Section 2.4.1 presents how the output of the FX correlation may be processed to isolate the source flux density. Section 2.4.2 presents a simulation demonstrating the technique developed in Section 2.4.1.

### 2.4.1 Theory

This section presents the theory for the technique used to isolate the source in  $v_{out}^{(m)}(t)$ . In the following analysis,  $v_{out}^{(m)}(t)$  represents one bin from the short-time Fourier transform. We assume this signal is narrowband; that is, the width of the bin  $\Delta\nu$  is sufficiently small such that  $v_{out}^{(m)}(t)$  is effectively independent of  $\Delta\nu$ .<sup>4</sup>

<sup>4</sup>For the results reported in this work,  $\Delta\nu = 65.1$  kHz. The narrowband assumption is justified by the fact that the maximum time-of-flight over the 300 m maximum baseline available to the instrument (see Chapter 3) is  $1 \mu\text{s} \ll (65.1 \text{ kHz})^{-1} = 15.4 \mu\text{s}$ .

The correlation between the two output signals is

$$\begin{aligned}
\rho_{mn}(t) &= \int_t^{t+\Delta t} v_{out}^{(m)}(t) (v_{out}^{(n)}(t))^* dt \\
&= H^{(m)}(H^{(n)})^* \langle v_{src}^{(m)}(v_{src}^{(n)})^* \rangle + H^{(m)}(H^{(n)})^* \langle v_{src}^{(m)}(v_g^{(n)})^* \rangle + H^{(m)}(G^{(n)})^* \langle v_{src}^{(m)}(v_n^{(n)})^* \rangle \\
&+ H^{(m)}(H^{(n)})^* \langle v_g^{(m)}(v_g^{(n)})^* \rangle + H^{(m)}(H^{(n)})^* \langle v_g^{(m)}(v_{src}^{(n)})^* \rangle + H^{(m)}(G^{(n)})^* \langle v_g^{(m)}(v_n^{(n)})^* \rangle \\
&+ G^{(m)}(G^{(n)})^* \langle v_n^{(m)}(v_n^{(n)})^* \rangle + G^{(m)}(H^{(n)})^* \langle v_n^{(m)}(v_{src}^{(n)})^* \rangle + G^{(m)}(H^{(n)})^* \langle v_n^{(m)}(v_g^{(n)})^* \rangle
\end{aligned} \tag{2.18}$$

where  $\Delta t$  is the integration time of the correlator. We have suppressed the time dependence within the time-averaging operators for clarity. For sufficiently large  $\Delta t$ ,<sup>5</sup> the signals from the source, the background, and the system noise are uncorrelated, such that

$$\begin{aligned}
\int_{-\infty}^{+\infty} c_i(t) (g_j(\psi, t))^* dt &= \int_{-\infty}^{+\infty} c_i(t) (n^{(m)}(t))^* dt \\
&= \int_{-\infty}^{+\infty} g_i(\psi, t) (n^{(m)}(t))^* dt \\
&= \int_{-\infty}^{+\infty} n^{(m)}(t) (n^{(n)}(t))^* dt = 0
\end{aligned} \tag{2.19}$$

Thus the correlation reduces to

$$\rho_{mn}(t) \cong H^{(m)}(H^{(n)})^* P^{src} + H^{(m)}(H^{(n)})^* P^g \tag{2.20}$$

where

$$\begin{aligned}
P^{src} &= \left\langle \left( \mathbf{l}_e(\hat{\mathbf{s}}) \cdot \mathbf{E}^{src}(\mathbf{0}, t) \right) \left( \mathbf{l}_e(\hat{\mathbf{s}}) \cdot \mathbf{E}^{src}(\mathbf{b}, t) \right)^* \right\rangle \\
&= |\mathbf{l}_e(\hat{\mathbf{s}})|^2 \frac{\eta}{2} S_\nu^{src} e^{-j\beta \hat{\mathbf{s}} \cdot \mathbf{b}}
\end{aligned} \tag{2.21}$$

---

<sup>5</sup> Larger  $\Delta t$  improves the approximation of Eq. (2.20), as it maximizes the signal-to-noise ratio. However,  $\rho_{mn}(t)$  must not change significantly over  $\Delta t$  to maintain coherence. In Appendix C, we show that for the baselines considered in this work,  $\rho_{mn}(t)$  changes by less than 1% for  $\Delta t < 137$  s. For the results reported in this work,  $\Delta t = 20$  s, which provides a sufficient signal-to-noise ratio and is well within the limit for coherence.

and  $l_e(\hat{\mathbf{s}})$  is the effective length projected in the direction of  $\hat{\mathbf{s}}$  (and is assumed to be equal for the two antennas), and

$$\begin{aligned} P^g &= \iint_{\Omega} \left\langle \left( \mathbf{l}_e(\hat{\mathbf{r}}'(\psi)) \cdot d\mathbf{E}^g(\mathbf{0}, \psi, t) \right) \left( \mathbf{l}_e(\hat{\mathbf{r}}'(\psi)) \cdot d\mathbf{E}^g(\mathbf{b}, \psi, t) \right)^* \right\rangle \\ &= \iint_{\Omega} |l_e(\psi)|^2 \frac{2\eta k}{\lambda^2} T(\psi) e^{j\beta \hat{\mathbf{r}}'(\psi) \cdot \mathbf{b}} d\Omega \end{aligned} \quad (2.22)$$

Note  $P^{src}$  and  $P^g$  have units of  $V^2 \text{ Hz}^{-1}$ .

The  $P^{src}$  factor in Eq. (2.20) is proportional to the source flux  $S_\nu^{src}$ , which is the quantity we seek. This factor may be written as

$$P^{src} = |P^{src}| e^{-j2\pi\nu\tau_g(t)} \quad (2.23)$$

where

$$|P^{src}| = |l_e(\hat{\mathbf{s}})|^2 \frac{\eta}{2} S_\nu^{src} \quad (2.24)$$

and

$$\tau_g(t) = \frac{\hat{\mathbf{s}}(t) \cdot \mathbf{b}}{c} \quad (2.25)$$

is the geometrical delay (see e.g. Fig. 1.5), and  $c$  is the speed of light in free space. Per Appendix C, for  $\Delta t < 137$  s and observation duration  $T < 6736$  s,  $\tau_g(t)$  around  $t_0$  is well approximated as a linear function of time

$$\tau_g(t) \cong \tau_g(t_0) - \frac{1}{\nu} f_g(t) t \quad (2.26)$$

where  $f_g(t)$  is source's fringe rate,  $t_0$  is the start of the observation, and  $t$  is measured such that for the first sample  $t = t_0$ . Fringe rate is defined as the instantaneous frequency of  $P^{src}$ , given by Eq. (C.8) as

$$f_g(t) \cong \nu (c_0 + c_1 t + c_2 t^2) \quad (2.27)$$

where the coefficients  $c_i$  can be solved for if  $\mathbf{b}$  is perfectly known (see Appendix C), or can

be estimated from  $\rho_{mn}(t)$  (as shown in Section 5.3). Note that fringe rate is a function of frequency, LST, the baseline, and the source's location on the celestial sphere.

Different sources produce different fringe rates, allowing for the use of Fourier techniques to isolate  $P^{src}$  from  $\rho_{mn}$ . Specifically,  $P^{src}$  may be isolated by “delay stopping” and fringe rate filtering  $\rho_{mn}(t)$ . Delay stopping, also called fringe-stopping or delay tracking, downconverts  $\rho_{mn}(t)$  by the fringe rate of the desired source.

To visualize this, we now transform to the fringe rate domain. Note that  $\rho_{mn}(t)$  is time-limited between  $\pm T/2$ . Thus, the Fourier integral is

$$\mathcal{F} \{ \rho_{mn}(t) e^{j2\pi f_g(t)t} \Pi(T) \} = \int_{-\infty}^{\infty} \left( \rho_{mn}(t) e^{j2\pi f_g(t)t} \Pi(T) \right) e^{j2\pi f_r t} dt \quad (2.28)$$

where  $\Pi(T)$  is a unit-amplitude, rectangular pulse of width  $T$  centered at  $t = 0$ . By applying Fourier transform identities we find

$$\begin{aligned} \mathcal{F} \{ \rho_{mn}(t) e^{j2\pi f_g(t)t} \Pi(T) \} &= H^{(m)} (H^{(n)})^* |P^{src}| T \text{sinc}(\pi T f_r) \\ &\quad + H^{(m)} (H^{(n)})^* \mathcal{F} \{ P^g \} * T \text{sinc}(\pi T f_r) * \mathcal{F} \left\{ e^{j2\pi\nu(c_0+c_1t+c_2t^2)t} \right\} \end{aligned} \quad (2.29)$$

where  $\text{sinc } x = (\sin x)/x$  and “\*” denotes convolution. The Galactic noise term  $P^g$  is dominated by the ever-present background noise, such that

$$\mathcal{F} \{ P^g \} \approx P^g \delta(f_r) \quad (2.30)$$

where  $\delta(f_r)$  is the Dirac delta function. Applying Eq. (2.30) to Eq. (2.29) yields

$$\begin{aligned} \mathcal{F} \{ \rho_{mn}(t) e^{j2\pi f_g(t)t} \Pi(T) \} &\approx H^{(m)} (H^{(n)})^* |P^{src}| T \text{sinc}(\pi T f_r) \\ &\quad + H^{(m)} (H^{(n)})^* P^g \delta(f_r) * T \text{sinc}(\pi T f_r) * \mathcal{F} \left\{ e^{j2\pi\nu(c_0+c_1t+c_2t^2)t} \right\} \end{aligned} \quad (2.31)$$

Applying the convolution property of the Fourier transform:

$$\begin{aligned} \mathcal{F} \left\{ \rho_{mn}(t) e^{j2\pi f_g(t)t} \Pi(T) \right\} &= H^{(m)} (H^{(n)})^* |P^{src}| T \operatorname{sinc}(T f_r) \\ &+ H^{(m)} (H^{(n)})^* P^g T \operatorname{sinc}(\pi T f_r) * \mathcal{F} \left\{ e^{j2\pi\nu(c_0+c_1t+c_2t^2)t} \right\} \end{aligned} \quad (2.32)$$

Applying the frequency shifting property of the Fourier transform:

$$\begin{aligned} \mathcal{F} \left\{ \rho_{mn}(t) e^{j2\pi f_g(t)t} \Pi(T) \right\} &= H^{(m)} (H^{(n)})^* |P^{src}| T \operatorname{sinc}(T f_r) \\ &+ H^{(m)} (H^{(n)})^* P^g T \operatorname{sinc}(\pi T (f_r - \nu c_0)) * \mathcal{F} \left\{ e^{j2\pi\nu(c_1t+c_2t^2)t} \right\} \end{aligned} \quad (2.33)$$

The factor containing the source flux is centered on  $f_r = 0$ . The interfering noise term associated with  $P^g$  is centered on  $f_r = \nu c_0$ . To isolate the desired signal, we “fringe rate filter” the output of the Fourier transform to excise all signals except at  $f_r = 0$ , leaving

$$P_{mn} = H^{(m)} (H^{(n)})^* |l_e(\hat{\mathbf{s}})|^2 \frac{\eta}{2} S_\nu^{src} \quad (2.34)$$

Equation (2.34) is the desired measurement equation from this technique. To use Eq. (2.34) we must obtain  $\rho_{mn}(t)$  from the sampled voltages according to Eq. (2.18). We then solve for  $S_\nu^{src}$  given  $H^{(m)}$ ,  $H^{(n)}$ , and  $l_e$ .  $H^{(m)}$  and  $H^{(n)}$  are determined *in situ* using a three-state switching system described in Section 2.7.2.  $l_e$  is determined *a priori*, as described in Sections 3.1.2 and 3.1.3. In the next section we consider an example of this technique.

## 2.4.2 Example of the Source Isolation

This section presents a simulation example of the source isolation procedure to illustrate the process and introduce how data will be presented in future chapters. We consider an interferometer with a 250 m East-West oriented baseline ( $\mathbf{b} = \hat{\mathbf{x}}250$  m) at a latitude of  $+34^\circ$ . The sky consists only of Cyg A, Cas A, and the Galactic background. Cyg A is

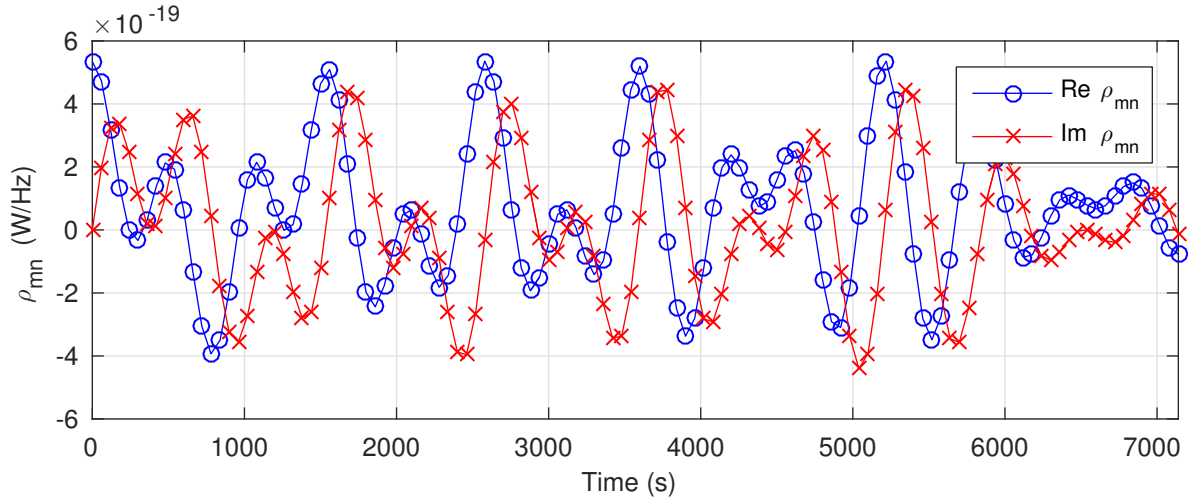


Figure 2.7: Fringes at 42 MHz for the simulation described in Section 2.4.2.  $\Delta\nu = 63$  kHz,  $\Delta t = 60$  s.

the desired source, and transits in the middle of the simulated two-hour observation. The Galactic background is assumed to be uniformly bright, such that it may be modeled by Eq. (A.8) derived in Appendix A. Additive white Gaussian noise is added to  $\rho_{mn}(t)$ , and the signal-to-noise ratio is 20 dB (roughly that seen in the measured data in this work). The receiver is assumed to be “ideal” and requires no calibration (i.e.  $|H^{(m)}||H^{(n)}| = 1$ ). The antenna is assumed to be isotropic and linearly polarized. The simulation is between 38 to 46 MHz (Band 2, using the naming convention established in Section 3.8).

Figure 2.7 shows  $\rho_{mn}(t)$  from the 42 MHz bin output from the FX correlation. A strong fringe pattern is visible. Figure 2.8 shows  $\rho_{mn}(t)$  for the entire frequency band.

Figure 2.9 shows the magnitude of the cross-correlation after applying a fast Fourier Transform (FFT) to each frequency channel in Fig. 2.8. Three sources are readily identifiable, corresponding to Cyg A ( $f_r \approx 1.75$  mHz), Cas A ( $f_r \approx 0.5\text{--}1.2$  mHz), and the “all sky” (Galactic background) term ( $f_r = 0$  mHz). The all sky term exhibits an oscillating dependence with  $\nu$ , which is expected (see Appendix A). Cyg A’s fringe rate is nearly constant because it transits in the middle of this dataset. Cas A’s fringe rate is changing significantly because it is rising.

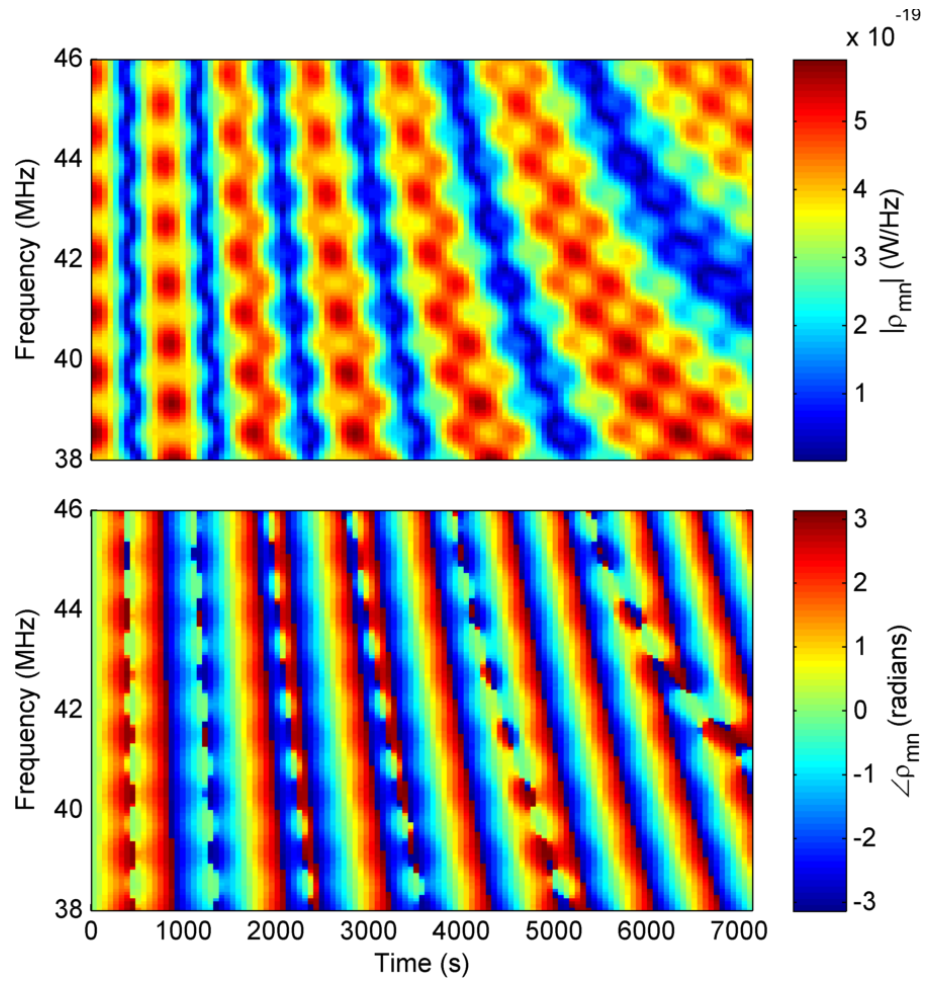


Figure 2.8: Cross-correlation for the simulation described in Section 2.4.2.  $\Delta\nu = 63$  kHz,  $\Delta t = 60$  s.

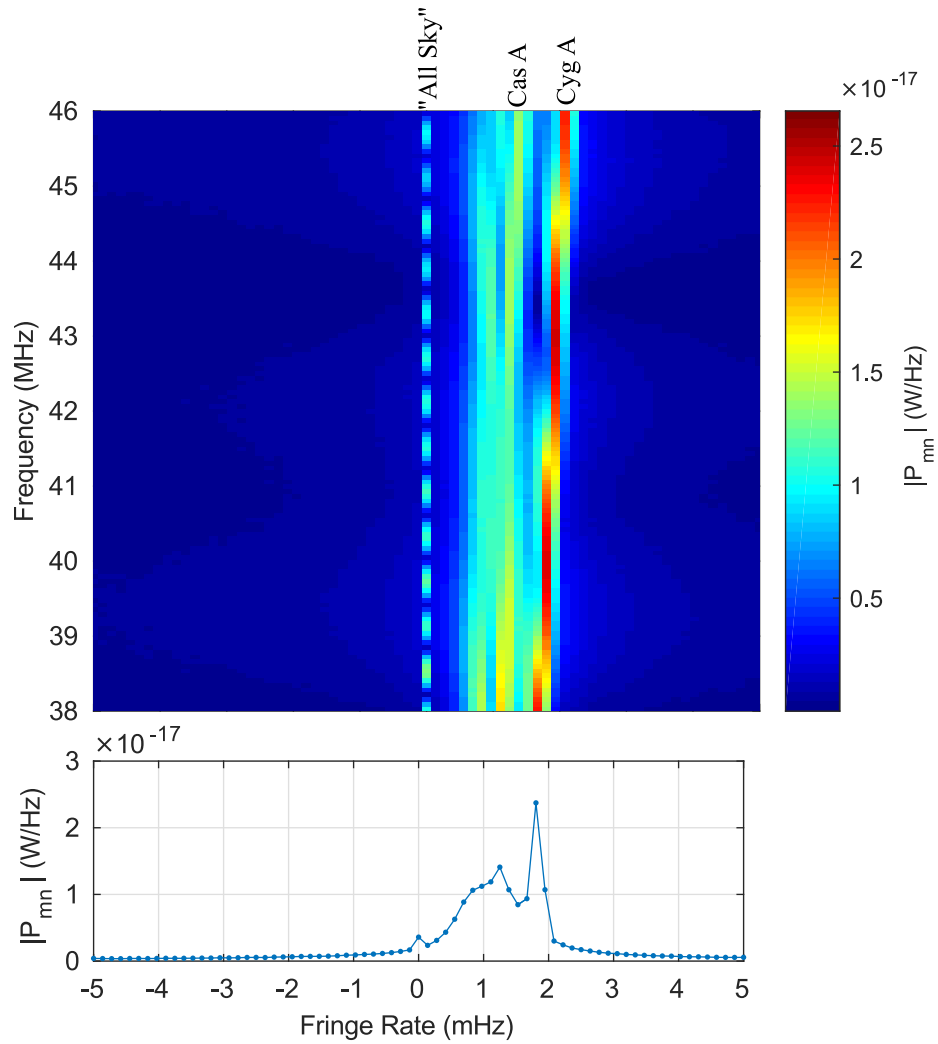


Figure 2.9: Magnitude of the per-channel FFT of the cross-correlation shown in Fig. 2.8. The bottom panel is a narrowband cut from the upper panel at  $\nu = 42$  MHz.  $\Delta\nu = 63$  kHz,  $\Delta t = 60$  s.

Figure 2.10 shows the magnitude of the cross-correlation after delay stopping Cyg A. Note the signal from Cyg A is now centered at the  $f_r = 0$  bin. The signals from the Cas A and the all sky term have been shifted by  $\sim -1.75$  mHz and spread due to the delay stopping.

Now we apply fringe rate filtering to exclude all bins except the  $f_r = 0$  bin, and then apply Eq. (2.34). Figure 2.11 shows the resulting estimate of the flux density of Cyg A. The ripple is caused by the proximity of Cas A to Cyg A in the fringe rate domain. To mitigate this interference, Cas A’s amplitude and fringe rate are estimated from the data and subtracted from the cross-correlation before delay stopping. The revised flux density estimate is also shown in Fig. 2.11. Note that significant error remains. The remaining error in the measurement motivates repeated observations on different baselines, so that averaging the different measurements might improve accuracy.

## 2.5 Antenna Temperature Model (ATM)

This section presents the Antenna Temperature Model (ATM). The ATM is an alternative to the CSM (Section 2.3) that operates on antenna temperature as opposed to electric field intensity. The primary intent of the ATM is to determine the receiver gain (Section 2.5.1), which is necessary to determine the absolute flux density, discussed in Section 2.7. The ATM is also used to estimate  $T_{sky}$  (Section 2.5.2), which is itself a topic of scientific interest. In Section 2.6.3 the ATM is applied, in conjunction with the known properties of  $T_{sky}$  discussed in Section 2.2, to determine the *in situ* corrections for the system parameters measured separately before the observation (“priors”) necessary to determine the receiver gain.

### 2.5.1 *In Situ* Calibration of the Receiver Gain

This section describes the process used to calibrate the receiver gain  $G_R(Z'_A)$ , defined below. This can be done using a system model defined in terms of equivalent noise temperatures,

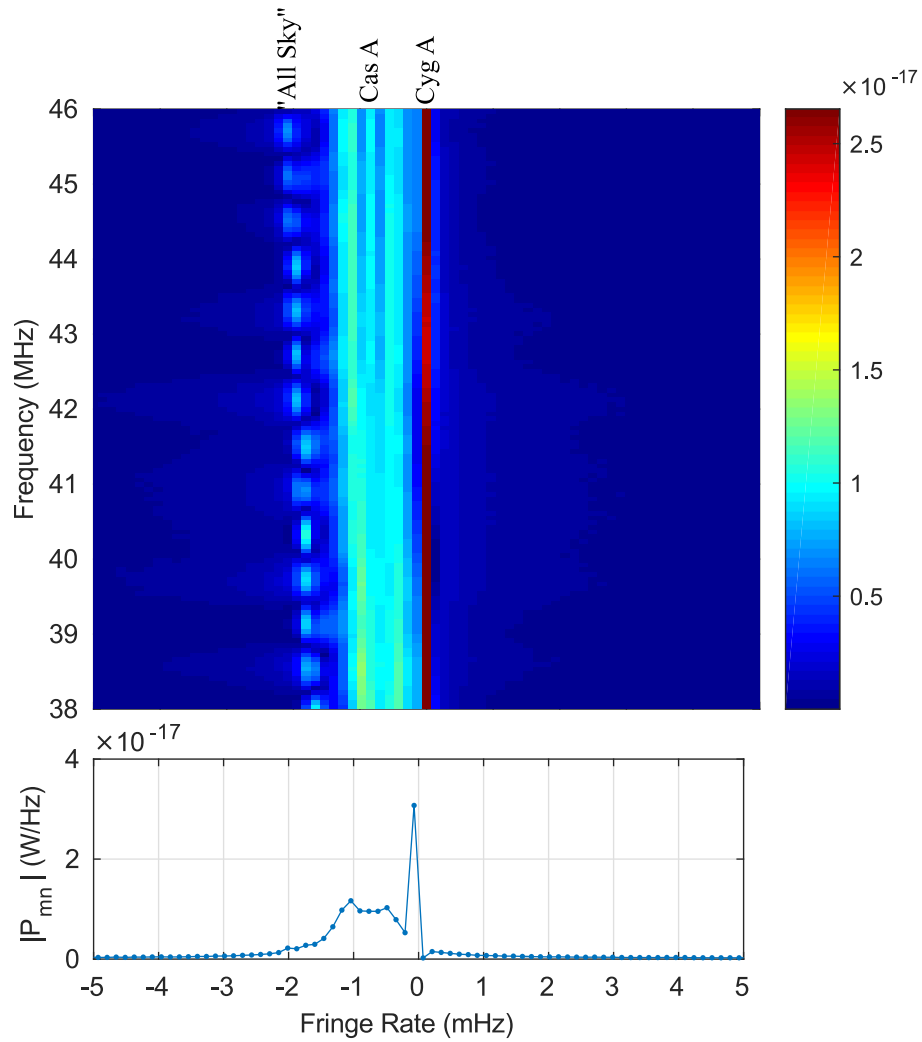


Figure 2.10: Magnitude of the per-channel FFT of the cross-correlation shown in Fig. 2.8 after delay stopping for Cyg A. The bottom panel is a narrowband cut from the upper panel at  $\nu = 42$  MHz.  $\Delta\nu = 63$  kHz,  $\Delta t = 60$  s.

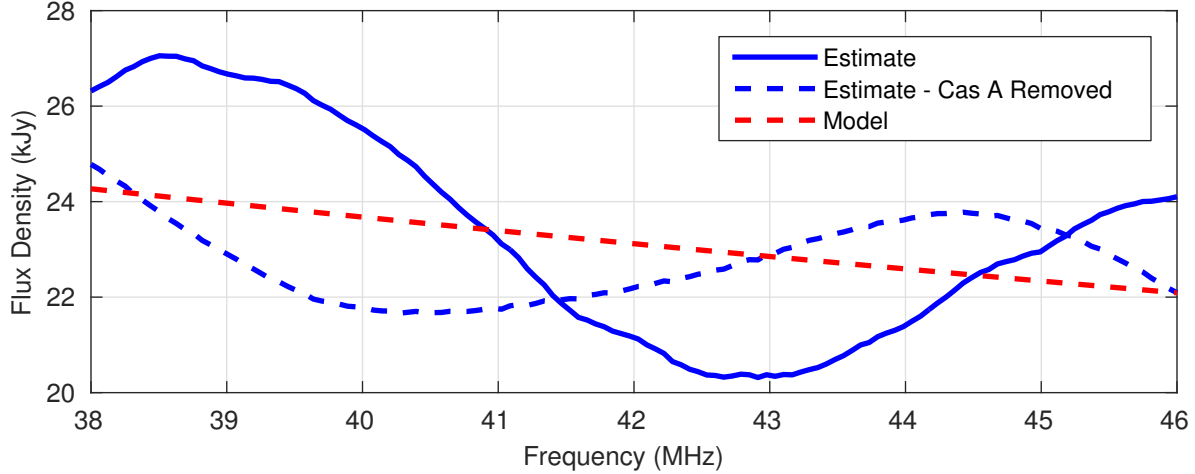


Figure 2.11: Estimate of the flux of Cyg A.

which leads to the ATM, summarized by Eqs. 2.45, 2.46, and 2.47.

The calibration is assumed to use a three-state switching receiver, as shown in Figure 2.12. This scheme is similar to that originally described in [35]. The input of the receiver is periodically switched between the antenna and a calibration circuit. The calibration circuit consists of a noise source and impedance matching components (for the specific implementation used in this work, see Section 3.2).

The states are defined as follows: In state 1, the “antenna state”, the receiver input is connected to the antenna; this is the state shown in Fig. 2.5 and the associated text. In state 2, the “cold state”, the receiver is connected to the calibration circuit, with the noise source off. In state 3, the “hot state”, the receiver is connected to the calibration circuit, with the noise source on.

Like the antenna, the calibration circuit is modeled by a Thévenin circuit with impedance  $Z_{cal} = R_{cal} + jX_{cal}$  and open circuit noise voltage spectral density  $v_{cal}$ . In state 2, the noise source is off, such that the noise is due entirely to ohmic losses in the calibration circuit. In this state we define  $v_{cal} = v_{cal,2}$ , and note

$$\langle |v_{cal,2}|^2 \rangle = 4kR_{cal}T_{amb} \quad (2.35)$$

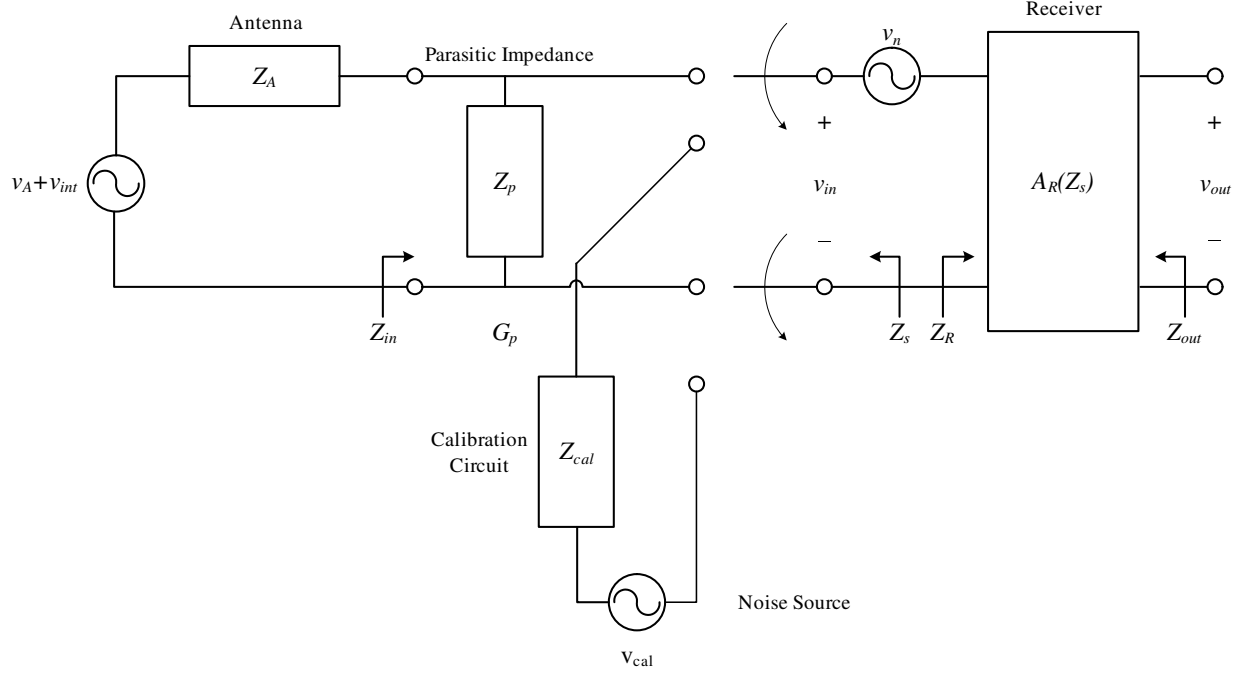


Figure 2.12: Block diagram of the three-state switching receiver.

where  $T_{amb}$  is the physical temperature. In state 3, the noise source is on, such that

$$\langle |v_{cal,3}|^2 \rangle = 4kR_{cal}(T_{amb} + T_{cal}) \quad (2.36)$$

where  $T_{cal}$  is defined as the PSD that the calibration circuit would deliver to a conjugate-matched load  $Z_{cal}^*$ , divided by  $k$ .

The sampled voltages are

$$v_{out,1}(t) = A_R(Z'_A) \left[ \frac{Z_{in}}{Z_{in} + Z_A} (v_A(t) + v_{int}(t)) + \frac{Z'_A}{Z'_A + Z_R} v_n(t) \right] \quad (2.37)$$

$$v_{out,2}(t) = A_R(Z_{cal}) \left[ \frac{Z_R}{Z_R + Z_{cal}} v_{cal,2}(t) + \frac{Z_{cal}}{Z_R + Z_{cal}} v_n(t) \right] \quad (2.38)$$

$$v_{out,3}(t) = A_R(Z_{cal}) \left[ \frac{Z_R}{Z_R + Z_{cal}} v_{cal,3}(t) + \frac{Z_{cal}}{Z_R + Z_{cal}} v_n(t) \right] \quad (2.39)$$

$$(2.40)$$

Note here we have made explicit the fact that  $A_R$  is a function of the source impedance  $Z_s$ , and  $Z'_A$  is defined as  $Z_A || Z_p$  at the end of Section 2.3.

The calibration is performed by measuring the received PSD in each state. The received PSD in state  $i$  is found by computing

$$S_{out,i} = \langle |v_{out,i}|^2 \rangle \quad (2.41)$$

so the PSDs in each state are

$$S_{out,1} = |A_R(Z'_A)|^2 \left[ \left| \frac{Z_{in}}{Z_{in} + Z_A} \right|^2 (\langle |v_A(t)|^2 \rangle + \langle |v_{int}(t)|^2 \rangle) + \left| \frac{Z'_A}{Z'_A + Z_R} \right|^2 \langle |v_n(t)|^2 \rangle \right] \quad (2.42)$$

$$S_{out,2} = |A_R(Z_{cal})|^2 \left[ \left| \frac{Z_R}{Z_R + Z_{cal}} \right|^2 \langle |v_{cal,2}(t)|^2 \rangle + \left| \frac{Z_{cal}}{Z_R + Z_{cal}} \right|^2 \langle |v_n(t)|^2 \rangle \right] \quad (2.43)$$

$$S_{out,3} = |A_R(Z_{cal})|^2 \left[ \left| \frac{Z_R}{Z_R + Z_{cal}} \right|^2 \langle |v_{cal,3}(t)|^2 \rangle + \left| \frac{Z_{cal}}{Z_R + Z_{cal}} \right|^2 \langle |v_n(t)|^2 \rangle \right] \quad (2.44)$$

Applying Eqs. (2.11), (2.12), (2.14), (2.35), and (2.36):

$$S_{out,1} = kG_R(Z'_A) \left[ G_p \left( T_A + T_{amb} \frac{R_{loss}}{R_{rad}} \right) + T_R(Z'_A) \right] \quad (2.45)$$

$$S_{out,2} = kG_R(Z_{cal}) [T_{amb} + T_R(Z_{cal})] \quad (2.46)$$

$$S_{out,3} = kG_R(Z_{cal}) [T_{amb} + T_{cal} + T_R(Z_{cal})] \quad (2.47)$$

where  $G_p$  is the transducer power gain (TPG<sup>6</sup>) of the parasitic impedance when terminated into  $Z'_A$ , and  $G_R(Z_s)$  is the TPG of the receiver when the input impedance is  $Z_s$ .  $G_p$ , derived in Appendix D.1, is given by

$$G_p = \frac{4R_A R'_A}{|Z'_A|^2} \left| \frac{Z_p || (Z'_A)^*}{Z_A + Z_p || (Z'_A)^*} \right|^2 \quad (2.48)$$

---

<sup>6</sup>TPG is defined as the ratio of the PSD delivered to the load to the PSD the source would deliver to a conjugate-matched load.

Equations 2.45 - 2.47 comprise the ATM.

From Eqs. (2.46) and (2.47),  $G_R(Z_{cal})$  is estimated by

$$G_R(Z_{cal}) = \frac{S_{out,3} - S_{out,2}}{kT_{cal}} \quad (2.49)$$

The relationship between  $G_R(Z_{cal})$  and  $G_R(Z'_A)$ , derived in Appendix D.2, is

$$G_R(Z'_A) = \frac{1 - |\Gamma_A|^2}{1 - |\Gamma_{cal}|^2} \cdot \frac{|1 - s_{11}\Gamma_{cal}|^2}{|1 - s_{11}\Gamma_A|^2} \cdot G_R(Z_{cal}) \quad (2.50)$$

where

$$s_{11} = \frac{Z_R/2 - Z_0}{Z_R/2 + Z_0} \quad (2.51)$$

$$\Gamma_{cal} = \frac{Z_{cal}/2 - Z_0}{Z_{cal}/2 + Z_0} \quad (2.52)$$

$$\Gamma_A = \frac{Z'_A/2 - Z_0}{Z'_A/2 + Z_0} \quad (2.53)$$

and  $Z_0$  is the reference impedance used to compute the  $s$ -parameters.

## 2.5.2 Estimation of the Galactic Background Noise

This section presents how the ATM may be used to estimate the contribution to antenna temperature from the Galactic background noise,  $T_{sky}$  (see Section 2.2). Measurement of  $T_{sky}$  is useful as a commissioning measurement and also has scientific value (see Section 6.3).

The primary difference in estimating  $T_{sky}$ , as opposed to estimating the flux density from a discrete source ( $S_\nu^{src}$ ), is the need to determine the receiver temperature  $T_R(Z'_A)$ . This is because the internally-generated noise from the two receivers is uncorrelated, and therefore  $T_R(Z'_A)$  nominally vanishes after the antenna signals are correlated.

The three-state switching receiver used in Section 2.5.1 to determine  $G_R(Z'_A)$  may also be

used to determine  $T_R(Z'_A)$ .  $T_R(Z'_A)$  may be determined from either  $S_{out,2}$  or  $S_{out,3}$ . We choose to use  $S_{out,3}$ , since  $S_{out,3} > S_{out,2}$  and therefore has a higher signal-to-noise ratio with respect to any quantization noise. From Eq. (2.47):

$$T_R(Z_{cal}) = \frac{S_{out,3}}{kG_R(Z_{cal})} - T_{amb} - T_{cal} \quad (2.54)$$

The relationship between  $T_R(Z_{cal})$  and  $T_R(Z'_A)$ , derived in Appendix D.3, is given by

$$T_R(Z'_A) = \frac{R_{cal}}{R'_A} T_R(Z_{cal}) \quad (2.55)$$

The antenna temperature  $T_A$  is then obtained from Eq. (2.45) as follows:

$$T_A = \left[ \frac{S_{out,1}}{kG_R(Z'_A)} - T_R(Z'_A) \right] \frac{1}{G_p} - T_{amb} \frac{R_{loss}}{R_{rad}} \quad (2.56)$$

The antenna temperature is comprised of the Galactic background noise  $T_{sky}$  and  $T_{gnd}$  from the ground, such that

$$T_A = \epsilon_A (T_{sky} + T_{gnd}) \quad (2.57)$$

where  $\epsilon_A$  represents ground loss efficiency. Thus,

$$T_{sky} = \frac{T_A}{\epsilon_A} - T_{gnd} \quad (2.58)$$

The value of  $\epsilon_A$  can be estimated using electromagnetic simulations, and is presented in Section 3.1.5. The value of  $T_{gnd}$  is significantly affected by the presence or absence of ground screen. For no ground screen,  $T_{gnd} \sim 150$  K, i.e.  $\sim 300$  K corresponding to the physical temperature of the ground divided by 2 since roughly half of the antenna pattern intersects the ground. For a perfectly-conducting infinite ground screen, the apparent brightness of the ground is equal to the apparent brightness from the sky, due to reflection, and so is  $\gg 150$  K. The antennas used in this work, described in Section 3.1, are above a small ( $\mathcal{O}[\lambda^2]$ ) ground

screen, and therefore receives a value of  $T_{gnd}$  somewhere between the two extremes. For example, a value of  $T_{gnd} \approx 400$  K is obtained from Eq. (3.21) at 45 MHz for  $T_{sky} \approx 8,000$  (from Fig. 2.2) and  $\epsilon_A \approx 0.95$  (from Fig. 3.15).

## 2.6 *In Situ* Calibration of Antenna Impedance and Internal Noise Source

As described in Section 2.5, the ATM requires prior values for the antenna impedance  $Z_A$  and internal noise source temperature  $T_{cal}$ . In the present work these were estimated through measurements and simulations. However, analysis of data indicated that these values may be significantly different than expected in the actual (field) conditions. Therefore, the values must be calibrated *in situ* using data from the field.

The rest of this section is organized as follows. Section 2.6.1 presents a circuit model used to calibrate  $Z_A$ . Section 2.6.2 explains how we calibrate  $T_{cal}$ . Section 2.6.3 describes how the ATM and the Galactic background noise discussed in Section 2.2 are used to jointly determine the additional parameters required to calibrate  $Z_A$  and  $T_{cal}$ .

### 2.6.1 Revised Antenna Model

The value of  $Z_A$  is initially estimated through electromagnetic simulation and field measurement, as described in Section 3.1.4. However, the simulations are limited by the model assumptions (e.g. lack of feed structure, ground conditions, etc.), and the measurements are limited by stray reactances and errors introduced by the components unique to the measurement setup. The associated error is large enough to severely bias the flux estimates (see Section 5.1.2), and must be corrected.

Figure 2.13 shows the revised antenna model. We introduce two capacitances to the measured antenna impedance,  $Z_{A,prior}$ .  $Z_{A,prior}$  is placed in parallel with a capacitor  $C_p$ . Physically,

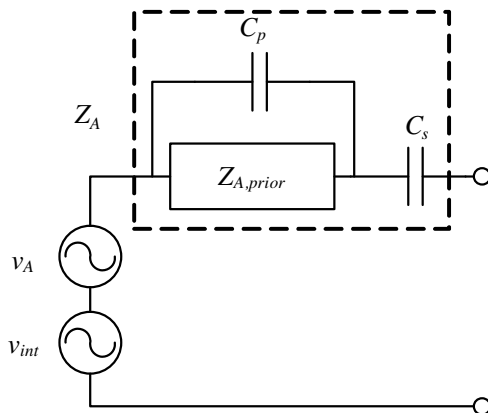


Figure 2.13: Equivalent circuit of the revised antenna impedance discussed in Section 2.6.1.

$C_p$  represents a possible change to the feed point capacitance between the measurement and actual operation, or a possible contribution from the measurement setup that was not present during the observations. The parallel combination of  $Z_{A,prior}$  and  $C_p$  is then placed in series with another capacitor  $C_s$ . Physically,  $C_s$  represents a possible capacitance associated with the structure around the antenna feed (such as the enclosure, see Section 3.2) that differed between the measurement and the observations.

The revised antenna impedance is therefore

$$Z_A = \left( Z_{A,prior} \parallel \frac{1}{j2\pi\nu C_p} \right) + \frac{1}{j2\pi\nu C_s} \quad (2.59)$$

The capacitances  $C_p$  and  $C_s$  are determined *in situ*, separately for each antenna. The process to determine  $C_p$  and  $C_s$  is described in Section 2.6.3.

## 2.6.2 Internal Noise Source

$T_{cal}$  is estimated in the laboratory, as described in Appendix E. The measurement process is intricate, and it is difficult to precisely determine  $T_{cal}$ . Further, the laboratory estimate is not consistent with that suggested by the data from the field. The associated error severely biases the flux density estimate, so  $T_{cal}$  must be calibrated *in situ*.

To calibrate  $T_{cal}$ , we add a constant value to the measured  $T_{cal,prior}$ , such that

$$T_{cal} = T_{cal,prior} + \Delta T_{cal} \quad (2.60)$$

The value of  $\Delta T_{cal}$  is determined for each antenna *in situ*. The process for determining  $\Delta T_{cal}$  is described in Section 2.6.3.

### 2.6.3 Joint Determination of $C_s$ , $C_p$ , and $\Delta T_{cal}$

We expect (1)  $T_{sky}$  to be a power law in frequency as noted in Section 2.2, and (2)  $T_{sky}$  to be identical for the two antennas, since both antennas see the same sky. Thus, the correct values of  $C_s$ ,  $C_p$ , and  $\Delta T_{cal}$  can be estimated as those which yield  $T_{sky}$  for each antenna, as determined from the ATM, that is the closest possible fit to a power law and which minimizes the differences between antennas. The specific optimization procedure used in this work is described in Section 5.2.

Note that the parameters of the power law are not restricted (i.e. to those determined by the GSM), but are allowed to vary freely, with the only goal being those specified above. Therefore, the resulting measurements are not linked to GSM or any other previously reported model or measurement of  $T_{sky}$ .

For the same reason, the resulting estimates of  $T_{sky}$ , obtained with the *in situ* calibrated values of  $C_s$ ,  $C_p$ , and  $\Delta T_{cal}$ , represent new and independent measurements of  $T_{sky}$ . These estimates are themselves scientifically interesting (as noted in Section 1.2), and are reported in Section 6.3.

## 2.7 Coherent Interferometry Model (CIM)

The fringe rate processing described in Section 2.4 isolates the source of interest. Therefore, the CSM is not necessary for the absolute flux density measurements. In this section, we present the ‘‘Coherent Interferometry Model’’ (CIM), which will be used to obtain the estimates of  $S_\nu^{src}$ .

The rest of this section is organized as follows. First, we derive the CIM from the CSM in Section 2.7.1. In Section 2.7.2, we relate the system response in the CIM ( $H^{(m)}$ , the same response in the CSM) to  $G_R(Z'_A)$ , which was determined in Section 2.5.1. Appendix F compares the CIM to the model traditionally used to conduct flux density measurements (i.e. those shown in Table 1.2), which we refer to as the ‘‘Radiometric Interferometry Model’’.

### 2.7.1 Derivation of the CIM Measurement Equation

The CIM assumes the fringe rate processing of Section 2.4.1 has perfectly eliminated all signals but that from the desired source. Under this assumption, Eq. (2.15) simplifies to

$$v_{out}^{(m)}(t) = H^{(m)} \mathbf{I}_e^{(m)}(\hat{\mathbf{s}}) \cdot \mathbf{E}^{src}(\mathbf{r}^{(m)}, t) \quad (2.61)$$

The output of the correlator (after fringe rate processing), from Eqs. (2.20), (2.23), and (2.24) simplifies to

$$\rho_{mn}(t) = H^{(m)} (H^{(n)})^* |l_e(\hat{\mathbf{s}})|^2 \frac{\eta}{2} S_\nu^{src} e^{-j2\pi\nu\tau_g(t)} \quad (2.62)$$

When estimating  $S_\nu^{src}$ , we only need to consider the magnitude of  $\rho_{mn}(t)$

$$|\rho_{mn}(t)| = |H^{(m)}| |H^{(n)}| |l_e(\hat{\mathbf{s}})|^2 \frac{\eta}{2} S_\nu^{src} \quad (2.63)$$

This is the CIM measurement equation. Estimation of  $S_\nu^{src}$  from the CIM therefore requires accurate knowledge of  $H^{(m)}$ ,  $H^{(n)}$ , and  $l_e$ . Sections 3.1.2 and 3.1.3 present how  $l_e$  is deter-

mined in this work. The following section presents how  $H^{(m)}$  and  $H^{(n)}$  are determined from  $G_R(Z'_A)$  for each receiver.

### 2.7.2 Determination of $H^{(m)}$

The estimation of the source flux  $S_\nu^{src}$  from the CIM requires knowledge of the system transfer functions  $H^{(m)}$  and  $H^{(n)}$ . As discussed in Section 2.5.1, the ATM is used to obtain an estimate of the receiver TPG  $G_R(Z'_A)$ . In this section, we derive the relationship between  $H^{(m)}$  and  $G_R(Z'_A)$ .

$G_R(Z'_A)$  is defined as the measured PSD output by the receiver to the PSD available from a Thévenin equivalent circuit having source impedance  $Z'_A$ ,  $S_A$ . With respect to Fig. 2.12:

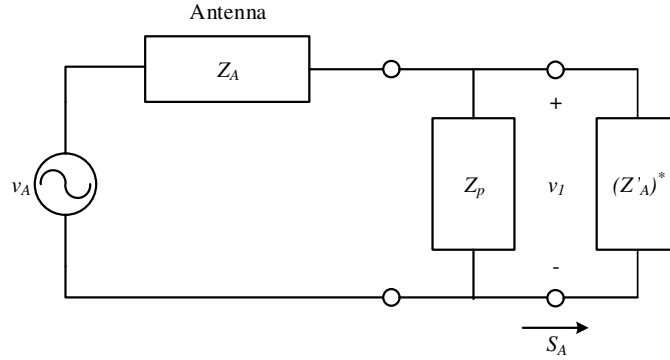
$$G_R(Z'_A) = \frac{\langle |v_{out}|^2 \rangle}{S_A} \quad (2.64)$$

To determine  $S_A$ , consider the circuit shown in Fig. 2.14. The PSD delivered to the conjugate matched load is

$$\begin{aligned} S_A &= \text{Re} \left\{ \left\langle v_1 \left( \frac{v_1}{(Z'_A)^*} \right)^* \right\rangle \right\} \\ &= \langle |v_1|^2 \rangle \frac{R'_A}{|Z'_A|^2} \\ &= \left| \frac{Z_p \|(Z'_A)^*\|}{Z_p \|(Z'_A)^*\| + Z_A} \right|^2 \langle |v_A|^2 \rangle \frac{R'_A}{|Z'_A|^2} \end{aligned} \quad (2.65)$$

Thus

$$G_R(Z'_A) = \left| \frac{Z_p \|(Z'_A)^*\| + Z_A}{Z_p \|(Z'_A)^*\|} \right|^2 \frac{\langle |v_{out}|^2 \rangle |Z'_A|^2}{\langle |v_A|^2 \rangle R'_A} \quad (2.66)$$

Figure 2.14: Equivalent circuit model to determine  $S_A$ .

Now,  $H^{(m)}$  is defined in Eq. (2.16). From Eq. (2.15):

$$H^{(m)} = \frac{v_{out}^{(m)}}{v_A^{(m)}} \quad (2.67)$$

$$H^{(n)} = \frac{v_{out}^{(n)}}{v_A^{(n)}}$$

Therefore, by applying Eq. (2.67) to Eq. (2.66) and solving for  $H^{(m)}$ , we obtain

$$|H^{(m)}| = \left| \frac{Z_p || (Z'_A)^*}{Z_p || (Z'_A)^* + Z_A} \right| \sqrt{G_R(Z'_A) \frac{R'_A}{|Z'_A|^2}} \quad (2.68)$$

and similarly for  $H^{(n)}$ .

Equations (2.63) and (2.68) together comprise the CIM. Given  $G_R(Z'_A)$ , estimated using the ATM, Eq. (2.68) is used to estimate  $|H^{(m)}||H^{(n)}|$ . The estimate of  $|H^{(m)}||H^{(n)}|$  and  $|l_e|^2$  (Sections 3.1.2 and 3.1.3) are then applied to Eq. (2.63) to estimate  $S_V^{src}$ .

## 2.8 Summary of Methodology

Figure 2.15 summarizes the methodology developed in this chapter. The ATM is employed first to obtain  $G_R(Z'_A)$ , which is required by the CIM; and  $T_{sky}$ , which serves both as *in situ*

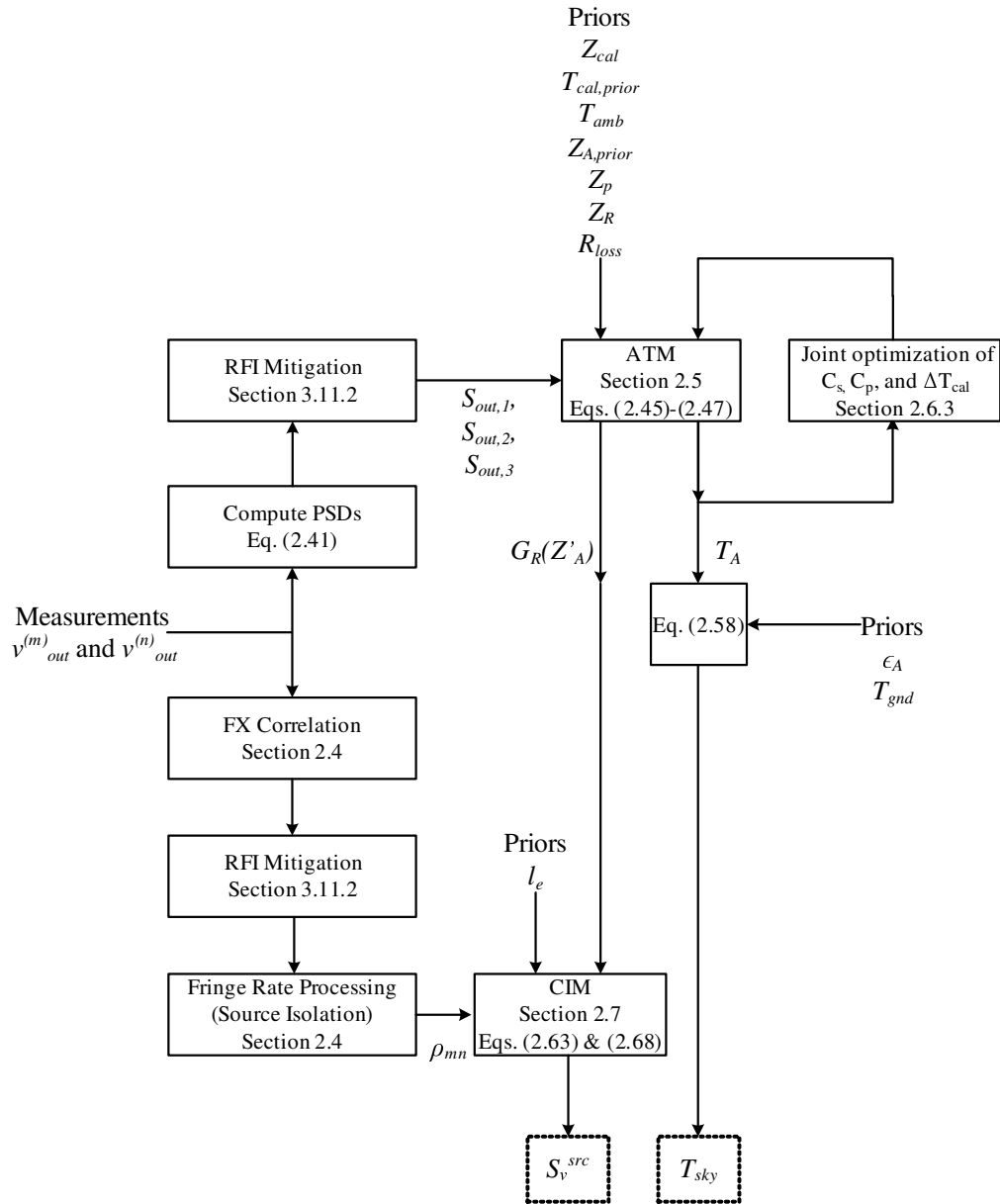


Figure 2.15: Overview of the methodology presented in this chapter.

Table 2.3: Priors required for the absolute flux density and Galactic background noise measurements, and where they are determined in this dissertation.

Prior	Reference
Priors required for $G_R(Z'_A)$	
$Z_{cal}$	Appendix E
$T_{cal,prior}$	Appendix E
$Z_{A,prior}$	Section 3.1.4
$Z_p$	Section 3.2.3
$Z_R$	Section 3.2.3
Additional priors required for $T_{sky}$	
$\epsilon_A$	Section 3.1.5
$T_{gnd}$	Section 3.1.5
$T_{amb}$	Section 3.2.1
$R_{loss}$	Section 3.1.4
Additional priors required for $S_\nu^{src}$	
$l_e$	Sections 3.1.2 and 3.1.3

commissioning and as a standalone scientific result.

Priors are shown in Fig. 2.15 where they first enter the processing. Table 2.2 identifies the origin of the required priors in the present work.

# Chapter 3

## Instrumentation

This chapter documents the new instrumentation developed to implement the methodology described in Chapter 2. The instrument was deployed during the campaign documented in Chapter 4 to obtain the absolute flux density measurements reported in Chapter 6. The instrument operates as a two-element interferometer; Fig. 3.1 shows the system diagram. An antenna is pictured in Fig. 3.2, and the back end is pictured in Fig. 3.3.

Section 3.1 documents the antenna design and characterization. The antenna is integrated with front end electronics (FEE; documented in Section 3.2). The cables which connect the antenna and FEE to the back end are documented in Section 3.3. The back end consists of the analog receiver (ARX; documented in Section 3.4) and digital receivers (DRXs; documented in Section 3.8). The ARX provides amplification and filtering to condition the signal for the DRX. Two DRXs are operated at any given time, one operating in the first Nyquist zone (NZ1) and the other in the second Nyquist zone (NZ2). Custom-designed anti-aliasing filters (AAFs; documented in Section 3.5) block all but the desired frequency range for each Nyquist zone. Data are recorded by a PC (data recorder, DR; documented in Section 3.8).

The rest of this chapter is organized as follows. Sections 3.1-3.8 document the instrument design, per the discussion above. The system's analog gain and sensitivity are analyzed in

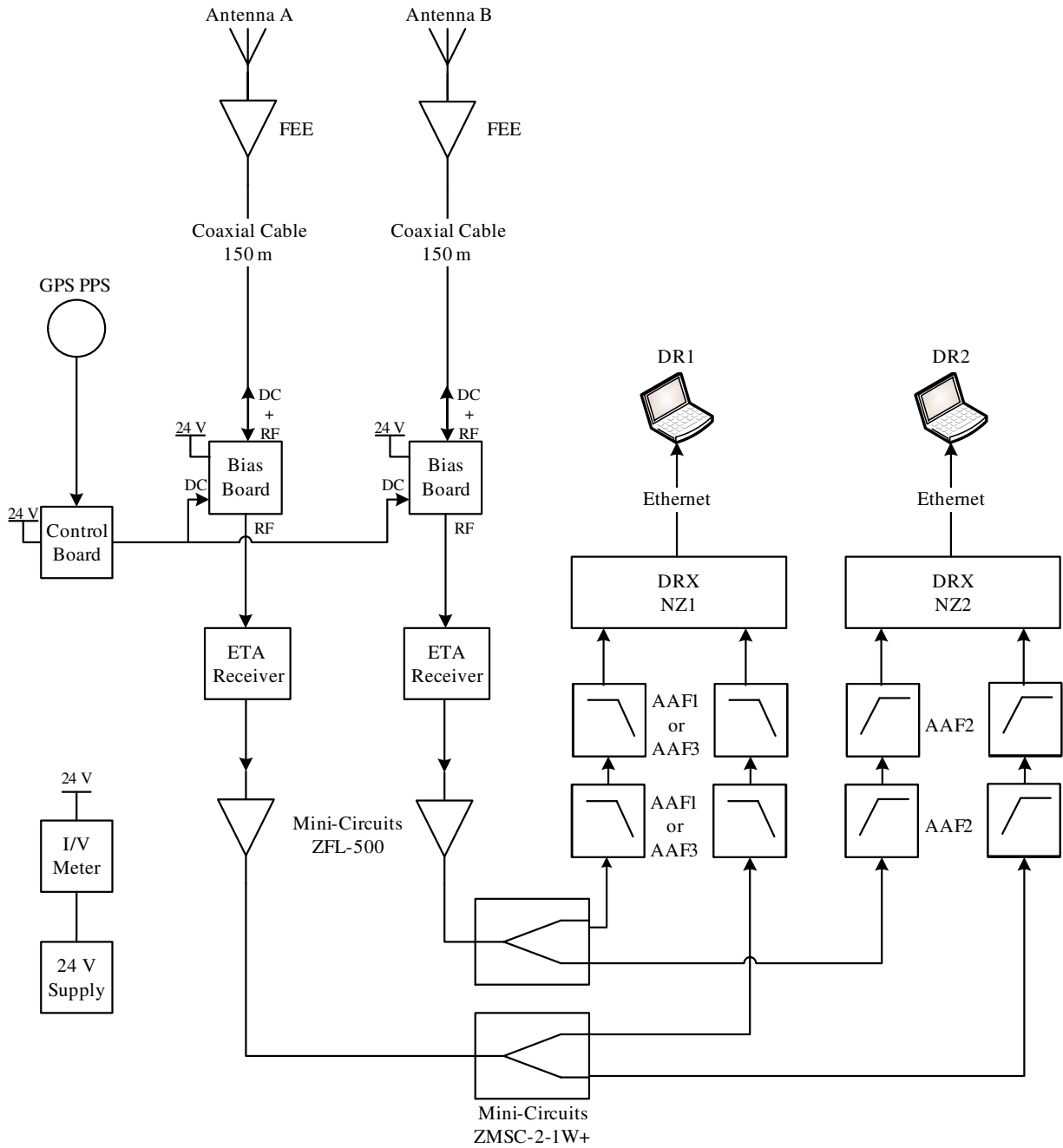


Figure 3.1: Block diagram of the two-element interferometer.



Figure 3.2: Deployed antenna, with the ground screen outlined. See Fig. 3.4 for dimensions.

Sections 3.6 and 3.7, respectively. The Bias and Control Boards, which regulate the power for the instrument, are documented in Section 3.9. Commissioning results are presented in Section 3.10. Finally, the RFI mitigation algorithm is detailed in Section 3.11.

## 3.1 Antennas

This section presents the design and characterization of the antennas. Similar to the systems discussed in Section 1.1, the antennas are simple, straight dipoles to facilitate accurate characterization of the antenna pattern and impedance. Additionally, the antennas were designed to be mechanically simple, to facilitate deployment to multiple sites and baselines.

The rest of this section is organized as follows. Section 3.1.1 presents the mechanical design of the antenna. Sections 3.1.2 and 3.1.3 present two characterizations of the effective length of the antenna. It will be seen in Section 6.1 that both models are required, because one is

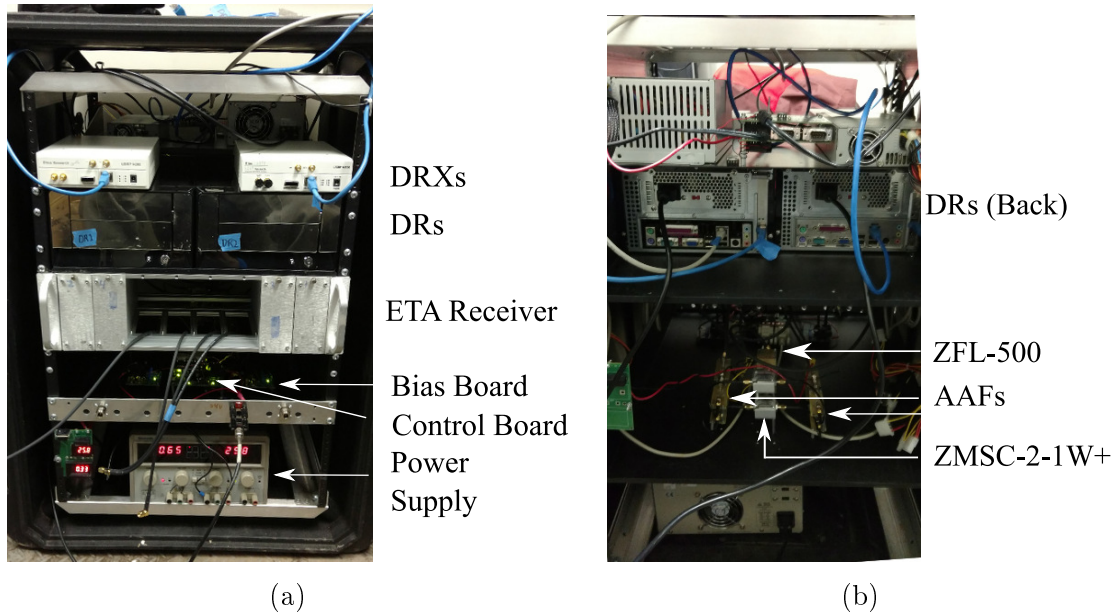


Figure 3.3: The back end, shown in its portable enclosure. (a) Front of the back end. (b) Back of the back end.

better for lower zenith angles, and the other is better for higher zenith angles. Section 3.1.4 presents the characterization of the antenna impedance. Finally, Section 3.1.5 discusses ground loss.

### 3.1.1 Mechanical Design

Figure 3.2 shows an antenna as deployed during a measurement. Figures 3.4 and 3.5 show mechanical diagrams for the overall antenna and the feed region, respectively. The antennas are constructed of two 1.52 m long  $\times$  2.54 cm diameter copper pipes positioned 1.52 m above a ground screen. The ground screen is made of 2 mm diameter wire in a 5 cm  $\times$  10 cm grid, having a total size of 7.6 m  $\times$  7.6 m. The antenna feed region droops by approximately 2 cm slightly relative to the ends of the antenna due to gravity.

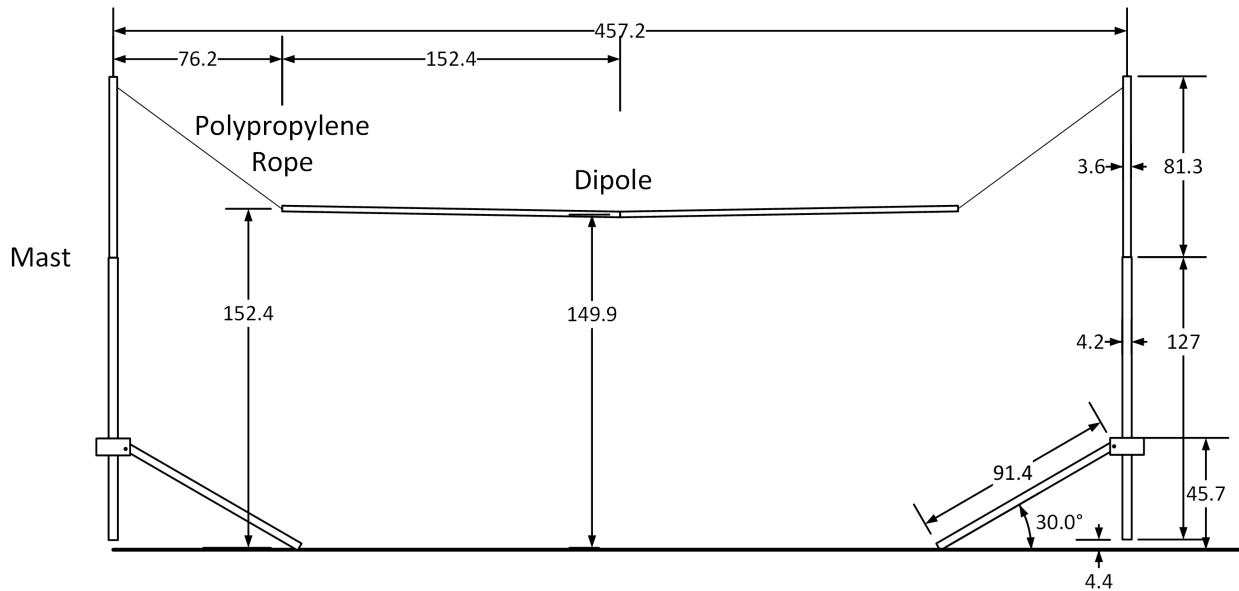


Figure 3.4: Mechanical diagram of the antenna, drawn to scale. All dimensions are in centimeters. Only one leg of each mast is shown; there are two other identical legs mutually separated by 120° to the pictured leg. Polypropylene guy wires (not shown, see e.g. Fig. 3.4) stabilize the masts.

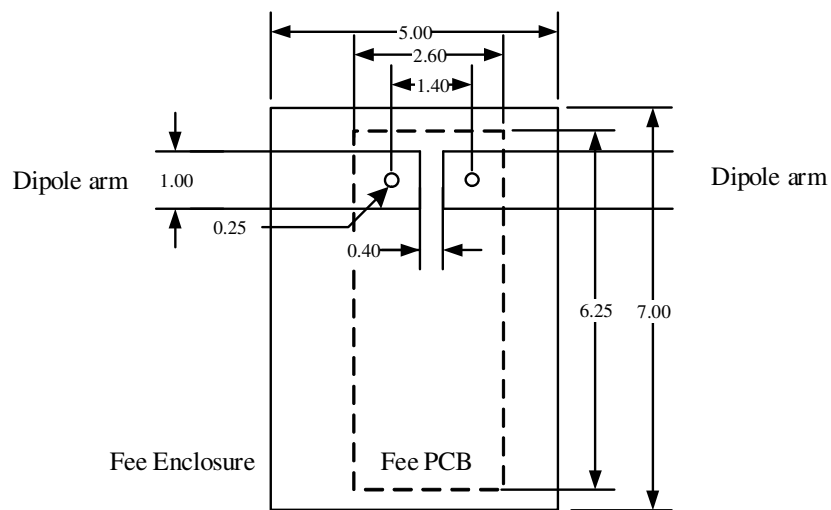


Figure 3.5: Mechanical diagram of the antenna feed, drawn to scale. Dimensions are in inches.

### 3.1.2 Effective Length: IT/PEC

As discussed in Section 2.7, the effective length projected in the direction of the source,  $l_e$ , of the antenna is required as a prior to estimate the source flux density. In this section, we present an idealized method, using image theory, to determine  $l_e$ . In Section 3.1.3, we introduce practical effects of the ground using the Method of Moments (MoM), and compare to the resulting  $l_e$  presented here.

The reciprocity theorem of electromagnetics may be applied to determine the VEL [41, Chapter 3.3.2]. First, apply a test current  $I_t$  to the antenna terminals. This test current gives rise to a current distribution  $I(l')$ , where  $l'$  parameterizes length along the antenna. The VEL may be calculated by

$$\mathbf{l}_e(\hat{\mathbf{r}}) = \frac{1}{I_t} \int_{\text{wire}} I(l') \left( \hat{\mathbf{l}}(l') \times \hat{\mathbf{r}} \times \hat{\mathbf{r}} \right) e^{-j\beta \mathbf{r}(l') \cdot \hat{\mathbf{r}}} dl' \quad (3.1)$$

where  $\hat{\mathbf{l}}(l')$  is the unit tangent to the antenna,  $\mathbf{r}(l')$  is the distance from the origin to the antenna at point  $l'$ , and  $\beta$  is the wavenumber.

The magnitude of the current along an infinitesimally-thin dipole in free space is well-modeled by [37, Chapter 5.1.1]

$$I(l') = I_t \frac{\sin \left[ \beta \left( \frac{L}{2} - |l'| \right) \right]}{\sin \frac{\beta L}{2}} \quad (3.2)$$

where  $I_t$  is the terminal current and  $L$  is the total length of the dipole. While this antenna is not infinitesimally-thin, the 2.54 cm diameter is less than 0.7% of a wavelength over the frequency range of interest. We therefore ignore the finite diameter of the antenna in this analysis.

When evaluated with Eq. (3.2) for an antenna oriented on the  $\hat{\mathbf{x}}$ -axis and the terminals

centered at the origin, Eq. (3.1) yields

$$\mathbf{l}_e(\hat{\mathbf{r}}) = \left( -\hat{\boldsymbol{\theta}} \cos \theta \cos \phi + \hat{\boldsymbol{\phi}} \sin \phi \right) 2 \frac{\cos \left[ \frac{\beta L}{2} \sin \theta \cos \phi \right] - \cos \frac{\beta L}{2}}{\beta \sin \frac{\beta L}{2} \left( 1 - \sin^2 \theta \cos^2 \phi \right)} \quad (3.3)$$

As described in Section 3.1.1, the antenna is above a ground screen. By assuming the ground screen approximates an infinite perfect electric conducting (PEC) ground, we may invoke image theory. The VEL of the antenna is found by adding the VEL of the antenna using (3.3) and its image, yielding:

$$\mathbf{l}_e(\hat{\mathbf{r}}) = \left( -\hat{\boldsymbol{\theta}} \cos \theta \cos \phi + \hat{\boldsymbol{\phi}} \sin \phi \right) \frac{\cos \left[ \frac{\beta L}{2} \sin \theta \cos \phi \right] - \cos \frac{\beta L}{2}}{\beta \sin \frac{\beta L}{2} \left( 1 - \sin^2 \theta \cos^2 \phi \right)} j4 \sin \left( \beta h \cos \theta \right) e^{-j\beta h \cos \theta} \quad (3.4)$$

where  $h$  is the height of the antenna over ground.

The resulting  $l_e$  is shown in Fig. 3.6, computed with Eq. (3.4). Due to the application of image theory, effects of the ground are potentially over-simplified in this model. In the next section, we will use MoM to introduce effects of the real Earth ground and the ground screen. We refer to the method presented here as “IT/PEC” to distinguish it from the MoM method presented in the following section.

### 3.1.3 Effective Length: MoM

The primary limitation of the IT/PEC model is the assumption of an infinite, perfect ground. As discussed in Section 3.1.1, the antenna is positioned over a finite wire ground screen above a real Earth ground, the relative permittivity  $\epsilon_r$  and conductivity  $\sigma$  of which are poorly known. In this section, we introduce a MoM solution for  $l_e$  which includes a realistic model for the ground.

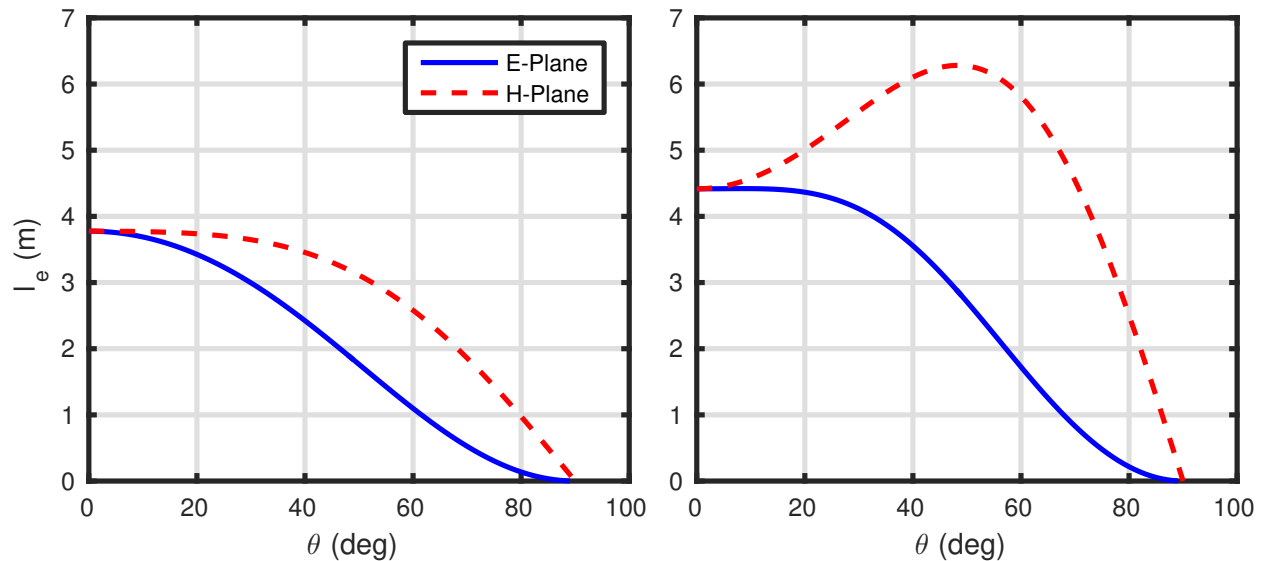


Figure 3.6: IT/PEC model of the projected effective length of the antenna at 47 MHz (left) and 74 MHz (right). Co-polarized components are shown.

The MoM implementation is NEC4.<sup>1</sup> NEC4 takes as input the user defined geometry and source, and returns the current distribution (which subsequently gives the antenna impedance) and the far field gain  $G$  as a function of pointing direction. We then use  $G(\theta, \phi)$  to estimate  $l_e$  as follows.  $G(\theta, \phi)$  is related to effective aperture by [37, Chapter 2.5]:

$$A_e = \frac{\lambda^2}{4\pi} G \quad (3.5)$$

The relationship between  $A_e$  and  $l_e$  is derived in Appendix F. By solving Eq. (F.4) for  $l_e$ :

$$l_e = \sqrt{\frac{4R_A}{\eta} A_e} \quad (3.6)$$

The antenna is modeled as a straight PEC wire 3.04 m long by 2.54 cm diameter, consisting of 21 segments, positioned 1.52 m above the ground. The ground is modeled in three ways: (1) as an infinite PEC ground, (2) as a medium dry ground, having a conductivity of 5 mS m<sup>-1</sup> and a relative permittivity of 15, and (3) as a very dry ground, having a conductivity of

<sup>1</sup><https://ipo.llnl.gov/technologies/nec>

0.1 mS m<sup>-1</sup> and a relative permittivity of 3 [42]. The Sommerfield-Norton method is used to model the ground in (2) and (3).

For (2) and (3), a model of the ground screen is included. The 5 cm × 10 cm grid would require over 23,000 segments to model the 7.6 m × 7.6 m ground screen. However, the number of segments is limited to about 12,000 due to memory limitations. As a compromise, the ground screen is modeled by 7.6 m wires, parallel to the antenna, 1 cm above the ground. The wires are spaced 5 cm apart with 11.6 cm long segments, for a total of 10,872 segments.<sup>2</sup> The antenna is fed by a 1 V source at the center segment. From the current distribution, NEC4 computes  $G(\theta, \phi)$  across the upper hemisphere, with a 1° resolution in both  $\theta$  and  $\phi$ .  $l_e$  is then computed as described above.

Figure 3.7 shows the resulting  $l_e$  for the three different ground models. Reasonable agreement is seen between the PEC ground and the medium and very dry ground, and also with the IT/PEC model shown in Fig. 3.6. Exceptional agreement is seen between the medium and very dry grounds, implying that the pattern is not sensitive to the ground conditions. We will adopt the very dry ground result as the sole MoM model going forward, since it is representative of the worst-case (i.e. most lossy) ground.

In Section 6.1, we will show that the difference between IT/PEC and MoM significantly affects the resulting estimate of  $S_\nu^{src}$ . Therefore, we cannot simply use one model in favor of the other, but must determine from the results when to use each model. We will show in Section 6.1 that MoM is more appropriate for  $\theta < 20^\circ$ , and that IT/PEC is more appropriate for  $\theta > 20^\circ$ .

---

<sup>2</sup> This model for the ground screen was compared to a different model which satisfied the limit on number of segments using a rectangular grid having spacing 15.5 cm × 7.7 cm. The difference in  $Z_A$  between the two ground screen models was < 3%, and the difference in  $\epsilon_A$  between the two ground screen models was < 1%. Therefore, the ground screen model used here is assumed to be reasonable.

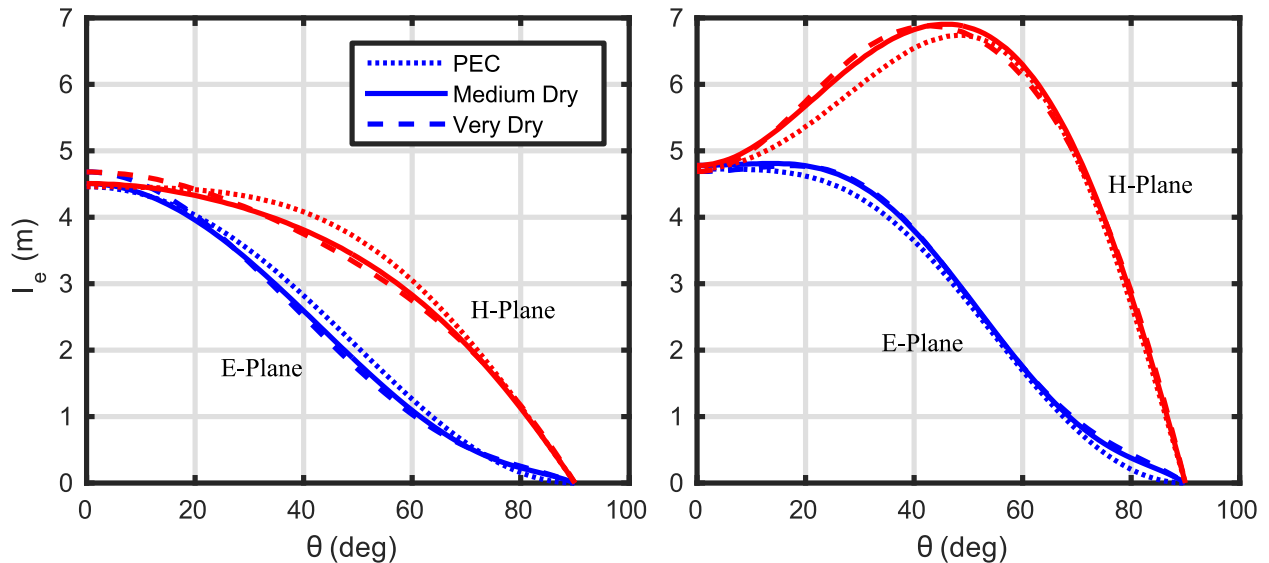


Figure 3.7: MoM calculations of projected effective length of the antenna at 47 MHz (left) and 74 MHz (right). Co-polarized components are shown.

### 3.1.4 Antenna Impedance

As illustrated in Fig. 2.15, the antenna impedance  $Z_A$  is required as a prior when invoking the ATM. In principle, it should be straightforward to determine  $Z_A$ , since the antenna is a simple dipole. However, the coupling between the antenna and the nearby real Earth ground complicates  $Z_A$ . Furthermore, the FEE enclosure (see Section 3.2.1) is adjacent to the high current density region around the antenna terminals, which also affects  $Z_A$ . In this section, we quantify the effects of the Earth ground and the enclosure through simulation and direct measurement.

NEC4 was used to model the effect of the ground screen over a realistic ground. The simulation setup is identical to that described in Section 3.1.3. The results are shown in Fig. 3.8. The difference between the PEC ground the real ground models is significant, motivating the *in situ* measurement of  $Z_A$ . Fortunately, the impedance is not sensitive to the ground conditions for either real Earth ground. Therefore it is not necessary to consider a range of ground conditions; any realistic ground is sufficient. In the following, we will consider the very dry ground when referring to the NEC4 simulation of  $Z_A$ .

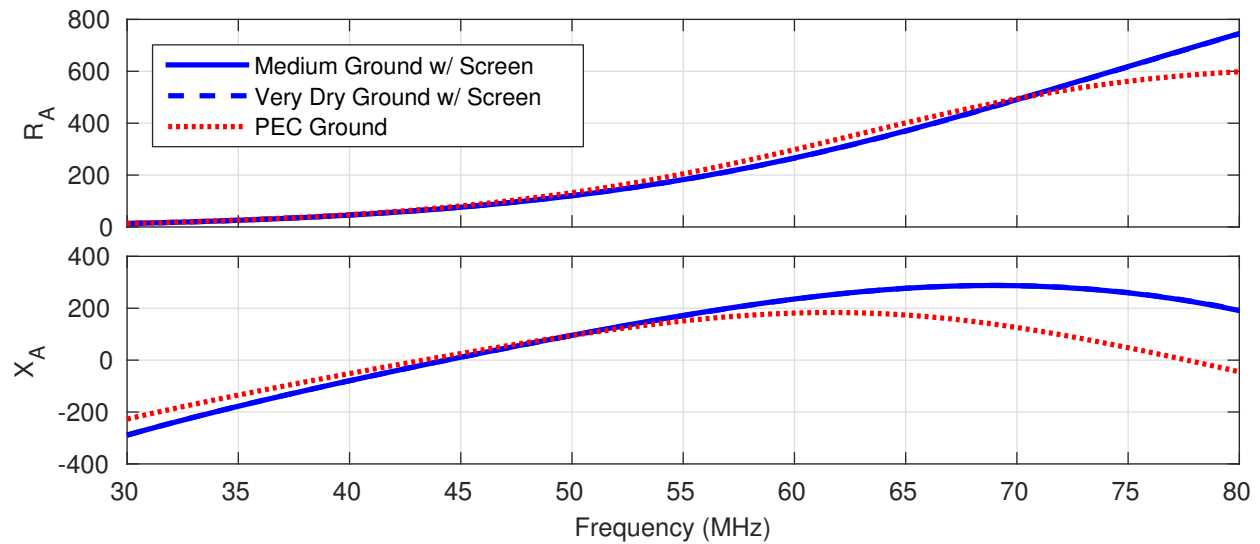


Figure 3.8: Comparison of  $Z_A$  over an infinite PEC ground and over a real ground (medium and very dry) with the ground screen. Note the difference in  $Z_A$  for the medium and very dry ground is negligible, such that the two curves are identical.

Figure 3.9 shows the geometry around the antenna terminals. HFSS<sup>3</sup> was used to quantify the effect of the features surrounding the antenna terminals. The antenna was simulated in free space, both with and without the enclosure, to determine the effect of the enclosure on  $Z_A$ . Additionally, the antenna and enclosure were simulated over a PEC ground to facilitate comparison with the NEC4 simulations.

The results of the HFSS simulations are shown in Fig. 3.10. It is evident by comparing the two free space simulations that the presence of the enclosure significantly affects the antenna impedance.

Since the ground conditions and the enclosure significantly affect  $Z_A$ , we performed an *in situ* measurement. The measurements were performed using a spectrum analyzer with a voltage standing wave ratio bridge, operating in tracking generator mode. The spectrum analyzer, which is single-ended, is interfaced to the antenna, which is differential, using a Mini-Circuits ADT1-1 balun. The balun and cable connecting the spectrum analyzer to the antenna are subsequently calibrated out of the measurement using the spectrum analyzer's

<sup>3</sup><http://www.ansys.com/Products/Electronics/ANSYS-HFSS>

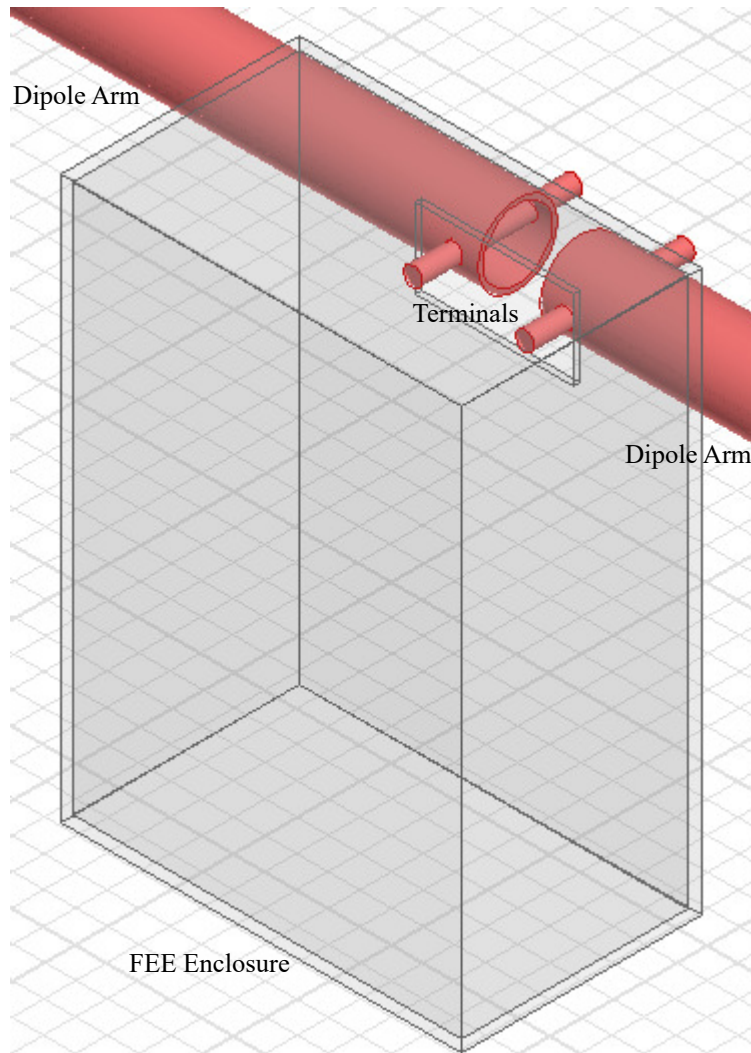


Figure 3.9: The antenna terminals and the surrounding features. See Fig. 3.5 for dimensions.

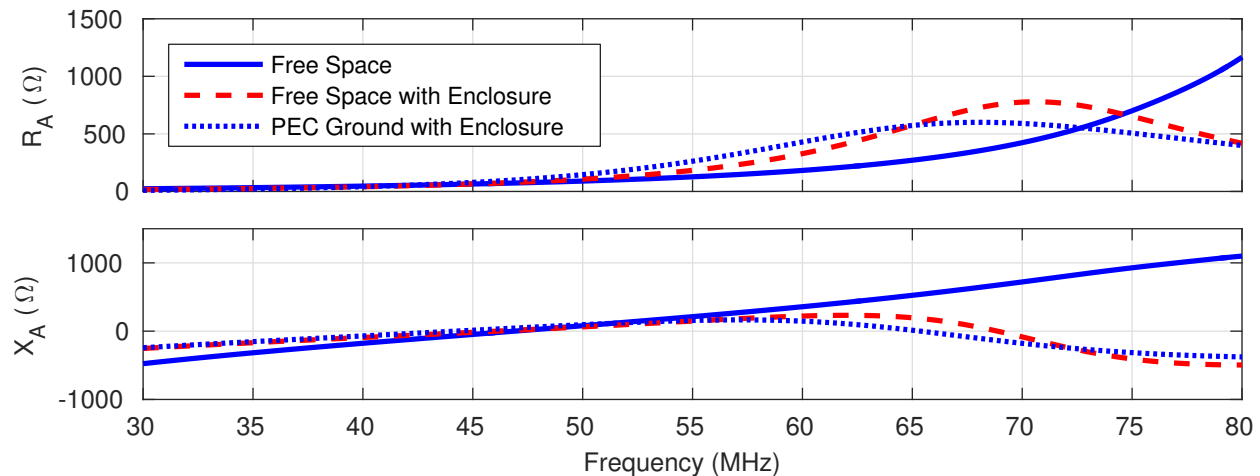


Figure 3.10: Resulting  $Z_A$  from full wave simulations including a detailed model of the feed.

Open-Short-Matched Load method.<sup>4</sup>

Figure 3.11 shows the antenna reflection coefficient,  $\Gamma_A$ , measured by the spectrum analyzer. This measurement was conducted near VLA (see Section 4.1).  $\Gamma_A$  is related to the antenna impedance by

$$\Gamma_A = \frac{Z_A - Z_0}{Z_A + Z_0} \quad (3.7)$$

where  $Z_0 = 50 \Omega$  is the input impedance of the spectrum analyzer.

Figure 3.12 shows the measured  $Z_A$ , calculated by solving Eq. (3.7) for  $Z_A$  given the measured  $\Gamma_A$  shown in Fig. 3.11. Figure 3.12 also shows the HFSS model (including the enclosure and PEC ground) and NEC4 model (no enclosure, but with a ground screen above a very dry ground). The measurement agrees generally with the HFSS result below about 50 MHz, and diverges from the HFSS result above  $\sim 50$  MHz. Since no result stands out as the most correct, we will use the measurement for  $Z_{A,prior}$ . Later in this section, we show the final  $Z_A$ , obtained by the modification to  $Z_{A,prior}$  discussed in Section 2.6.1.

The simulations described in this section assumed the antenna is a straight wire, and perfectly

<sup>4</sup> This method assumes the balun has an infinite common mode rejection ratio (CMRR). The ADT1-1 has a reported amplitude imbalance of 0.31 dB and phase imbalance of  $1.44^\circ$  at 40 MHz, which correspond to a CMRR of 28.4 dB. Therefore, error in the measured  $Z_A$  associated with neglecting the CMRR is expected to be about  $\sim 0.1\%$ .

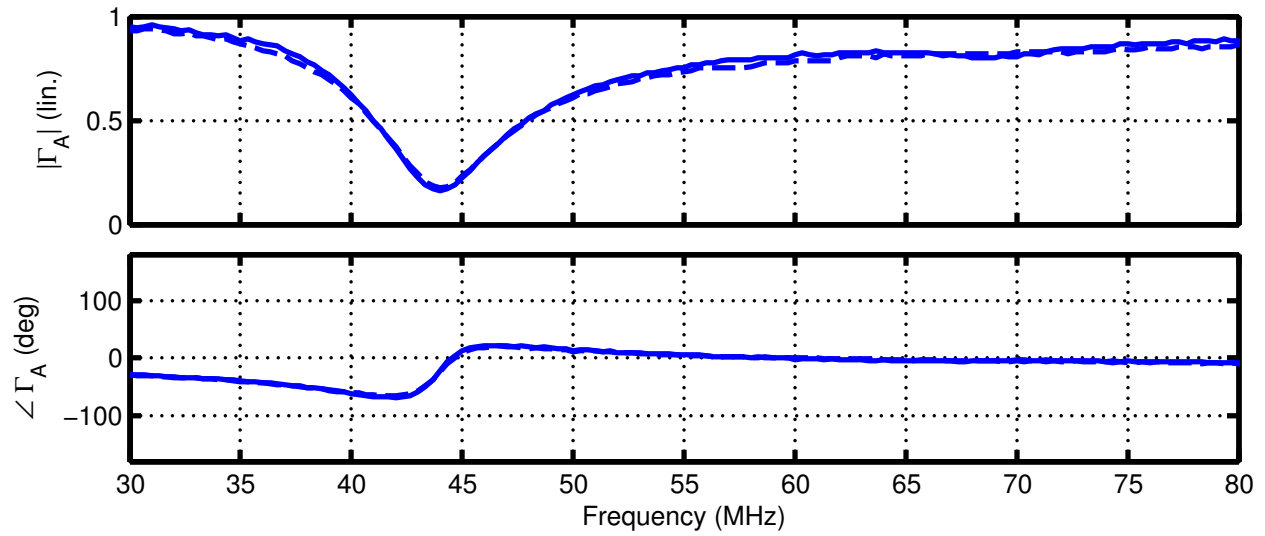


Figure 3.11: Measured reflection coefficient at the antenna terminals. The different curves are for the two antenna; solid for Antenna A, dashed for Antenna B.

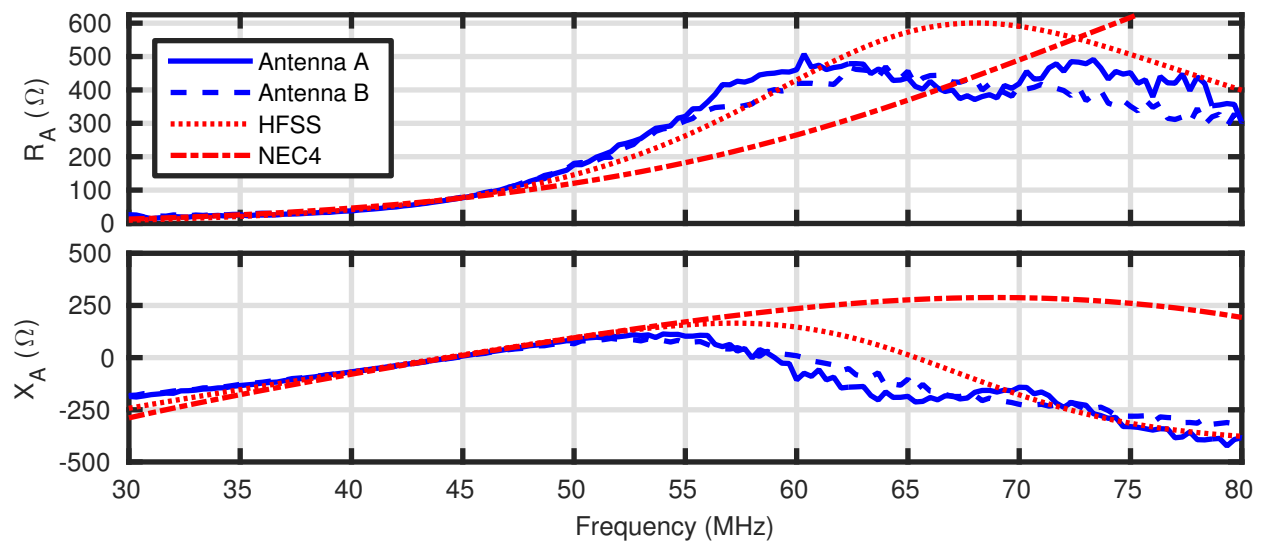


Figure 3.12: Impedance of the antenna.

aligned with the ground screen. As discussed in Section 3.1.1, the antenna terminals droop by  $\sim 2$  cm relative to the ends of the antenna. Method of Moment (NEC2) simulations were conducted to determine the effects of the droop of the antenna terminals relative to the ends of the antenna. The droop was found to cause negligible ( $< 0.2\%$ ) change in impedance over the frequency range of interest.

Additionally, the deployed antenna exhibited a rotation of up to  $\sim 5^\circ$  relative to the wires in the ground screen due to factors such as error during the setup and wind moving the antenna. NEC2 simulations were performed to determine the effect of this rotation on the antenna impedance and pattern. The simulations predicted a negligible ( $< 0.1\%$ ) change in impedance for rotations of less than  $5^\circ$  over the frequency range of interest.

The simulations described above assumed the antenna was constructed of a PEC. Therefore the real part of the simulated impedance is simply  $R_{rad}$ . As discussed in Section 3.1.1, the antenna is made of copper, which gives rise to a small but finite ohmic resistance  $R_{loss}$ .  $R_{loss}$  may be approximated by

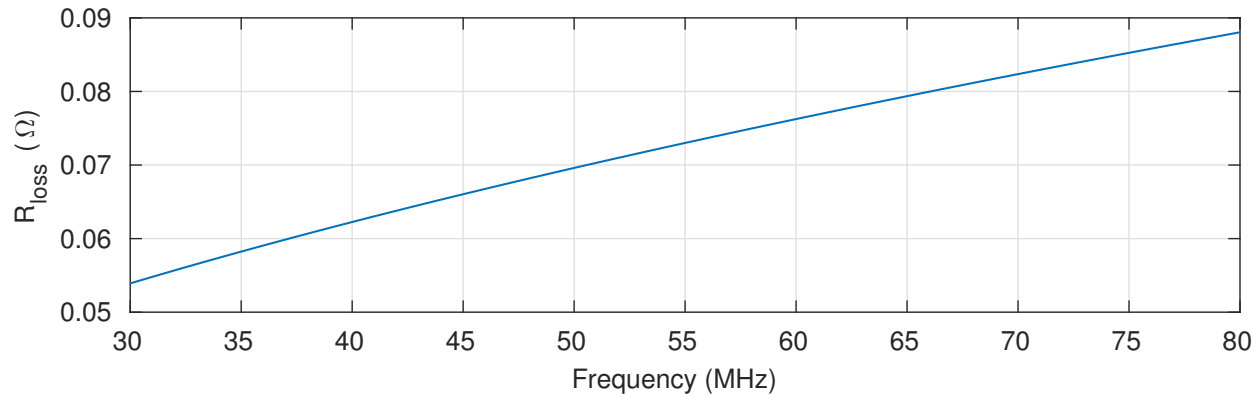
$$R_{loss} \cong \rho_{Cu} \frac{L}{2\pi a \delta_{Cu}} \quad (3.8)$$

where  $\rho_{Cu} \approx 1.68 \times 10^{-8} \Omega \text{ m}$  is the resistivity of copper;  $L = 3.05$  m and  $a = 1.27$  cm are the length and radius, respectively, of the antenna described in Section 3.1; and  $\delta_{Cu}$  is the skin depth of copper. Equation (3.8) is derived by assuming  $\delta_{Cu} \ll a$ . The “good conductor” approximation may be used to obtain the skin depth (see e.g. [43])

$$\delta_{Cu} \cong \sqrt{\frac{\rho_{Cu}}{\mu_0 \pi \nu}} \quad (3.9)$$

where  $\mu_0 \approx 4\pi \times 10^{-7} \text{ H m}^{-1}$  is the permeability of free space. Therefore  $\delta_{Cu}$  is  $11.2 \mu\text{m}$  at 30 MHz and  $7.3 \mu\text{m}$  at 80 MHz, validating the assumption that  $\delta_{Cu} \ll a$ .

Figure 3.13 shows the resulting estimate of  $R_{loss}$ . While small,  $R_{loss}$  is  $\mathcal{O}[1\%]$  of  $R_{rad}$  below  $\sim 40$  MHz. Therefore  $R_{loss}$  is not negligible and must be applied when invoking the ATM to estimate  $T_{sky}$ .

Figure 3.13: Estimate of  $R_{\text{loss}}$ .

In summary, the ground and the enclosure have a significant effect on  $Z_A$ . The measurements of  $Z_A$  shown in Fig. 3.12 serve as the best prior estimate of  $Z_A$ . However, as will be seen in Section 5.1.2, the uncertainty in this estimate of  $Z_A$  is still significant enough to bias the result. Therefore, we introduce two capacitances,  $C_p$  and  $C_s$ , to modify the antenna impedance, as discussed in Section 2.6.1. The new impedance model is shown in Fig. 2.13. In Section 5.2, we determine  $C_p$  and  $C_s$  to be  $-5$  pF and  $150$  pF for Antenna A, respectively, and  $-7$  pF and  $120$  pF for Antenna B, respectively. Figure 3.14 shows the resulting modified  $Z_A$  that is when invoking the ATM. It is interesting to note the improved agreement with the NEC4 model despite the fact that  $C_p$  and  $C_s$  are determined independently of MoM. This suggests that the effect of the ground on  $Z_A$  is more significant than the effect of the feed.

### 3.1.5 Ground Loss

This section describes the evaluation of the ground loss efficiency  $\epsilon_A$ . As described in Section 2.5.2,  $\epsilon_A$  is required when invoking the ATM to determine  $T_{\text{sky}}$ . For an infinite PEC ground,  $\epsilon_A = 1$ . We use NEC4 to determine  $\epsilon_A$  for the medium dry and very dry ground.

As before, we will use NEC4 to simulate a transmitting antenna. From reciprocity considerations, let us assume that the transmit and receive case are the same. For a transmitting

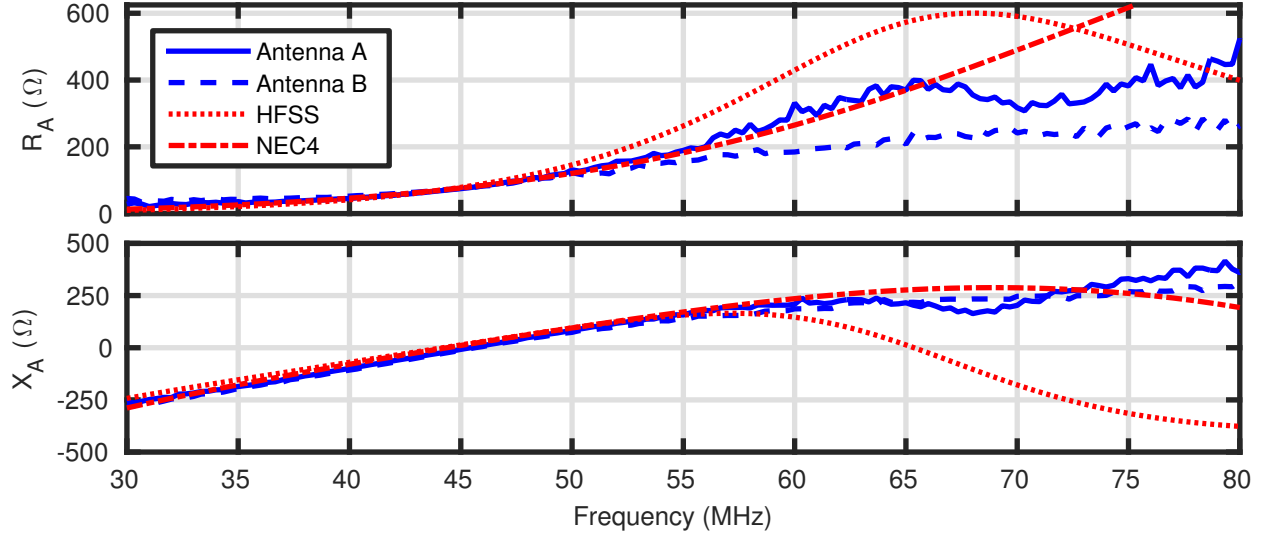


Figure 3.14: Same as Fig. 3.12 but including estimated  $C_p$  and  $C_s$  determined in Section 5.2.

antenna,  $\epsilon_A$  may be expressed as

$$\epsilon_A = \frac{P_{\theta \leq 90^\circ}}{P_{\theta \leq 90^\circ} + P_{\theta > 90^\circ}} \quad (3.10)$$

where  $P_{\theta \leq 90^\circ}$  is the power radiated into the upper half plane, and  $P_{\theta > 90^\circ}$  is the power dissipated in the ground. Given the peak electric field amplitude  $E$  (i.e. from NEC4):

$$P_{\theta \leq 90^\circ} = \int_{\theta=0}^{\pi/2} \int_{\phi=0}^{2\pi} \frac{|E|^2}{2\eta} R^2 \sin \theta d\phi d\theta \quad (3.11)$$

where  $R$  is the distance to the far field. We cannot compute  $P_{\theta > 90^\circ}$  directly, since NEC4 cannot calculate the antenna pattern below the ground. Instead, we can compute the power delivered to the antenna as follows:

$$\begin{aligned} P_{in} &= \frac{1}{2} \text{Re} \left\{ v_t \left( \frac{v_t}{Z_A} \right)^* \right\} \\ &= \frac{1}{2} |v_t|^2 \frac{R_A}{|Z_A|^2} \end{aligned} \quad (3.12)$$

where  $v_t$  is the peak terminal voltage (which we set to 1 V, as described in Section 3.1.3).

Now note that, for a PEC antenna exhibiting no ohmic loss,

$$P_{in} = P_{\theta \leq 90^\circ} + P_{\theta > 90^\circ} \quad (3.13)$$

Applying Eq. (3.13) to (3.10):

$$\epsilon_A = \frac{P_{\theta \leq 90^\circ}}{P_{in}} \quad (3.14)$$

Figure 3.15 shows the ground loss efficiency computed in this manner, for the medium dry and very dry ground conditions discussed in Section 3.1.3. The ground screen model discussed in Section 3.1.3 is included in the simulation.  $\epsilon_A$  is significant for both ground models, in that the ground absorbs  $\sim 2 - 9\%$  of the incident power, depending on the ground conditions. The very dry ground exhibits greater loss than the medium dry ground, which is expected due to the lower permittivity and conductivity of the very dry ground.

Figure 3.15 also shows  $\epsilon_A$  computed for an infinite PEC ground, as a sanity check. For this scenario,  $\epsilon_A$  should be unity, since no power is dissipated by the ground. The simulation predicts  $\epsilon_A$  slightly greater than 1, which is attributed to numerical error. However, since  $|\epsilon_A - 1|$  for the PEC ground is much less than  $|\epsilon_A - 1|$  for Earth ground models, we can assume the estimate of  $\epsilon_A$  for the Earth grounds are significant. Therefore, we use the very dry ground model for  $\epsilon_A$  in estimates of  $T_{sky}$ , since it is representative of the worst-case (i.e. most lossy) ground.

## 3.2 Front End Electronics (FEE)

This section documents the FEE that was developed for the absolute flux density measurements. The FEE was designed to (1) establish the sensitivity of the system (2) provide high linearity to facilitate measurements in locations with significant RFI, and (3) implement the three-state calibration technique described in Section 2.5. This section summarizes the design of the FEE; additional details and a discussion of higher-level issues can be found in

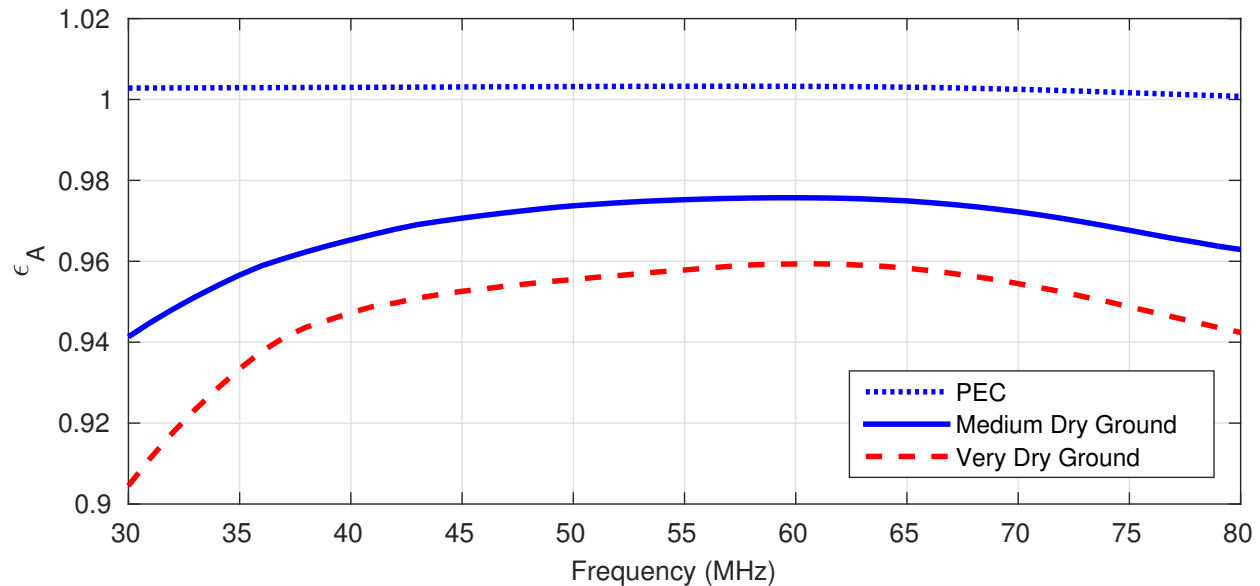


Figure 3.15: Ground loss efficiency for various ground conditions.

a journal paper [34].

The rest of this section is organized as follows. Section 3.2.1 presents an overview of the FEE design. Section 3.2.2 summarizes the performance of the FEE. Finally, Section 3.2.3 characterizes the input impedance of the FEE.

### 3.2.1 FEE Design

This section summarizes the design of the FEE. Figure 3.16 shows a FEE affixed to its enclosure, which doubles as a heat sink. The schematic, printed circuit board (PCB) layout, and bill of materials are included in Appendix G.1.

A block diagram of the FEE is shown in Fig. 3.17. HELA-10 amplifiers are used as a pre-amplifier and a line driver, respectively. The HELA-10s were selected for their superior performance relative to the linearity-sensitivity tradeoff identified in [34]. Preceding the first amplifier are notch filters designed to trap the strong signals from Citizen Band (CB) and FM radio at 26.5–27.5 and 88–108 MHz, respectively. An absorptive second-order Butterworth

filter sets the bandpass of the FEE to 30–80 MHz (3 dB). The signal path is differential (i.e. balanced) from the antenna through the output of the FEE, at which point a balun converts the signal path to 50  $\Omega$  single-ended.

As discussed in Section 2.5.2, the ambient temperature  $T_{amb}$  is required to estimate  $T_R(Z'_A)$ .  $T_{amb}$  is measured during the temperature data loggers,<sup>5</sup> which are affixed to the inside of the FEE enclosure. During the measurement, one value of  $T_{amb}$  is recorded for each FEE at 60 s intervals.

Each FEE draws  $\sim 0.8$  A of DC current for a DC voltage ranging from 16–20 V. As shown in Fig. 3.17, the RF output is blocked to the DC bias by a 0.1  $\mu\text{F}$  capacitor. A 4.7 mH inductor acts as a RF choke to block the RF signal from the DC bias and control circuit.

### 3.2.2 FEE Performance

This section describes the RF performance of the FEE. Table 3.1 compares the FEE used in this work to those employed in other contemporary radio telescopes. The different FEEs are compared in terms of input-referred noise temperature  $T_F$  as a metric for sensitivity, and input-referred 1 dB compression point  $P_{1dB}$  as a metric for linearity.  $P_{1dB}$  is defined as the input power at which the FEE gain is 1 dB lower than the expected (linear) gain.

Additional linearity metrics include the input-referred second and third order intercept points, IIP2 and IIP3, respectively. IIP3 is defined as the input power at which the power in the output third-order intermodulation products (i.e. the cross-frequency terms output in response to a two-tone input signal) is equal to the power in the fundamental tone. IIP2, is defined as the input power at which the power in the second harmonic is equal to the power in the fundamental tone. The measured  $P_{1dB}$  and IIP3 are +11 dBm and +25 dBm, respectively, at 50 MHz, and the achieved IIP2 was again beyond our ability to measure (i.e. greater than +70 dBm).

---

<sup>5</sup><http://www.onsetcomp.com/products/data-loggers/ua-001-64>

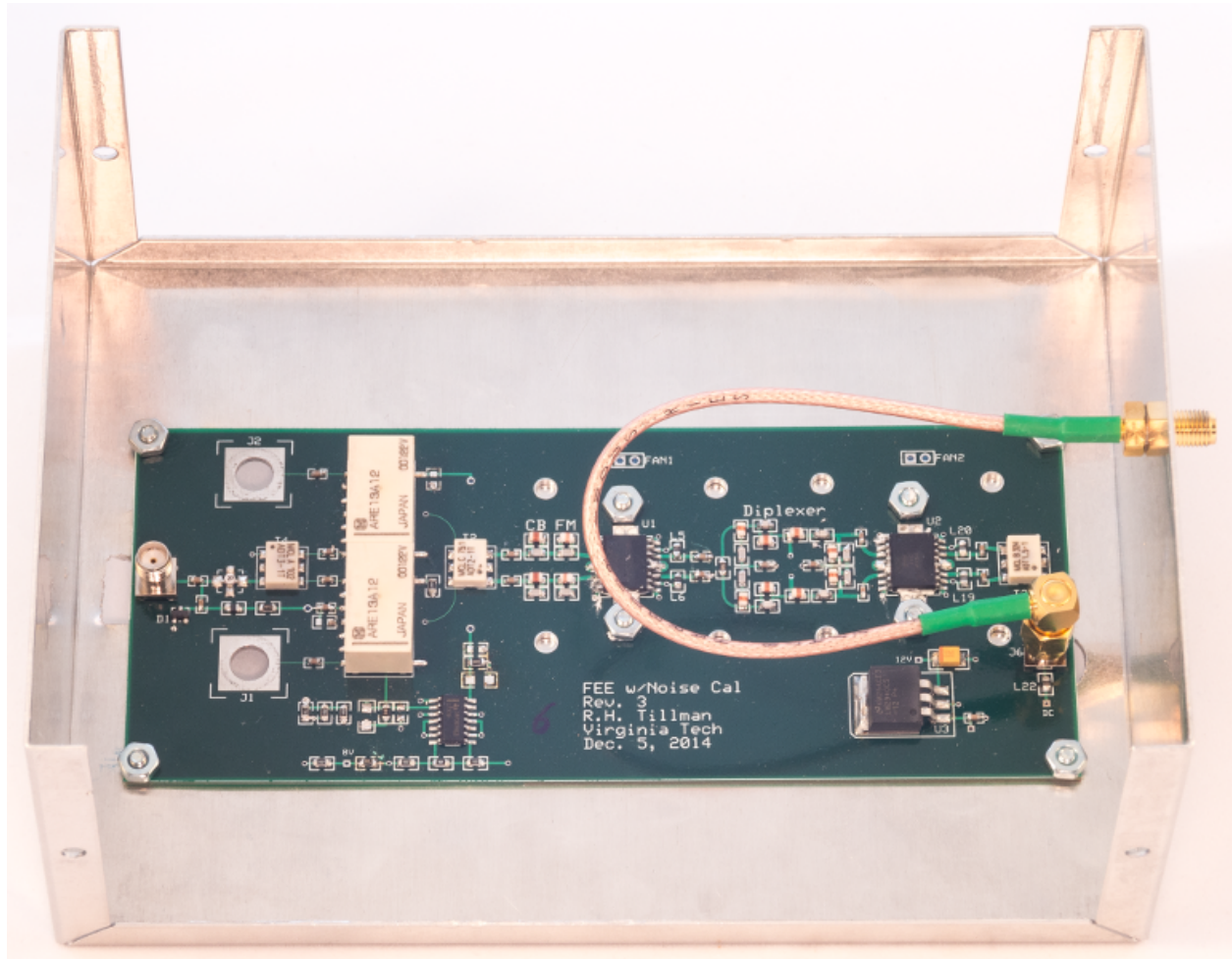


Figure 3.16: A fabricated FEE within its enclosure, with the cover removed.

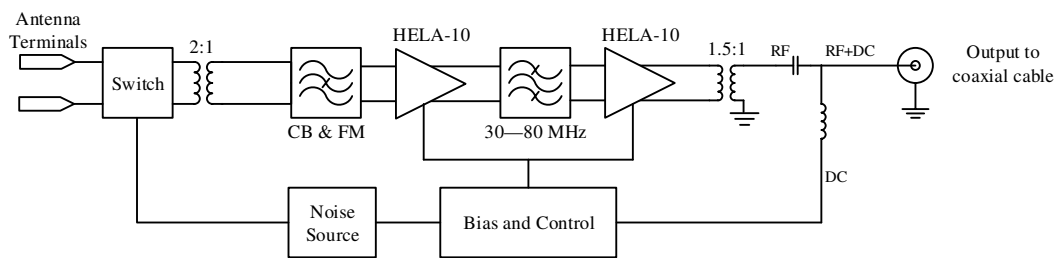


Figure 3.17: Block diagram of the FEE.

Table 3.1: Comparison of the new FEE to those of other contemporary radio telescopes.

	This Work	EVLA [44]	LWA1 [45]	LOFAR Low-band Array [46]
Antenna	Straight Dipole	Cassegrain Reflector	Bowtie V-Dipole	Straight V-Dipole
$\nu$	30–80 MHz	50-86 MHz	10-88 MHz	10-80 MHz
$T_F$	295* K	710** K	225 K	800 K
Input $P_{1dB}$	+11 dBm	–13 dBm	–18 dBm	–12 <sup>†</sup> dBm
Internal Cal?	Yes	Yes	No <sup>‡</sup>	No

\*The measured  $T_F$  is significantly better than the datasheet reported value of 330 K. The reason for the discrepancy is unknown, however it does not bear on the results presented here.

\*\*Includes 2 dB cable loss between antenna and FEE.

<sup>†</sup>The measured  $P_{1dB}$  for LOFAR’s active balun has not been reported in the literature. This value is for the transistor used in the active balun under recommended bias conditions.

<sup>‡</sup>LWA1 has five “outrigger” antennas with internal cal, but which are not part of the “core” array of 512 dipoles.

Figure 3.18 shows the typical (average from the four constructed units) FEE gain  $G_F$  and input-referred noise temperature  $T_F$ . To measure the gain, a 3:1 balun is used to interface the 50  $\Omega$  single-ended spectrum analyzer to the 150  $\Omega$  differential nominal input impedance of the FEE. The gain of this balun was measured and removed from Fig. 3.18. The difference between the measurement and the model above  $\sim 80$  MHz is attributed to parasitics in the components used in the filters.

### 3.2.3 FEE Input Impedance

Following the circuit model shown in Fig. 2.5, the FEE presents an input impedance  $Z_{in}$  to the antenna.  $Z_{in}$  may be expressed in terms of the input impedance of the receiver,  $Z_R$ , and the parasitic impedance  $Z_p$ , as

$$Z_{in} = \left[ \frac{1}{Z_p} + \frac{1}{Z_R} \right]^{-1} \quad (3.15)$$

As illustrated in Fig. 2.15, prior estimates of  $Z_R$  and  $Z_p$  are required when invoking the ATM. In this section, we determine  $Z_p$  using HFSS, and  $Z_R$  from measurements.

The parasitic impedance  $Z_p$  is nominally an open circuit. However, the geometry of the FEE

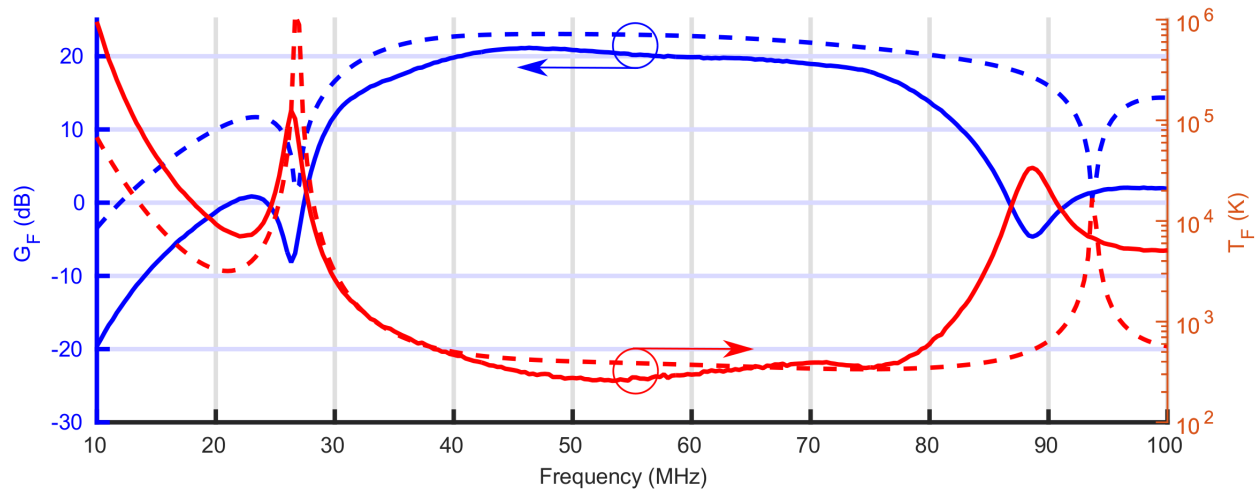
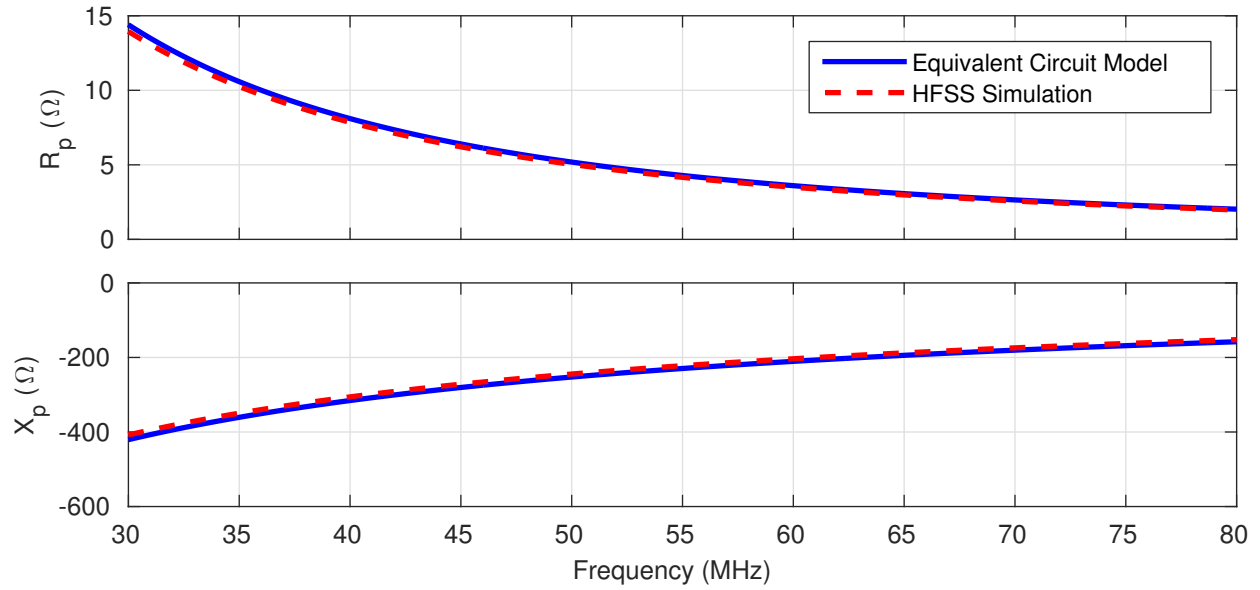
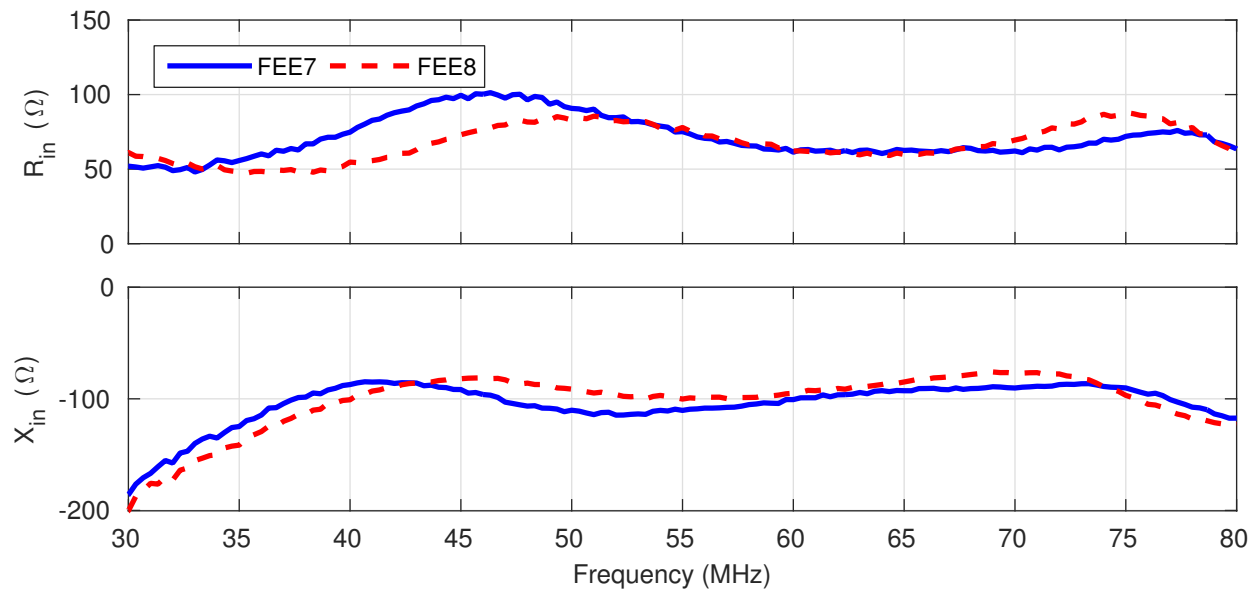


Figure 3.18: Measured (solid) and predicted (dashed) gain and noise temperature of the FEE.

printed circuit board (PCB) (see Fig. G.3) suggest a possible parasitic capacitance between the PCB feed terminals and the inner copper layers. HFSS simulations of the FEE PCB were performed to estimate  $Z_p$ . The geometry of the PCB was modeled according to the manufacturer specifications, and assuming FR-4 substrate having a relative permittivity of 4.6.

Figure 3.19 shows the simulated  $Z_p$ . The parasitic impedance is well modeled by a 12.3 k $\Omega$  resistor in parallel with a 12.6 pF capacitor, also shown in Fig. 3.19.

$Z_{in}$  was measured via the same technique used to measure  $Z_A$  discussed in Section 3.1.4. Figure 3.20 shows the measured  $Z_{in}$  for the two fabricated FEEs used in the measurement campaign reported in Chapter 4, identified as FEE7 and FEE8. Figure 3.21 shows  $Z_R$  estimated by solving Eq. (3.15) for  $Z_R$ , given the measured  $Z_{in}$  and the modeled  $Z_p$ . The estimated  $Z_R$  agrees reasonably with the nominal value expected from the schematic, but exhibits a significant frequency dependence. The estimated  $Z_R$  and the modeled  $Z_p$  are used as the priors.

Figure 3.19: The parasitic impedance  $Z_p$ .Figure 3.20: The FEE input impedance  $Z_{in}$ .

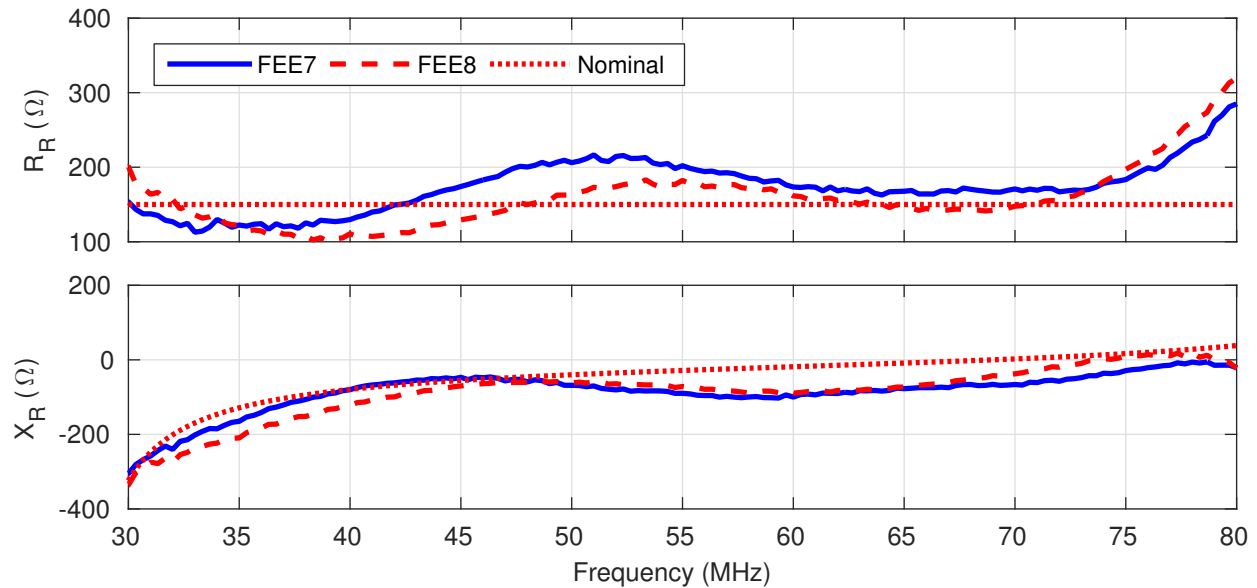


Figure 3.21: The receiver input impedance  $Z_R$ . The nominal value is determined from the schematic (see Fig. G.1), assuming a constant  $75 \Omega$  input impedance for the HELA-10.

### 3.3 Cables

This section describes the long cables which connect the FEE to the back end (see Fig 3.1). The maximum baseline length is 300 m, i.e. the sum of the lengths of the 150 m coaxial sections. This corresponds to baseline lengths of  $30\lambda$  and  $80\lambda$  and 30 and 80 MHz, respectively. This length is sufficiently long to facilitate the source isolation, but long enough to resolve the source (see Section 2.4).

A diagram of a cable assembly is shown in Fig. 3.22. 150 m of Times LMR-400<sup>6</sup> provides most of the baseline length, and sections of 2.4 m RG-58 on each end connect the male N-type connectors on the LMR-400 to the female SMA-type connectors on the FEE and Bias Board.

LMR-400 has a loss of 2.2 and 2.9 dB/100 m at 30 and 80 MHz, respectively. The RG-58 has a loss of 4.6 and 16.1 dB/100 m at 10 and 100 MHz, respectively. Figure 3.23 shows the expected and measured gain of the cable assemblies. The difference between the measurement

<sup>6</sup><https://www.timesmicrowave.com/documents/resources/LMR-400.pdf>

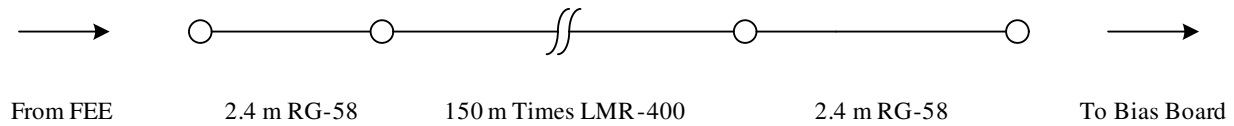


Figure 3.22: Diagram of the cables connecting the FEE to the back end.

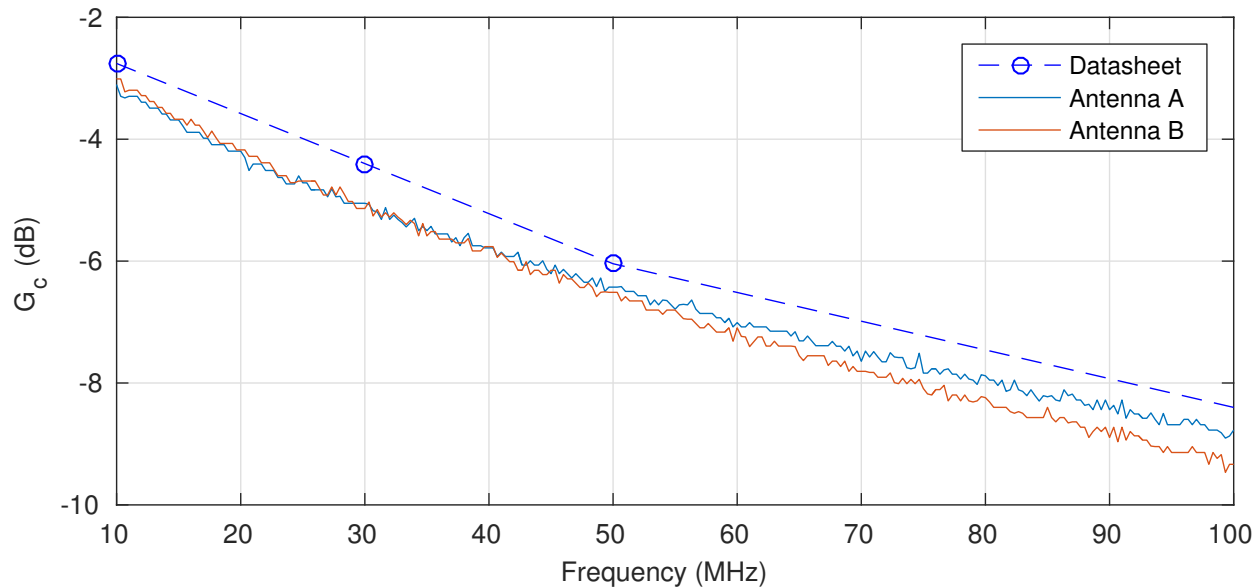


Figure 3.23: Measured and expected (from datasheet values) gain of the cable assemblies.

and the expected gain is about 0.5 dB, and is attributed to the adapters between the two sections of RG-58 and the LMR-400.

Ideally, the delay associated with the cable is frequency independent. In practice the cables introduce dispersion. Dispersion has a potential to impact the source isolation (see Section 2.4) in two ways. One effect of dispersion is a change in the phase of the signal at the output of the two cables. This effect is irrelevant since the two cables are the same length (see Fig. 3.1). Additionally, dispersion may smear the delay-stopped signal to other frequency bins. We will now show that this effect is also negligible.

The delay associated with the cable is [47]

$$\tau_c(\nu) = \tau_0 + \tau_d(\nu) \quad (3.16)$$

where  $\tau_0$  is the nominal (non-dispersive) delay and

$$\tau_d(\nu) = \tau_0 \frac{1}{8\sqrt{\pi\mu}} \left( \frac{\sigma_a^{-1/2}}{a_c} + \frac{\sigma_b^{-1/2}}{b_c} \right) \left( \ln \frac{b_c}{a_c} \right)^{-1} \nu^{-1/2} \quad (3.17)$$

is the excess delay due to dispersion. The constituent parameters for LMR-400 are:

- Radius of the inner conductor  $a_c = 2.74$  mm,
- Radius of the inward facing wall of the outer conductor  $b_c = 7.24$  mm,
- Conductivity of the inner and outer conductor  $\sigma_a$  and  $\sigma_b$ , respectively. Accounting for the materials typically used, we assume  $\sigma_a = \sigma_b = 10^6$  S/m is reasonable.
- Permeability of free space  $\mu = 4\pi \times 10^{-7}$  H/m.

LMR-400 has a propagation velocity of  $0.85c$ , where  $c \approx 3 \times 10^8$  is the free space speed of light. Thus, for 150 m of LMR-400,  $\tau_0 \approx 588$  ns, and  $\tau_d \leq 4$  ns for  $\nu \geq 30$  MHz.

If significant, dispersion would negatively impact the delay-stopping by smearing the delay-stopped signal away from  $f_r = 0$ . However, for the 65.1 kHz bandwidth used by the FX correlator, the time-resolution is  $1/65.1$  kHz =  $15.4\mu\text{s} \gg \tau_d$ . Therefore dispersion is considered negligible.

### 3.4 Analog Receiver (ARX)

This section describes the ARX. Referring to Fig. 3.1, the ARX consists of the receiver designed for the Eight-meter Transient Array (ETA) [48], Mini-Circuits ZFL-500 connected amplifiers, Mini-Circuits ZMSC-2-1W+ power splitters, and custom designed AAFs. The ETA receiver, shown in Fig. 3.24, provides bandpass filtering between 15 and 85 MHz (3 dB bandwidth) and adjustable gain between 53 to 85 dB in 4 dB steps [49, 50]. After the ETA receiver, Mini-Circuits ZFL-500 amplifiers provide an additional 21 dB of gain over

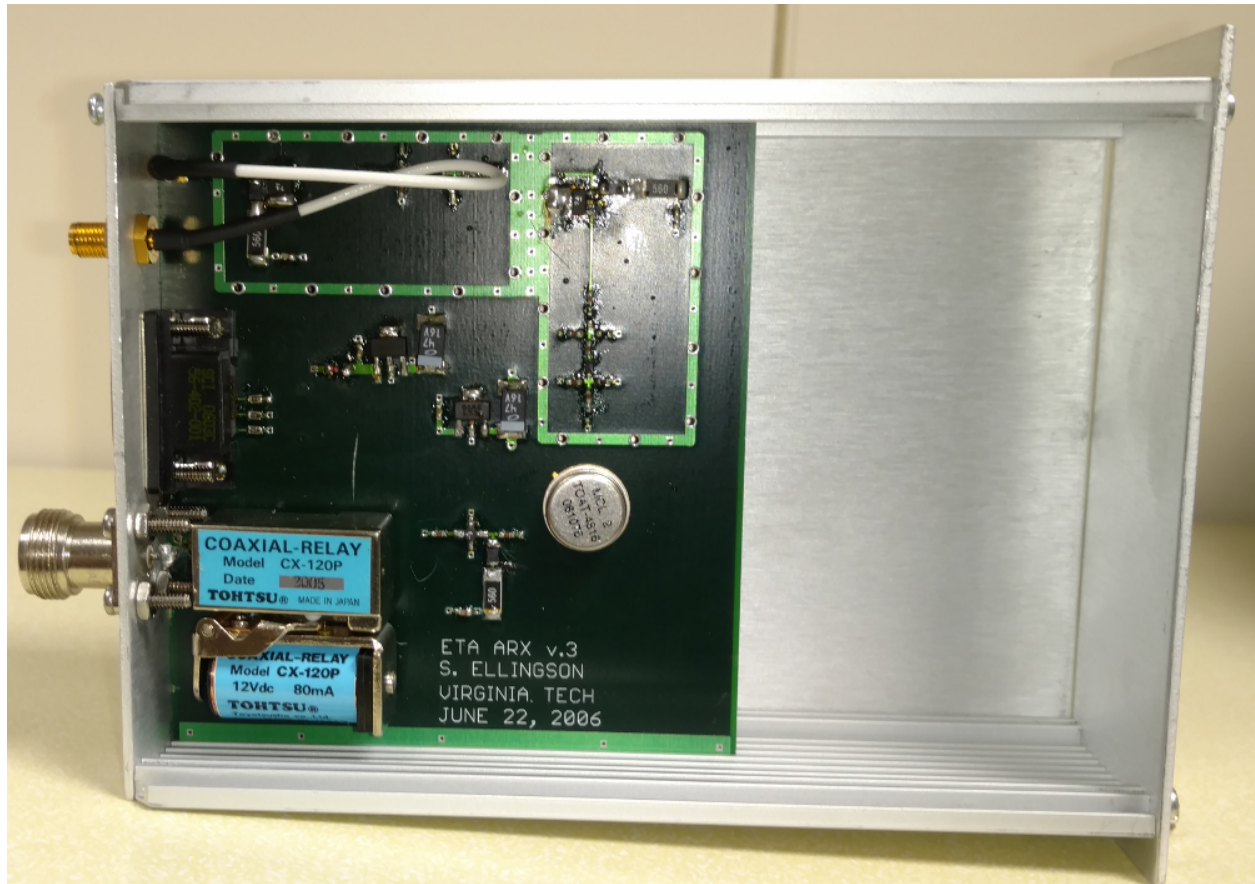


Figure 3.24: The ETA receiver within its enclosure.

the entire passband. Finally, Mini-Circuits ZMCS-2-1-W+ splitters divide the signal into two signal paths; one signal path goes to a low-pass AAF, the other to a high-pass AAF. The AAFs, considered a part of the ARX from a system perspective, are presented in the following section.

### 3.5 Anti-Aliasing Filters (AAF)

The AAFs filter block all but the desired frequency range for each Nyquist zone. Different AAFs are used for the two different models of DRX (see Section 3.8); one, the USRP, samples at 100 MHz; the other, the S60, samples at 120 MHz. Three different AAFs filters

are employed, depending on the DRX model and desired Nyquist zone. Two of each type of AAF are operated in cascade to increase the aliasing rejection near the Nyquist frequency. A bill of materials for each type of AAF is included in Appendix G.2.

A schematic of AAF1 is shown in Fig. 3.25(a), and is pictured in Fig. 3.26(a). AAF1 is a seventh-order Chebyshev low-pass filter with a 48 MHz corner frequency. AAF1 is used with the USRP operating in the first Nyquist zone (NZ1).

A schematic of AAF2 is shown in Fig. 3.25(b), and is pictured in Fig. 3.26(b). AAF2 is a seventh-order Chebyshev high-pass filter with a 52 MHz corner frequency. AAF2 is used with the USRP operating in the second Nyquist zone (NZ2).

A schematic of AAF3 is shown in Fig. 3.25(c), and is pictured in Fig. 3.26(c). AAF3 is a seventh-order Butterworth low-pass filter with two notch filters to further increase the anti-aliasing rejection. The low-pass filter has a 50 MHz corner frequency, and the notches are resonant at 58 MHz and 69 MHz. AAF3 is used with the S60 operating in NZ1.

Figure 3.27 shows the gain of two AAFs in cascade for each AAF version. Figure 3.28 shows the aliasing rejection, defined as the ratio of the received power at the aliased frequency to the received power at the desired frequency. For example, for AAF1, a 0 dBm signal at 54 MHz appears as a  $-50$  dBm signal at 46 MHz to the USRP operating in NZ1. Aliasing rejection of greater than 30 dB is deemed sufficient, as less than 0.1% of the received power in any frequency channel is due to aliasing. By this criteria, 47.3–53 MHz are unusable by the USRPs. The S60, used in 48.16–50.16 MHz, receives negligible aliased power when using AAF3, and thus completes the coverage.

## 3.6 Summary of the Analog System Response

This section summarizes the expected and measured performance of the analog system, the components of which are documented above in Sections 3.2-3.5. We will consider the system's

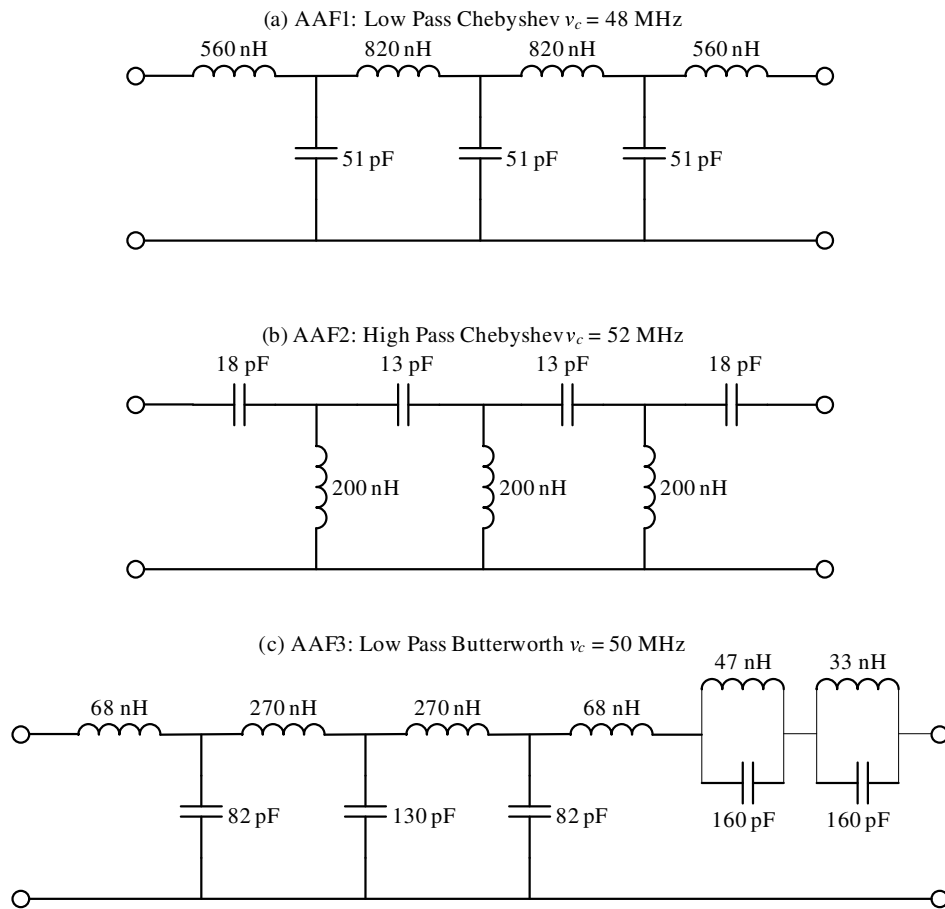


Figure 3.25: Schematic diagram of the AAFs.

(a) AAF1



(b) AAF2



(c) AAF3

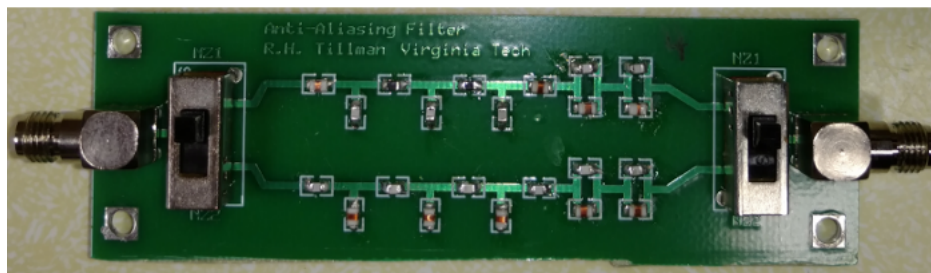


Figure 3.26: The fabricated AAFs. Note the AAF3 board also contains the dual high-pass version of AAF3, selectable with a switch, which was never used.

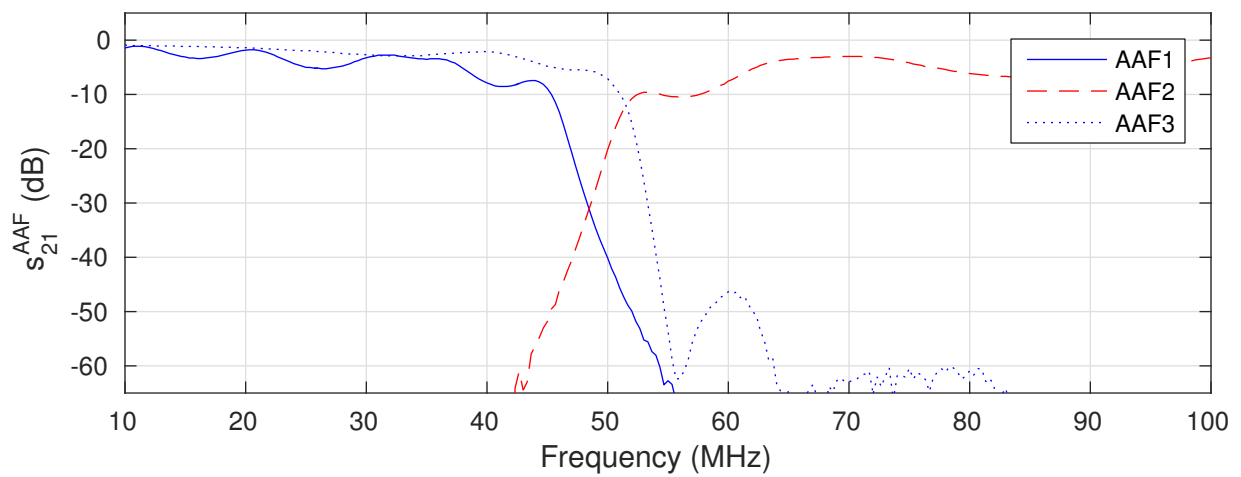


Figure 3.27: Measured gain of two AAFs in cascade.  $Z_0 = 50\Omega$ .

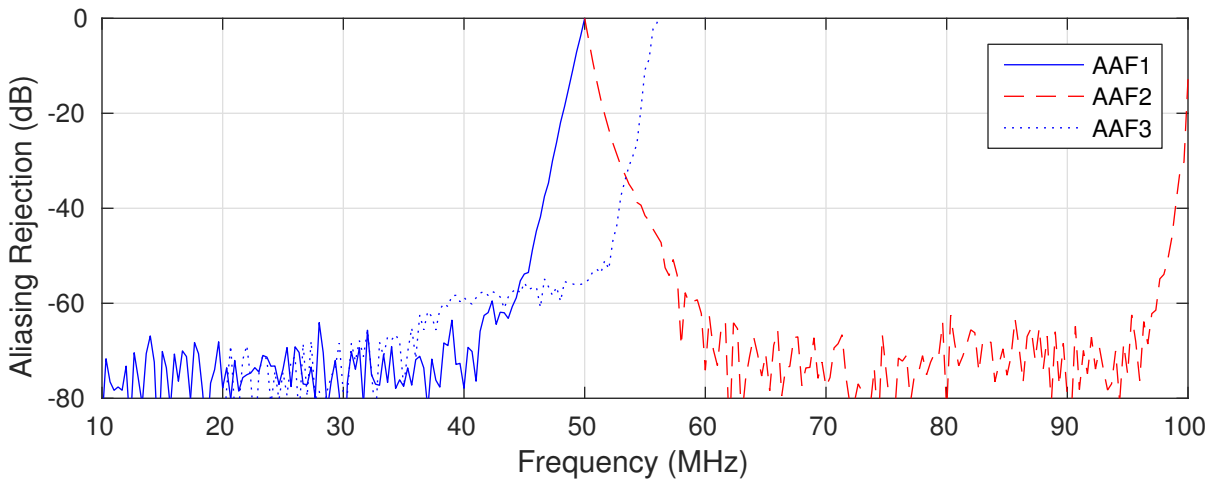


Figure 3.28: Aliasing rejection of each AAF.

gain, noise, and linearity.

Figure 3.29 shows the measured gain of the receiver in both Nyquist zones. This is the receiver TPG, defined in Section 2.5.1, for a source impedance of 150  $\Omega$ .

GNL analysis (see Appendix H) is used to determine the expected performance of the receiver. The input-referred  $P_{1dB}$  is used as the linearity metric, instead of IIP3, since it was provided by the manufacturer for more components. The values used in this analysis are determined as follows:

- *FEE*: The FEE's contribution to  $G_R$  and  $T_R$  are measured and shown in Fig. 3.18. The FEE's  $P_{1dB}$  of +11 dBm was measured at 50 MHz.
- *Cables*: The cable's gain  $G_c$  is measured and was shown in Fig. 3.23. The noise temperature of the cable is calculated as

$$T_c = T_{amb} \left( \frac{1}{G_c} - 1 \right) \quad (3.18)$$

where  $T_{amb} \approx 290$  K is the ambient physical temperature. The  $P_{1dB}$  of the cable is assumed to be large enough not to affect the system  $P_{1dB}$ , and so is arbitrarily set to 200 dBm.

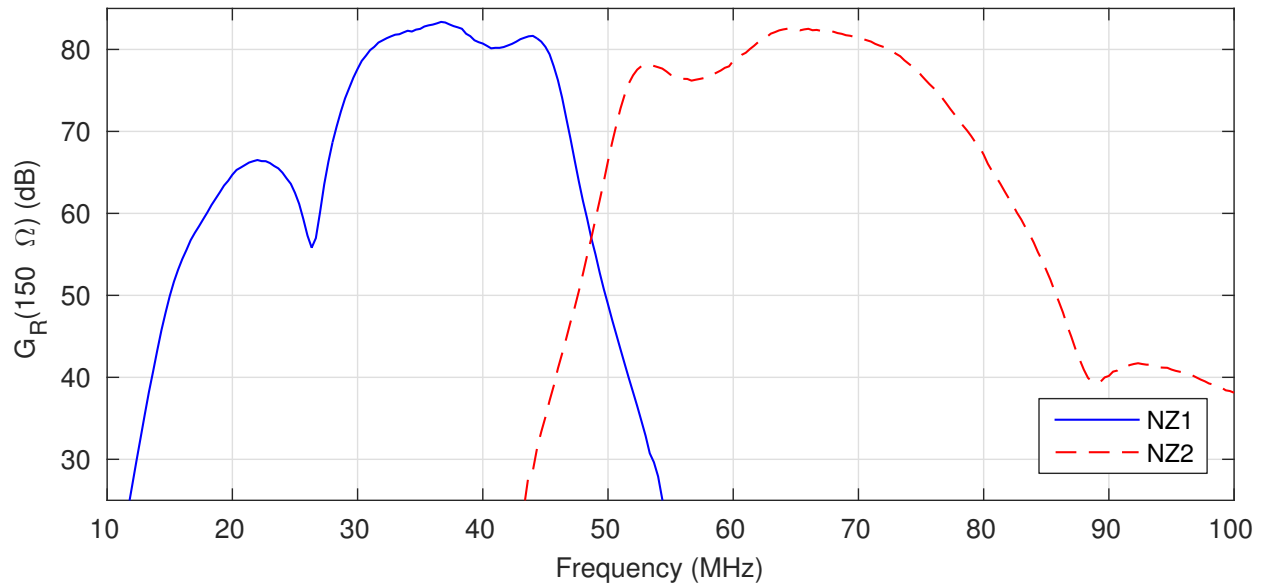


Figure 3.29: Measured cascade gain of the receiver, from the antenna terminals on the FEE to the input of the DRX.

- *ETA Receiver*: The gain and noise temperature of the ETA receiver are estimated using a GNL analysis of the components. This analysis is shown in Table 3.2. The parameters are estimated at 50 MHz, but are well approximated as constant over the frequency range considered.
- *ZFL-500*: The datasheet reports values at 3.9, 47.9, and 192.3 MHz. The values change by less than 0.1 dB. Therefore values reported at 47.9 MHz are assumed for this work, and assumed constant over the frequency range of interest.
- *ZMSC-2-1*: The datasheet value of the gain  $G_s = -3.2$  dB is assumed to be constant over the frequency range of interest. Equation (3.18) is evaluated with  $G_c = G_s + 3$  dB =  $-0.2$  dB to compute the noise temperature of the splitter  $T_s$ . The difference of 3 dB accounts for the fact that the only the loss in the splitter in excess of the ideal 3 dB, due to the splitting of power, generates noise. The maximum rated input power of 30 dBm is used for the  $P_{1dB}$ .
- *AAF*: The gain of the AAF  $G_{AAF}$  is measured, and is shown in Fig. 3.27. Of this

Table 3.2: GNL analysis of the ETA receiver. These values are approximately independent of frequency over 30–78 MHz.

Stage	Function	Stage			Cascade		
		Gain (dB)	$T$ (K)	$P_{1dB}$ (dBm)	Gain (dB)	$T$ (K)	$P_{1dB}$ (dBm)
1	ERA6SM	13	509	5	13	509	5
2	ATTN	-9	76	0	4	513	-13
3	BPF	-1	76	200	3	546	-13
4	GALI74	25	250	-6	28	684	-14
5	BPF	-1	76	200	27	684	-14
6	GALI74	25	250	-6	<b>52</b>	<b>684</b>	<b>-32</b>

insertion loss, no more 1 dB is believed to be due to ohmic loss. Therefore, Eq. (3.18) is evaluated with  $G_c = -1$  dB to approximate  $T_{AAF}$ . This approximation is well justified, since the  $> 80$  dB of gain prior to the AAF cause  $T_{AAF}$  to have minor impact on the cascade noise temperature. The  $P_{1dB}$  of the AAF is assumed to be large enough not to affect the system  $P_{1dB}$ , and so is arbitrarily set to 200 dBm.

Table 3.3 shows the results of the GNL analysis of the receiver at 45 MHz, near the resonant frequency of the antenna. Differences between the estimate and the measurement are attributed to uncertainty in the gain of each stage.

The  $\sim 76$  dB of gain is required to amplify the signal to an appropriate level for detection from the digitizer. The 323 K is roughly an order of magnitude below the expected antenna temperature due to the Galactic synchrotron radiation, as discussed in Section 2.2. 30–78 MHz contains relatively weak RFI, such that  $P_{1dB}$  of  $\sim -77$  dBm is sufficiently high in the 30-80 MHz passband. The FEE includes notch and bandpass filtering to provide additional protection from out-of-band interference.

Table 3.3: GNL stage-cascade analysis of the receiving system used in the two-element interferometer at 42 MHz, the center of band 2 (see Section 3.8).

Stage	Function	Stage			Cascade		
		Gain (dB)	$T$ (K)	$P_{1dB}$ (dBm)	Gain (dB)	$T$ (K)	$P_{1dB}$ (dBm)
1	FEE	21	295	11	21	295	11
2	Cable	-6	860	200	15	302	11
3	ETA Receiver	52	684	-32	67	323	-47
4	ZFL-500	21	792	-10	88	323	-77
5	ZMSC-2-1	-3	14	30	85	323	-77
6	AAF1	-8	76	200	<b>76</b>	<b>323</b>	<b>-77</b>

### 3.7 System Sensitivity

At this point, we are able to quantify the system sensitivity. We assume the digitizer does not degrade sensitivity, which we confirm in the Section 3.8. In this section, we evaluate the system sensitivity using two metrics: (1) system temperature,  $T_{sys}$ , and (2) the system equivalent flux density (SEFD).

Following the ATM, the DRX receives the PSD (see Eqs. (2.45) and (2.57))

$$S_{out,1} = kG_R(Z'_A)G_p\epsilon_A T_{sky} + kG_R(Z'_A)G_p\epsilon_A T_{gnd} + kG_R(Z'_A)G_p T_{amb} \frac{R_{loss}}{R_{rad}} + kG_R(Z'_A)T_R(Z'_A) \quad (3.19)$$

The system temperature  $T_{sys}$  is then found by dividing  $S_{out,1}$  by  $k\epsilon_A G_R(Z'_A)G_p$ :

$$T_{sys} = \frac{S_{out,1}}{k\epsilon_A G_R(Z'_A)G_p} = T_{sky} + T_{gnd} + T_{amb} \frac{R_{loss}}{R_{rad}} + \frac{T_R(Z'_A)}{\epsilon_A G_p} \quad (3.20)$$

Figure 3.30 shows the estimated contributions to, and the resulting  $T_{sys}$ , for the system reported in this work.  $T_{sky}$  is estimated by Eq. (2.2) with  $T_{ref} = 9120$  K at  $\nu_{ref} = 39$  MHz, and  $\alpha = -2.55$ .  $T_R$  is assumed to be dominated by the FEE input-referred noise temperature, so  $T_F$  in Fig. 3.18 is used for  $T_R$ .  $\epsilon_A$  is given in Fig. 3.15 for a very dry ground. To approximate

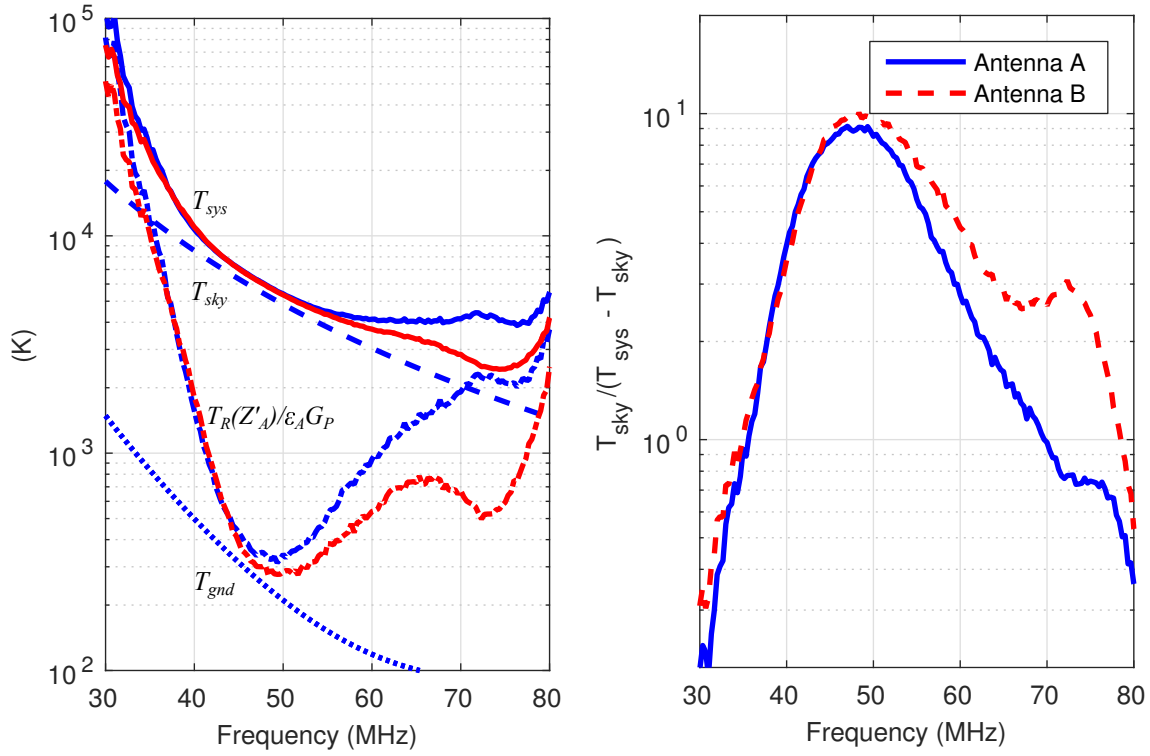


Figure 3.30: (Left): Contributions to the apparent  $T_{sys}$ . (Right):  $T_{sky}$  relative to other sources of noise.

the value of  $T_{gnd}$ , we assume a uniformly bright sky with  $T(\theta, \phi) = T_{sky}$ , such that

$$T_{gnd} \approx T_{sky}(1 - \epsilon_A) \quad (3.21)$$

which follows from the discussion in Section 3.1.5.  $T_{amb}R_{loss}/R_{rad}$  is  $10^{-3}$  below the other curves in Fig. 3.30, and is not shown, but is included in  $T_{sys}$ .

Figure 3.30 also shows the ratio of  $T_{sky}$  to the other contributions to  $T_{sys}$ . Clearly, a  $T_{sky}$  dominates the noise delivered to the receiver over a large fraction of the bandwidth considered. This is desirable, since  $T_{sky}$  is ubiquitous and irreducible. Note that the vertical axis of the right plot in Fig. 3.30 may be interpreted as a measure of the integration time required to achieve a specific signal-to-noise ratio.

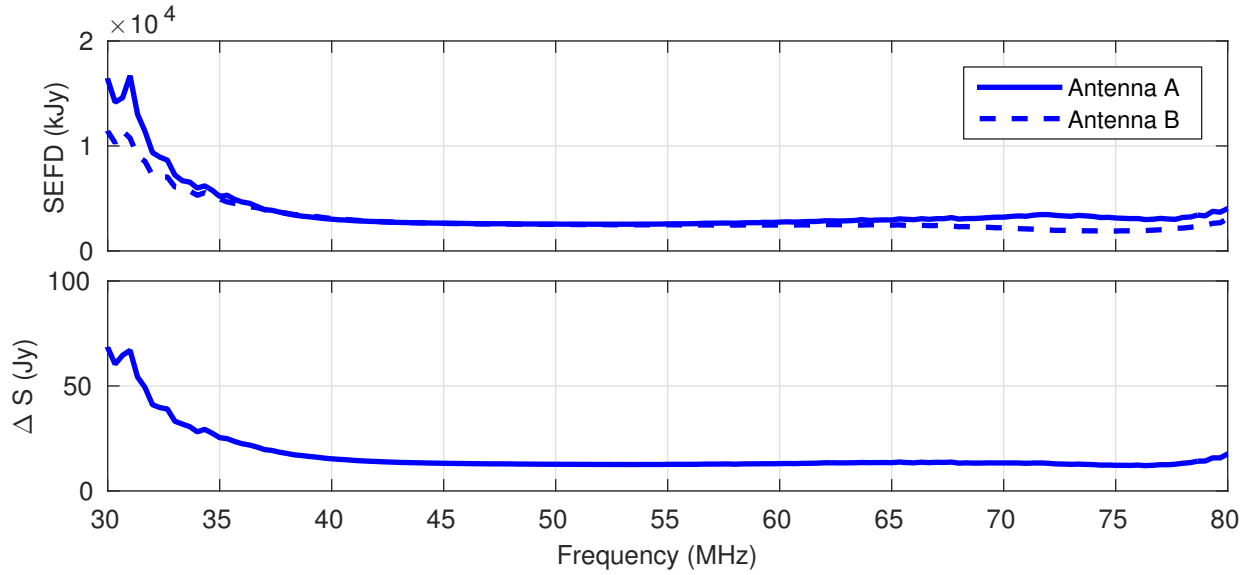


Figure 3.31: (Top): SEFD for each antenna. (Bottom): Resulting noise in the cross correlation.

While  $T_{sys}$  is useful for discussing the sensitivity of the system for radiometry, it is an inappropriate metric for the sensitivity of the system when acting as an interferometer. This is because (1) the 10s of  $\lambda$  baselines suppress the diffuse emission (see Appendix A), and (2) by fringe rate filtering, we can isolate the desired sources from the diffuse emission. Instead, the SEFD is a more appropriate metric for the system as an interferometer.

The SEFD is defined as the flux density of a source that would double the received PSD. The SEFD of a single signal path may be expressed as

$$\text{SEFD} = \frac{2\epsilon_A k}{A_e} T_{sys} \quad (3.22)$$

Figure 3.31 shows the SEFD for each signal path, with  $\epsilon_A$  given in Fig. 3.15 for a very dry ground,  $T_{sys}$  given in Fig. 3.30, and zenith  $A_e$  for a very dry ground (see Section 3.1.3).

For an interferometer, the noise in the output of the cross correlation is given by [51]

$$\Delta S_{mn} = \sqrt{\frac{\text{SEFD}^{(m)} \text{SEFD}^{(n)}}{2\Delta\nu\Delta t}} \quad (3.23)$$

$\Delta S_{mn}$  is also shown in Fig. 3.31, for  $\Delta\nu = 8.33$  MHz and  $\Delta t = 2400$  s (the values used in the flux density estimates summarized in Section 6.2.5). In this frequency range, we expect the flux density of Cyg A and Cas A to be about 20 kJy, and the flux density of Vir A and Tau A to be about 5 kJy. We see  $\Delta S_{mn}$  is at least two orders of magnitude below the expected flux density of each of the A-Team sources. Therefore, the analog system is sufficiently sensitive.

In the next section we discuss the data acquisition used to collect the data output from the analog system.

### 3.8 Digital Receiver (DRX)

This section documents the DRXs (see Fig. 3.1) that comprise the data recording system. Different DRXs, referred to as the USRP and the S60, are employed depending on the frequency range being observed. During a measurement, two DRXs operate in parallel: one with an AAF for the first Nyquist zone (NZ1), the with an AAF for the second Nyquist zone (NZ2). The NZ1 DRX may be either a USRP or S60, depending on the center frequency of the measurement. The NZ2 DRX is always a USRP.

The USRP is an Ettus Research USRP-N200<sup>7</sup>, and was used for the majority of the bands. The USRP uses a Xilinx Spartan 3A-DSP 1800 field programmable gate array (FPGA) with two 14-bit analog-to-digital converters (ADC) sampling at 100 MSPS. The FPGA down-converts, filters, and decimates the received samples and outputs 8-bits real (I), 8-bits imaginary (Q) per antenna at 8.33 MSPS over Ethernet. The USRP N200 is reportedly capable of supporting up to 50 MSPS streaming; however our DRs were only able to write up to 8.33 MSPS to disk without loss of samples. As noted in Section 3.5, the USRP was not used near 50 MHz due to aliasing.

The S60, a DRX used by ETA and during commissioning of LWA1, provides coverage between 48.16 and 50.16 MHz [52]. The S60 is implemented on an Altera Stratix II EP2S60 DSP

---

<sup>7</sup><https://www.ettus.com/product/details/UN200-KIT>

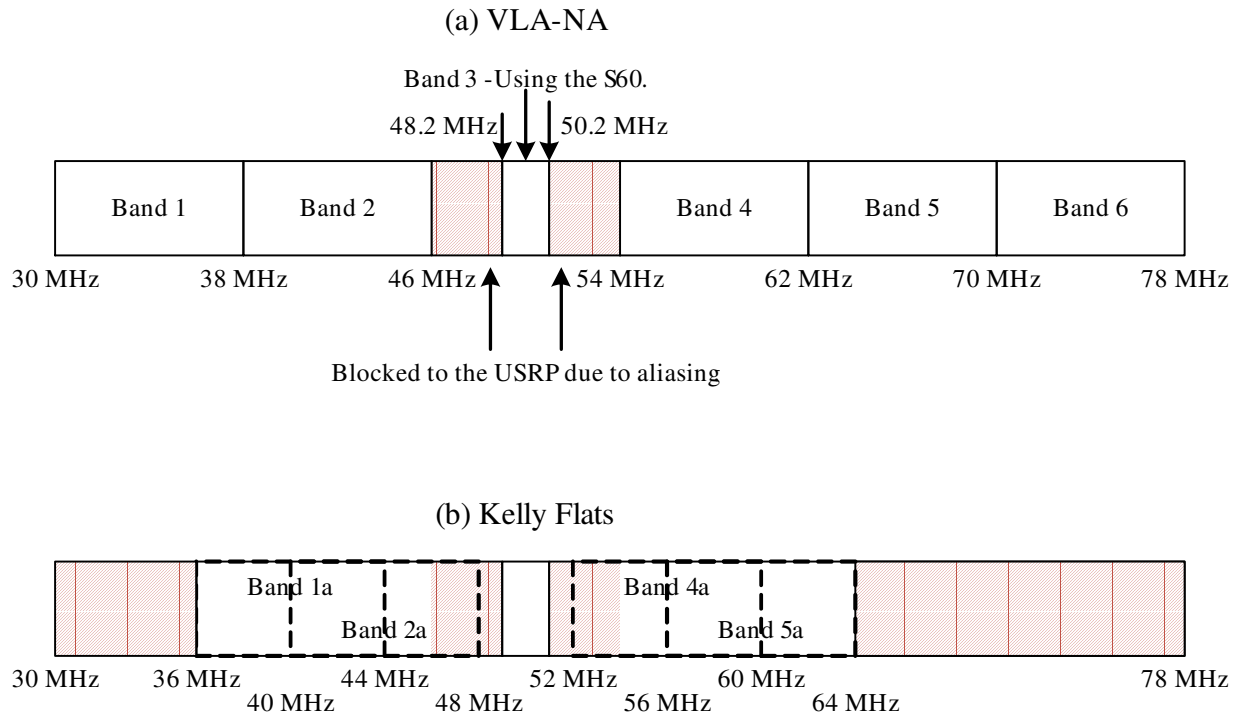


Figure 3.32: Frequency band identification. The shaded regions indicate regions within 30–78 MHz in which data was not collected.

development board with two on-board 12-bit ADCs sampling at 120 MSPS. The FPGA down-converts, filters, and decimates the received samples and outputs 7-bits I, 7-bits Q per antenna at 2.5 MSPS over Ethernet.

Figure 3.32(a) summarizes the nomenclature used to identify different frequency bands used during the VLA North Arm measurement campaign (see Chapter 4). Data was also collected at Kelly Flats before the VLA-NA frequency scheme was developed. The frequency bands used at Kelly Flats are shown in Figure 3.32(b).

Each DRX is connected to a DR. A DR is a mini-ITX form-factor PC (see Fig. 3.3) running Ubuntu Linux 14.04. The DRs have Intel Atom CPUs with 2 GB of RAM and 2 TB hard disk drive (HDD). Data is captured using Python scripts. The USRP scripts require GNURadio<sup>8</sup>

<sup>8</sup><http://gnuradio.org/>

and the USRP Hardware Driver.<sup>9</sup> The S60 requires only Python.<sup>10</sup>

The 2 TB HDDs are able to store up to 15 hours of USRP data, or 50 hours of S60 data, for a recording size of 1.8 TB. The USRP data are formatted in two files, one for each antenna. Each sample is written as two consecutive bytes, one byte for I, one for Q. The S60 data is written in one file, and the samples from the two antennas are written one after the other. Each sample is again written as two consecutive bytes, one byte for I, one for Q.

We now wish to show that the noise delivered to the input of the DRX dominates over the quantization noise generated by the ADC in the DRX. We will consider the noise delivered in the cold state, which represents the minimum noise delivered to the DRX. It is well-known that the input-referred quantization noise of an ideal ADC is (see e.g. [53])

$$P_Q = -1.76 - 6.02N_b \quad [\text{dB relative to } P_{clip}] \quad (3.24)$$

where  $N_b$  is the number of bits, and  $P_{clip}$  is the input power corresponding to the maximum (voltage) level the ADC can properly encode. In practice  $P_Q$  is typically about 2 dB worse due to additional analog noise generated by the ADC, so a simpler and more realistic model is

$$P_Q \approx -6N_b \quad [\text{dB relative to } P_{clip}] \quad (3.25)$$

Modern ADCs typically encode full-scale at a peak voltage of about  $2 V_{pp}$  into  $50 \Omega$ . Thus,  $P_{clip}$  is typically about +10 dBm. Assuming  $P_{clip} = +10$  dBm,  $P_Q = -74$  dBm for the USRP ( $N_b = 14$ ) and  $-62$  dBm for the S60 ( $N_b = 12$ ).

In the cold state, the noise delivered to the input of the DRX is

$$P_n = G_R[k(T_R + T_{amb})B] \quad (3.26)$$

where  $B$  is the bandpass of the ARX. For NZ1  $B \approx 20$  MHz, and for NZ2  $B \approx 30$  MHz.

---

<sup>9</sup><http://files.ettus.com/manual/>

<sup>10</sup>Python 2.7.6 was used in the measurements.

From the GNL analysis in Table 3.3,  $G_R = 76$  dB and  $T_R = 323$  K. Assuming  $T_{amb} \approx 290$  K,  $P_n \approx -22$  dBm for NZ1 and  $P_n \approx -20$  dBm for NZ2. Clearly  $P_n \gg P_Q$  for either digitizer in both Nyquist zones, confirming that analog noise dominates over quantization noise.

In Section 3.10, we show the ratio of the PSD delivered to the DRX in the hot state to the PSD in the cold state is about 8 dB at 42 MHz (see Fig. 3.38). In Section 5.1.1, we show the same ratio for the digitized signals is also about 8 dB at 42 MHz (see Fig. 5.3). Therefore the signal processing, and subsequently the DRX, does not limit the sensitivity of the system.

### 3.9 Bias and Control Circuits

This section describes the Bias and Control Boards shown in Fig. 3.1. These boards regulated the 24 V DC supply to the various levels required by the different system components. The DC supply is provided either from batteries or a lab bench power supply. The lab bench power supply was used during the measurements described in Section 4.1, and the batteries were used during the measurements described in Section 4.2. Detailed schematics and PCB layouts are included in Appendix G.3.

The Control Board regulates the  $\sim 24$  V DC supply to the various DC levels required by the ARX and USRPs (the S60 was always powered using a AC power adapter). Note these connections are not shown in Fig. 3.1 for clarity. Figures 3.33 and 3.34 show the block diagram and picture of the Control Board. 5 V brushless fans keep the Control Board from overheating. In addition to voltage regulation, the Control Board uses the pulse-per-second (PPS) clock from a GPS unit (Garmin GPS18x LVC<sup>11</sup>) and digital logic (detailed in Appendix G.3) to control the FEE calibration state cycle. The state is determined on the Control Board, and set by the Bias Board.

The Bias Board sets the bias voltage applied to the FEE from the 24 V DC supply and the calibration state determined by the control circuit according to Table G.2. Figures 3.35 and

---

<sup>11</sup><https://buy.garmin.com/en-US/US/oem/sensors-and-boards/gps-18x-oem/prod27594.html>

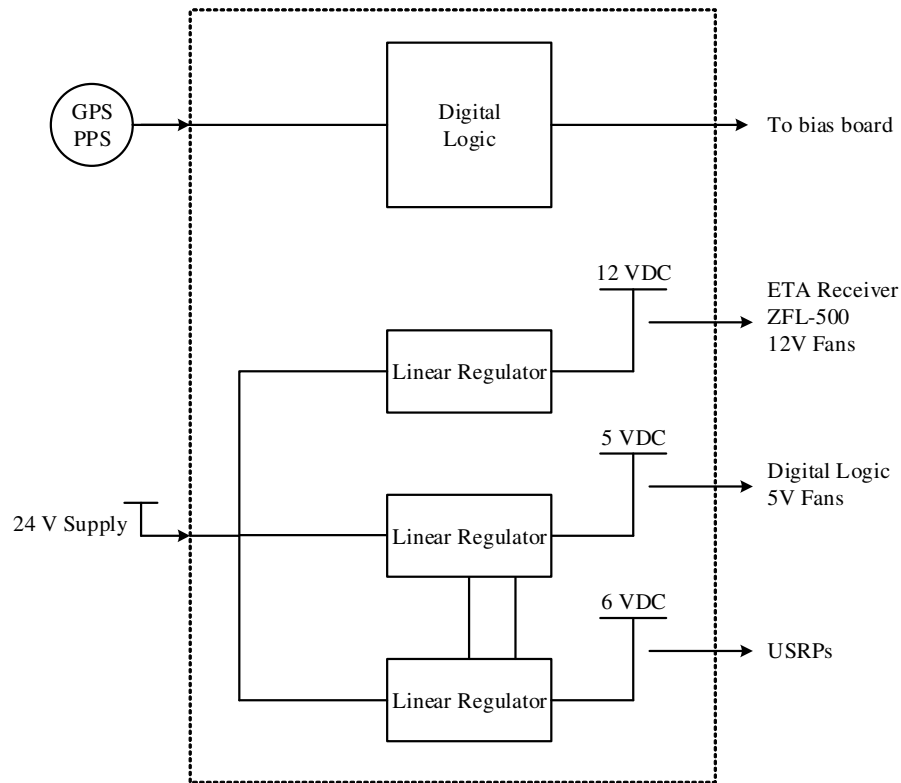


Figure 3.33: Block diagram of the Control Board.

3.36 shows the block diagram for the Bias Board. Because the FEE draws  $\sim 0.8$  A, each FEE is powered by a separate Bias Board. Each Bias Board is then kept from overheating with a 12 V brushless fan.

## 3.10 System Commissioning

This section presents the various experiments performed to verify the performance of the system. These experiments demonstrate the system operating under laboratory and field conditions.

Figure 3.37 shows normalized histograms of 10,00 samples measured by a USRP for each of the FEE calibration states. The samples were collected under laboratory conditions. The “antenna” simulated with an Agilent HP346C noise source, amplified by 3 so that the



Figure 3.34: A fabricated Control Board.

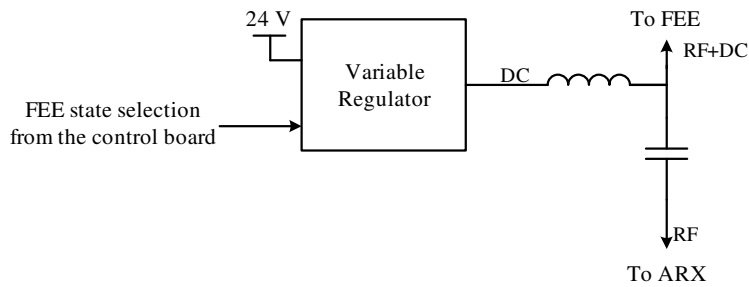


Figure 3.35: Block diagram of the Bias Board.

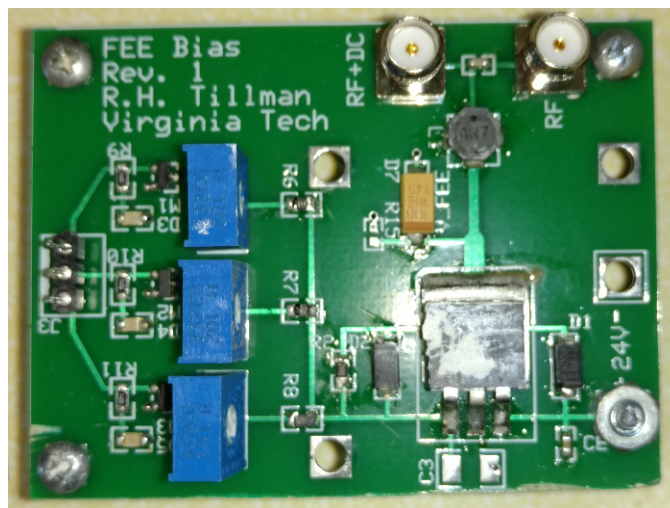


Figure 3.36: A fabricated Bias Board.

noise temperature at the input of the FEE was  $\sim 10,000$  K. The USRP was tuned to Band 2. The histograms in each state exhibit the expected zero-mean, Gaussian distribution. The maximum sample magnitude in the cold state, the lowest received power state, is  $\pm 7$ , corresponding to 4 bits toggling. Thus, van Vleck correction is not appropriate.

A laboratory experiment was conducted to evaluate the USRP for loss of samples (glitching). A similar experiment was performed to evaluate the S60 in [54]. A 25.083 MHz signal with an amplitude of  $0.6 V_{pp}$  was input to the USRP. The USRP was tuned to a center frequency of 25 MHz, and 100 baseband cycles were collected. No glitching was observed. The short 12 ms test is only a small fraction of the duration of an observation. A test having a duration comparable to an observation was not done. However, there is no evidence of glitching in the data considered in this work.

A radiometry measurement was performed to confirm external-noise dominated performance of the system. The data was collected at the VLA-NA site (see Section 4.1) at 22:25 LST. The measurement was taken with a spectrum analyzer, replacing DRX so that the entire bandwidth of the analog signal path could be observed in one measurement. Figure 3.38 shows the measured PSD in the antenna and two calibration states, for the two antennas, in both Nyquist zones. The difference between the hot and cold calibration states is nearly constant, as expected. Mismatch between the antenna and the FEE causes the measured PSD from the antenna to vary significantly over the observable bandwidth. This is also as expected. In Section 5.1.2, we demonstrate how to calibrate the measured PSDs to estimate  $T_{sky}$ .

As discussed in Section 2.2,  $T_{sky}$  is a function of both antenna pattern and LST. This functional dependence can be used to commission the instrument. We performed multi-day observations of  $T_{sky}$  at 38, 44, and 74 MHz and obtained reasonable agreement with the model obtained from the convolution of the GSM with the antenna pattern predicted by IT/PEC. In Section 6.3, we report measurements of  $T_{sky}$  that show very good agreement with the model over the 30-78 MHz frequency band (see Table 6.2).

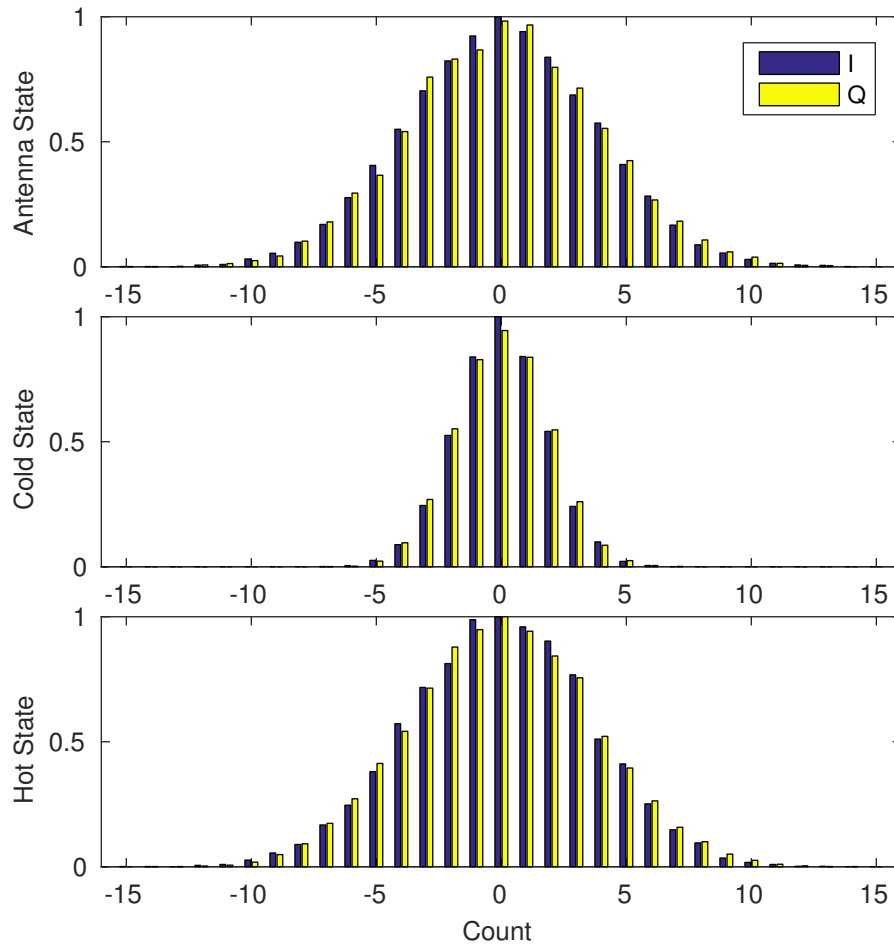


Figure 3.37: Normalized histogram of DRX output samples in each FEE calibration state.

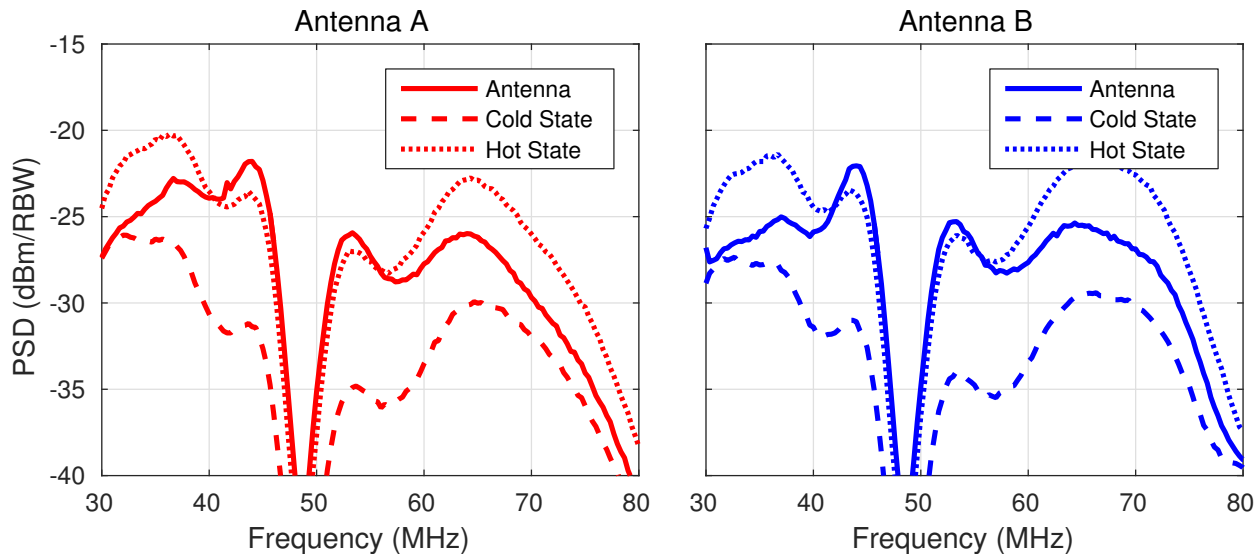


Figure 3.38: Measured PSD at the output of the ARX in each state, for each antenna.  $\Delta\nu = 1$  MHz,  $\Delta t = 3.3$  ms.

We conclude this section with a demonstration of the instrument’s ability to operate as an interferometer. An observation of Cas A is presented at 42 MHz, with 2 hours recorded beginning at Cas A’s transit. The baseline is  $\sim 250$  m, east-west oriented, at the measurement site described in Section 4.1. Figure 3.39 shows the power spectrum from the observation. The data have not yet been calibrated for gain. The system is clearly very stable and, in this particular observation, free from RFI. Figures 3.40 and 3.41 show magnitude and phase of the cross correlation for the observation, respectively.

Figure 3.42 shows fringes calculated from the collected data. The data has not been delay-stopped or fringe-rate filtered. Nevertheless, a clear fringe pattern is visible with a high signal-to-noise ratio.

Figure 3.42 also shows the expected fringes, including the contributions both from Cas A and Cyg A, from the theory presented in Section 2.4. The difference between the model and the measurement is attributed to uncertainty in the baseline location (see Section 4.1). As noted in Section 5.3, this will be of no consequence since the fringe rate can be estimated from the data. Also, note that there is a small offset between the I and Q channels, attributed to the

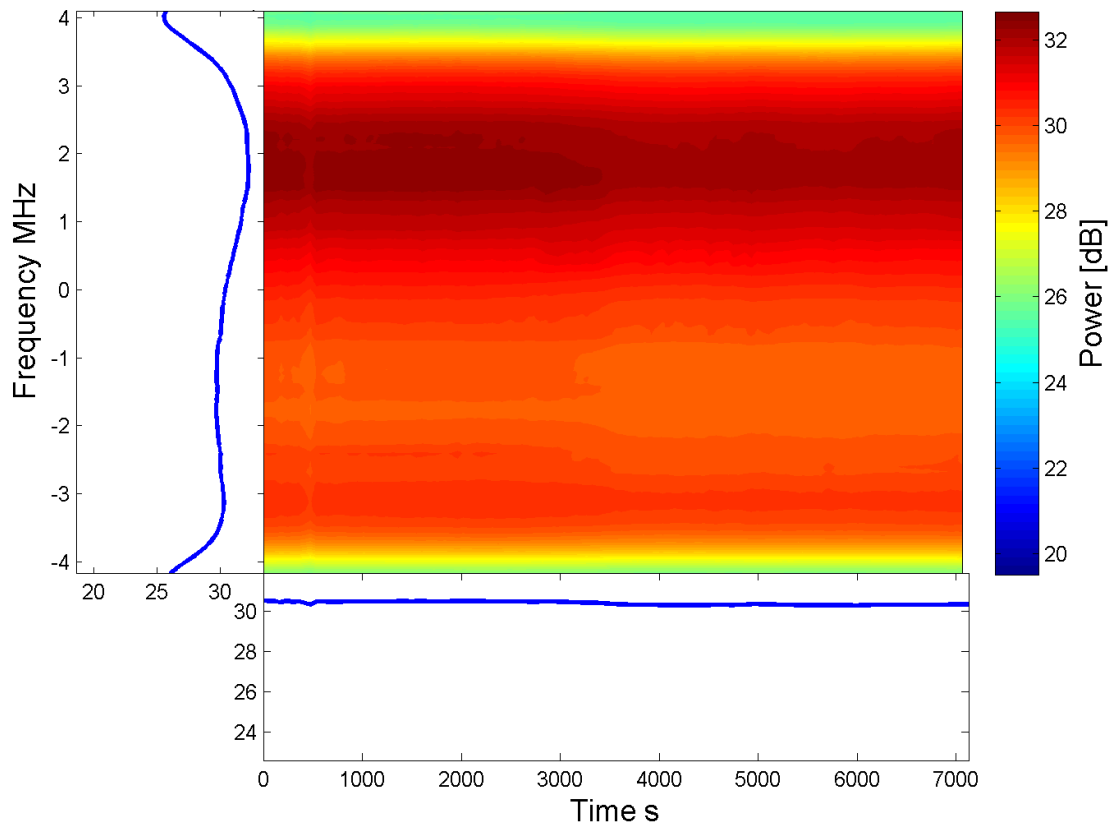


Figure 3.39: Power spectrum from the observation considered in this section. The left pane is the time-average of each frequency bin. The bottom pane is the continuum power.  $\Delta\nu = 65$  kHz,  $\Delta t = 20$  s, 42 MHz center frequency.

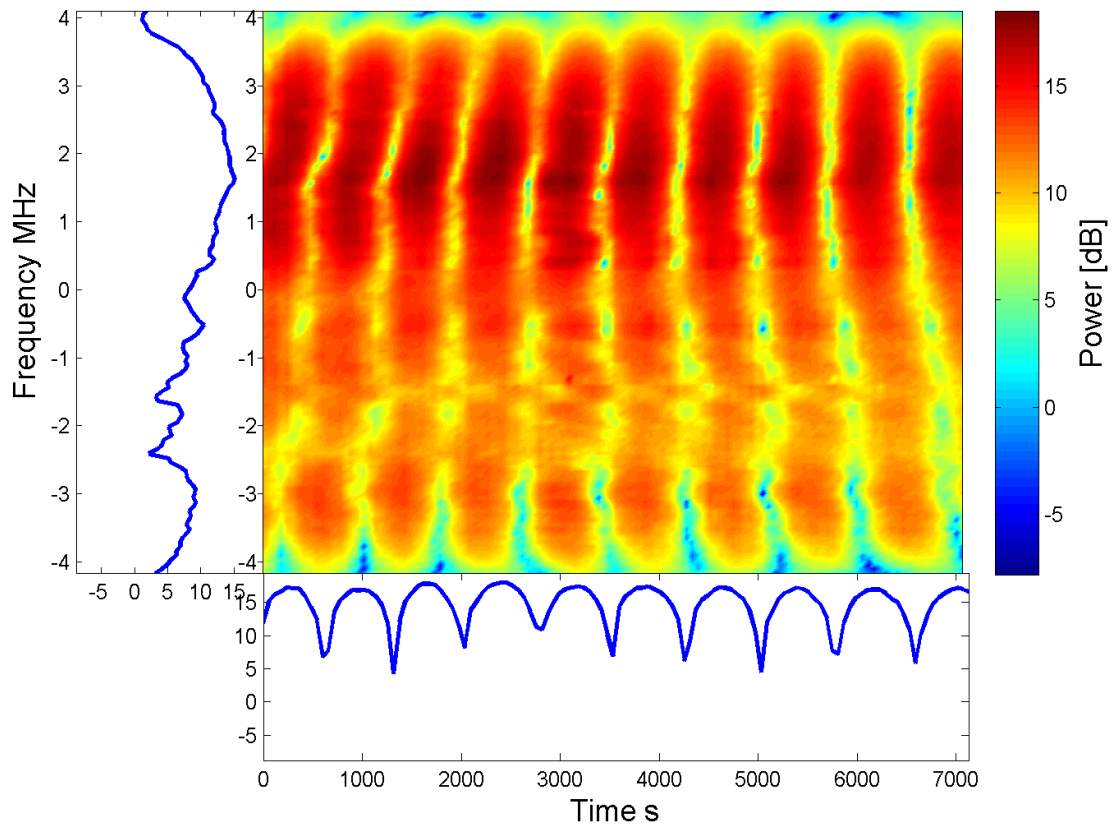


Figure 3.40: Magnitude of the cross correlation.  $\Delta\nu = 65$  kHz,  $\Delta t = 20$  s, 42 MHz center frequency.

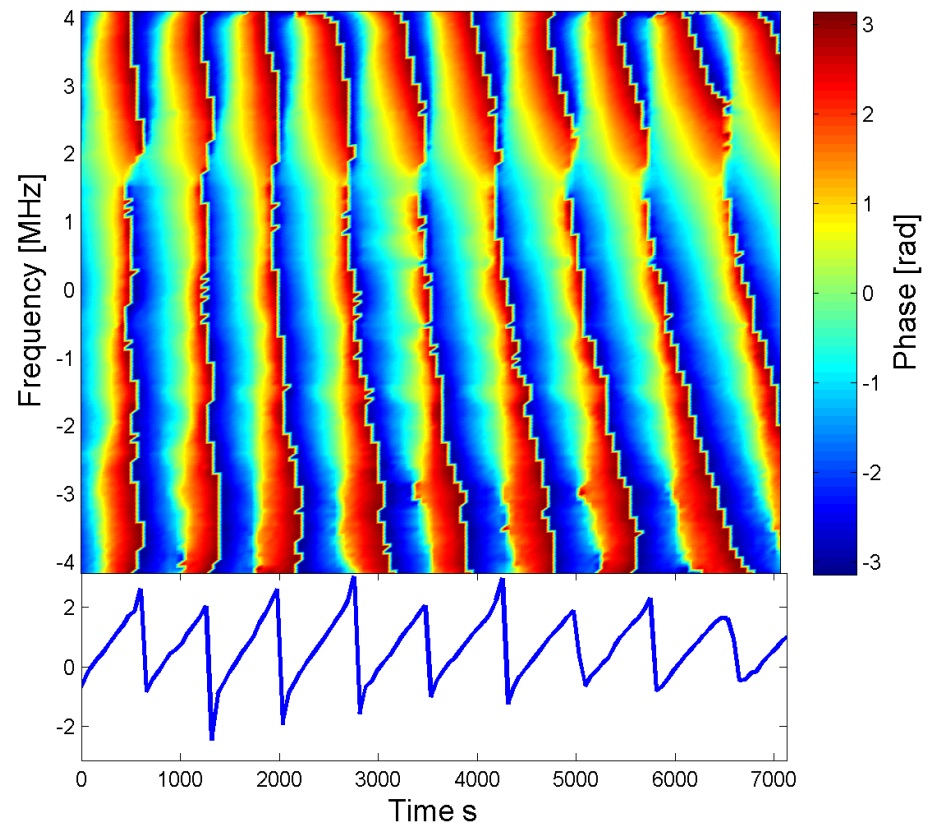


Figure 3.41: Phase of the cross correlation.  $\Delta\nu = 65$  kHz,  $\Delta t = 20$  s, 42 MHz center frequency.

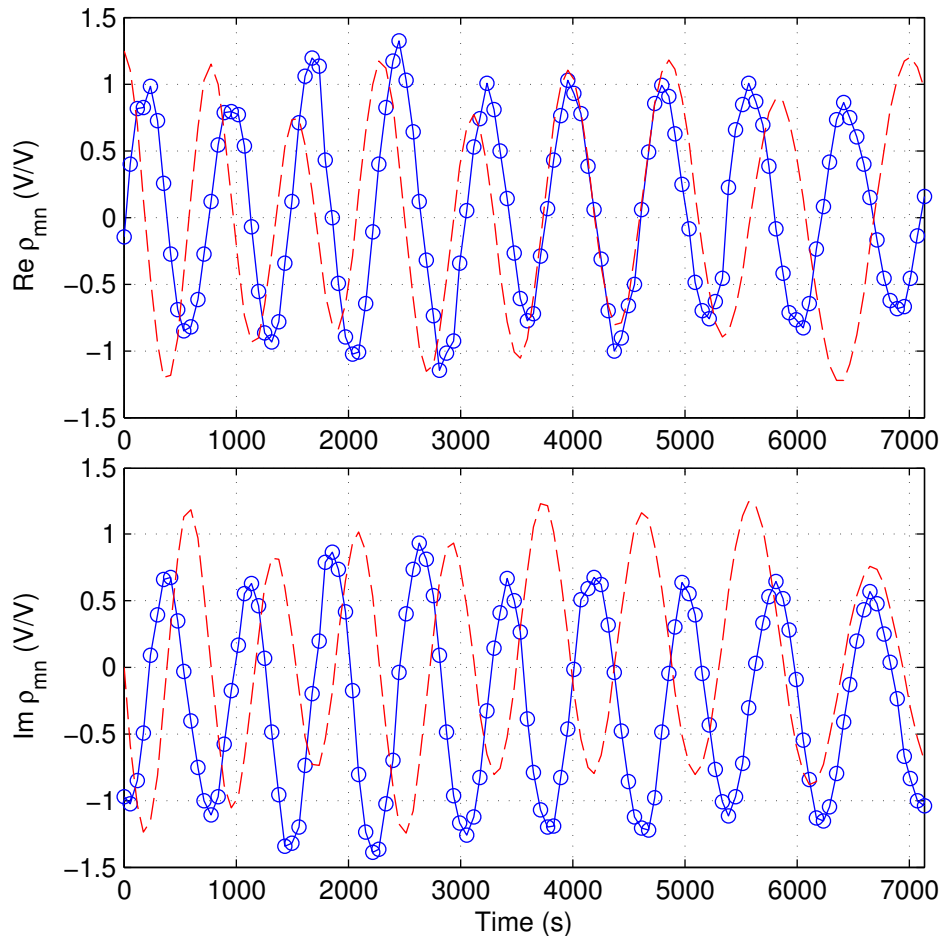


Figure 3.42: Measured (solid) and modeled (dashed) fringes from Cas A ( $f_g \approx 1.3$  mHz).  $\Delta\nu = 65$  kHz,  $\Delta t = 20$  s, 42 MHz center frequency, 23:30-01:30 LST. Amplitude has been normalized for a unit RMS amplitude; i.e. this is not gain calibrated.

all-sky term (see e.g. Fig. 2.7).

### 3.11 RFI Mitigation

This section describes the RFI mitigation technique used to excise RFI from the data. Nominally, the power spectrum received from each antenna is well characterized as colored Gaussian noise, as seen in Fig 3.39. However, the system occasionally receives RFI, an example of which is shown in Figure 3.43. Examples of strong RFI such as this typically affect only

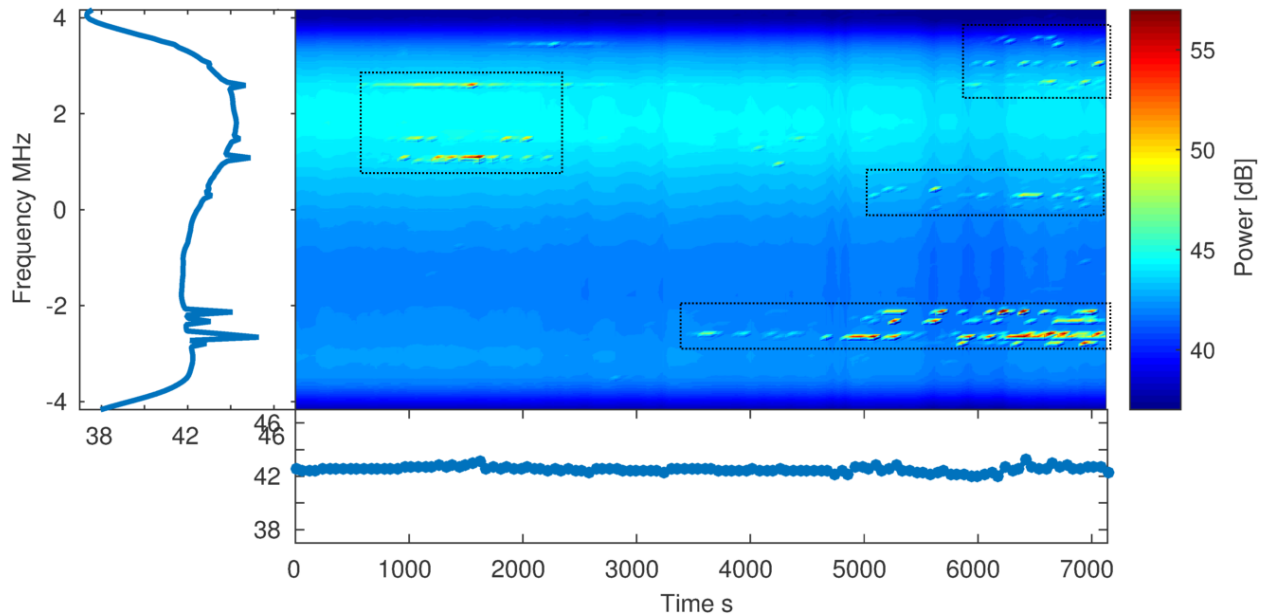


Figure 3.43: Power spectrum for an observation exhibiting significant RFI, indicated by the dashed outline boxes.  $\Delta\nu = 65$  kHz,  $\Delta t = 20$  s, 42 MHz center frequency.

daytime observations. An RFI survey at the LWA1 site showed the most likely sources of RFI to be land mobile radio, analog and digital TV stations, and power lines [55].

Figure 3.44 shows the magnitude of the cross correlation from the same dataset shown in Fig. 3.43. Figure 3.45 is the same as Fig. 3.44 but in the cold state. That the RFI is not present in cold state confirms the source of the RFI is external to the system.

Impulsive RFI from power lines is believed to be the primary source of RFI in the observed data. Section 3.11.1 shows the time domain data that leads to this hypothesis. Mitigation of the RFI in the time-domain was ineffective; instead a joint time-frequency domain mitigation is demonstrated in Section 3.11.2.

### 3.11.1 Time Domain RFI Mitigation

One possible source of RFI is impulsive RFI from power lines, a known issue for the measurement location discussed in Section 4.1. Figure 3.46 shows a segment of data sampled by

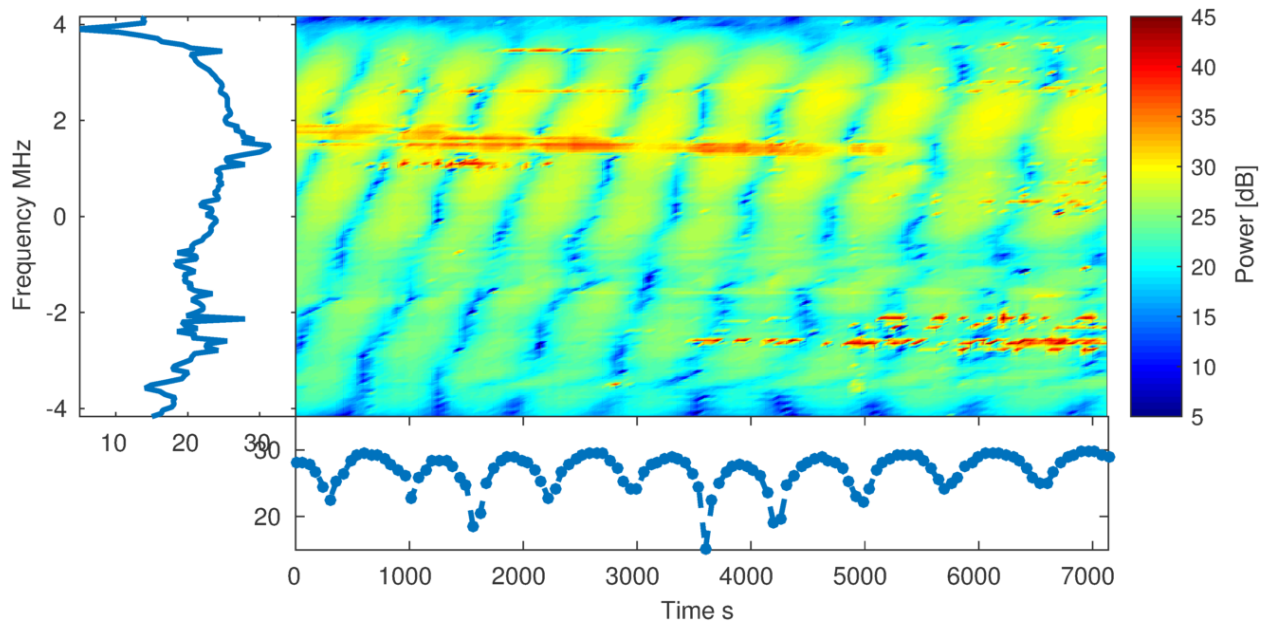


Figure 3.44: Magnitude of the cross correlation for an observation exhibiting significant RFI.  $\Delta\nu = 65$  kHz,  $\Delta t = 20$  s, 42 MHz center frequency.

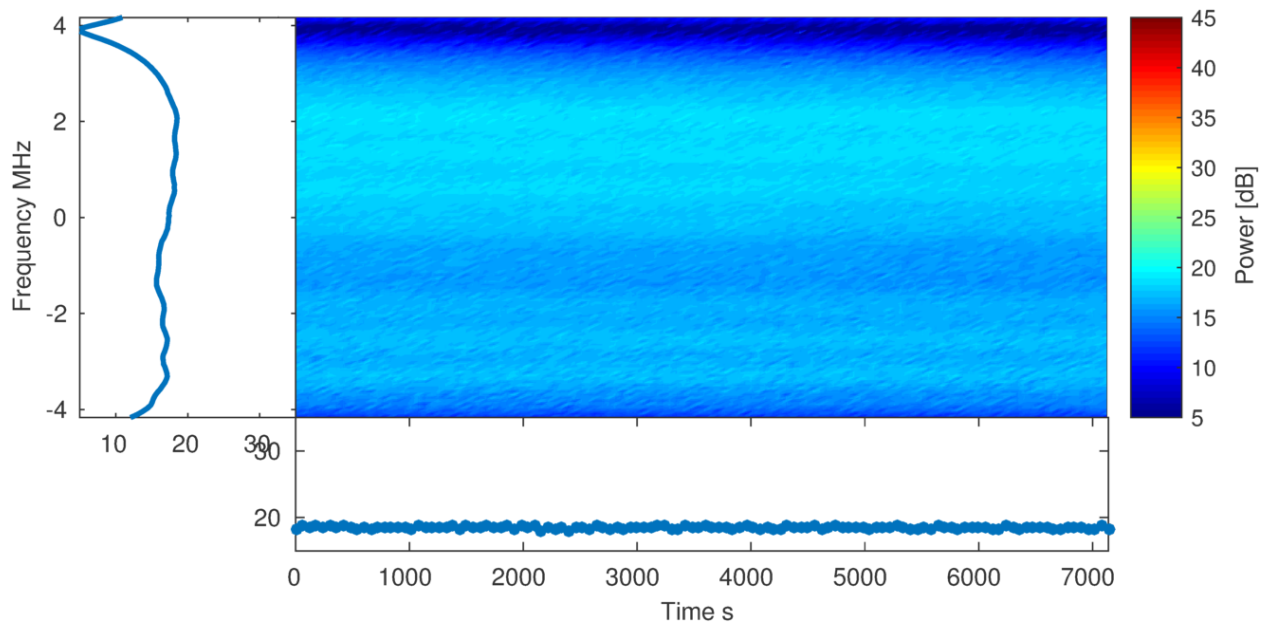


Figure 3.45: Same as Fig. 3.44, but in the cold state.  $\Delta\nu = 65$  kHz,  $\Delta t = 20$  s, 42 MHz center frequency.

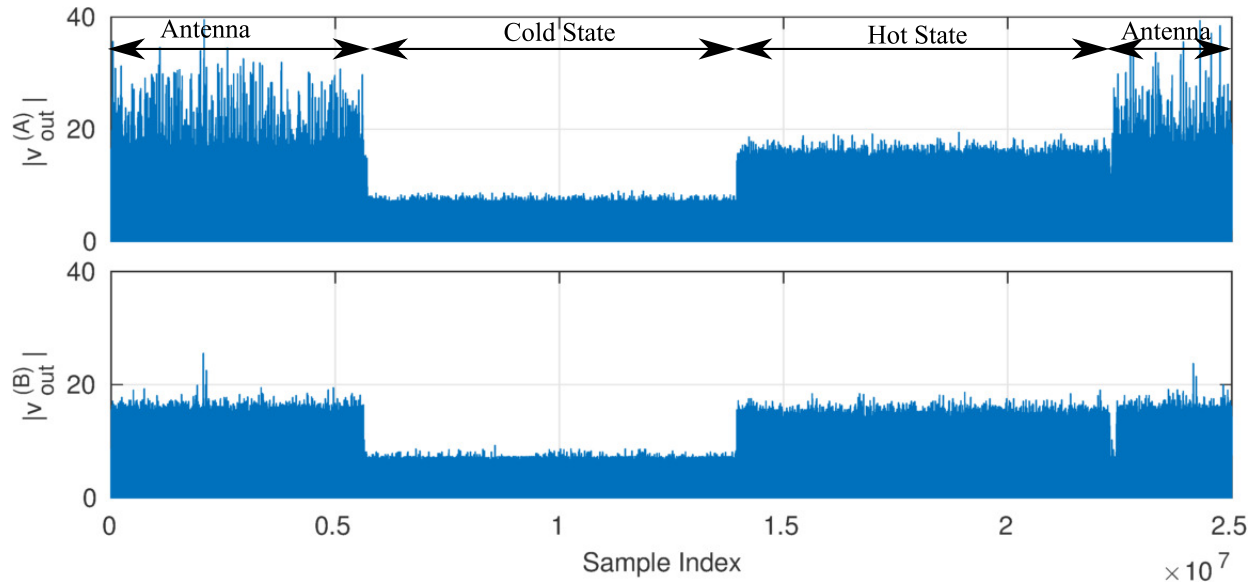


Figure 3.46: Raw voltage samples before mitigation.  $\Delta\nu = 8.33$  MHz,  $\Delta t = 12$   $\mu$ s, 42 MHz center frequency.

the DRX. Impulsive RFI is strongly affecting Antenna A, and is less pronounced Antenna B. For this measurement, power lines were near ( $< 50$  m) Antenna A, and about 300 m from Antenna B, implicating the power lines as the source of the RFI.

Even though impulsive RFI is present, it only affects about 0.01% of the samples. As a result, the presence of the impulsive RFI has no measurable effect on the data, so time domain RFI mitigation was not done. Instead, a joint time-frequency domain approach was employed.

### 3.11.2 Joint Time-Frequency Domain RFI Mitigation

A summary of the time-frequency domain process follows:

1. For each antenna's power spectrum: For each time bin, compute the mean  $\mu$  and standard deviation  $\sigma$  for the entire observation (typically 2 hours). Flag all pixels having magnitude  $> 3\sigma + \mu$ . Exclude flagged pixels with from further processing.
2. Repeat this process, recomputing  $\sigma$  and  $\mu$ , until all pixels in the power spectrum have

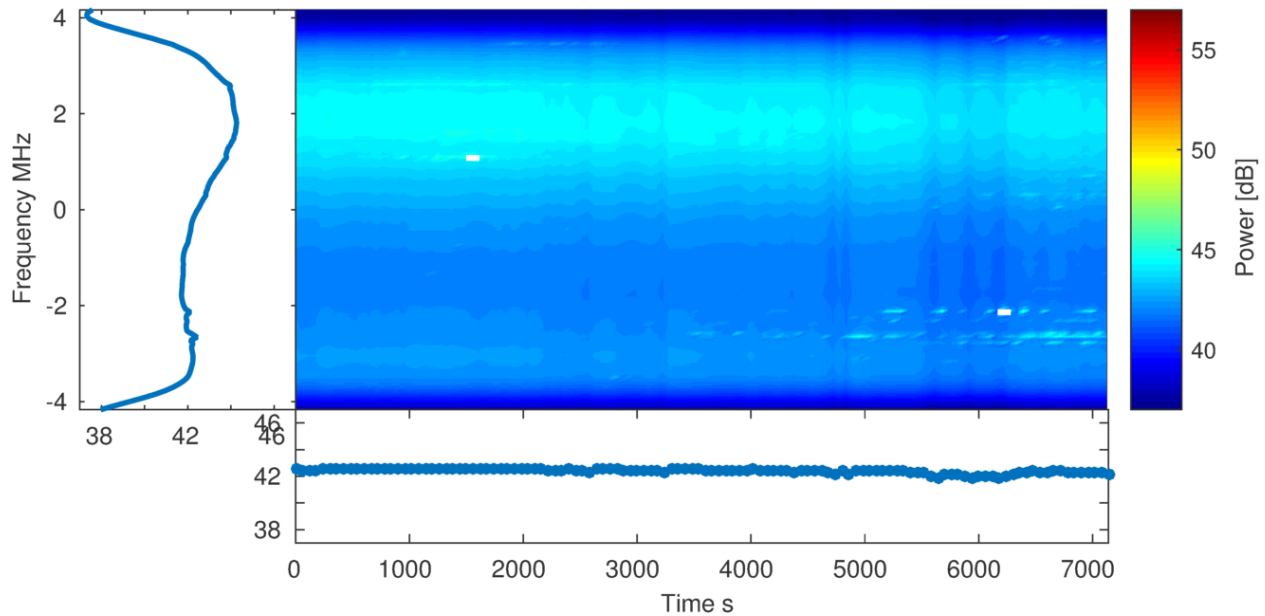


Figure 3.47: Power spectrum for an observation after excising RFI. 0.38% of pixels excised.  $\Delta\nu = 65$  kHz,  $\Delta t = 20$  s, 42 MHz center frequency

$$\text{amplitude} < 3\sigma + \mu.$$

3. Exclude pixels flagged for either antenna from the cross correlation.

Figures 3.47 and 3.48 show the power spectrum and cross correlation, respectively, after applying the above algorithm to the data shown in Figs. 3.43 and 3.44. Three passes were needed to reach the stopping criterion. A total of 0.38%, 0.35%, and 0.43% of pixels were excised from Antenna A, Antenna B, and the cross correlation, respectively. The power spectrum is significantly improved. The cross correlation is not significantly improved, implying the algorithm is not able to mitigate RFI to the level of sensitivity required for the flux density measurements. The RFI mitigation algorithm was still employed, as the improvement to the power spectrum is useful for the  $T_{sky}$  measurements, which are subsequently used to calibrate the instrument as described in Section 2.6.3. However, datasets such as the one considered in this section were not included in the flux density estimates.

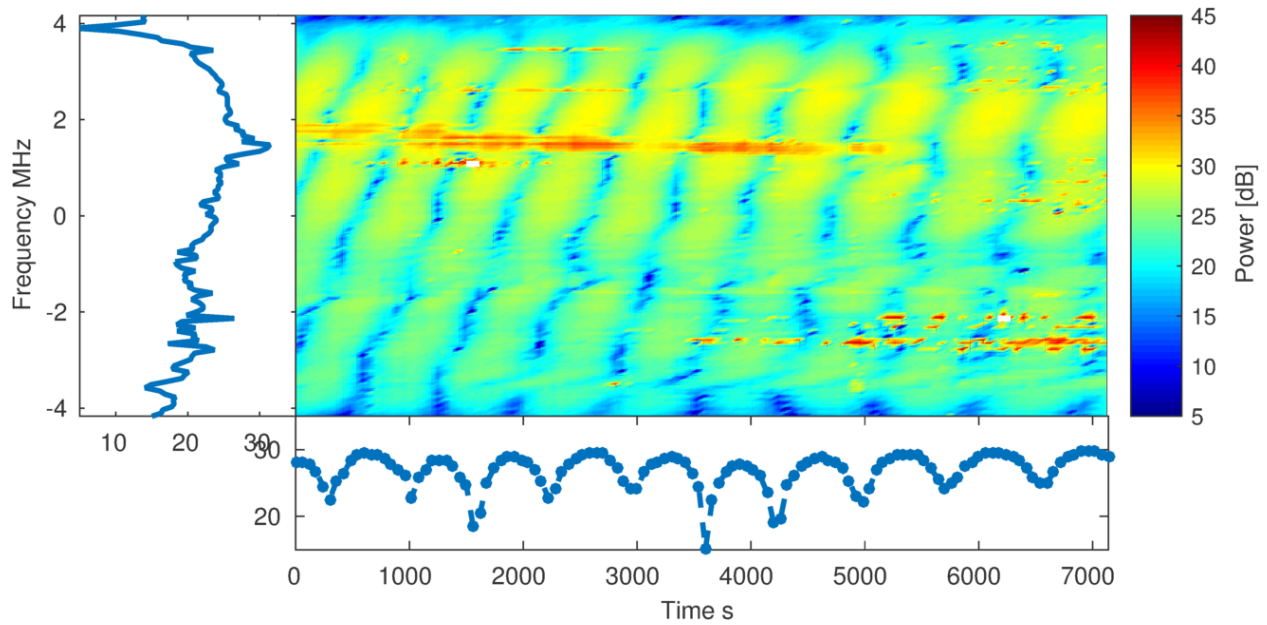


Figure 3.48: Magnitude of the cross correlation after excising RFI. 0.43% of pixels excised.  $\Delta\nu = 65$  kHz,  $\Delta t = 20$  s, 42 MHz center frequency

# Chapter 4

## Measurement Campaign

This chapter documents the measurement campaign conducted to collect data for the absolute flux density estimates. The majority of the data was collected near the north arm of the Very Large Array (VLA), at a development site operated by the University of New Mexico as part of the LWA project. This site will be referred to as the VLA-NA. Data was collected at VLA-NA during January 2016. Section 4.1 summarizes the measurements conducted at VLA-NA.

In addition to VLA-NA, commissioning and initial flux density measurements were conducted at Kelly Flats in the Jefferson National Forest near Pembroke, VA. Data was collected at Kelly Flats between May and November of 2015. Section 4.2 summarizes the flux density measurements conducted at Kelly Flats.

### 4.1 VLA North Arm Site

Figure 4.1 shows the VLA-NA location relative to the center of the VLA. Figure 4.2 shows a satellite image of the VLA-NA measurement site.<sup>1</sup> The location is at latitude, longitude

---

<sup>1</sup><https://www.google.com/maps/@34.2470731,-107.6404191,463m/data=!3m1!1e3!>



Figure 4.1: Location of VLA-NA relative to the core of the VLA. The VLA-NA is in the boxed region, and is shown in Fig. 4.2.



Figure 4.2: Google Maps screen shot of the VLA-NA measurement site. The site’s fence is indicated by the black square. Each side of the fence is 120 m.

$+34.25^\circ$ ,  $-107.64^\circ$ , and an elevation of 2120 m. The terrain is flat, and the horizon free of obstruction for elevation angles above  $\sim 10^\circ$ , where the distant mountains are visible. The soil is sandy, typical of high desert. For the first week of the measurement campaign, the ground was covered in  $< 10$  cm of snow. The ground screens were setup on top of the snow (see e.g. Fig. 3.2). The antenna and ground screen were adjusted as snow melted throughout the campaign to ensure consistency with the dimensions shown in Fig. 3.4.

Figure 4.3 shows the three different baselines used during the VLA-NA measurement campaign. Table 4.1 shows crude estimates of the baseline vectors. The data used to measure the baseline is documented in Appendix I. As described in Section 2.4, the baseline can be used to estimate the fringe rate for use in delay stopping. However, we are able to more accurately determine the fringe rate from the cross correlation, as will be shown in Section 5.3. The baseline estimates in Table 4.1 provide an initial estimate of the fringe rate, which is then refined using the data.

Table 4.2 summarizes the observations recorded during the VLA-NA measurement campaign. “X” polarization indicates the antenna was co-aligned with the East-West axis; similarly “Y” polarization indicates the antenna was co-aligned with the North-South axis. Each

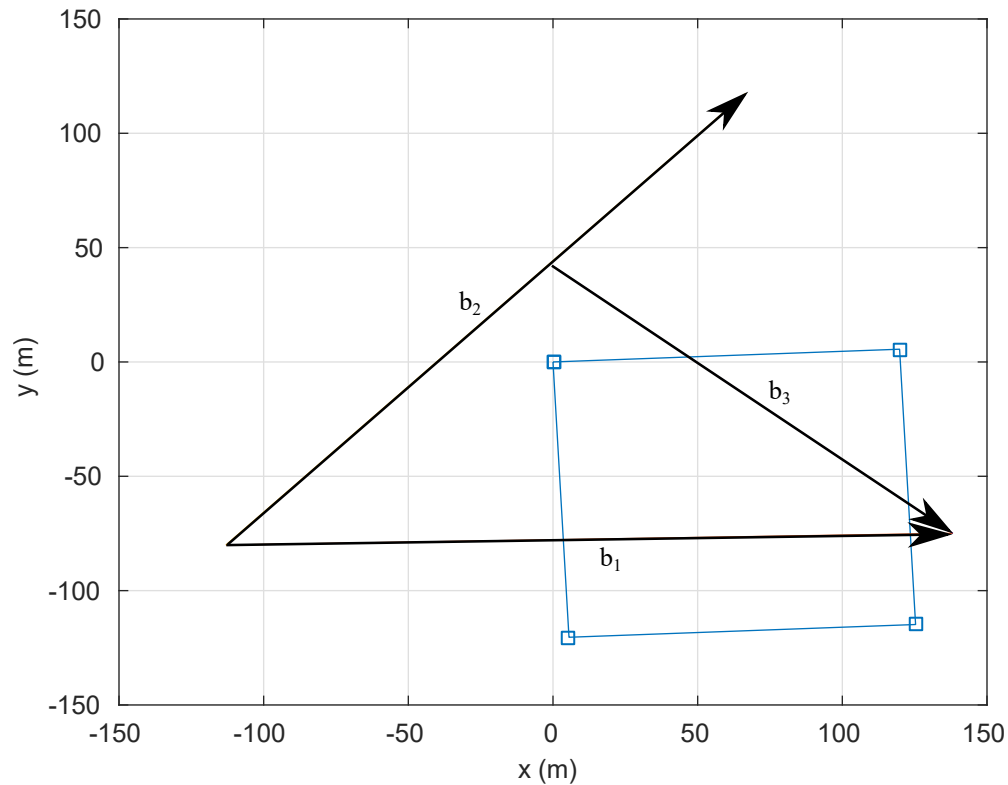


Figure 4.3: Baselines used at the VLA-NA site. The site's fence is indicated by the square.  $+x$  is East and  $+y$  is North. The origin is at the Northwest corner of the fence, located at latitude, longitude  $+34.2475^\circ$ ,  $-107.6416^\circ$ .

observation consists of four measurements, and each measurement targets a different source of interest.

## 4.2 Kelly Flats

Figure 4.4 shows a satellite image of the Kelly Flats measurement site.<sup>2</sup> The location is at latitude, longitude  $37.4237^\circ$ ,  $-80.5644^\circ$ , and elevation  $\sim 500$  m. The terrain is hilly, grassy earth, and due to trees surrounding the measurement site, only one baseline was available at this site. The baseline is identified as  $\mathbf{b}_4$ , and a crude estimate of the components of  $\mathbf{b}_4$  are given in Table 4.1. Appendix I includes the data used to estimate  $\mathbf{b}_4$ .

<sup>2</sup><https://www.google.com/maps/@37.4237396,-80.5644371,1270m/data=!3m1!1e3!>

Table 4.1: Components of the baseline vectors used at the VLA-NA.  $+x$  is East and  $+y$  is North. Antenna A is taken as the origin for each baseline. The uncertainty of each coordinate is  $<10$  m.

Baseline	$b_x$	$b_y$
$\mathbf{b}_1$	251 m	5 m
$\mathbf{b}_2$	180 m	198 m
$\mathbf{b}_3$	138 m	-117 m
$\mathbf{b}_4^\dagger$	250 m	110 m

$^\dagger$ Baseline used at Kelly Flats (see Section 4.2).

Table 4.3 summarizes the observations recorded at Kelly Flats. Only three observations from Kelly Flats were used in this work. Data from the other observations, identified by an asterisk in Table 4.3, exhibited problems due to equipment malfunction. These problems were fixed prior to the VLA-NA campaign.

### 4.3 Available Data for Each Source

This section documents the data available for each source, including usable segments of the observations made at both VLA-NA and Kelly Flats. The data processing is documented in Chapter 5, and the resulting flux density estimates are presented in Chapter 6.

Table 4.4 identifies the data used to measure Cyg A. The nominal observing times were identified in Table 2.2. Figure 4.5 shows the source tracks traced out by Cyg A and potentially interfering sources during the range of times of the Cyg A observation.<sup>3</sup> During the VLA-NA campaign, the Sun transits within an hour of Cyg A's transit. This results in their fringe rates being very similar, thus difficult to isolate. To reduce interference from the Sun, the OBS5 and OBS15 measurements were collected before Cyg A's transit, and the OBS19 measurement was collected after Cyg A's transit.

<sup>3</sup>The source tracks are shown for the VLA-NA campaign. Since Kelly Flats is only  $\sim 3^\circ$  north of VLA-NA, the change in the source tracks for Kelly Flats is negligible.

Table 4.2: Observations collected during the VLA-NA measurement campaign. Missing observations (e.g. OBS3, OBS6-9) were planned, but were not performed due to time constraints.

Start Date (UTC) YYMMDD	ID	Start LST	Stop LST	Frequency Band		Sample Frequency (MSPS)	Baseline	Polarization
				NZ1	NZ2			
160115	OBS1	12:01	06:35	1	4	8.33	<b>b<sub>1</sub></b>	X
160116	OBS2	11:31	06:36	2	5	8.33	<b>b<sub>1</sub></b>	X
160118	OBS4	11:31	07:34	1	4	8.33	<b>b<sub>1</sub></b>	Y
160119	OBS5	11:31	06:39	2	5	8.33	<b>b<sub>1</sub></b>	Y
160121	OBS10	11:32	06:35	1	4	8.33	<b>b<sub>2</sub></b>	Y
160122	OBS11	11:31	06:35	2	5	8.33	<b>b<sub>2</sub></b>	Y
160123	OBS12	19:00	13:31	3	6	2.50	<b>b<sub>2</sub></b>	Y
160124	OBS13	19:00	13:32	1	4	8.33	<b>b<sub>3</sub></b>	X
160125	OBS14	19:00	13:32	2	5	8.33	<b>b<sub>3</sub></b>	X
160126	OBS15	18:00	13:35	3	6	2.50	<b>b<sub>3</sub></b>	X
160127	OBS19	20:30	13:36	2	4	8.33	<b>b<sub>3</sub></b>	Y

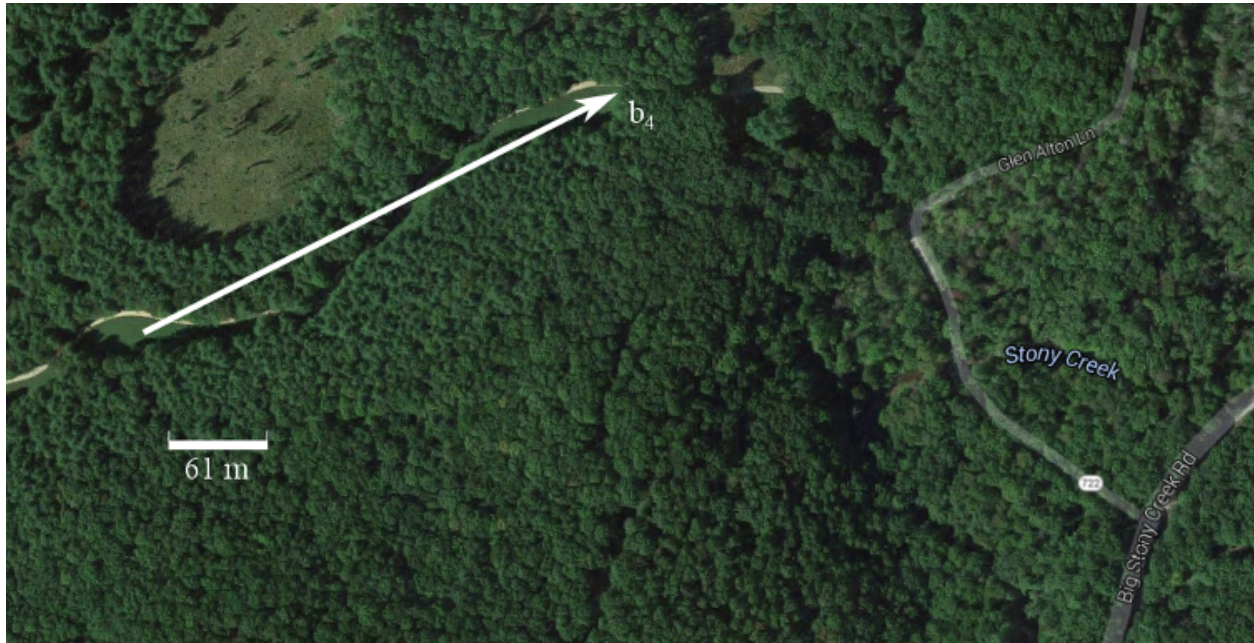


Figure 4.4: Google Maps screen shot of the Kelly Flats measurement site.

Table 4.3: Observations collected during the Kelly Flats measurement campaign. The asterisks indicate datasets that were not used in the results presented in this work (see text).

Start Date (UTC) YYMMDD	ID	Start LST HH:MM	Stop LST HH:MM	Frequency Band		Sample Frequency (MSPS)		Pol
				NZ1	NZ2	NZ1	NZ2	
150511	OBS21*	00:16	06:16	2a	-	8.33	-	X
150520	OBS22	05:20	11:20	2a	-	8.33	-	X
150611	OBS23*	18:41	00:42	2a	-	8.33	-	X
150629	OBS24*	18:52	01:09	-	4a	-	8.33	X
150731	OBS25	18:31	02:07	1a	-	8.33	-	X
150815	OBS26*	18:38	02:13	1a	-	8.33	-	X
151007	OBS27*	18:33	01:59	1a	5a	8.33	8.33	Y
151123	OBS28	18:25	12:25	2a	-	8.33	-	X

Table 4.4: Data used in the flux density estimates of Cyg A. Horizontal spaces demarcate the frequency bands.

ID	Band	$\nu_0$ (MHz)	Baseline	Pol	Start LST (HH:MM)	Duration (s)
OBS1	1	34	<b>b<sub>1</sub></b>	X	18:59	7200
OBS4	1	34	<b>b<sub>1</sub></b>	Y	18:03	5400
OBS10	1	34	<b>b<sub>2</sub></b>	Y	18:59	7200
OBS13	1	34	<b>b<sub>3</sub></b>	X	18:59	7200
OBS25	1a	40	<b>b<sub>4</sub></b>	X	18:31	10800
OBS2	2	42	<b>b<sub>1</sub></b>	X	18:59	7200
OBS5	2	42	<b>b<sub>1</sub></b>	Y	16:00	7200
OBS11	2	42	<b>b<sub>2</sub></b>	Y	18:59	7200
OBS14	2	42	<b>b<sub>3</sub></b>	X	18:59	7200
OBS19	2	42	<b>b<sub>3</sub></b>	Y	20:30	5400
OBS28	2a	44	<b>b<sub>4</sub></b>	X	18:25	7200
OBS1	4	58	<b>b<sub>1</sub></b>	X	18:59	7200
OBS4	4	58	<b>b<sub>1</sub></b>	Y	18:03	5400
OBS10	4	58	<b>b<sub>2</sub></b>	Y	18:59	7200
OBS13	4	58	<b>b<sub>3</sub></b>	X	18:59	7200
OBS19	4	58	<b>b<sub>3</sub></b>	Y	20:30	5400
OBS2	5	66	<b>b<sub>1</sub></b>	X	18:59	7200
OBS5	5	66	<b>b<sub>1</sub></b>	Y	16:00	7200
OBS11	5	66	<b>b<sub>2</sub></b>	Y	18:59	7200
OBS14	5	66	<b>b<sub>3</sub></b>	X	18:59	3600
OBS12	6	74	<b>b<sub>2</sub></b>	Y	18:59	3600
OBS15	6	74	<b>b<sub>3</sub></b>	X	17:59	7200

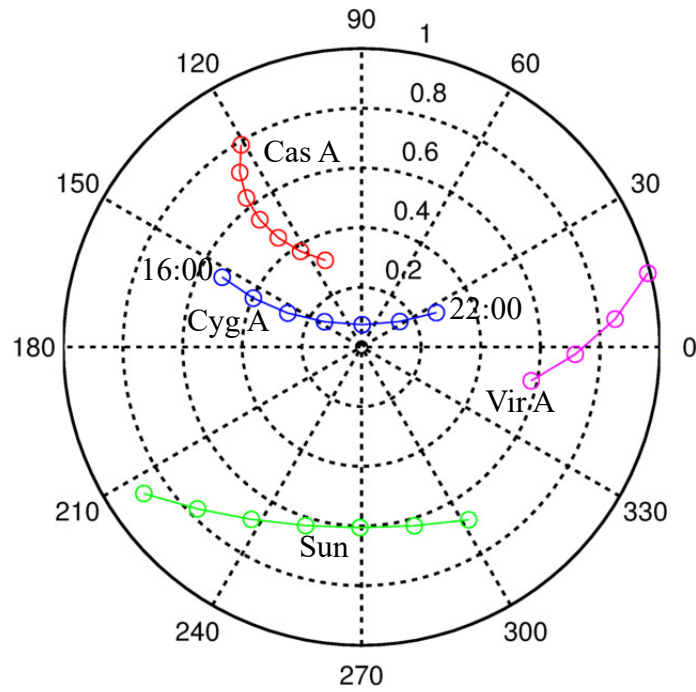


Figure 4.5: Source tracks of each source during the Cyg A measurements. Points are for every hour between 16:00-22:00 LST. (see Fig. 2.1 and associated text for interpretation.)

Tables 4.5-4.7, similar to Table 4.4, identify the measurements of Cas A, Vir A, and Tau A, respectively. Figures 4.6, 4.7, and 4.8, similar to 4.5, show the source tracks of Cas A, Vir A, and Tau A; respectively.

Table 4.5: Data used in the flux density estimates of Cas A. Horizontal spaces demarcate the frequency bands.

ID	Band	$\nu_0$ (MHz)	Baseline	Pol	Start LST (HH:MM)	Duration (s)
OBS1	1	34	<b>b<sub>1</sub></b>	X	23:23	7200
OBS4	1	34	<b>b<sub>1</sub></b>	Y	23:23	7200
OBS10	1	34	<b>b<sub>2</sub></b>	Y	23:24	7200
OBS13	1	34	<b>b<sub>3</sub></b>	X	23:12	7200
OBS25	1a	40	<b>b<sub>4</sub></b>	X	23:07	10800
OBS2	2	42	<b>b<sub>1</sub></b>	X	23:24	7200
OBS5	2	42	<b>b<sub>1</sub></b>	Y	23:24	7200
OBS11	2	42	<b>b<sub>2</sub></b>	Y	23:24	7200
OBS14	2	42	<b>b<sub>3</sub></b>	X	23:24	7200
OBS19	2	42	<b>b<sub>3</sub></b>	Y	23:24	7200
OBS28	1a	44	<b>b<sub>4</sub></b>	X	23:00	7200
OBS12	3	49.16	<b>b<sub>2</sub></b>	Y	23:24	7200
OBS15	3	49.16	<b>b<sub>3</sub></b>	X	23:24	7200
OBS1	4	58	<b>b<sub>1</sub></b>	X	23:23	7200
OBS4	4	58	<b>b<sub>1</sub></b>	Y	23:23	7200
OBS10	4	58	<b>b<sub>2</sub></b>	Y	23:24	7200
OBS13	4	58	<b>b<sub>3</sub></b>	X	23:12	7200
OBS19	4	58	<b>b<sub>3</sub></b>	Y	23:24	7200
OBS2	5	66	<b>b<sub>1</sub></b>	X	23:24	7200
OBS5	5	66	<b>b<sub>1</sub></b>	Y	23:24	7200
OBS11	5	66	<b>b<sub>2</sub></b>	Y	23:24	7200
OBS14	5	66	<b>b<sub>3</sub></b>	X	23:24	7200
OBS12	6	74	<b>b<sub>2</sub></b>	Y	23:24	7200
OBS15	6	74	<b>b<sub>3</sub></b>	X	23:24	7200

Table 4.6: Data used in the flux density estimates of Vir A. Horizontal spaces demarcate the frequency bands.

ID	Band	$\nu_0$ (MHz)	Baseline	Pol	Start LST (HH:MM)	Duration (s)
OBS1	1	34	<b>b<sub>1</sub></b>	X	12:01	7200
OBS4	1	34	<b>b<sub>1</sub></b>	Y	11:35	7200
OBS10	1	34	<b>b<sub>2</sub></b>	Y	11:31	7200
OBS13	1	34	<b>b<sub>3</sub></b>	X	11:31	7200
OBS2	2	42	<b>b<sub>1</sub></b>	X	11:31	7200
OBS5	2	42	<b>b<sub>1</sub></b>	Y	11:31	7200
OBS11	2	42	<b>b<sub>2</sub></b>	Y	11:31	7200
OBS14	2	42	<b>b<sub>3</sub></b>	X	11:31	7200
OBS19	2	42	<b>b<sub>3</sub></b>	Y	11:35	7200
OBS12	3	49.16	<b>b<sub>2</sub></b>	Y	11:31	7200
OBS15	3	49.16	<b>b<sub>3</sub></b>	X	11:35	7200
OBS4	4	58	<b>b<sub>1</sub></b>	Y	11:35	7200
OBS10	4	58	<b>b<sub>2</sub></b>	Y	11:31	7200
OBS13	4	58	<b>b<sub>3</sub></b>	X	11:31	7200
OBS19	4	58	<b>b<sub>3</sub></b>	Y	11:35	7200
OBS2	5	66	<b>b<sub>1</sub></b>	X	11:31	7200
OBS5	5	66	<b>b<sub>1</sub></b>	Y	11:31	3600
OBS11	5	66	<b>b<sub>2</sub></b>	Y	11:31	7200

Table 4.7: Data used in the flux density estimates of Tau A. Horizontal spaces demarcate the frequency bands.

ID	Band	$\nu_0$ (MHz)	Baseline	Pol	Start LST (HH:MM)	Duration (s)
OBS1	1	34	<b>b<sub>1</sub></b>	X	4:34	7200
OBS4	1	34	<b>b<sub>1</sub></b>	Y	5:34	7200
OBS10	1	34	<b>b<sub>2</sub></b>	Y	4:35	7200
OBS13	1	34	<b>b<sub>3</sub></b>	X	4:35	7200
OBS2	2	42	<b>b<sub>1</sub></b>	X	4:35	7200
OBS5	2	42	<b>b<sub>1</sub></b>	Y	4:39	7200
OBS11	2	42	<b>b<sub>2</sub></b>	Y	4:35	7200
OBS14	2	42	<b>b<sub>3</sub></b>	X	4:35	7200
OBS19	2	42	<b>b<sub>3</sub></b>	Y	4:39	7200
OBS22	2a	44	<b>b<sub>4</sub></b>	X	5:20	10800
OBS12	3	49.16	<b>b<sub>2</sub></b>	Y	4:35	7200
OBS15	3	49.16	<b>b<sub>3</sub></b>	X	4:39	7200
OBS1	4	58	<b>b<sub>1</sub></b>	X	4:34	7200
OBS4	4	58	<b>b<sub>1</sub></b>	Y	5:34	5400
OBS10	4	58	<b>b<sub>2</sub></b>	Y	4:35	7200
OBS13	4	58	<b>b<sub>3</sub></b>	X	4:35	7200
OBS19	4	58	<b>b<sub>3</sub></b>	Y	4:39	7200
OBS2	5	66	<b>b<sub>1</sub></b>	X	4:35	7200
OBS5	5	66	<b>b<sub>1</sub></b>	Y	4:39	7200
OBS11	5	66	<b>b<sub>2</sub></b>	Y	4:35	7200
OBS14	5	66	<b>b<sub>3</sub></b>	X	4:35	7200
OBS12	6	74	<b>b<sub>2</sub></b>	Y	4:35	7200
OBS15	6	74	<b>b<sub>3</sub></b>	X	4:39	7200

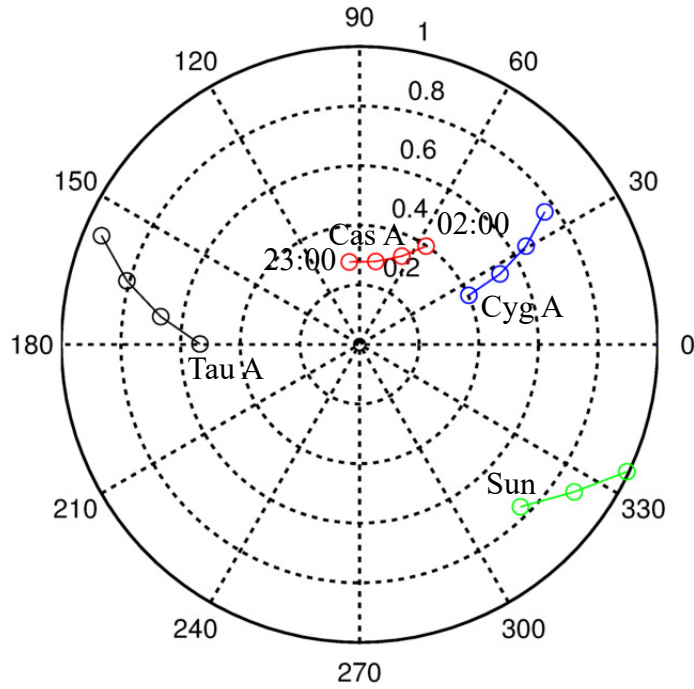


Figure 4.6: Source tracks of each source during the Cas A measurements. Points are for every hour between 23:00-02:00 LST.

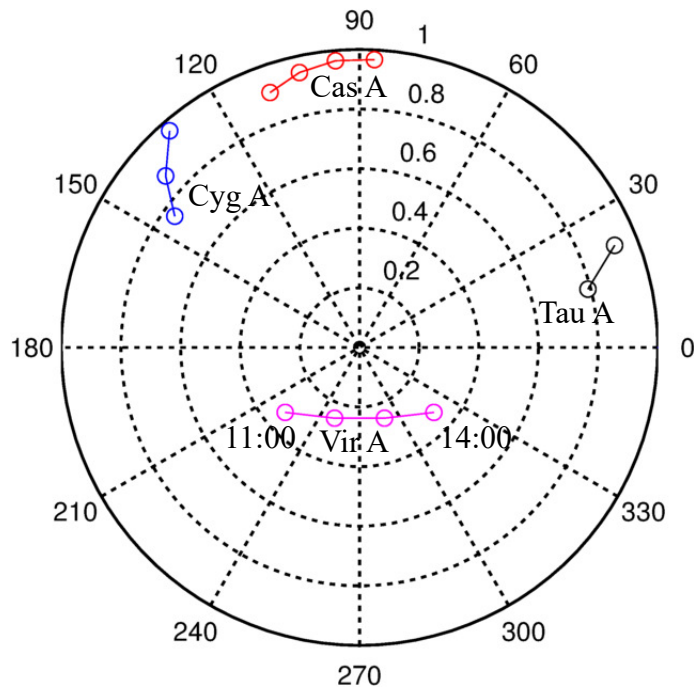


Figure 4.7: Source tracks of each source during the Vir A measurements. Points are for every hour between 11:00-14:00 LST.

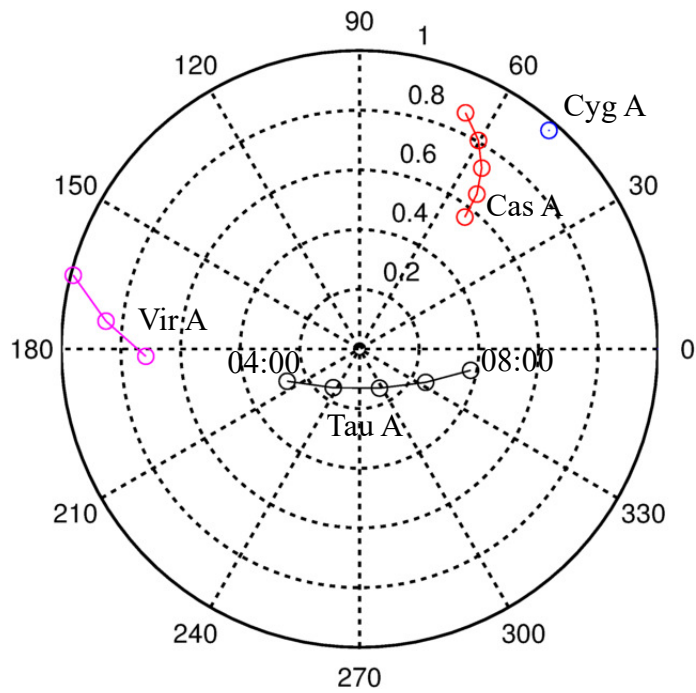


Figure 4.8: Source tracks of each source during the Tau A measurements. Points are for every hour between 04:00-08:00 LST.

# Chapter 5

## Data Reduction

This chapter demonstrates the process used to reduce the data collected from the measurement campaign reported in Chapter 4. The methodology was described in Chapter 2, and summarized in Fig. 2.15.

The dataset considered in this chapter is the Cyg A observation from OBS2, described in Section 4.1. For this observation, the baseline is  $\mathbf{b}_1$  (see Table 4.1) and the antennas are oriented in the X (East-West)-polarization. The frequency band is Band 2 (38-46 MHz). Cyg A transits in the middle of the dataset. Note the conditions of this dataset are similar to those of the example presented in Section 2.4.2.

Figures 5.1 and 5.2 shows the power spectrum and cross correlation, respectively, for the entire two-hour observation. The system appears to be stable and free of RFI. RFI mitigation was performed as described in Section 3.11, however less than 0.1% of the pixels were flagged in this dataset. There was no measurable difference in the results.

The rest of this chapter is organized as follows. Section 5.1 shows the estimate of the receiver TPG  $G_R(Z'_A)$  and the Galactic background noise  $T_{sky}$ , using only the unmodified priors (i.e,  $C_p = 0$ ,  $C_s = \infty$ , and  $\Delta T_{cal} = 0$ ). Section 5.2 presents the *in situ* calibration of these priors as proposed in Section 2.6. Section 5.3 presents the fringe rate processing used to isolate

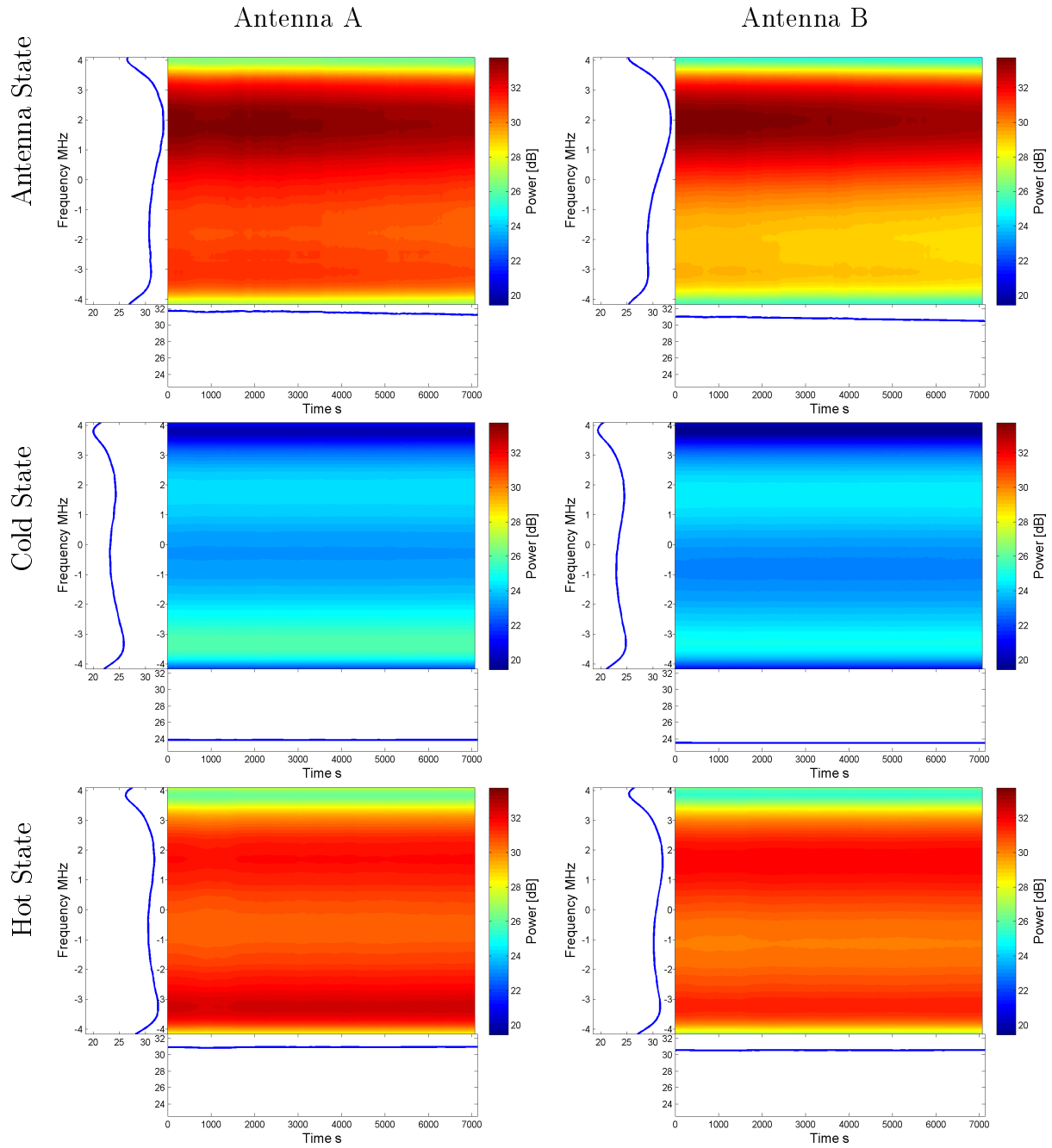


Figure 5.1: PSD ( $S_{out,i}$ ) in each state ( $i = 1, 2, 3$ ).  $\Delta\nu = 65.1$  kHz,  $\Delta t = 20$  s.

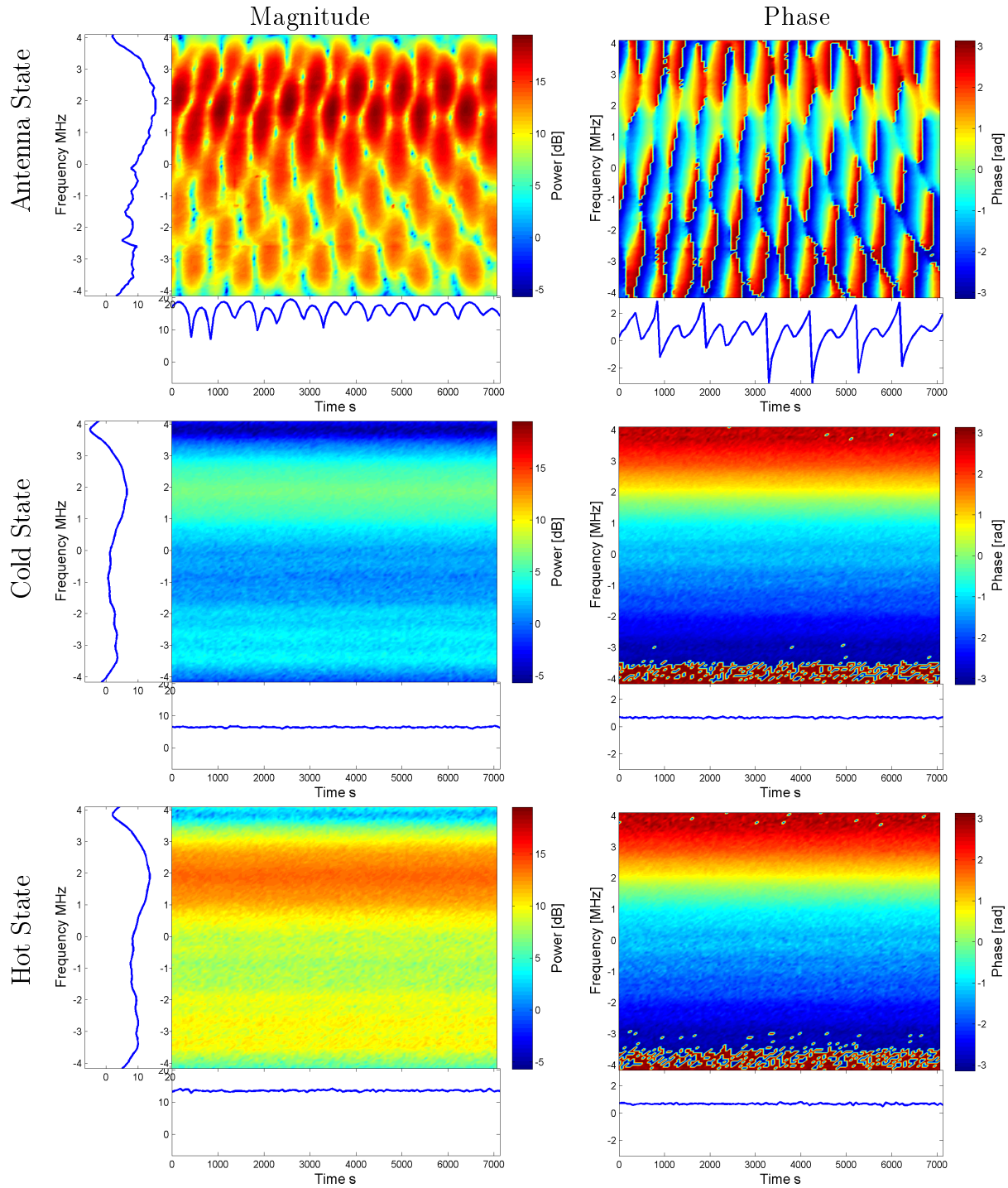


Figure 5.2: Cross correlation ( $\rho_{mn}$ ) in each state.  $\Delta\nu = 65.1$  kHz,  $\Delta t = 20$  s.

Table 5.1: Prior measurements required to estimate  $G_R(Z'_A)$ .

Parameter	Value	Reference
$Z_A$	Fig. 3.12 (Measured)	Section 3.1.4
$Z_p$	12.3 k $\Omega$    12.6 pF (Simulated)	Section 3.2.3
$Z_R$	Fig. 3.21 (Measured)	Section 3.2.3
$Z_{cal}$	Fig. E.5 (Measured)	Appendix E
$T_{cal}$	Fig. E.10 (Measured)	Appendix E

Cyg A's flux density from the cross-correlation shown in Fig. 5.2. Finally, Section 5.4 shows how the CIM is used to estimate the absolute flux density density of Cyg A.

## 5.1 ATM Phase of the Data Reduction

This section presents an example of one iteration of the ATM phase of the processing shown in Fig. 2.15. The theory was presented in Section 2.5.1, and is demonstrated here in Section 5.1.1 with the priors identified in Table 5.1. A side result of the ATM is an independent estimate of  $T_{sky}$ . The process was described in Section 2.5.2, and is demonstrated here in Section 5.1.2.

### 5.1.1 Estimation of $G_R(Z'_A)$

The ATM is used to estimate  $G_R(Z'_A)$  from the measured PSD in each state. Figure 5.3 shows these PSDs for both antennas. The PSDs in the hot and cold states are then used in conjunction with the priors to determine  $G_R(Z'_A)$ .

The receiver TPG in the calibration states,  $G_R(Z_{cal})$ , is estimated from Eq. (2.49). Figure 5.4 shows the resulting  $G_R(Z_{cal})$ .  $G_R(Z_{cal})$  is then converted to  $G_R(Z'_A)$  by Eq. (2.50). Figure 5.4 also shows the resulting  $G_R(Z'_A)$ .

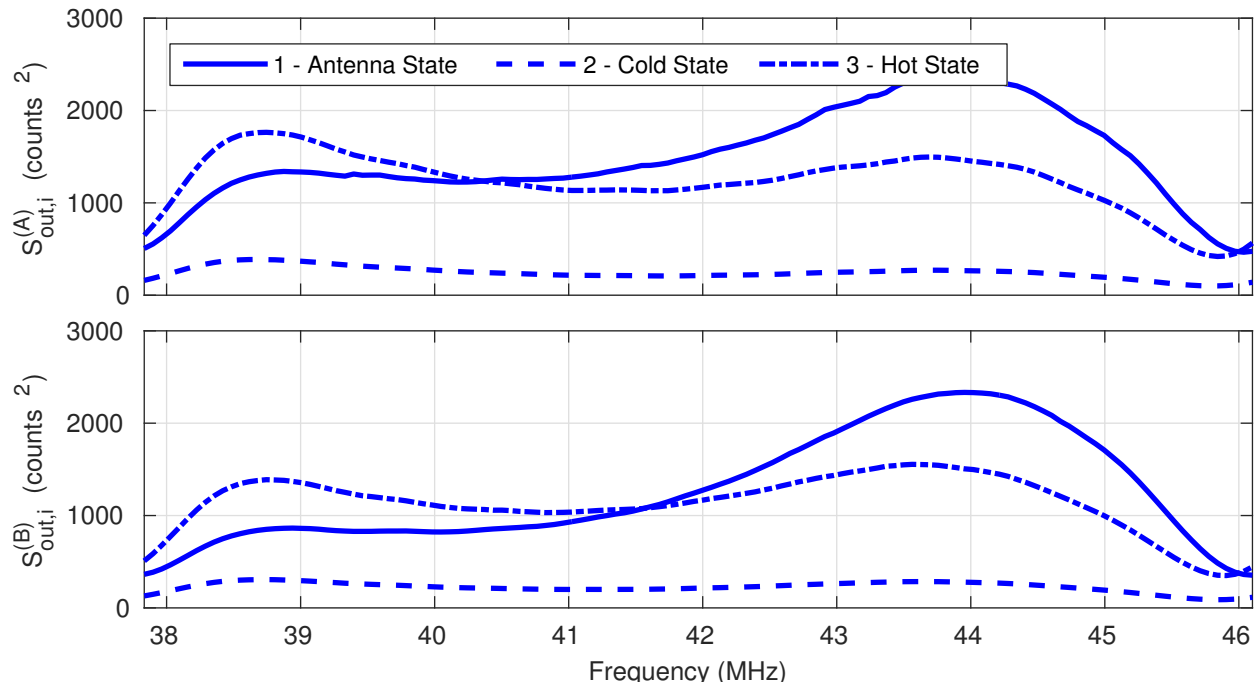


Figure 5.3: Measured PSD in each state, from each antenna. This is the same as the first time index in each state shown in Fig. 5.1.  $\Delta\nu = 65.1$  kHz,  $\Delta t = 20$  s.

### 5.1.2 Estimation of $T_{sky}$

Now we show the estimation of  $T_{sky}$ . Doing so requires additional priors, which are identified in Table 5.2.

First, the receiver temperature  $T_R(Z_{cal})$  is estimated from Eq. (2.54). Equation (2.55) then converts  $T_R(Z_{cal})$  to  $T_R(Z'_A)$ . Figure 5.4 shows the resulting  $T_R$  for both source impedances. Note that the resulting  $T_R(Z'_A)$  makes sense: it should increase with decreasing frequency, since the impedance match with the antenna is getting worse and therefore more internal noise is reflected back into the receiver. This is in contrast to  $T_R(Z_{cal})$ , which is well-matched over the band.

Next,  $T_A$  is estimated by Eq. (2.56), and is shown in Fig. 5.5. Note the bias tails near the DRX band edges below  $\sim 38.5$  MHz and above  $\sim 45.5$  MHz. These are attributed to noise that is introduced later in the signal path (i.e. in a manner that is not accounted for in the

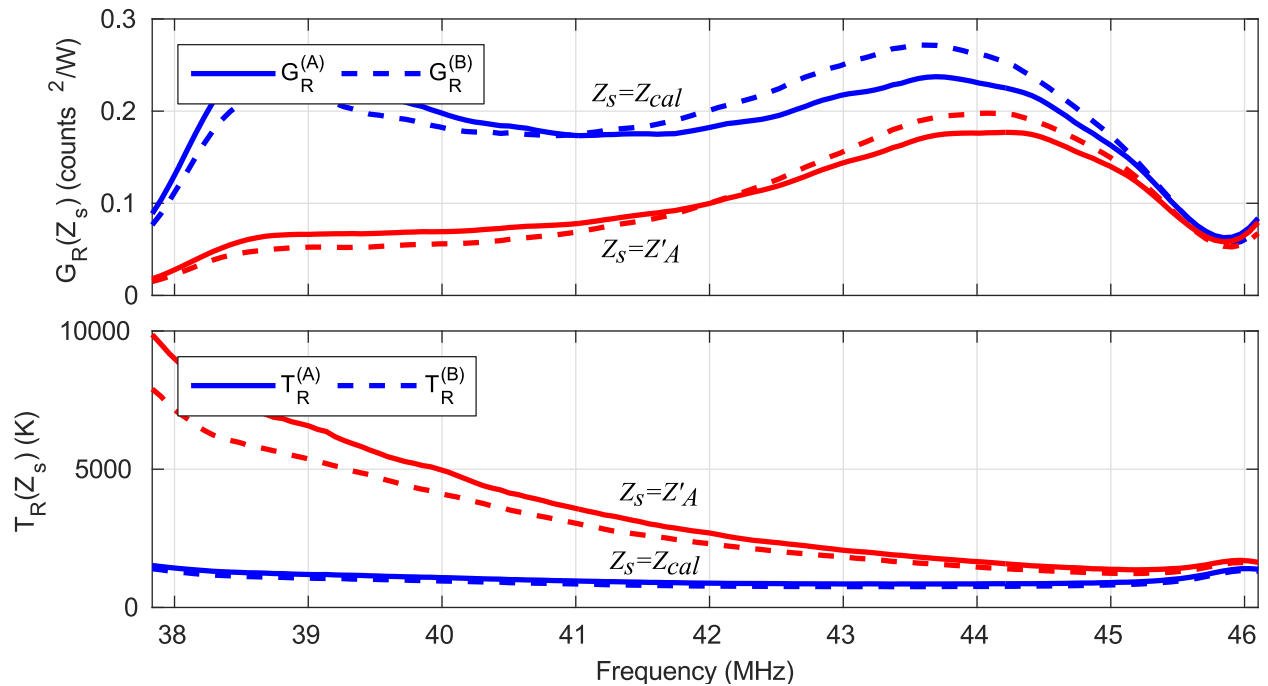


Figure 5.4: Estimate of the receiver gain (top) and noise temperature (bottom) for each antenna, for the first iteration of the ATM phase of data reduction.

Table 5.2: Additional priors required to estimate  $T_R(Z'_A)$  and  $T_{sky}$ .

Parameter	Value	Reference
$T_{amb}$	292 K (Measured)	Section 3.2.1
$\epsilon_A$	Fig. 3.15 (Simulated, very dry ground)	Section 3.1.5
$T_{gnd}$	Fig. 3.21 (Simulated)	Section 3.7
$R_{loss}$	Fig. 3.13 (Theory)	Section 3.1.4

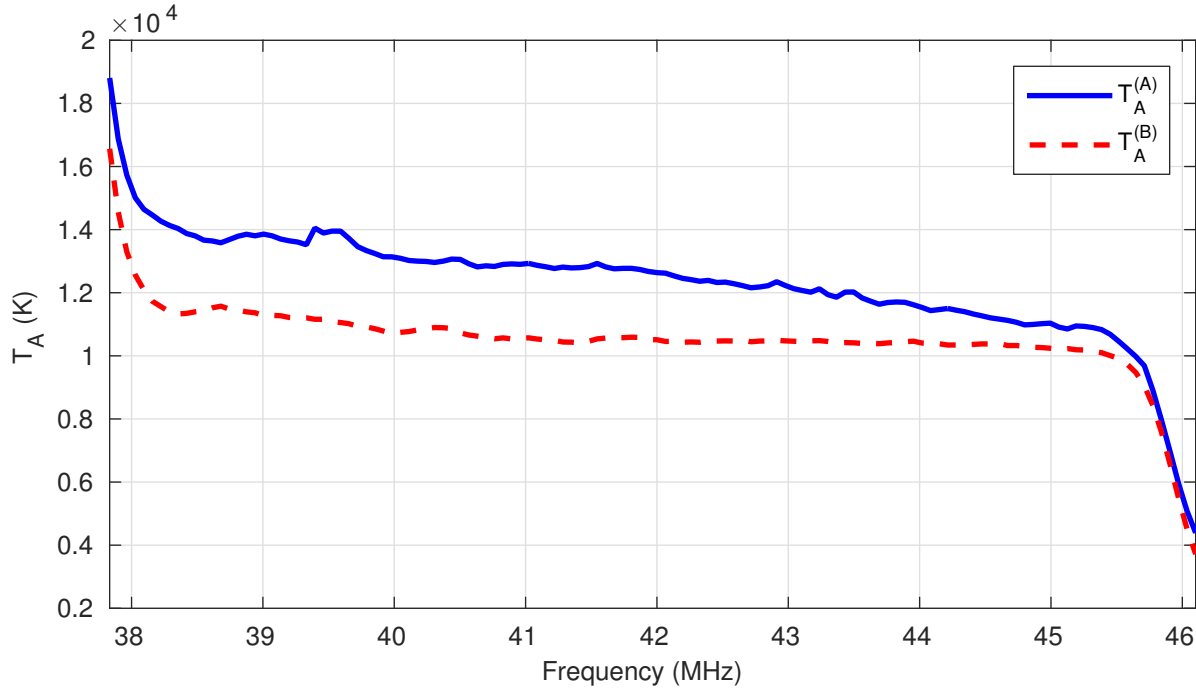


Figure 5.5: Estimate of  $T_A$  from the first iteration of the ATM phase of data reduction.  $\Delta\nu = 65.1$  kHz,  $\Delta t = 20$  s.

calibration of  $G_R(Z'_A)$  or  $T_R(Z'_A)$ ). When considering more than just one frequency band, we will clip the bias tails so as to not obfuscate the result.

Finally, Eq. (2.58) is used to estimate  $T_{sky}$ , shown in Fig. 5.6. The estimated  $T_{sky}$  exhibits a rough agreement with the model, which was computed using Eq. (2.1), using GSM for  $T(\theta, \phi)$  and  $P(\theta, \phi)$  derived from the IT/PEC for  $l_e$ . However, we expect  $T_{sky}$  to be a power law in frequency and equal for both antennas. In the next section, we take advantage of this knowledge to calibrate the priors, and thereby improve the estimate of  $T_{sky}$ .

## 5.2 Joint Optimization of $C_p$ , $C_s$ , and $\Delta T_{cal}$

It is evident from Fig. 5.6 that the error in the priors is large enough to bias the results of the work. As proposed in Section 2.6, we introduce three modifications to the priors to mitigate this bias:  $C_p$ ,  $C_s$ , and  $\Delta T_{cal}$ . As proposed in Section 2.6.3, the modifications are

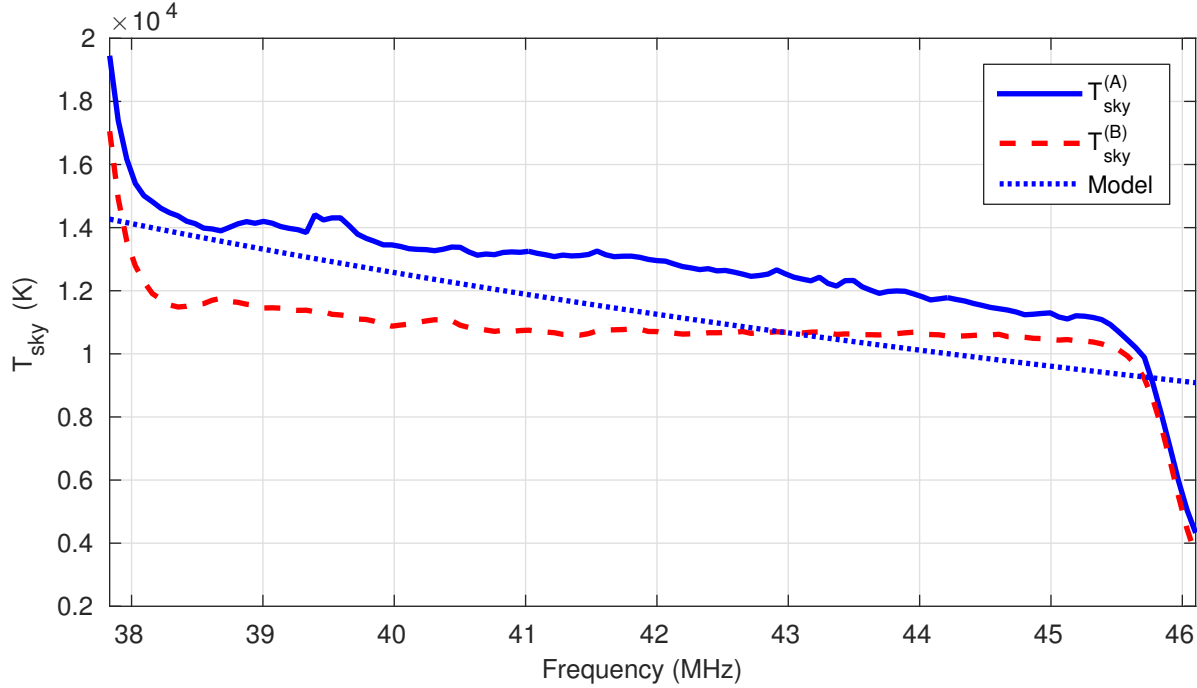


Figure 5.6: Estimate of  $T_{sky}$  from the first iteration of the ATM phase of data reduction. X-pol,  $\Delta\nu = 65.1$  kHz,  $\Delta t = 20$  s.

determined separately for each antenna, with the objective that the resulting estimate of  $T_{sky}$  should be (1) a power law in frequency, and (2) identical for the two antennas. In this section, we determine the values of the modifications.

To determine  $C_p$ ,  $C_s$ , and  $\Delta T_{cal}$ , we use the ATM to estimate  $T_{sky}$  from all Cyg A datasets from VLA-NA at 19:00 LST. This is the closest LST to the transit of the Galactic center ( $\sim 17:00$ ) for which there were multiple (13) unique measurements. As a result,  $T_{sky}$  is near a maximum with respect to the diurnal variation, improving the signal-to-noise ratio with respect to  $T_R(Z'_A)$ . Figure 5.7 shows the resulting  $T_{sky}$  for all such observations.

We now iteratively vary  $C_p$ ,  $C_s$ , and  $\Delta T_{cal}$ , separately for each antenna. We employ a brute force search to best satisfy the above criteria. We varied  $C_p$  in 1 pF increments,  $C_s$  in 10 pF increments, and  $\Delta T_{cal}$  in 100 K increments. The optimization is simplified by the fact that  $C_p$  affects primarily the high frequency bands,  $C_s$  affects primarily the low frequency bands, and  $\Delta T_{cal}$  affects primarily the difference between the antennas. The resulting modifications

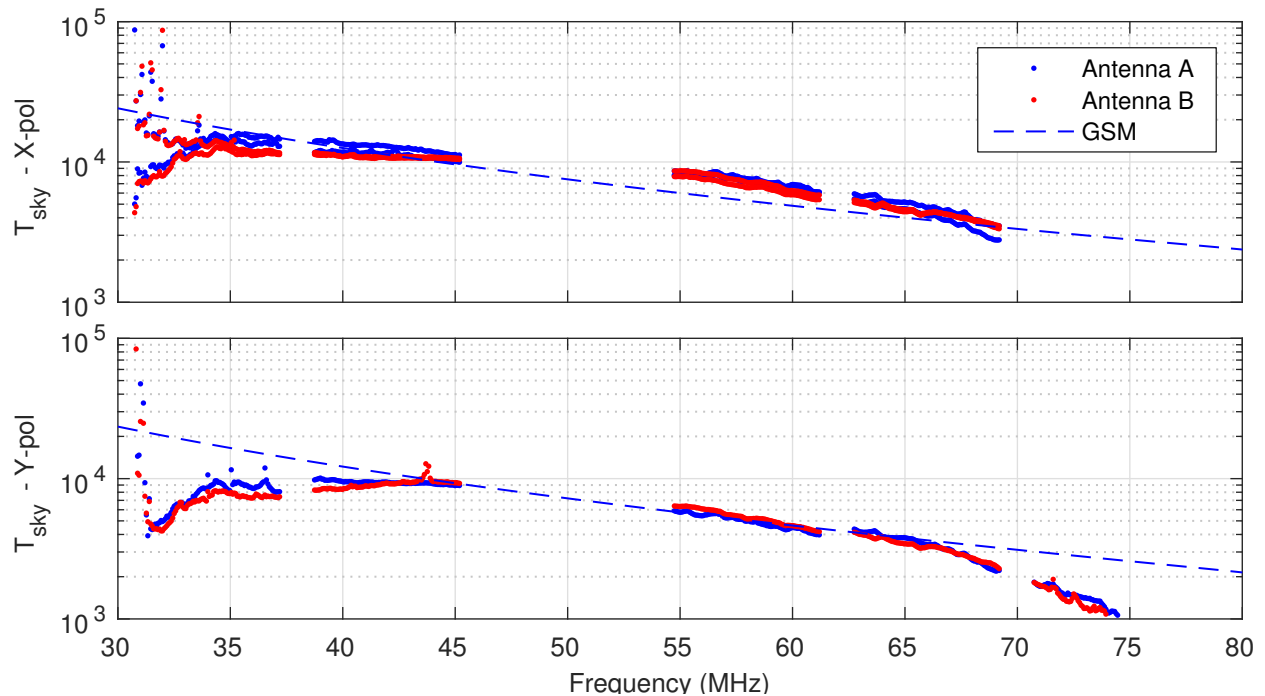


Figure 5.7: Same as Fig. 5.6, but now for all available observations and polarizations, and bias tails excluded.

are shown in Table 5.3. Note the negative values for  $C_p$  are reasonable; this indicates only that  $X_{A,prior}$  is too low.

Figure 5.8 shows the resulting estimate of  $T_{sky}$  after the iterative process described above. The estimate shows excellent agreement with the model for Bands 4 (54–62 MHz) and 5 (62–70 MHz). This approach is clearly effective in this range.

The approach is less effective for Band 2 (38–46 MHz), and only small improvement is seen in Band 1 (30–38 MHz). This may be due to the model of Fig. 2.13 being inadequate to describe this frequency range, or may be due to some frequency dependence in  $\Delta T_{cal}$  that becomes significant. Addressing this is identified as future work. In the present work, we consider the Band 2 results to be valid, and the Band 1 results to be valid albeit with a significant bias toward lower temperatures.

We are unable to make conclusions in Band 6 (70–78 MHz) due to the limited amount of available data, and due to a lack of sensitivity in the available data (see Section 3.7). No

Table 5.3: Modifications to the priors used by the ATM. See text for details.

Correction	Antenna 1	Antenna 2
$C_p$	-5 pF	-7 pF
$C_s$	150 pF	120 pF
$\Delta T_{cal}$	500 K	1000 K

data is available in Band 3 (48.2–50.2 MHz) for this LST, so no conclusion can be made about the effectiveness of this approach in Band 3. However, results in Chapter 6 indicate this technique is effective in that range as well.

Figure 5.8 also shows a fit to Eq. (2.2) using the resulting estimate of  $T_{sky}$  in all frequency bands for each polarization. The fit was obtained using the method of least squares. The resulting spectral indices are indicated in the legends of Fig. 5.8. Note that the spectral index is consistent with the spectral index predicted by Eq. (2.1), when evaluated with GSM and IT/PEC. Additionally, the spectral index is consistent with those reported in other work (e.g. about  $-2.5$  in [35], and  $-2.27$  in [56]). This agreement provides confidence in the technique used to determine the modifications. Furthermore, it was seen in Fig. 3.14 that the modifications to  $Z_A$  improve the agreement with the result from MoM. This agreement provides confidence in the validity of the model of Fig. 2.13.

### 5.3 Isolation of the Source Flux

As illustrated in Fig. 2.15, we must isolate the desired signal in the cross correlation before invoking the CIM phase of data reduction. In this section, we isolate Cyg A from the other signals.

Figure 5.9 shows the cross correlation shown in Fig. 5.2 after transformation into the fringe rate domain. Three sources are clearly visible, corresponding to Cyg A ( $f_r \sim 2$  mHz), Cas A ( $f_r \sim 0.75$  mHz), and the “DC” all sky term ( $f_r = 0$  mHz). This plot is comparable Fig. 2.9

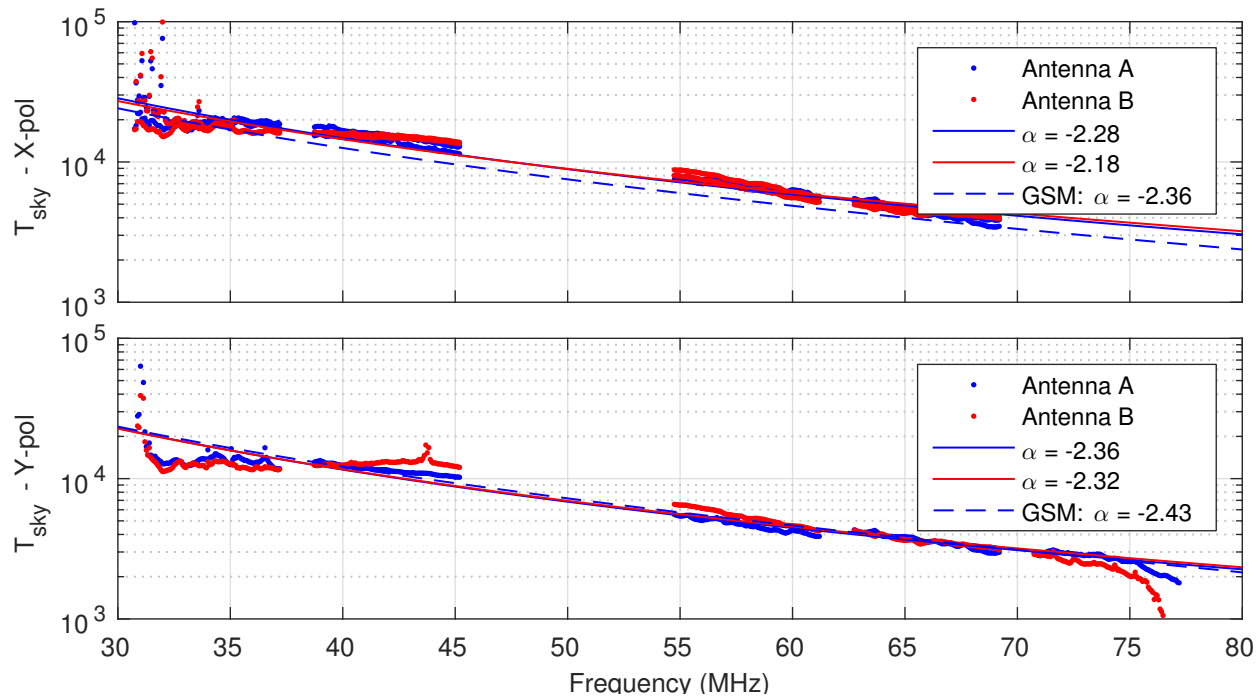


Figure 5.8: Estimate of  $T_{sky}$  after determining  $C_p$ ,  $C_s$ , and  $\Delta T_{cal}$ .

from the example discussed in Section 2.4.2. Note that the oscillatory dependence with  $\nu$  of the all sky term noted in Appendix A and Fig. 2.9 is present. However, it is faint, due to internal cross-talk.

Section 2.4 defined the technique used to isolate the source from the background. Briefly: the cross correlation is delay-stopped for the desired source, and filtered to excise all data except that corresponding to the fringe rate of the source. This requires knowledge of the baseline. However, as discussed in Sections 4.1 and 4.2, the accuracy of the baseline measurements is only  $\sim 10$  m for VLA-NA, and worse still for Kelly Flats. Consequently, the fringe rate estimated from the measured baselines is not sufficiently accurate for the delay stopping operation. Instead, the source's fringe rate is estimated from the data as follows. Following Appendix C, the fringe rate is well-modeled by the power series

$$f_g(t) \approx \nu (c_0 + c_1 t + c_2 t^2) \quad (5.1)$$

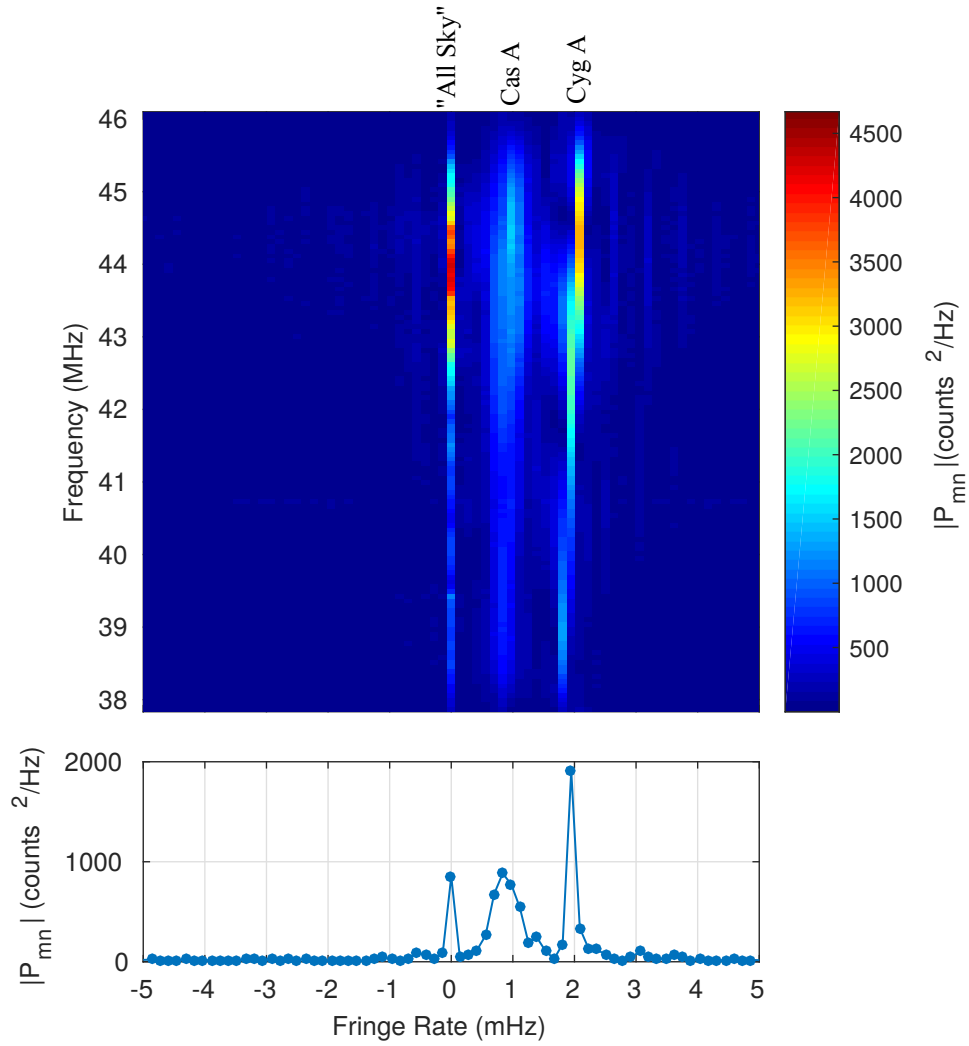


Figure 5.9: Cross correlation shown in Fig. 5.2 after transformation to the fringe rate domain.

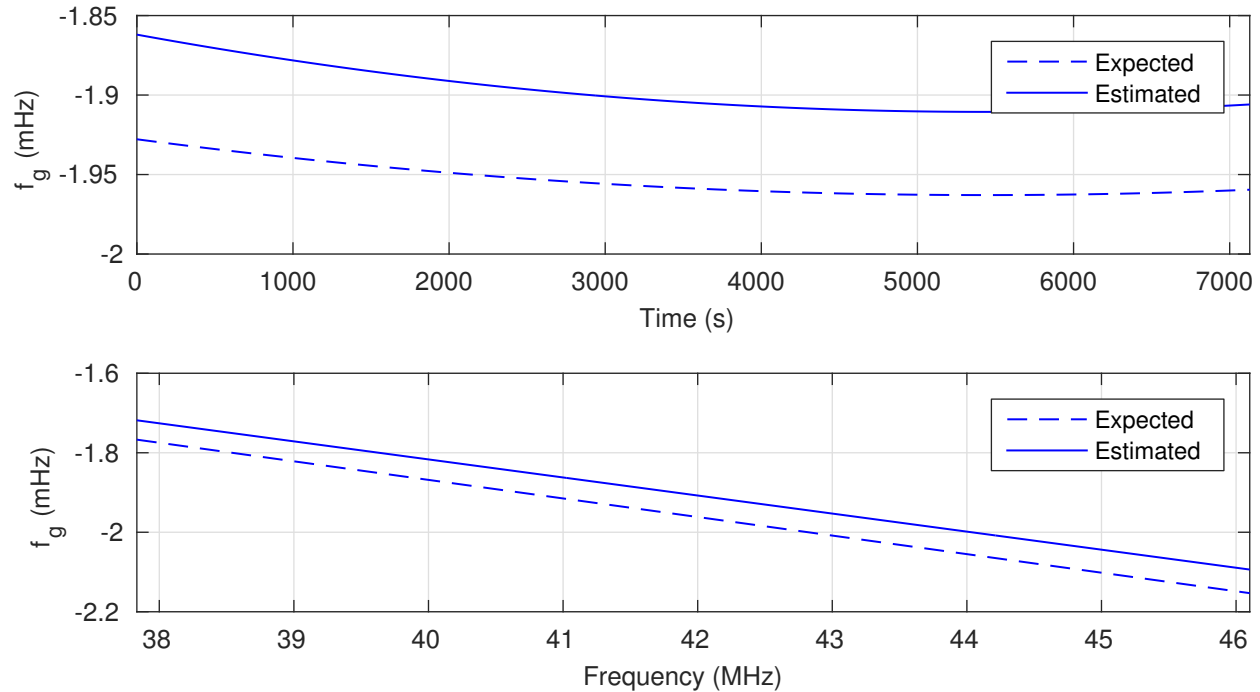


Figure 5.10: Comparison of the estimated fringe rate to the expected fringe rate (top) at 42 MHz, and (bottom) at LST=20:00.

The measured baselines are used for initial guesses for the  $c_i$  parameters using Eqs. (C.9). The parameters are then refined using a search around the initial guess, such that

$$[c_0, c_1, c_2] = \arg \max_{c_0, c_1, c_2} \int_0^T \rho_{mn}(t) e^{-j\nu(c_0 + c_1 t + c_2 t^2)} dt \quad (5.2)$$

where  $T$  is the duration of the observation.

Figure 5.10 shows the estimated fringe rate as a function of both frequency and LST using the procedure described in Eqs. (5.1) and (5.2). Figure 5.11 shows the delay-stopped cross correlation in the fringe rate domain. The signal from Cyg A is now isolated at  $f_r = 0$ , and the signals from Cas A and the diffuse emission have been shifted and spread accordingly.

Finally, we fringe-rate filter to exclude all but the desired signal at  $f_r = 0$ . The resulting signal for Cyg A is shown in Fig. 5.12. This is the input to the CIM phase of the data reduction.

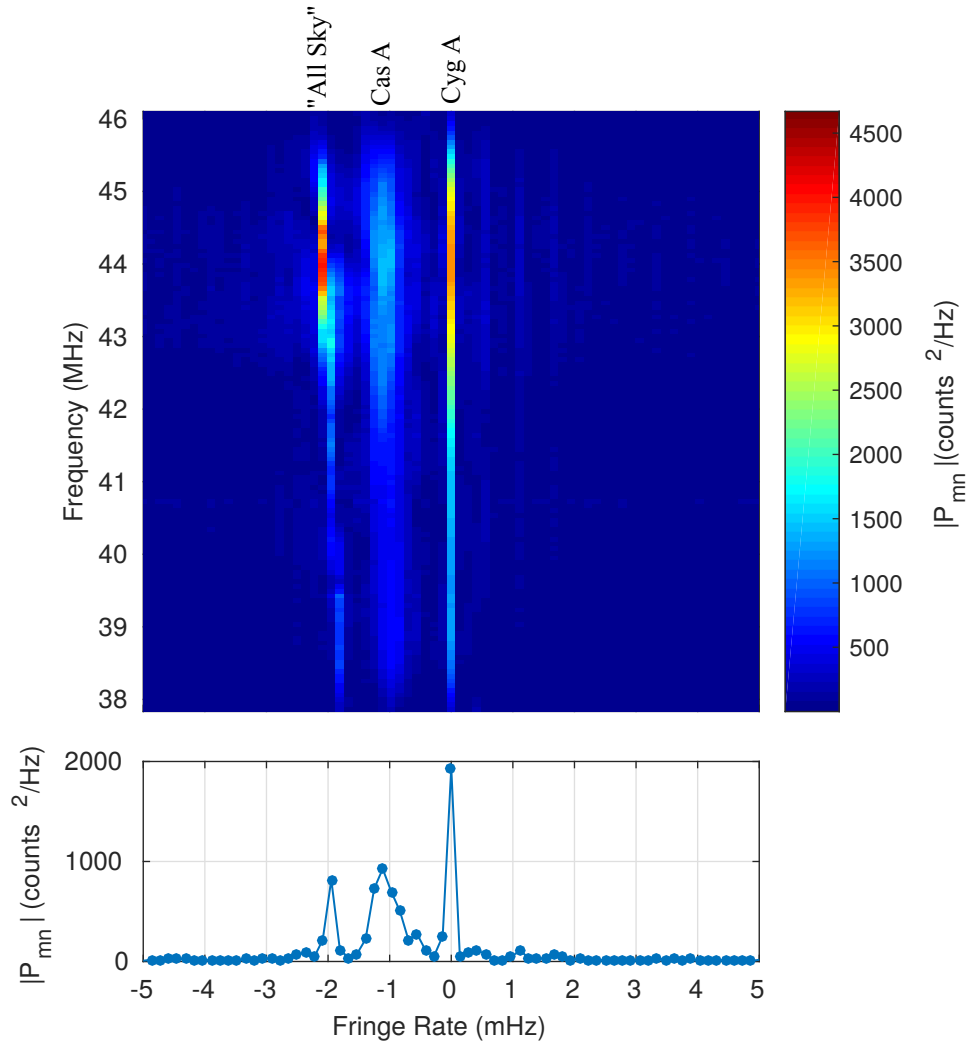


Figure 5.11: Same as Fig. 5.9, but after delay stopping using the estimated fringe rate shown in Fig. 5.10.

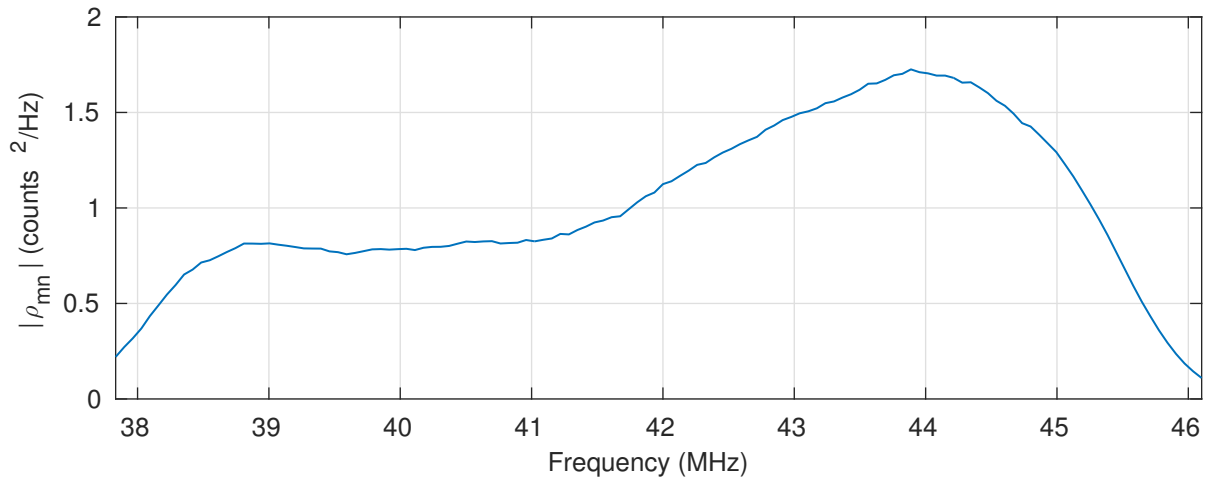


Figure 5.12: Cross correlation spectrum after fringe rate processing to isolate Cyg A.

## 5.4 CIM Phase of the Data Reduction

Following Fig. 2.15, it remains to transform Fig. 5.12 the flux density estimate. This is done by invoking the CIM, as described in Section 2.7. In this section, we apply the outputs from the ATM phase of data reduction and the fringe rate processing in order to obtain  $S_\nu^{src}$  for Cyg A.

We obtain an estimate of  $G_R(Z'_A)$  for each antenna by invoking the ATM (Fig. 5.4), which must be converted to  $|H^{(m)}|$  and  $|H^{(n)}|$ . The relationship between  $|H^{(m)}|$  (or  $|H^{(n)}|$ ) and  $G_R(Z'_A)$  was derived in Section 2.7.2, and is given by Eq. (2.68). Figure 5.13 shows the resulting  $|H^{(m)}H^{(n)}|$  for the observation considered in this chapter.

We also require the effective length of the antenna projected in the direction of the source,  $l_e$ . As discussed in Section 3.1, we have two models for  $l_e$ : the IT/PEC model and the MoM model. In Section 6.1 we will show that the MoM model is more accurate for  $\theta < 20^\circ$ , and so MoM is used for this dataset. Figures 5.14 shows  $l_e$  in the direction of Cyg A for the observation considered in this chapter.

Figure 5.15 shows the resulting absolute flux density estimate. The estimate is consistent with the Baars flux scale. The apparent bias to the spectral index is the same observed in

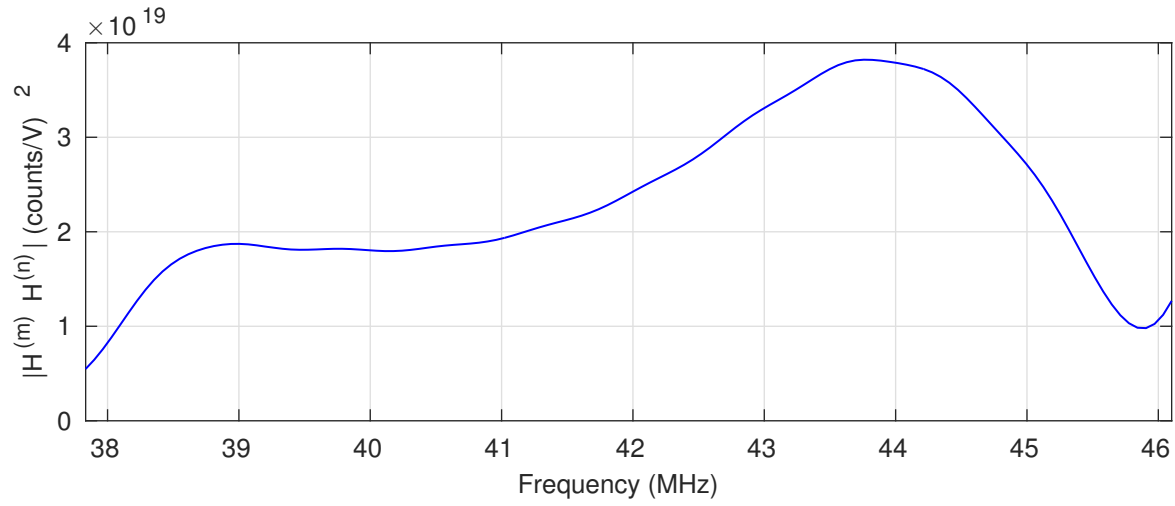


Figure 5.13: Product of the transfer functions of the two receivers.

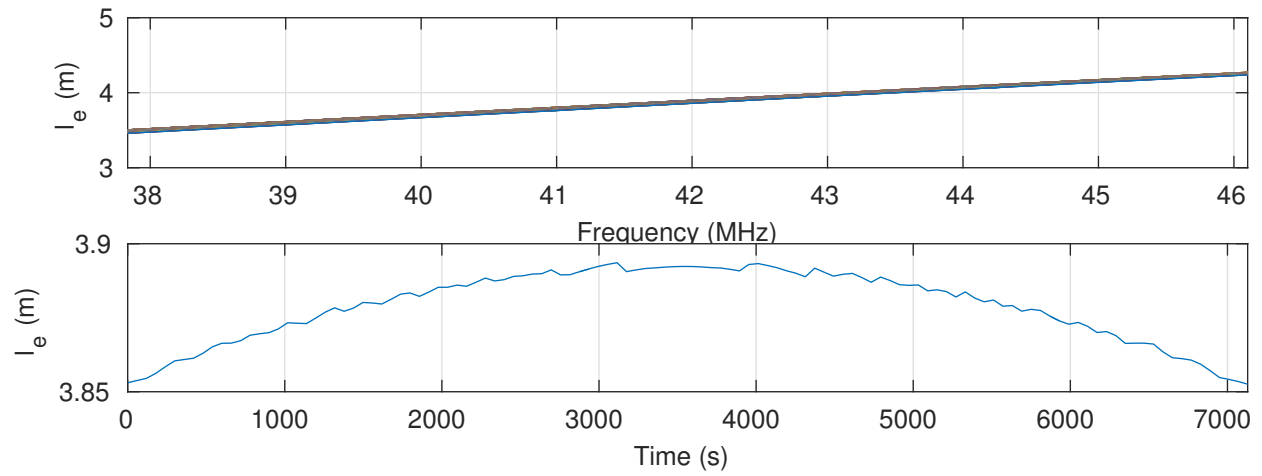


Figure 5.14: The projected effective length.

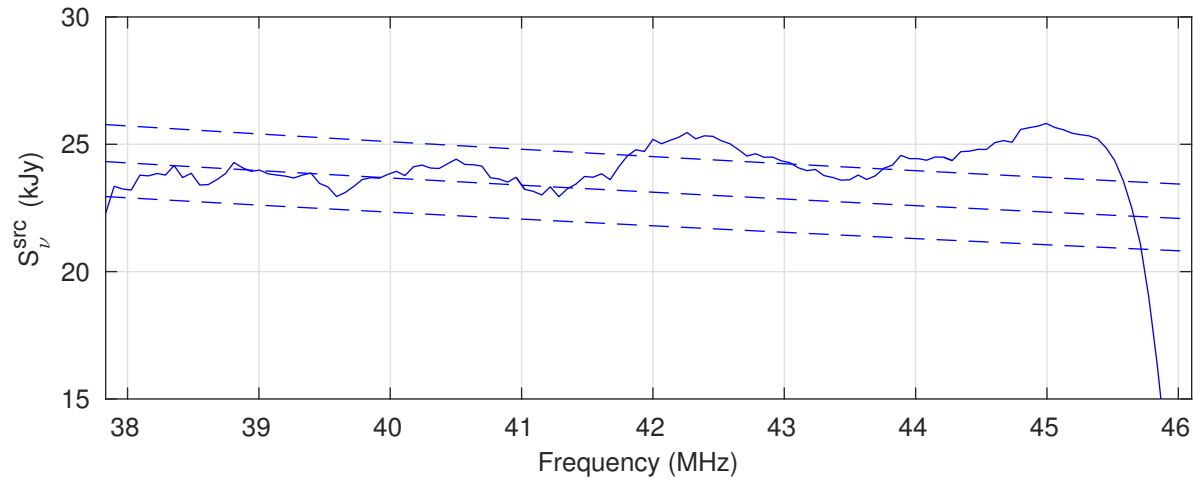


Figure 5.15: Flux density estimate of Cyg A from the OBS2 measurement. The dashed lines are the Baars flux scale and its associated error.

the estimate of  $T_{sky}$  in Fig. 5.8. This implies that the source of the bias is not  $l_e$ , since  $l_e$  is not used to estimate  $T_{sky}$ . Therefore, the bias is likely due to uncertainty in  $Z_A$  or  $T_{cal}$ , or both. Identifying and correcting this bias is identified as future work.

The apparent ripple seen in Fig. 5.15 is attributed to the proximity Cas A's fringe rate relative to Cyg A's, as already seen in Section 2.4.2. As will be seen in the next chapter, this can be partially mitigated by averaging multiple measurements which used different baselines. Further improvement in mitigating this ripple is identified as future work.

We applied the data reduction process described in this chapter to each of the observations identified in Section 4.3. In the next chapter, we present the results for all of the observations of each source.

# Chapter 6

## Results

This chapter summarizes the results from the measurement campaign described in Chapter 4. The data processing described in Chapter 5 has been completed for each measurement. The final flux density estimates are summarized in Fig. 1.7. This chapter shows intermediate results leading to those estimates.

The rest of this chapter is ordered as follows. In Section 6.1 we evaluate the two effective length models presented in Section 3.1 and determine when each model will be used. Section 6.2 documents the new flux density estimates. Section 6.3 reports new measurements of the Galactic background noise.

### 6.1 Evaluation of Effective Length Models

Sections 3.1.2 and 3.1.3 presented two models for the effective length of the antenna: IT/PEC and one based on the MoM, respectively. In this section, we compare the flux density estimated in each case. In doing so, we will show that MoM performs better when the source is near zenith, and that IT/PEC performs better when the source is at lower elevation.

The criterion used to evaluate the two models is similar to that used to calibrate  $Z_A$  and  $T_{cal}$

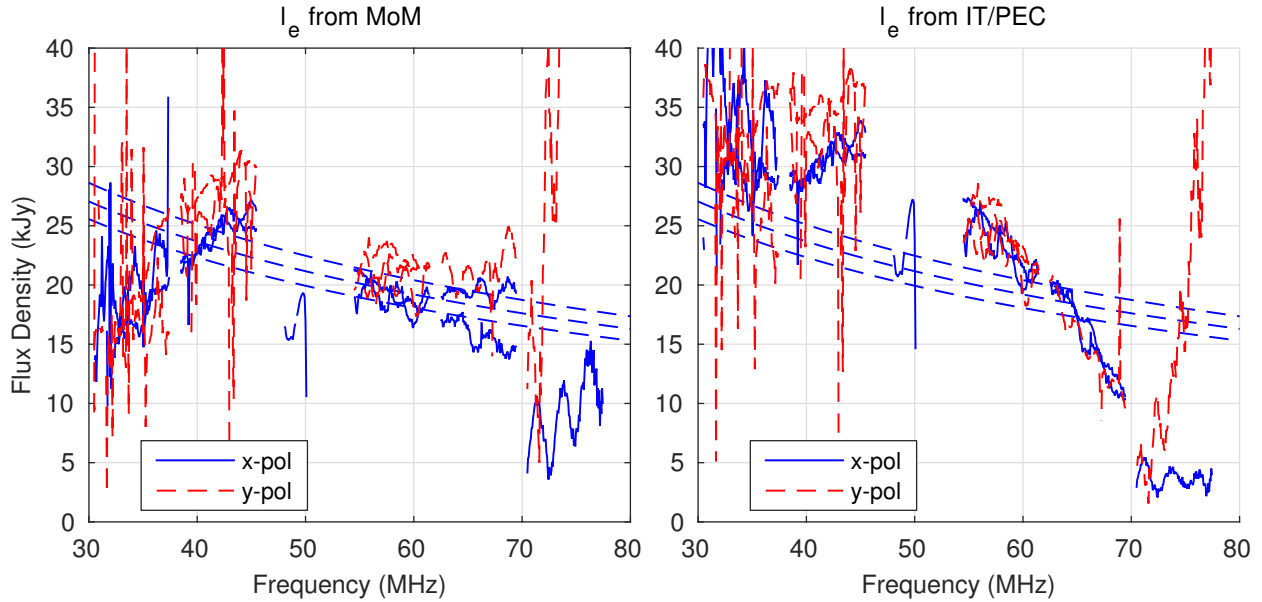


Figure 6.1: Flux density of Cyg A, estimated with the effective length computed by (left) MoM and (right) IT/PEC. Only data taken when Cyg A is greater than  $70^\circ$  above the horizon are included. The dashed lines represent the Baars flux scale and associated error.

(see Section 2.6.3): We expect that the flux density spectrum should (1) be well-modeled by a power law, and (2) be independent of the antenna polarization. Thus, the better pattern model at a given zenith angle ( $\theta$ ) is the one that yields  $S_\nu^{src}$  that is the closest possible fit to a power law and which minimizes the difference between polarizations, and does so jointly over all available data.

Figure 6.1 shows the estimated flux density for Cyg A, using both models, from all of the measurements for which  $\theta < 20^\circ$ . Note that MoM yields a better fit to a power law between 50–70 MHz, although is not quite as effective from the perspective of achieving the same estimate between polarizations. The apparent error in Band 1 is attributed to the same error seen in the estimate of  $T_{sky}$  (see Section 5.2). In Band 6, the cross-correlation was not sufficiently sensitive to Cyg A, such that the source isolation failed. We will continue to show the data in these bands throughout this chapter for completeness.

Figure 6.2 shows the estimated flux density for Cas A, using both effective length models. Cas A reaches a minimum  $\theta$  of  $25^\circ$  at VLA-NA. Using IT/PEC clearly in better satisfies both

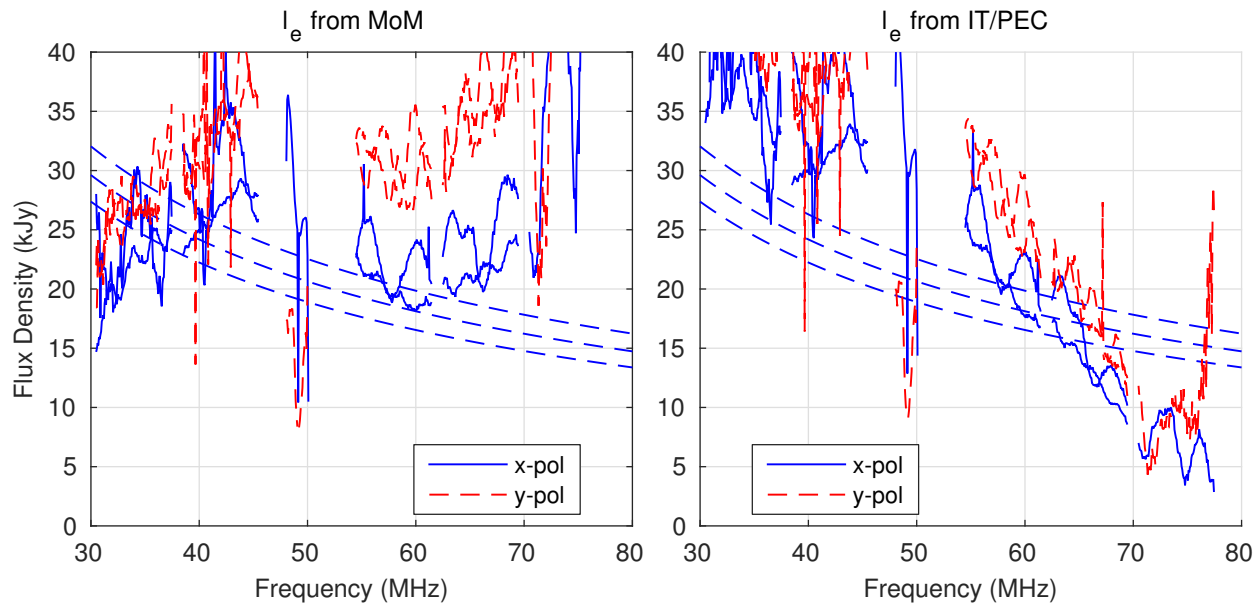


Figure 6.2: Flux density of Cas A, estimated with the effective length computed by (left) MoM and (right) IT/PEC. The dashed lines represent the Baars flux scale and associated error.

the power law and minimizes the difference between polarizations. Additionally, IT/PEC results in better agreement with the Baars flux scale.

Figure 6.3 shows the estimated flux density for Vir A, using both effective length models. Vir A reaches a minimum  $\theta$  of  $22^\circ$  at VLA-NA. IT/PEC clearly better satisfies both the power law criterion and minimizes the difference between polarization.

Figure 6.4 shows the estimated flux density for Tau A, using both effective length models. Tau A reaches a minimum  $\theta$  of  $12^\circ$  at VLA-NA. Neither estimate stands out as being better, perhaps due to the relative weakness of this source.

In summary, the MoM model is clearly a better choice for  $\theta < 20^\circ$ , and the IT/PEC model is a better choice for  $\theta > 20^\circ$ . Therefore, the flux density estimates reported in the next section were evaluated using IT/PEC for Cas A and Vir A since these sources are always below  $\theta = 20^\circ$  in our datasets. The MoM model is used for Tau A since it is always above  $\theta = 20^\circ$ . Similarly, the Cyg A flux density estimates were evaluated using the MoM model,

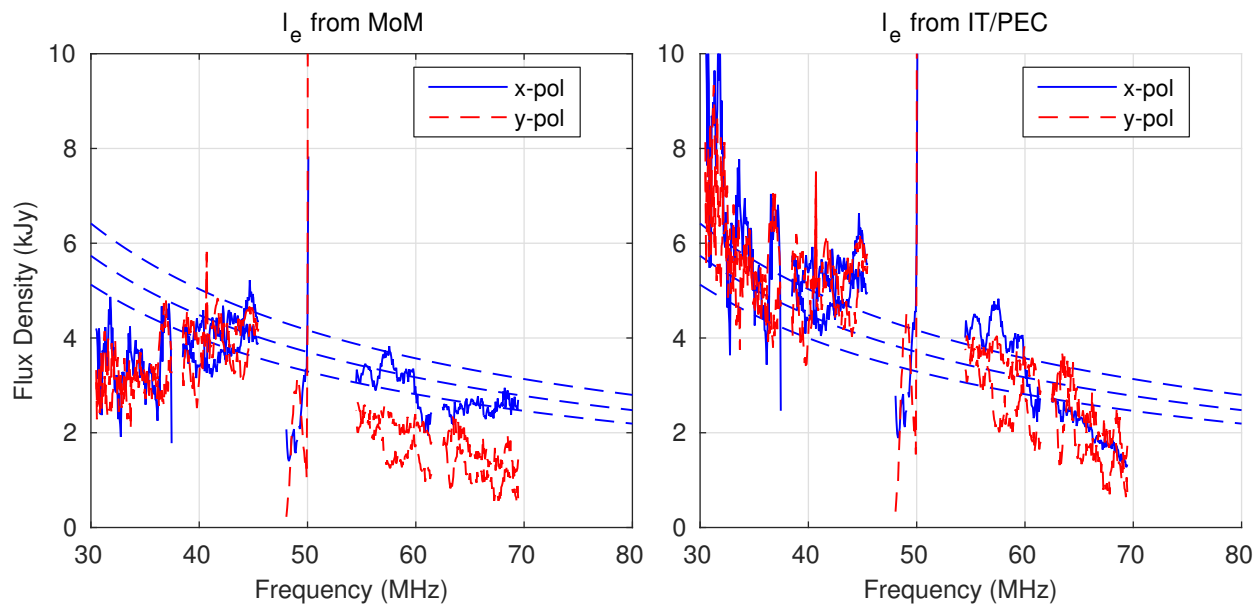


Figure 6.3: Flux density of Vir A, estimated with the effective length computed by (left) MoM and (right) IT/PEC. The dashed lines represent the Baars flux scale and associated error.

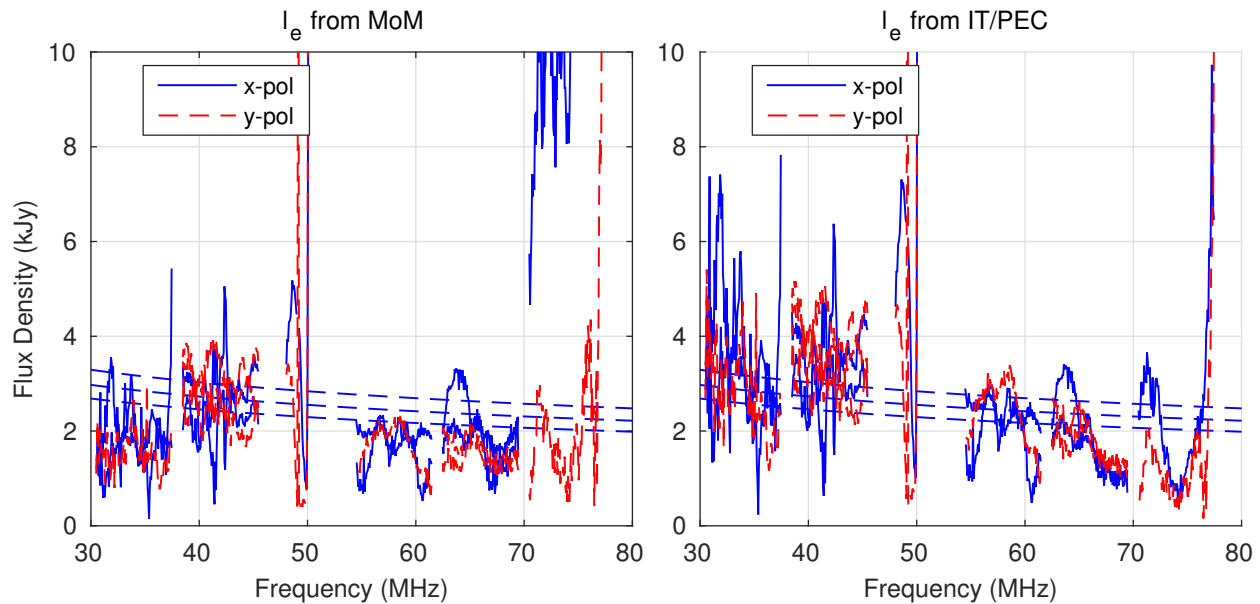


Figure 6.4: Flux density of Tau A, estimated with the effective length computed by (left) MoM and (right) IT/PEC. The dashed lines represent the Baars flux scale and associated error.

with the exception of one dataset (OBS5) for which  $\theta \geq 30^\circ$ , and so is evaluated using IT/PEC.

The difference between flux density estimates from the two effective length models considered in this section is large, despite the close agreement between the two models (see Figs. 3.6 and 3.7). This is due to the fact that the flux density estimate is proportional to  $l_e^2$ , and is therefore sensitive to small changes in  $l_e$ . It may be possible to further improve the results presented in this work by employing a parametric model for  $l_e$ . Such a model could be calibrated *in situ* according to the same criteria used to evaluate the the IT/PEC and MoM models.

## 6.2 The Flux Density Estimates

This section presents the flux density estimates for each of the A-Team sources as follows. The results for Cyg A are presented in Section 6.2.1. Section 6.2.1 also provides some additional details about the data reduction process. The results for Cas A are presented in Section 6.2.2. The results for Tau A are presented in Section 6.2.3. The results for Vir A are presented in Section 6.2.4. We conclude this section with a summary of the results in Section 6.2.5.

### 6.2.1 Cyg A

Figure 6.5 shows the estimates of the flux density of Cyg A for observations identified in Table 4.4. We wish to obtain a single flux density estimate per frequency band, and its associated error. To facilitate this, we average the observations, as shown in Fig. 6.6. A power law in the form of Eq. (1.2) is then fit to the data, separately per frequency band. The parameters of the power law are determined by the method of least squares. Figure 6.6 shows the resulting fits. The spectral index implied by this fit is certainly dominated by

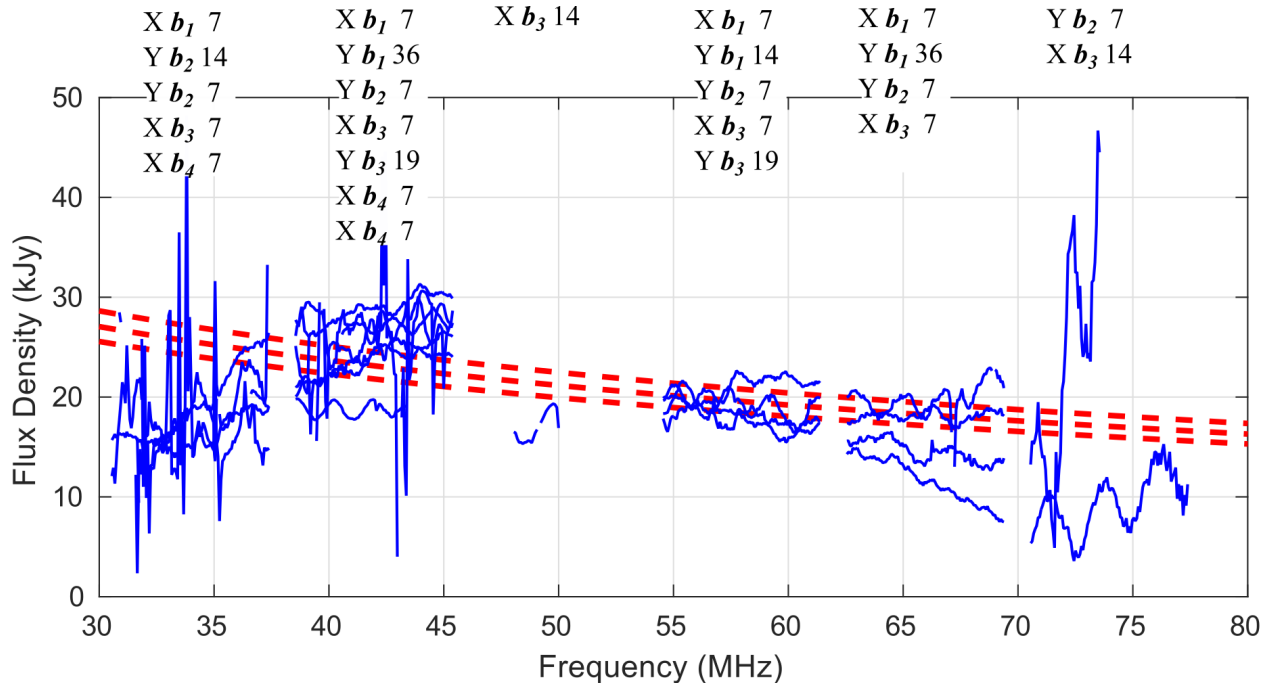


Figure 6.5: Flux density estimate for every available each observation of Cyg A. The text above each frequency band lists the polarization, baseline, and  $\theta$  in degrees at the middle of each observation. The dashed lines represent the Baars flux scale and its associated error.

instrumental/calibration error, and should not be interpreted as physical; that is, associated with the source.

The flux density estimate is then taken to be the center point of the fit in each band. The error is estimated as the root-mean-square difference from each point in Fig. 6.5 to the fit in Fig. 6.6. Figure 6.7 shows the final flux density estimate of Cyg A.

We consider the Band 2, 4, and 5 results to be valid without reservation. The results in these bands are consistent with the Baars flux scale, and suggest a possibly larger (more negative) spectral index than predicted by Baars. The Band 3 result is also considered valid without reservation. However, the limited number of observations in this frequency band results in an artificially small estimate of the error. More data would be required in Band 3 to increase confidence in the result. Band 1 is considered valid, but is expected to be biased toward a lower estimated flux density (see Section 5.4); this is what is observed in Fig. 6.7.

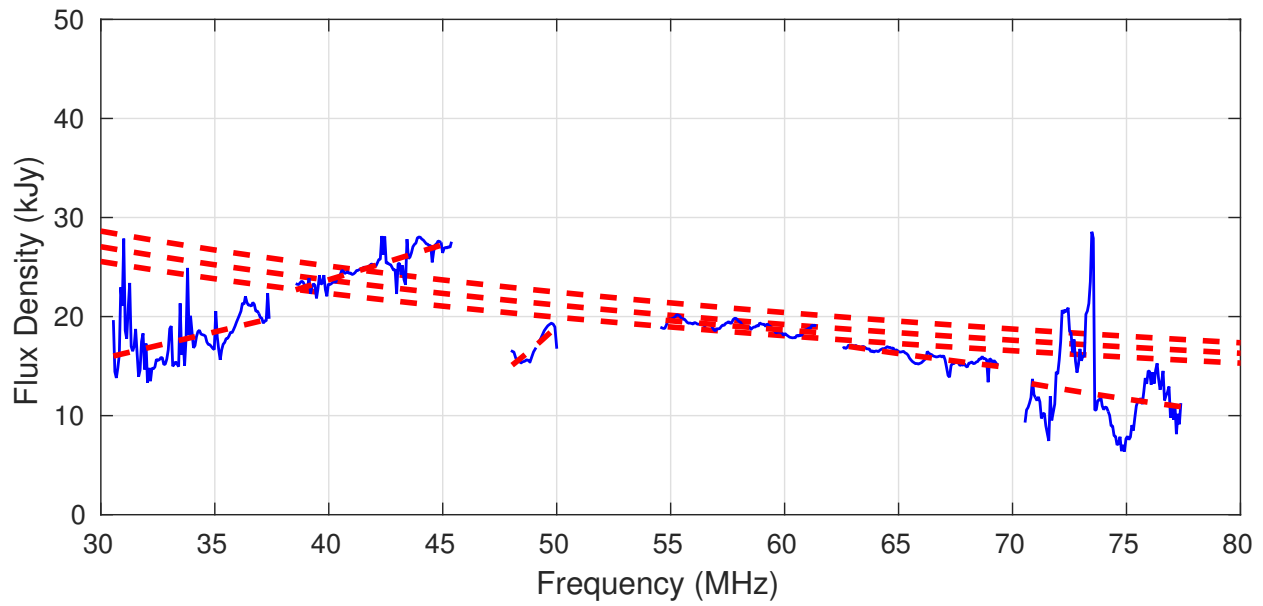


Figure 6.6: Average of the observations shown in Fig. 6.5. Per-band power law fits are shown as dashed lines. The dashed lines represent the Baars flux scale and its associated error.

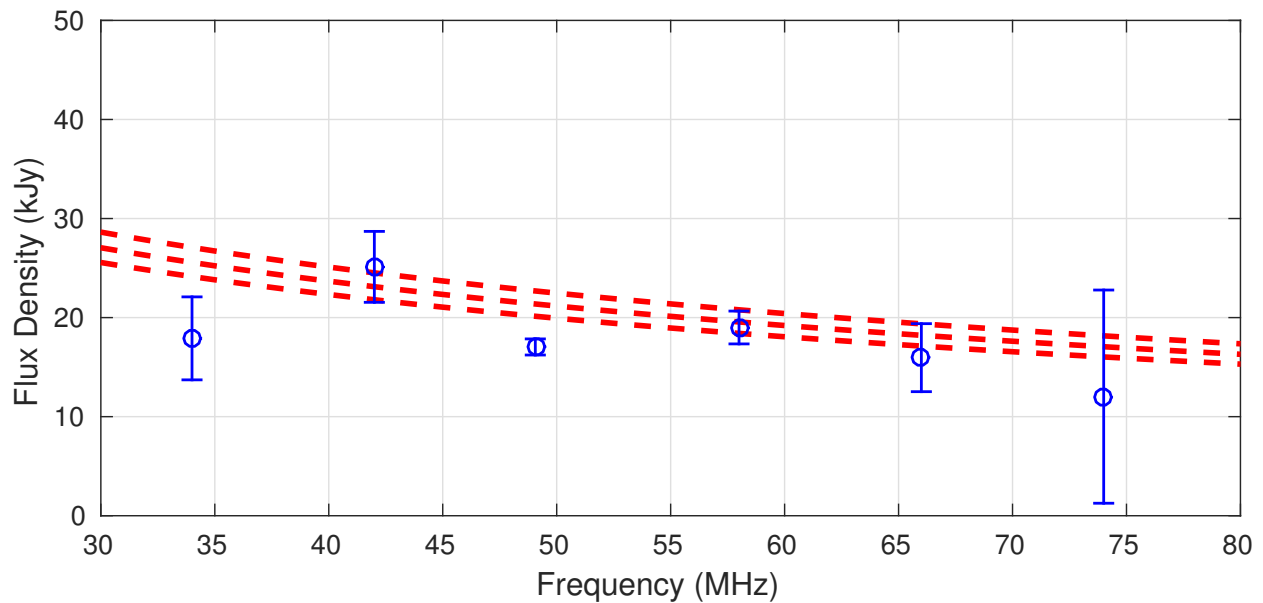


Figure 6.7: Final flux density of Cyg A. The circles indicate the nominal values; the error bars indicate the  $1\sigma$  uncertainty. The dashed lines represent the Baars flux scale and its associated error.

The Band 6 result is expected to exhibit a relatively large error (see Section 5.2). This is what is observed in Fig. 6.7.

Overall, our results are not significantly different or better than the expectations from the Baars flux scale. Thus, the principal achievement here is three additional points between the existing 38 MHz and 81 MHz measurements (see Fig. 1.7) which were used to determine the Baars flux scale.

### 6.2.2 Cas A

Figure 6.8 shows the estimates of the flux density of Cas A for observations identified in Table 4.5. Figure 6.9 shows the average of the observations, and the resulting power law fit in each frequency band. Figure 6.10 shows the final flux density estimates for Cas A, and the associated error.

These results indicate a spectral bias which is much larger than the uncertainty of the existing measurements. This bias results in a spectral index that is apparently much more negative than seems plausible given the Baars flux scale or its constituent measurements (particularly those at 38 MHz and 81 MHz; see Fig. 1.7). Comparing results for the four sources, we note this spectral bias also appears (albeit to a lesser extent) in the Vir A measurements (Fig. 6.16). These data have the common feature that they are taken while the source is at relatively low elevations;  $\theta > 22^\circ$  for all observations. This suggests the antenna pattern determined by IT/PEC, despite being superior to MoM in this elevation range (as demonstrated in Section 6.1), is nevertheless not sufficiently accurate. An improved antenna pattern model applied to the same data may be sufficient to eliminate the spectral bias and yield valid estimates.

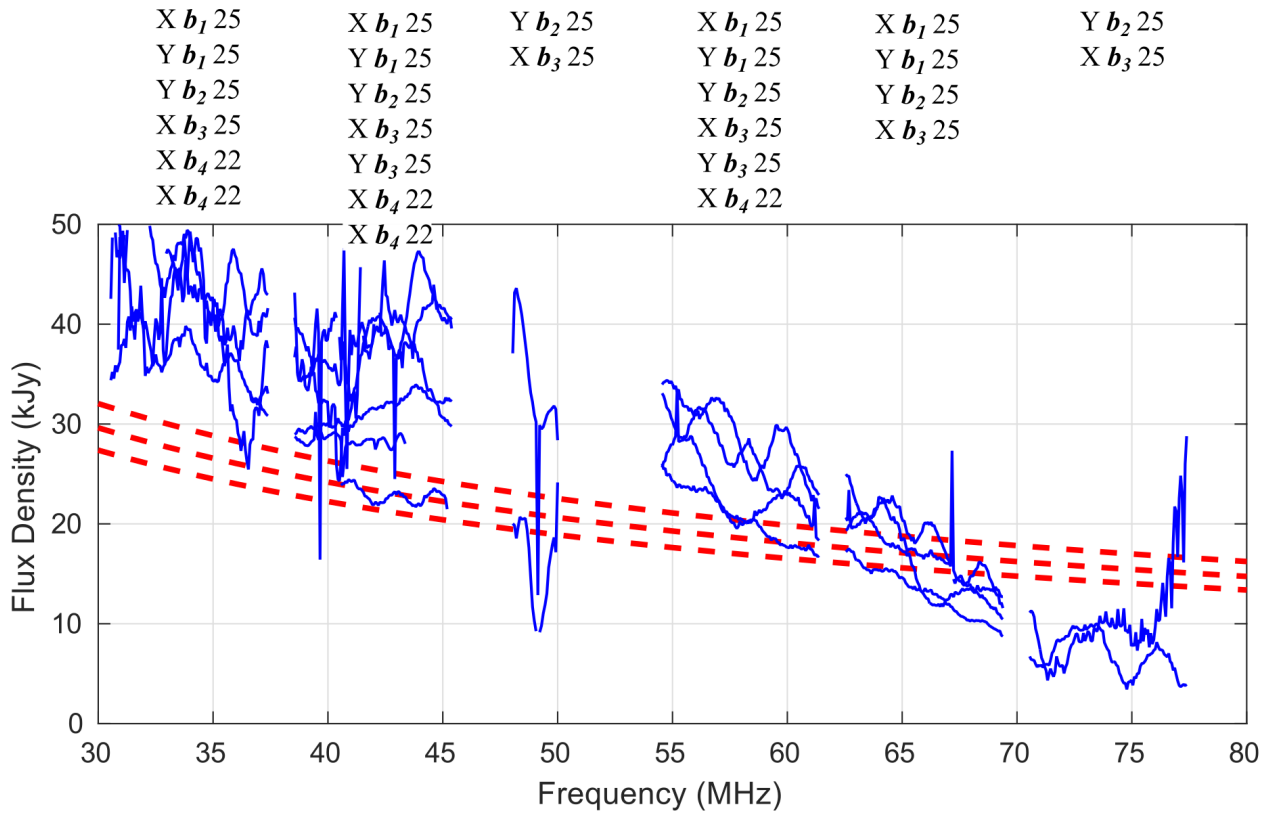


Figure 6.8: Same as Fig. 6.5, but now for Cas A.

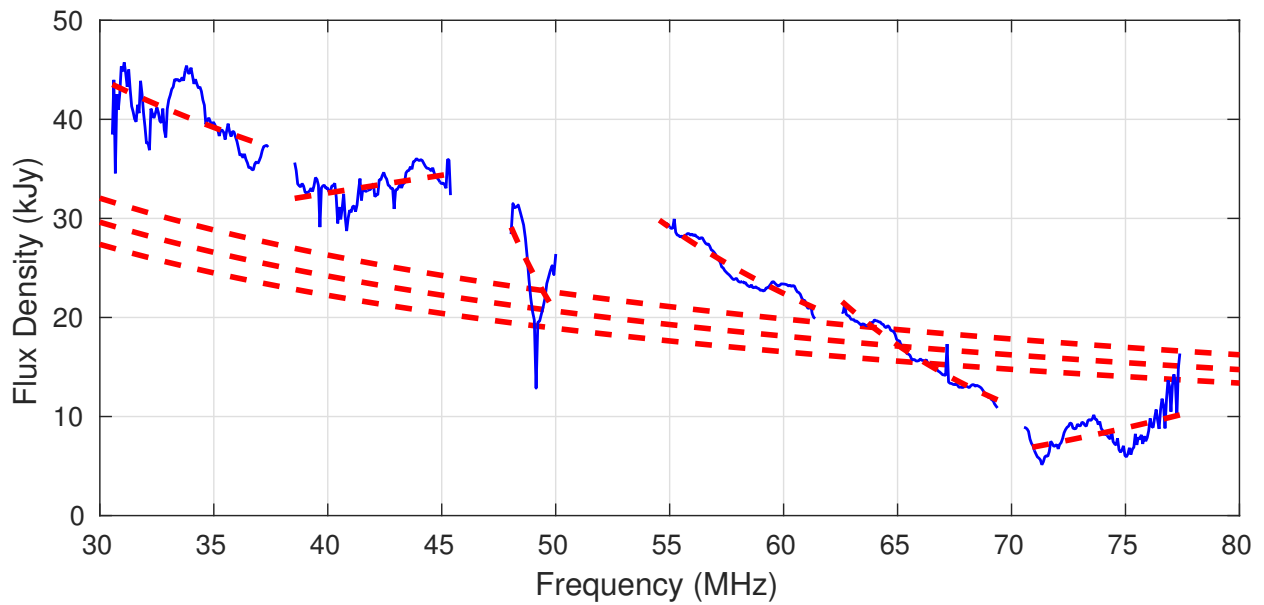


Figure 6.9: Same as Fig. 6.6, but now for Cas A.

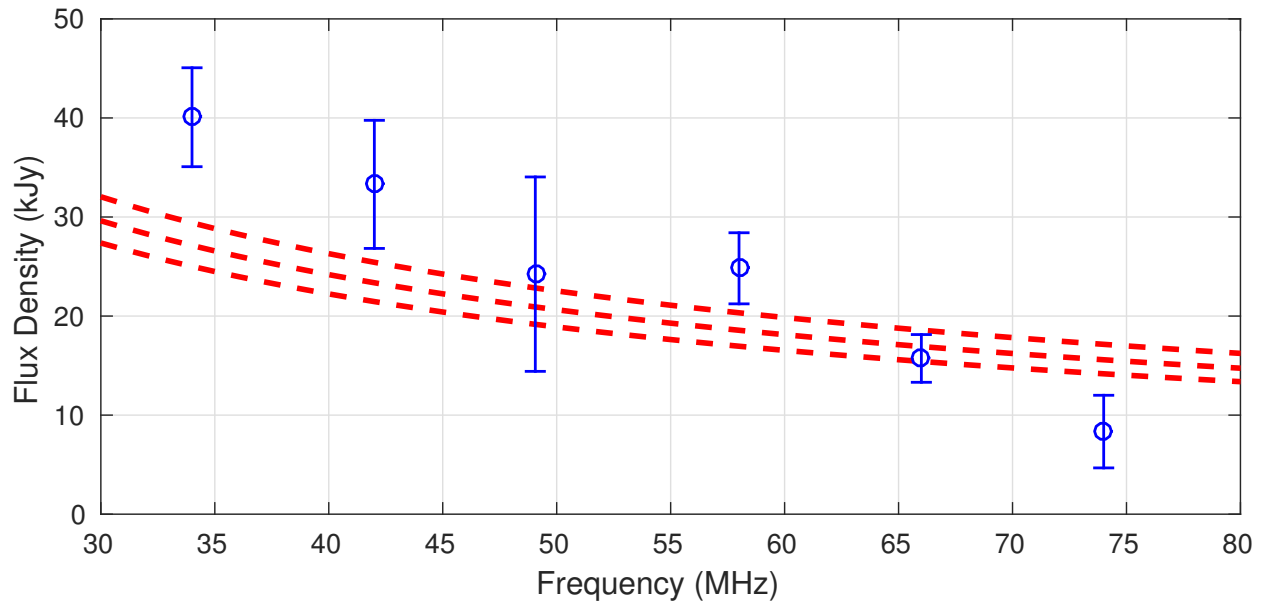


Figure 6.10: Same as Fig. 6.7, but now for Cas A.

### 6.2.3 Tau A

Figure 6.11 shows the estimates of the flux density of Tau A for observations identified in Table 4.7. Figure 6.12 shows the average of the observations, and the resulting power law fit in each frequency band. Figure 6.13 shows the final flux density estimates for Tau A, and the associated uncertainty.

As was the case with Cyg A, the Band 2, 4, and 5 results are considered valid without reservation. The Band 1 result is also considered valid, but exhibits the same bias towards a lower flux density seen in the Band 1 estimate for Cyg A. The Band 3 measurements for this source have been affected by a high amount of interference, resulting in a large error. The Band 6 estimate is expected, and is observed, to have a large error.

### 6.2.4 Vir A

Figure 6.14 shows the estimates of the flux density of Vir A for observations identified in Table 4.6. Figure 6.15 shows the average of the observations, and the resulting power law



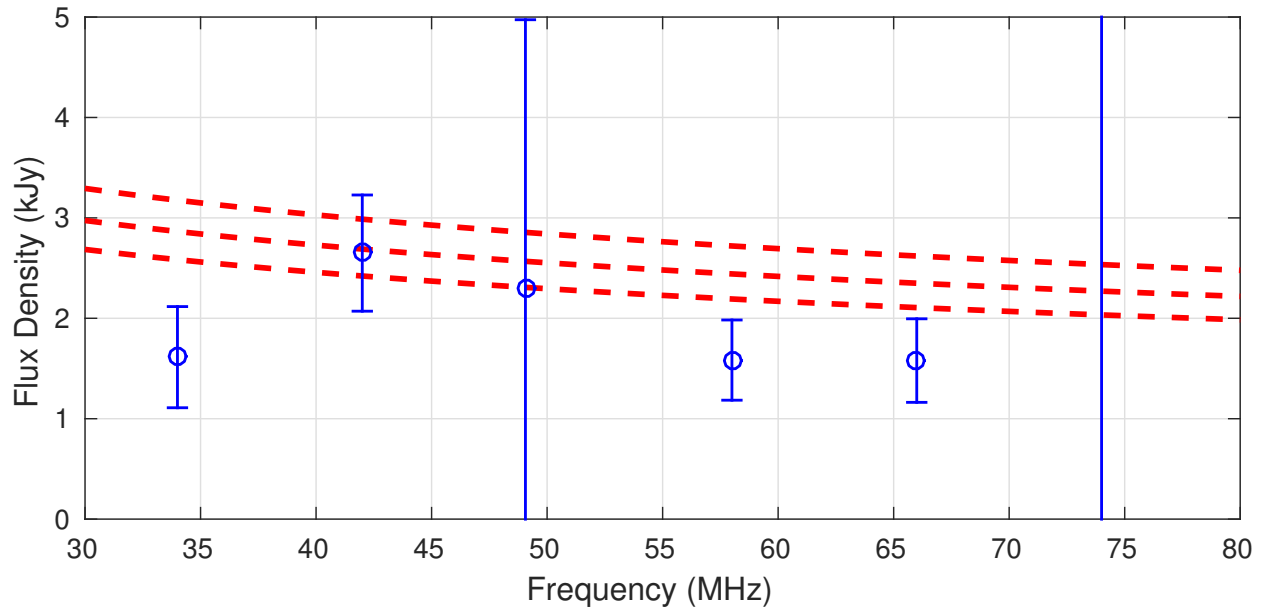


Figure 6.13: Same as Fig. 6.7, but now for Tau A.

fit in each frequency band. Figure 6.16 shows the final flux density estimates for Vir A, and the associated uncertainty.

These results exhibit a similar spectral bias seen in the Cas A results, although to a lesser extent. This is again attributed to the IT/PEC antenna pattern model. In spite of this apparent bias, the results in all bands is consistent with the Baars flux scale. There are no comparable results for Vir A in this frequency range. Therefore, these estimates provide additional confidence of the Baars flux scale in this frequency range for Vir A.

### 6.2.5 Summary of the Flux Density Estimates

Table 6.1 lists the flux density estimates of the A-Team sources, and the associated uncertainty, determined by this work. Figure 1.7 shows these results combined with the past measurements that were used in the Baars flux scale. We only show the estimates we believe to be valid without reservation, i.e. we have excluded the Band 6 data points.

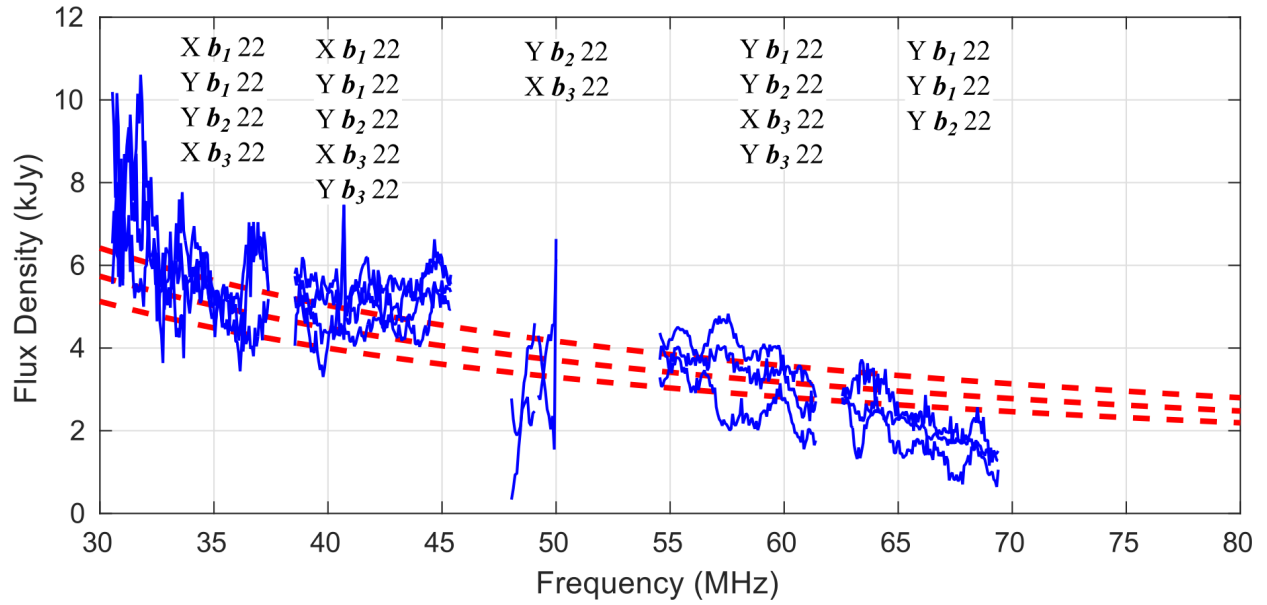


Figure 6.14: Same as Fig. 6.5, but now for Vir A.

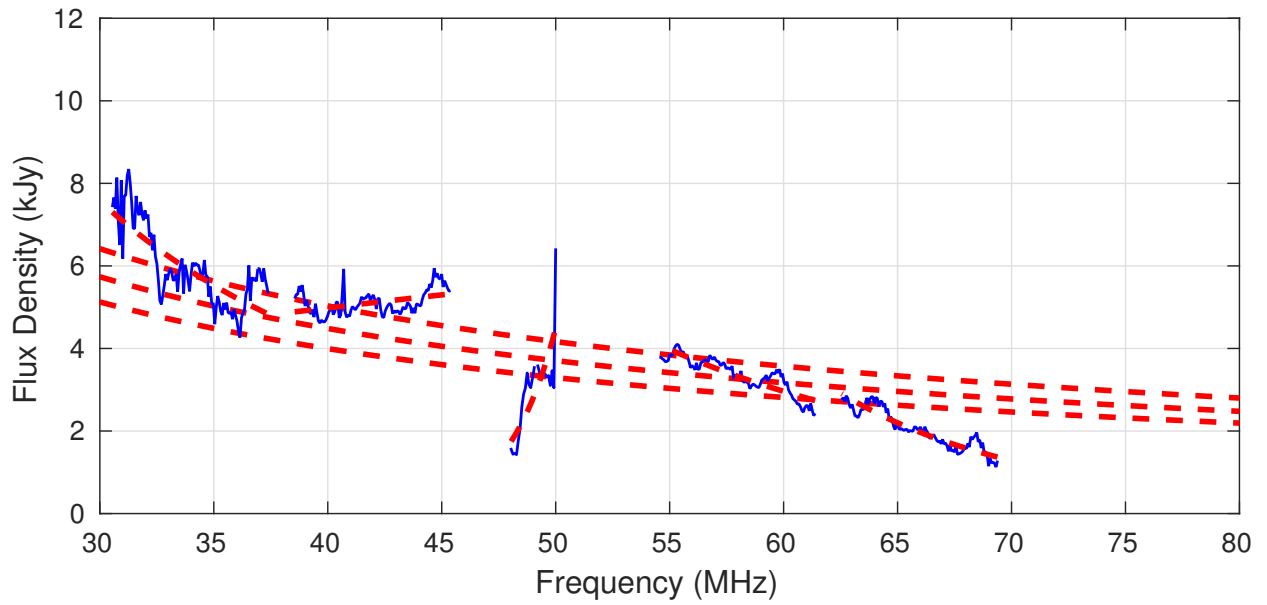


Figure 6.15: Same as Fig. 6.6, but now for Vir A.

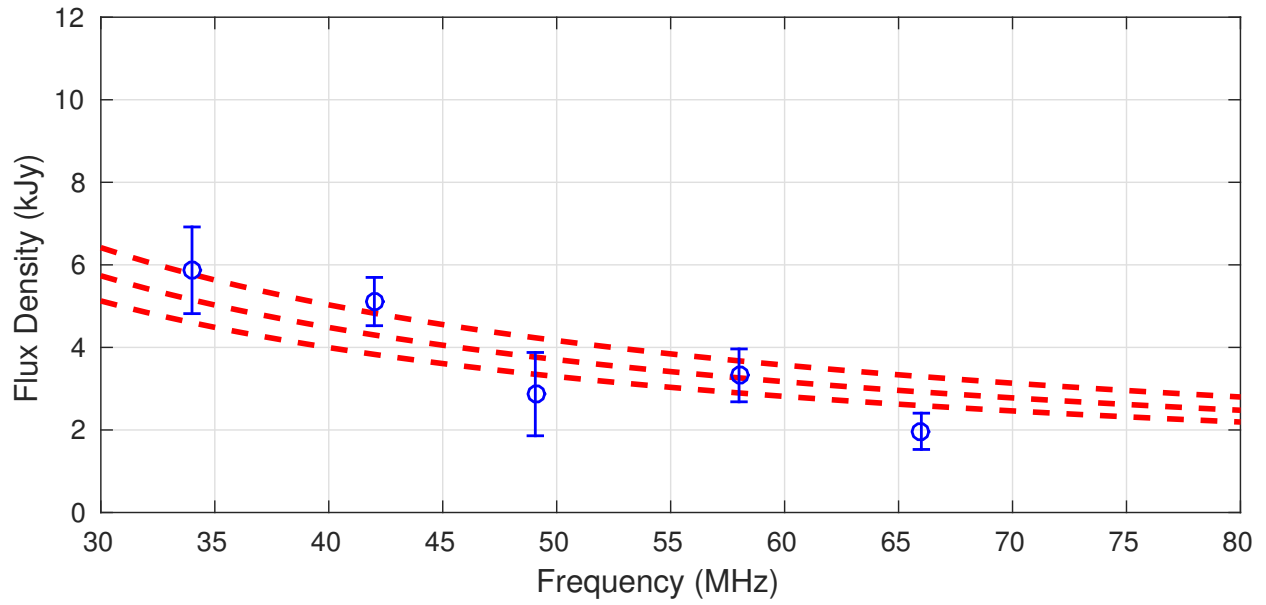


Figure 6.16: Same as Fig. 6.7, but now for Vir A.

Table 6.1: Summary of new flux density estimates for the A-Team sources.

$\nu$ MHz	Cyg A		Cas A		Tau A		Vir A	
	kJy	$1\sigma$	kJy	$1\sigma$	kJy	$1\sigma$	kJy	$1\sigma$
34	18.5	24%	40.2	12%	1.7	34%	5.9	18%
42	26.1	12%	35.9	13%	2.7	22%	5.1	12%
49	17.0	5%	24.2	41%	2.3	117%	2.9	35%
58	19.9	7%	24.8	14%	1.7	25%	3.3	19%
66	17.0	24%	15.7	15%	1.7	27%	2.0	23%

## 6.3 Measurements of the Diffuse Sky Emission in 30–78 MHz

In this section, we report new measurements of the antenna temperature due to the diffuse Galactic emission,  $T_{sky}$ . As noted in Chapters 2 and 5, these are obtained as intermediate data products in the reduction of the source flux data reported in Section 6.2.

Figure 6.17 shows the estimate of  $T_{sky}$  from each of the observations collected at 19:00 LST. This was previously shown as Fig. 5.8. We wish to reduce this to one estimate per polarization for  $T_{sky}$  at 19:00 LST. Similar to the way we obtained the flux density estimates, we average the observations for each antenna separately. This is shown in Fig. 6.18. We then fit a power law to the estimate of  $T_{sky}$ , using the method of least squares simultaneously for all bands. Figure 6.19 shows the fit and the associated spectral index.

The above process was repeated for 23:30, 04:30, and 11:30 LST, and the results are shown in Figs. 6.20, 6.21, and 6.22, respectively. In each figure, the result is compared to the expected  $T_{sky}$  from Eq. (2.1), using GSM for  $T(\theta, \phi)$  and  $P(\theta, \phi)$  derived from the IT/PEC model for  $l_e$ .

Table 6.2 summarizes the results in terms of the parameters of the fit. The spectral indices are seen to range from  $-2.15$  to  $-2.65$  depending on LST and polarization. This compares well to the spectral indices from the model (GSM+IT/PEC), which range from  $-2.21$  to  $-2.44$ . The absolute values are also consistent with the model, and exhibit the expected diurnal variation.

Table 6.3 shows the ratio of the parameters determined in this work to those obtained using the model, as well as the ratio of X-pol to Y-pol. Good agreement is seen between the measurement and the model. Differences are relatively small compared to those observed in the flux density estimates of Section 6.2. This provides further evidence that the antenna pattern is a limiting factor in the flux density measurements, as  $T_{sky}$  should be less sensitive

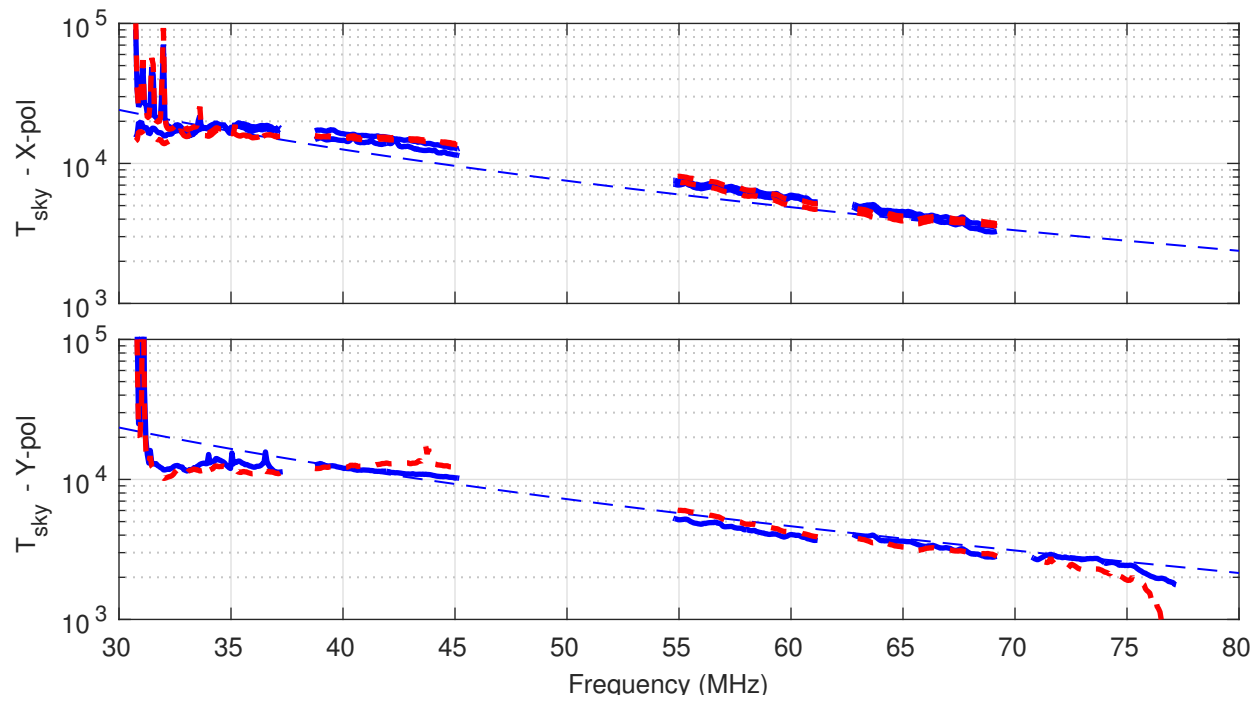


Figure 6.17: Estimate of  $T_{\text{sky}}$  for each observation at 19:00 LST.  $\Delta\nu = 65.1$  kHz,  $\Delta t = 20$  s.

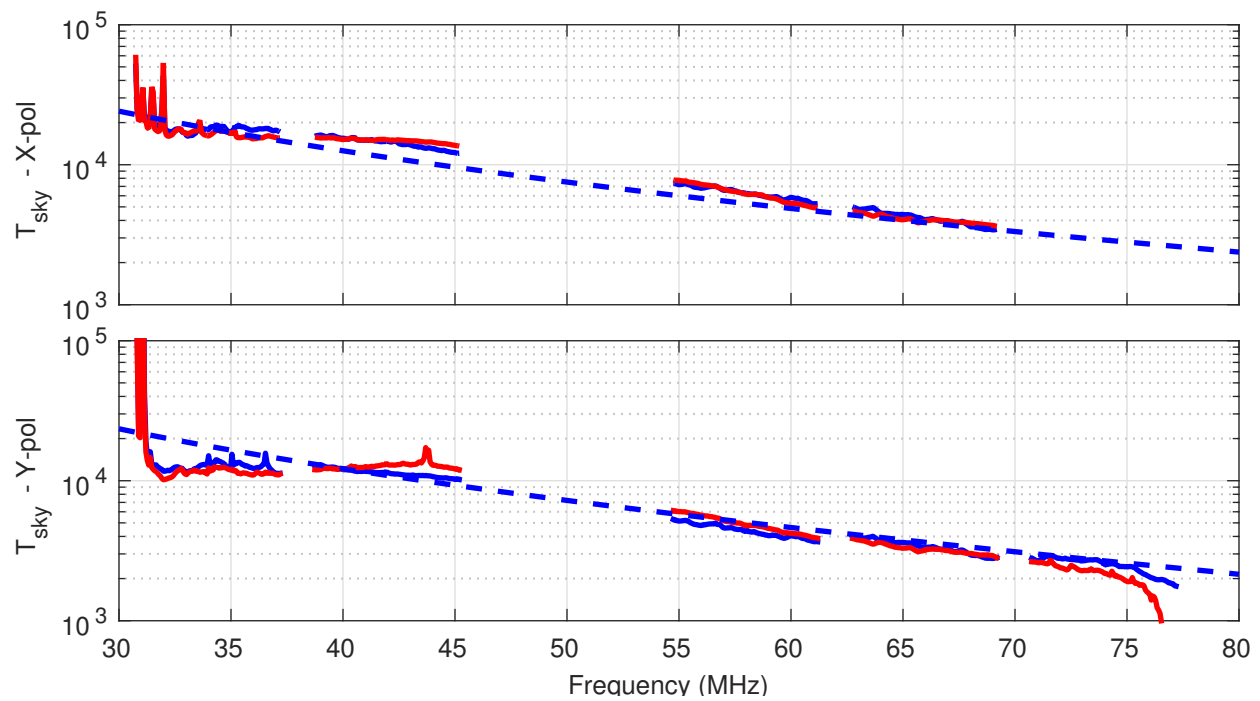


Figure 6.18: Average of the observations shown in Fig. 6.17.  $\Delta\nu = 65.1$  kHz,  $\Delta t = 20$  s.

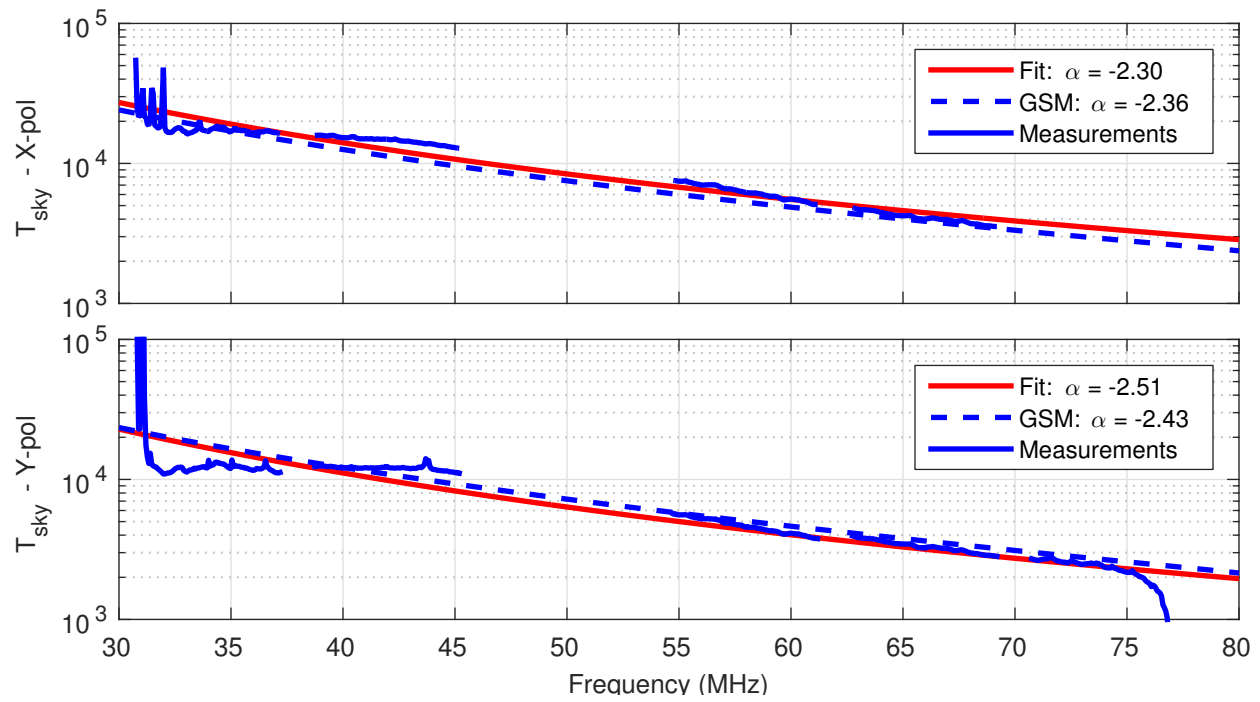


Figure 6.19: Final estimate of  $T_{sky}$  at 19:00 LST.  $\Delta\nu = 65.1$  kHz,  $\Delta t = 20$  s.

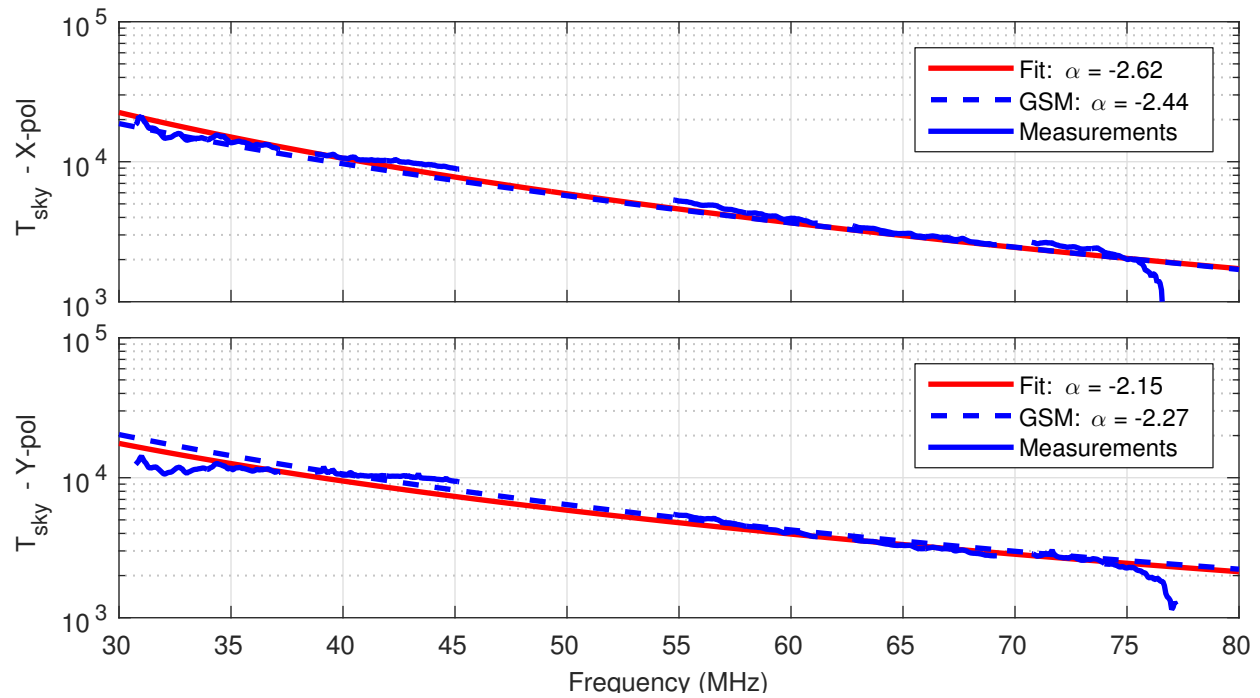


Figure 6.20: Final estimate of  $T_{sky}$  for 23:30 LST.  $\Delta\nu = 65.1$  kHz,  $\Delta t = 20$  s.

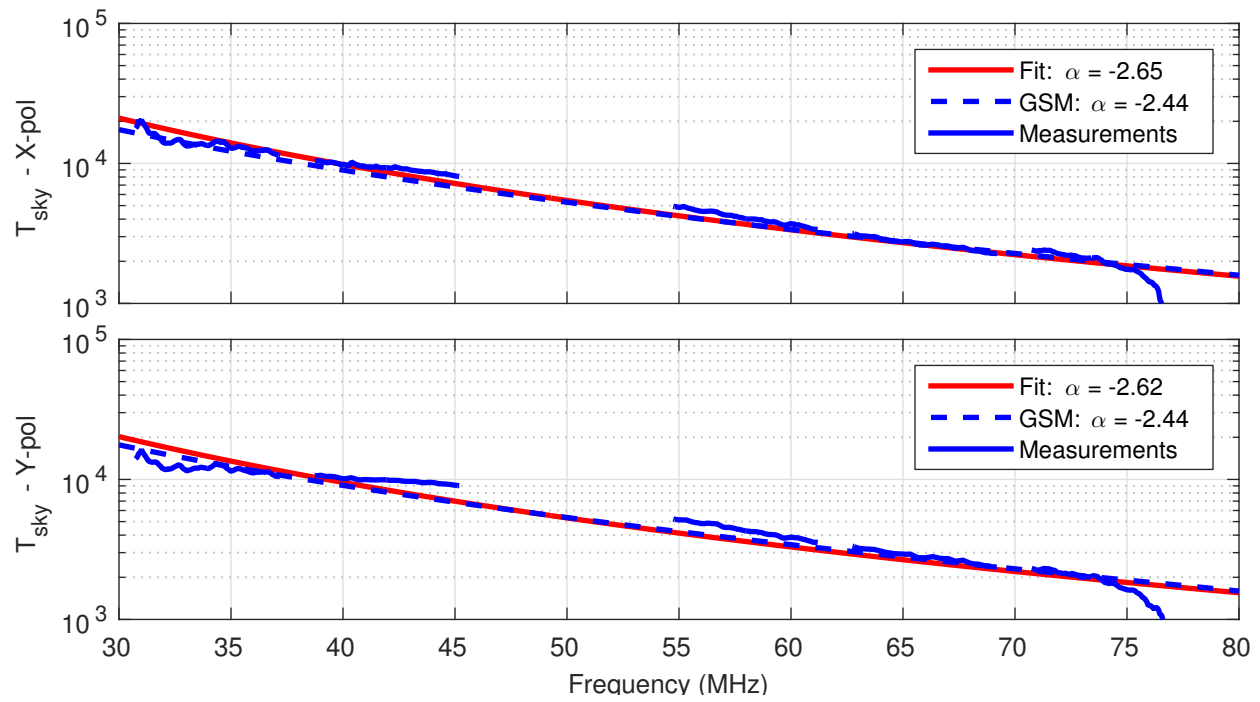


Figure 6.21: Final estimate of  $T_{sky}$  for 04:30 LST.  $\Delta\nu = 65.1$  kHz,  $\Delta t = 20$  s.

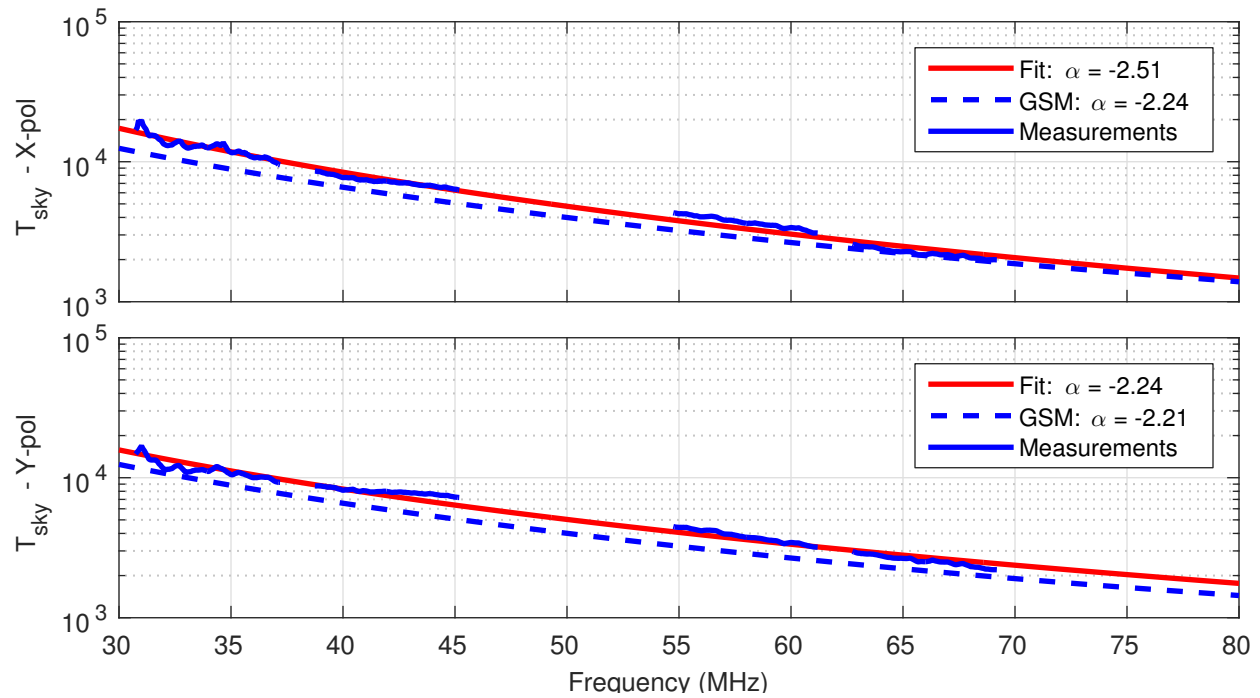


Figure 6.22: Final estimate of  $T_{sky}$  for 11:30 LST.  $\Delta\nu = 65.1$  kHz,  $\Delta t = 20$  s.

Table 6.2: Summary of the measurements of  $T_{sky}$ .  $T_{ref}$  is given for  $\nu_{ref} = 58$  MHz.

LST (HH:MM)	Measurement				GSM+IT/PEC			
	X-pol		Y-pol		X-pol		Y-pol	
	$T_{ref}$ (K)	$\alpha$	$T_{ref}$ (K)	$\alpha$	$T_{ref}$ (K)	$\alpha$	$T_{ref}$ (K)	$\alpha$
04:30	3671	-2.65	3600	-2.62	3622	-2.44	3661	-2.44
11:30	3311	-2.51	3612	-2.24	2861	-2.24	2895	-2.21
19:00	6267	-2.30	4560	-2.51	5230	-2.36	4943	-2.43
23:30	3999	-2.62	4257	-2.15	3908	-2.44	4588	-2.27

Table 6.3: Comparison between  $T_{sky}$  determined by this work to the model (GSM+IT/PEC)

LST (HH:MM)	Ratio of measurement to GSM+IT/PEC				Ratio of X-pol to Y-pol			
	X-pol		Y-pol		Measurement		GSM+IT/PEC	
	$T_{ref}$	$\alpha$	$T_{ref}$	$\alpha$	$T_{ref}$	$\alpha$	$T_{ref}$	$\alpha$
04:30	1.01	1.09	0.98	1.07	1.02	1.01	0.99	1.00
11:30	1.16	1.12	1.25	1.01	0.92	1.12	0.99	1.01
19:00	1.20	0.97	0.92	1.03	1.37	0.92	1.06	0.97
23:30	1.02	1.07	0.93	0.94	0.94	1.22	0.85	1.07

to the antenna pattern.

# Chapter 7

## Summary and Future Work

This dissertation presented new flux density measurements of the “A-Team” sources Cyg A, Cas A, Tau A, and Vir A at 34, 42, 49, 58, 66, and 74 MHz. We also presented new measurements of the antenna temperature associated with the diffuse Galactic background noise between 30–78 MHz. By carefully accounting for the mismatch between the antenna and the FEE, we were able to conduct these measurements with a single, thin, 45 MHz-resonant dipole antenna over a large ( $> 90\%$ ) bandwidth. We showed how the Galactic background may be used to precisely calibrate the antenna impedance and internal noise source *in situ*.

In this chapter we conclude this dissertation with a summary of the principal findings of this research (Section 7.1), and suggest future work (Section 7.2).

### 7.1 Findings

The principal findings of the research presented in this dissertation are:

1. *Additional Flux Density Measurements:* The new flux density measurements of the A-team sources between 30–70 MHz are the primary contribution of the research presented in this dissertation. The results are summarized in Fig. 1.7 and Table 6.1.

We have determined new flux density estimates at 34, 42, 49, 58, and 66 MHz. Most of these estimates do not significantly improve on the predictions of the existing Baars flux scale, and have comparable uncertainty. In the case of Vir A, we have obtained measurements which seem to validate Baars in this frequency range. This is significant because the Baars flux scale for Vir A uses no measurements below 400 MHz.

The principal limitation appears to be uncertainty in the antenna pattern. Once this is resolved (see Section 7.2.1), the existing data are likely to lead to significantly better estimates. In the meantime, the value of the new measurements is to confirm existing understanding of the flux densities in this range, which was previously constrained only by measurements above and below the frequencies considered here.

2. *Measurement of the Diffuse Galactic Emission:* New measurements of the antenna temperature associated with the diffuse Galactic emission between 30–78 MHz are summarized in Table 6.2. These measurements appear to be consistent with models of sky brightness at these frequencies and are useful due to the paucity of existing measurements. As noted in Section 1.2.2, this has applications in multiple disciplines, including 21 cm cosmology.
3. *Broadband Low Frequency Radiometry/Interferometry with Simple Antennas Exhibiting a Large Impedance Mismatch:* A new two-element interferometer, presented in Chapter 3, was developed to facilitate the flux density measurements. The antenna is a simple dipole to ease deployment to multiple sites and baselines, and to facilitate an accurate model for the antenna pattern. In Chapter 2, and summarized in Fig. 2.15, we developed methodology to effectively account for the impedance mismatch and to precisely calibrate the antenna impedance and internal noise source *in situ*. This subsequently allowed for precise radiometry (to estimate the contribution of the Galactic background to the antenna temperature) and interferometry (to estimate the flux density of discrete sources). These concepts may be employed in a wide range of other applications, such as 21 cm cosmology and spectrum sensing at sites subject to strong

out-of-band interference.

## 7.2 Suggested Future Work

### 7.2.1 Improved Flux Density Measurements of the A-Team Sources

The estimates presented in this work could be improved. Some suggestions for improvements are:

- *Improved Characterization of the Antenna Pattern:* As demonstrated in Section 6.1, small changes in the presumed effective length  $l_e$  result in large changes in the flux density estimates. This is believed to be the predominant source of error in the flux density estimates reported in this work. By improving the accuracy of the antenna pattern model, we expect these estimates, and the associated uncertainty, to improve greatly.

One way to improve the antenna pattern model would be to develop a parametric model for the pattern that interpolates between the IT/PEC and MoM models. The parameters of the model could then be adjusted to meet the same criteria used to evaluate the IT/PEC and MoM models in Section 6.1, i.e. that the resulting  $S_\nu^{src}$  agrees between polarizations and is well-modeled by a power law. Additional parameters would be required to address the poor performance of IT/PEC at low elevations.

- *Improved Source Isolation:* The flux density estimate from both the simulation in Section 2.4.2 and measurement processed in Chapter 5 exhibited a ripple due to the proximity of Cas A to Cyg A in the fringe rate domain. The fringe rate processing described in Section 2.4 might be improved to account for the presence of multiple sources which are nearby in the fringe rate domain. To do this, one might develop a parametric signal model including both Cyg A and Cas A, and then estimate the parameters from the data (e.g. with a maximum likelihood estimator).

- *Improve the In Situ Calibration:* In Section 5.2 we demonstrated a technique that used the properties of  $T_{sky}$  to calibrate the priors required to estimate  $T_{sky}$  and  $S_{\nu}^{src}$ . This technique was very effective above  $\sim 40$  MHz, but did not completely correct for the bias below  $\sim 35$  MHz. The measurements reported here could be improved by addressing this bias. It is possible that the revisions to the antenna model (see Section 2.6.1) could be modified based on some physical quantity not already accounted for. It is also possible that there is some frequency dependence in  $\Delta T_{cal}$  that accounts for this bias.
- *Improved RFI Mitigation:* The RFI mitigation technique described in Section 3.11 significantly improved the power spectrum (and correspondingly the  $T_{sky}$  estimates). However, the cross correlation (and correspondingly the flux density estimates) were not significantly improved. Data exhibiting a large amount of RFI were not included in the flux density estimates reported in this work. An improved understanding of the RFI in these data would allow for improved mitigation, allowing the inclusion of more data and thereby improving the estimates.
- *Collect Additional Data:* As noted above, improved measurements could be obtained from the data already collected. However, additional data would supplement the results in this work by improving the statistics, facilitating identification and exclusion of outliers, and improving the estimates and associated uncertainty. As discussed in Chapter 4, several measurements were planned (e.g. OBS3, OBS6) but not executed due to time constraints. Observations of Cyg A at times when the Sun is not present in the sky would mitigate the possibility of interference from the Sun. Additionally, collecting data when the sources are at different elevations could help diagnose the antenna pattern model.
- *Broadband Digitizer:* The data acquisition system was only able to observe at most 8.33 MHz of the 30–78 MHz frequency range of interest at a time. As a result, similar measurements (e.g. same polarization or baseline) were conducted over multiple days

to cover the entire frequency range. A broadband digitizer (such as the 196 MSPS digitizer used by LWA1) would decrease the amount of time required to cover the entire frequency range. This might also improve consistency of the measurements, since the entire spectrum would be observed simultaneously.

### 7.2.2 Other Applications of this Work

Aspects of this research have applications beyond the scope of radio astronomy. Some such applications include:

- *Spectrum Monitoring*: There is recent increased interest in applications that would benefit from wideband spectrum monitoring. We have demonstrated precise radiometry using electrically-small antennas with filtering to protect against out-of-band RFI, both in this work and in [57]. A similar technique could be applied to spectrum monitoring, with potential government and commercial applications.
- *In Situ Antenna Pattern Measurement*: Measurements to obtain antenna patterns in the HF/VHF range are complicated by the large distance to the far field, large antenna size, variable ground loss, and near-field scattering. Techniques for overcoming these challenges include flying a calibrated source over the antenna under test, and near-field measurements [58]. Unmanned aerial vehicles have recently been proposed (e.g. [59, 60]). Alternatively, the sources used in absolute flux density calibration could be employed for antenna measurements, as their positions are accurately known, they are always located in the far field, and they are wideband. Precise characterization and modeling of the antennas was required for the absolute flux density measurements, as explained in Section 2.3. However, the problem may be reversed; one may measure the characteristics of HF/VHF antennas using the same procedures. Precise flux density information would not necessarily be required; only the knowledge that the flux density is independent of the source's position.

- *Geolocation*: Usually the Global Positioning System (GPS) can be used to accurately determine location. However, there are many scenarios in which GPS is unavailable or unreliable. In such cases, backup solutions are needed. The radio sources of interest in this work present novel signals of opportunity for geolocation. In particular, the fringe rate of the A-Team sources may be used to perform geolocation. Work has begun on this concept and culminated in an initial paper [61].

# Appendix A

## A Note on the Galactic Background

In this appendix, we present a model for  $P^g$ , the uniformly bright component of the diffuse Galactic background noise. This component manifests as a “DC” offset in the cross correlation. The model derived in this Appendix was used in the example presented in Section 2.4.2.

The contribution of the Galactic background noise to the cross correlation, given by Eq. (2.22), is

$$P^g = \iint_{\Omega} |l_e(\psi)|^2 \frac{2\eta k}{\lambda^2} T(\psi) e^{j\beta \hat{\mathbf{r}}'(\psi) \cdot \mathbf{b}} d\Omega \quad (\text{A.1})$$

The “DC” contribution to the received fringe rate spectra is due to the all-sky portion of  $T(\psi)$ , which is essentially a uniform brightness distribution  $T(\psi) = T_0$ . Assuming two identical, isotropic,  $\hat{\mathbf{x}}$ -polarized antennas such that  $|l_e(\psi)|^2 = l_{e0}$ , (A.1) reduces to

$$P^g = \frac{2\eta k l_{e0}^2}{\lambda^2} T_0 \iint_{\Omega} e^{j\beta \hat{\mathbf{r}}'(\psi) \cdot \mathbf{b}} d\Omega \quad (\text{A.2})$$

Now, assuming an East-West baseline of length  $D$ ,  $\mathbf{b} = \hat{\mathbf{x}}D$  such that the phase of the integrand is  $\beta D \sin \theta \cos \phi$ . (In this coordinate system,  $\theta$  is the zenith angle and  $\phi$  is the

azimuth angle, measured east towards north.) For an East-West baseline

$$P^g = \frac{2\eta k l_{e0}^2}{\lambda^2} T_0 \int_{\theta=0}^{\pi} \sin \theta \int_{\phi=0}^{2\pi} e^{j\beta D \sin \theta \cos \phi} d\phi d\theta \quad (\text{A.3})$$

For the  $\phi$  integral we use the identity [62]:

$$J_n(z) = \frac{1}{2\pi} \int_{-\pi}^{\pi} e^{-j(z \sin v - nv)} dv \quad (\text{A.4})$$

where  $J_n(z)$  is the Bessel function of the first kind. The expression is now reduced to

$$P^g = \frac{4\pi\eta k l_{e0}^2}{\lambda^2} T_0 \int_0^{\pi} \sin \theta J_0(\beta D \sin \theta) d\theta \quad (\text{A.5})$$

For the  $\theta$  integral we use the identity [63]:

$$\int_0^{\pi} \sin(2\mu\theta) J_{2\nu}(2z \sin \theta) d\theta = \pi \sin(\mu\pi) J_{\nu+\mu}(z) J_{\nu-\mu}(z) \quad (\text{A.6})$$

with the result

$$P^g = \frac{4\pi^2\eta k l_{e0}^2}{\lambda^2} T_0 J_{1/2}(\beta D/2) J_{-1/2}(\beta D/2) \quad (\text{A.7})$$

This may be simplified by applying properties of the Bessel function as follows [63]:

$$\begin{aligned} P^g &= \frac{4\pi^2 k \eta l_{e0}^2}{\lambda^2} T_0 J_{1/2}(\beta D/2) J_{-1/2}(\beta D/2) \\ &= \frac{4\pi^2 k \eta l_{e0}^2}{\lambda^2} T_0 \frac{4}{\pi \beta D} \sin(\beta D/2) \cos(\beta D/2) \\ &= \frac{8\pi k \eta l_{e0}^2}{\lambda^2} T_0 \frac{\sin(\beta D)}{\beta D} \\ &= \frac{8\pi k \eta l_{e0}^2}{\lambda^2} T_0 \text{sinc}(\beta D) \end{aligned} \quad (\text{A.8})$$

where  $\text{sinc } x = \sin x/x$ .

Equation (A.8) provides a closed form expression for the contribution of the diffuse Galactic emission. Also note that Eq. (A.8) predicts a null in  $P^g$  when  $D$  is an integer multiples of

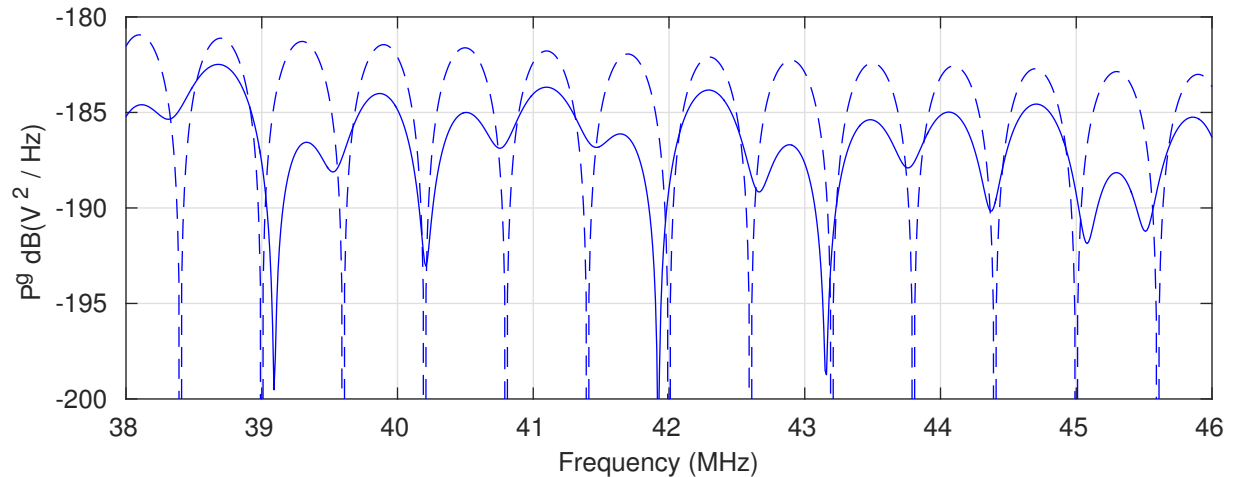


Figure A.1: Contribution of the Galactic background radiation to the cross correlation. The dashed line is Eq. (A.8). The solid line is the result of the numerical integration of Eq. (A.1) using the realistic (non-uniform) sky temperature distribution discussed in Section 2.2.

$\lambda/2$ .

As an example, Fig. A.1 shows  $P^g$  for  $D = 250$  m over Band 2 (see Section 3.8). In this example,  $T_0$  is determined by Eq. (2.2), and  $l_e = 1$  m. Despite the assumption of isotropic antennas, this result agrees well with the  $x$ -baseline result in Fig. 1 of [64], which used half-wavelength dipoles.

Also shown in Fig. A.1 is Eq. (A.1) computed using the sky brightness distribution shown in Fig. 1.3. Both exhibit the same periodic nulls. The difference between the two is due to the sky noise not being completely uniform, resulting in more complex behavior in  $P^g$ .

The periodic nulling effect can be seen in Fig. 2.9, but is not readily observed in field measurements (see e.g. Fig. 5.9). This is due to internal cross talk between signal paths, which tends to dilute the effect.

# Appendix B

## Conversion from Celestial Equatorial Coordinates to Local Azimuth and Elevation

In this appendix we present the transformation between the different coordinates used in the system model presented in Chapter 2. The coordinates of celestial objects are typically given in equatorial coordinates. However, the interferometer coordinates are known in the local Cartesian coordinates, and the antenna pattern is characterized using the local spherical coordinates.

The conversion from equatorial coordinates, given in right ascension  $\alpha$  and declination  $\delta$ , to azimuth  $\mathcal{A}$  and elevation  $\mathcal{E}$  is [65, Chapter 4]

$$\mathcal{E} = \sin^{-1}(\sin \mathcal{L} \sin \delta + \cos \mathcal{L} \cos \delta \cos H) \quad (\text{B.1})$$

$$\mathcal{A} = \tan^{-1}\left(\frac{\sin H}{\cos H \sin \mathcal{L} - \tan \delta \cos \mathcal{L}}\right) \quad (\text{B.2})$$

where  $\mathcal{A}$  is measured from north towards east,  $\mathcal{L}$  is the local latitude, and

$$H = t - \alpha \tag{B.3}$$

is the source's hour angle at local sidereal time  $t$ .

# Appendix C

## Taylor Series Approximation of the Geometric Delay

In this appendix, we consider the approximation of the geometric delay  $\tau_g$  as a Taylor series, as proposed in Section 2.4. The objective of this approximation is to: (a) Evaluate the maximum integration time  $\Delta t$  over which the fringe rate  $f_g$  changes by less than 1%, and (b) Evaluate the longest observation time  $T$  over which the fringe rate is accurately modeled by a 3<sup>rd</sup>-order Taylor series.

For a baseline  $\mathbf{b} = \hat{\mathbf{x}}b_x + \hat{\mathbf{y}}b_y$  at a latitude  $\mathcal{L}$ ,  $\tau_g$  is (see e.g. [65])

$$\tau_g(t) = -\frac{b_x}{c} \cos \delta \sin H(t) + \frac{b_y}{c} \left( \cos \mathcal{L} \sin \delta - \sin \mathcal{L} \cos \delta \cos H(t) \right) \quad (\text{C.1})$$

where  $\delta$  and  $H(t)$  are the source's declination and hour angle, respectively. The Taylor series expansion of the delay around  $t = t_0$  is

$$\tau_g(t) = \tau_g(t_0) + \tau_g'(t_0)(t - t_0) + \frac{1}{2}\tau_g''(t_0)(t - t_0)^2 + \frac{1}{6}\tau_g'''(t_0)(t - t_0)^3 + \dots \quad (\text{C.2})$$

where a prime indicates a derivative with respect to time. For later convenience, we compute

$$\tau'_g(t_0) = -\omega_E \cos \delta \left[ \frac{b_x}{c} \cos H - \frac{b_y}{c} \sin \mathcal{L} \sin H \right] \quad (\text{C.3})$$

$$\tau''_g(t_0) = \omega_E^2 \cos \delta \left[ \frac{b_x}{c} \sin H + \frac{b_y}{c} \sin \mathcal{L} \cos H \right] \quad (\text{C.4})$$

$$\tau'''_g(t_0) = \omega_E^3 \cos \delta \left[ \frac{b_x}{c} \cos H - \frac{b_y}{c} \sin \mathcal{L} \sin H \right] \quad (\text{C.5})$$

where  $dH/dt = \omega_E \cong 2\pi/(24 \times 3600) \approx 7.27 \times 10^{-5}$  rad/s is the rate of rotation of the earth.

To determine the maximum integration time, we let  $\Delta t = t - t_0$ . Now consider the factor  $\tau'_g(t_0)$ . This factor is upper-bounded by  $\omega_e D/c = 7.27 \times 10^{-11}$  s/s for a  $D = 300$  m baseline. Thus,  $\tau'_g(t_0)$  becomes significant at the 1% level, relative to  $\tau_g(t_0)$ , for integration times  $\Delta t > 137$  s. The third term in the expansion becomes significant at the 1% level only for integration times greater by orders of magnitude [66]. Therefore,  $\Delta t$  should be less than 137 s. An integration time of 60 s is used to obtain the estimates presented in Chapter 5, and is well within this limit.

Now, we show that  $f_g$  may be modeled by a 3<sup>rd</sup>-order polynomial. We claim four terms of Eq. (C.2) are sufficient to model  $\tau_g(t)$  for 2-hour observations. Under this assumption

$$\tau_g(t) \cong \tau_g(t_0) + \left( \tau'_g(t_0) + \frac{1}{2}\tau''_g(t_0)T + \frac{1}{6}\tau'''_g(t_0)T^2 + \frac{1}{24}\tau''''_g(t_0)T^3 \right) T \quad (\text{C.6})$$

where  $T = t - t_0$  is now the observation time. The third term in the parenthesis  $1/6\tau'''_g(t_0)T^2$  becomes significant to 1% compared to the first term  $\tau'_g(t_0)$  for  $T > 3368$  s. The fourth term of the expansion,  $1/24\tau''''_g(t_0)T^3$ , becomes significant to 1% compared to the first term for  $T > 8546$  s. This is much less than the observation time of 7200 s used to obtain the estimates presented in Chapter 5. Thus the delay is well approximated by

$$\tau_g(t) \cong \tau_g(t_0) - \frac{1}{\nu} f_g(t)t \quad (\text{C.7})$$

where

$$f_g(t) = \nu (c_0 + c_1 t + c_2 t^2) \tag{C.8}$$

is the fringe rate of the source, and

$$c_0 = -\tau'_g(t_0) \tag{C.9a}$$

$$c_1 = -\frac{1}{2}\tau''_g(t_0) \tag{C.9b}$$

$$c_2 = -\frac{1}{6}\tau'''_g(t_0) \tag{C.9c}$$

# Appendix D

## Derivation of Equations Used in the Receiver Calibration

The Antenna Temperature Model (ATM) presented in Section 2.5 is used to perform receiver calibration (i.e. to determine the receiver transducer power gain (TPG)  $G_R$  and noise temperature  $T_R$ ). Use of the ATM requires characterization of

- The gain of parasitic impedance,  $G_p$ .
- The relationship of  $G_R$  for different source impedances.
- The relationship of  $T_R$  for different source impedances.

This appendix presents the derivation of expressions for these quantities and relationships.

### D.1 Available Gain of the Parasitic Impedance

As described in Section 2.3, there is a parasitic impedance  $Z_p$  at the interface between the antenna and the front end electronics (FEE). Per the ATM, the effect of the parasitic

impedance is described by its available power gain  $G_p$ .  $G_p$  is defined as the ratio of the power spectral density (PSD) available from the antenna after  $Z_p$  to the PSD available from the antenna before  $Z_p$ . Here, we derive  $G_p$ .

Considering Fig. 2.5, the PSD available from the antenna is

$$S_A = \frac{\langle |v_A(t)|^2 \rangle}{4R_A} \quad (\text{D.1})$$

From circuit theory, the PSD delivered to the receiver is

$$S_R = \langle |v_A|^2 \rangle \left| \frac{Z_p || Z_R}{Z_A + Z_p || Z_R} \right|^2 \frac{R_R}{|Z_R|^2} \quad (\text{D.2})$$

The ratio of  $S_R$  to  $S_A$  is in general (i.e. for any terminating impedance  $Z_R$ )

$$\frac{S_R}{S_A} = \frac{4R_A R_R}{|Z_R|^2} \left| \frac{Z_p || Z_R}{Z_A + Z_p || Z_R} \right|^2 \quad (\text{D.3})$$

The *available* power gain  $G_p$  is obtained by evaluating Eq. (D.3) with  $Z_R = (Z_A || Z_p)^*$ :

$$G_p = \frac{4R_A R'_A}{|Z'_A|^2} \left| \frac{Z_p || (Z'_A)^*}{Z_A + Z_p || (Z'_A)^*} \right|^2 \quad (\text{D.4})$$

where  $Z'_A = R'_A + jX'_A = Z_A || Z_p$ .

## D.2 Recalculation of Transducer Power Gain for Different Source Impedances

The ATM is used to determine the TPG  $G_R(Z_{cal})$ , i.e. the TPG of the receiver for a source impedance of  $Z_{cal}$ . However, combination of the antenna and parasitic impedance present an impedance  $Z'_A = Z_A || Z_p$  to the receiver, and it is  $G_R(Z'_A)$  that is required to estimate the source flux density. Here, we derive the relationship between  $G_R(Z_{cal})$  and  $G_R(Z'_A)$  to

facilitate the necessary conversion.

To convert from  $G_R(Z_{cal})$  to  $G_R(Z'_A)$ , we invoke the theory of scattering ( $s$ ) parameters (see e.g. [67]). We assume the receiver is unilateral<sup>1</sup> such that

$$G_R(Z_{cal}) = \frac{1 - |\Gamma_{cal}|^2}{|1 - s_{11}\Gamma_{cal}|^2} |s_{21}|^2 \frac{1 - |\Gamma_L|^2}{|1 - s_{22}\Gamma_L|^2} \quad (D.5)$$

where

$$s_{11} = \frac{Z_R/2 - Z_0}{Z_R/2 + Z_0} \quad (D.6)$$

$$\Gamma_{cal} = \frac{Z_{cal}/2 - Z_0}{Z_{cal}/2 + Z_0} \quad (D.7)$$

$$\Gamma_L = \frac{Z_L - Z_0}{Z_L + Z_0} \quad (D.8)$$

and  $Z_L$  is the input impedance of the digital receiver. In  $s_{11}$ ,  $Z_R$  is divided by 2 to account for the fact that it is differential, whereas the  $s$ -parameters and associated reference impedance  $Z_0$  is single-ended. The same is true for  $Z_{cal}$  in  $\Gamma_S$ . For  $G_R(Z'_A)$ ,

$$G_R(Z'_A) = \frac{1 - |\Gamma_A|^2}{|1 - s_{11}\Gamma_A|^2} |s_{21}|^2 \frac{1 - |\Gamma_L|^2}{|1 - s_{22}\Gamma_L|^2} \quad (D.9)$$

where

$$\Gamma_A = \frac{Z'_A/2 - Z_0}{Z'_A/2 + Z_0} \quad (D.10)$$

Therefore, we have the relationship

$$\begin{aligned} G_R(Z'_A) &= \frac{G_R(Z'_A)}{G_R(Z_{cal})} G_R(Z_{cal}) \\ &= \frac{1 - |\Gamma_A|^2}{1 - |\Gamma_{cal}|^2} \cdot \frac{|1 - s_{11}\Gamma_{cal}|^2}{|1 - s_{11}\Gamma_A|^2} \cdot G_R(Z_{cal}) \end{aligned} \quad (D.11)$$

---

<sup>1</sup> For a unilateral receiver,  $s_{12} = 0$ . Analysis of the receiver used in this work (see Chapter 3) estimated  $s_{12} = -150$  dB. The resulting unilateral figure of merit is  $3 \times 10^{-5}$ , so that the error in  $G_R$  by assuming the receiver is unilateral is  $\ll 1\%$ .

Equation (D.11) can be used to convert  $G_R(Z_{cal})$  to  $G_R(Z'_A)$ , which is required for the source flux density measurement and the antenna temperature measurement.

### D.3 Recalculation of Receiver Noise Temperature for a Different Source Impedance

When estimating the diffuse Galactic emission, as described in Section 2.5.2, the ATM is used to determine the receiver noise temperature  $T_R$ . Specifically, the ATM is used to determine  $T_R(Z_{cal})$ , the receiver noise temperature when connected to the calibration circuit. We must then convert  $T_R(Z_{cal})$  to  $T_R(Z'_A)$ , the receiver noise temperature when connected to the antenna. These are different because a different amount of receiver noise escapes through the receiver input for the two source impedances. In this appendix we derive the expression for this conversion.

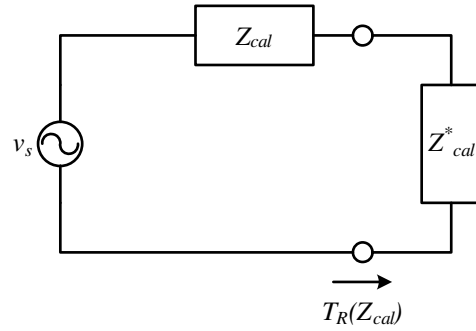
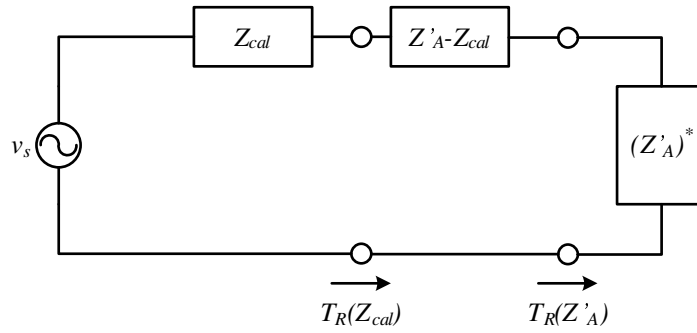
We first refer to Fig. D.1.  $T_R(Z_{cal})$  is defined as the equivalent noise temperature that a source with impedance  $Z_{cal} = R_{cal} + jX_{cal}$  would deliver to a conjugate-matched impedance  $Z_{cal}^*$ . From elementary circuit theory,

$$T_R(Z_{cal}) = \frac{\langle |v_s|^2 \rangle}{4kR_{cal}} \quad (\text{D.12})$$

We next modify Fig. D.1 to obtain the model shown in Fig. D.2. The source is the same, with available noise temperature  $T_R(Z_{cal})$ . However, the receiver sees a source impedance  $Z'_A = R'_A + jX'_A$ , the impedance presented to the receiver in the antenna state. Therefore the noise temperature delivered to the receiver in Fig. D.2 is equivalent to  $T_R(Z'_A)$ .

Again from elementary circuit theory we find

$$T_R(Z'_A) = \frac{\langle |v_s|^2 \rangle}{4kR'_A} \quad (\text{D.13})$$

Figure D.1: Model defining  $T_R(Z_{cal})$ .Figure D.2: Modification of Fig. D.1 used to determine  $T_R(Z'_A)$ .

By solving Eq. (D.12) for  $\langle |v_s|^2 \rangle$  and applying to Eq.(D.13):

$$T_R(Z'_A) = \frac{R_{cal}}{R'_A} T_R(Z_{cal}) \quad (\text{D.14})$$

Equation (D.14) can be used to convert  $T_R(Z_{cal})$  to  $T_R(Z'_A)$ , which is required for the antenna temperature measurement.

# Appendix E

## Noise Diode Characterization

This appendix documents the theory and measurements used to determine  $T_{cal}$ .  $T_{cal}$  is defined in Section 2.5.1 as the power spectral density (PSD) available from the calibration circuit (i.e. the PSD that the calibration circuit would deliver to a conjugate matched load) divided by Boltzmann’s constant  $k$ . A prior estimate of  $T_{cal}$  is required when using the Antenna Temperature Model (ATM) to characterize the system gain and noise.

Figure E.1 shows the equivalent circuit model for the calibration circuit. The calibration circuit is implemented on the front end electronics (FEE; see Section 3.2). The noise diode is modeled as a Thévenin equivalent circuit having voltage  $v_D$  and impedance  $Z_D = R_D + jX_D$ . The attenuator and balun (ATTN3 and T4 in Fig. G.1) are modeled as a single two-port network having available power gain  $G_{ATTN}$ , input impedance  $Z_{ATTN}$ , and output impedance  $Z_{cal}$ . The attenuator and balun will be referred to as “the two-port” throughout this appendix.

The PSD available from the noise diode is

$$S_D = \frac{\langle |v_D(t)|^2 \rangle}{4R_D} \quad (\text{E.1})$$

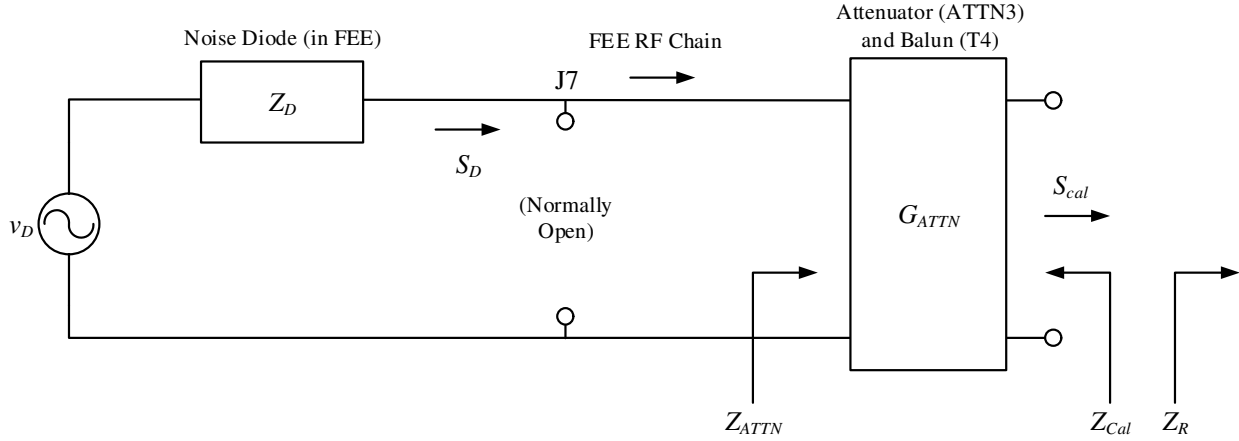


Figure E.1: Equivalent circuit of the calibration circuit.

which is related to the PSD available from the calibration circuit by

$$S_{cal} = G_{ATTN} S_D \quad (\text{E.2})$$

$T_{cal}$  is then related to  $S_{cal}$  by

$$T_{cal} = \frac{S_{cal}}{k} \quad (\text{E.3})$$

Figure E.2 shows the equivalent circuit model for the calibration circuit during the characterization measurement. During the measurement, the noise diode test port (J7, see Fig. G.1) is connected to a test jig. Figure E.3 shows a block diagram of the test jig, which consists of Mini-Circuits amplifiers and attenuators and a Rhode & Schwarz FSH3 spectrum analyzer. The test jig is characterized by a transducer power gain (TPG)  $G_{jig}$ , input-referenced noise temperature  $T_{jig}$ , and input impedance  $Z_{jig}$ . During the characterization measurement, the FEE is in State 3, the hot state. In the hot state, the relays are connected to the two-port, such that the two-port sees the receiver impedance  $Z_R$  at its second port. Thus the spectrum analyzer measures

$$S_{out} = G_{jig}(Z_{par}) [S_1 + kT_{jig}(Z_{par})] \quad (\text{E.4})$$

where  $Z_{par} = Z_D || Z_{ATTN}$ .  $S_1$  is defined as the PSD that would be delivered to a test jig with

a conjugate-matched input impedance  $Z_{jig} = Z_{par}^*$ . From elementary circuit analysis,  $S_D$  is related to  $S_1$  by

$$S_1 = S_D \left| \frac{Z_{ATTN} || Z_{par}^*}{Z_{ATTN} || Z_{par}^* + Z_D} \right|^2 \frac{4R_D R_{par}}{|Z_{par}|^2} \quad (\text{E.5})$$

Estimation of  $T_{cal}$  from the measurement of  $S_{out}$  is achieved as follows:

1. Measure the  $Z_{jig}$ ,  $Z_{ATTN}$ ,  $Z_{par}$ , and  $Z_{cal}$ .
2. Estimate  $Z_D$  from  $Z_{ATTN}$  and  $Z_{par}$  by solving  $Z_{par} = Z_D || Z_{ATTN}$  for  $Z_D$ .
3. Measure  $G_{jig}(Z_0)$  and  $T_{jig}(Z_0)$ , where  $Z_0 = 50 \Omega$ .
4. Convert  $G_{jig}(Z_0)$  to  $G_{jig}(Z_{par})$ .  $G_{jig}(Z_0)$  is related to  $G_{jig}(Z_{par})$  by a comparable relationship to Eq. (D.11) (with  $s_{11} = 0$  since  $Z_0 = 50 \Omega$  is also used as the  $s$ -parameter reference impedance)

$$G_{jig}(Z_{par}) = \frac{1 - |\Gamma_s|^2}{1 - |\Gamma_{jig}|^2} G_{jig}(Z_0) \quad (\text{E.6})$$

where

$$\Gamma_s = \frac{Z_{par} - Z_0}{Z_{par} + Z_0} \quad \text{and} \quad \Gamma_{jig} = \frac{Z_{jig} - Z_0}{Z_{jig} + Z_0} \quad (\text{E.7})$$

5. Convert  $T_{jig}(Z_0)$  to  $T_{jig}(Z_{par})$ .  $T_{jig}(Z_0)$  is related to  $T_{jig}(Z_{par})$  by the same theory presented in Appendix D (see Eq. (D.14))

$$T_{jig}(Z_{par}) = \frac{Z_0}{R_{par}} T_{jig}(Z_0) \quad (\text{E.8})$$

where  $R_{par}$  is the real part of  $Z_{par}$ .

6. Measure the  $s$ -parameters of the two-port,  $s^{ATTN}$ .  $G_{ATTN}$ , the *available* gain of the two-port, is then given by [67, Section 12.1]

$$G_{ATTN} = \frac{1 - |\Gamma_D|^2}{|1 - s_{11}^{ATTN} \Gamma_D|^2} |s_{21}^{ATTN}|^2 \frac{1}{1 - |\Gamma_{cal}|^2} \quad (\text{E.9})$$

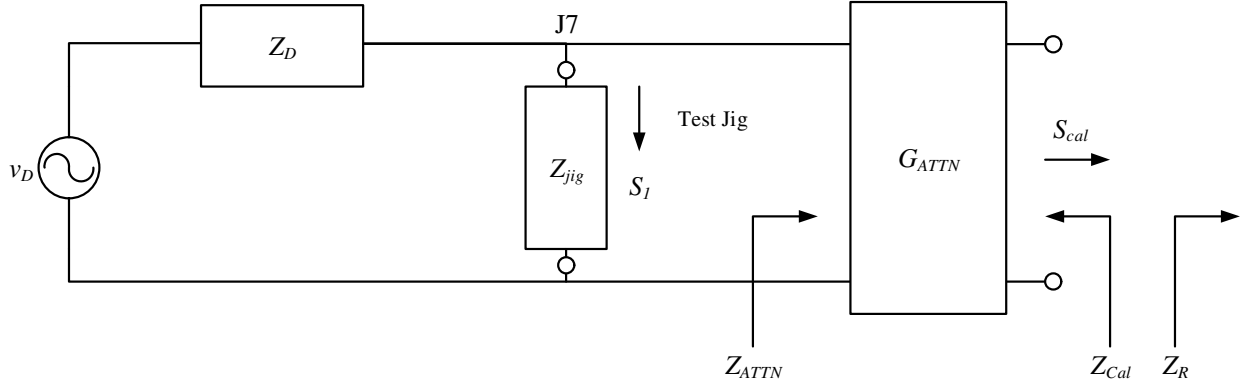


Figure E.2: Equivalent circuit of the calibration circuit for the noise diode calibration measurement. See text for explanation of the notation.

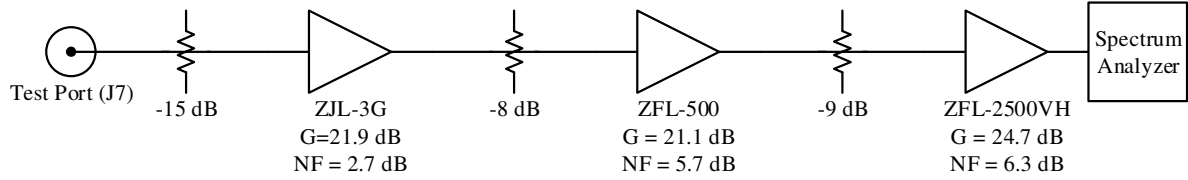


Figure E.3: Block diagram of the test jig used in the  $T_{cal}$  measurement. The displayed gain and noise figure (NF) are at the closest frequency to 50 MHz that is reported by the manufacturer.

where

$$\Gamma_D = \frac{Z_D - Z_0}{Z_D + Z_0} \quad \text{and} \quad \Gamma_{cal} = \frac{Z_{cal} - Z_0}{Z_{cal} + Z_0} \quad (\text{E.10})$$

7. Measure  $S_{out}$ .

8. Estimate  $S_1$  from  $S_{out}$  by solving Eq. (E.4) for  $S_1$ :

$$S_1 = \frac{S_{out}}{G_{jig}(Z_{par})} - kT_{jig}(Z_{par}) \quad (\text{E.11})$$

9. Estimate  $S_D$  from the estimated  $S_1$  according to Eq. (E.5).

10. Estimate  $T_{cal}$  from the estimated  $S_D$  according to Eqs. E.2 and E.3.

Figure E.4 shows the measured  $Z_{jig}$ ,  $Z_{ATTN}$ , and  $Z_{par}$ .  $Z_{jig}$  and  $Z_{ATTN}$  are both close to

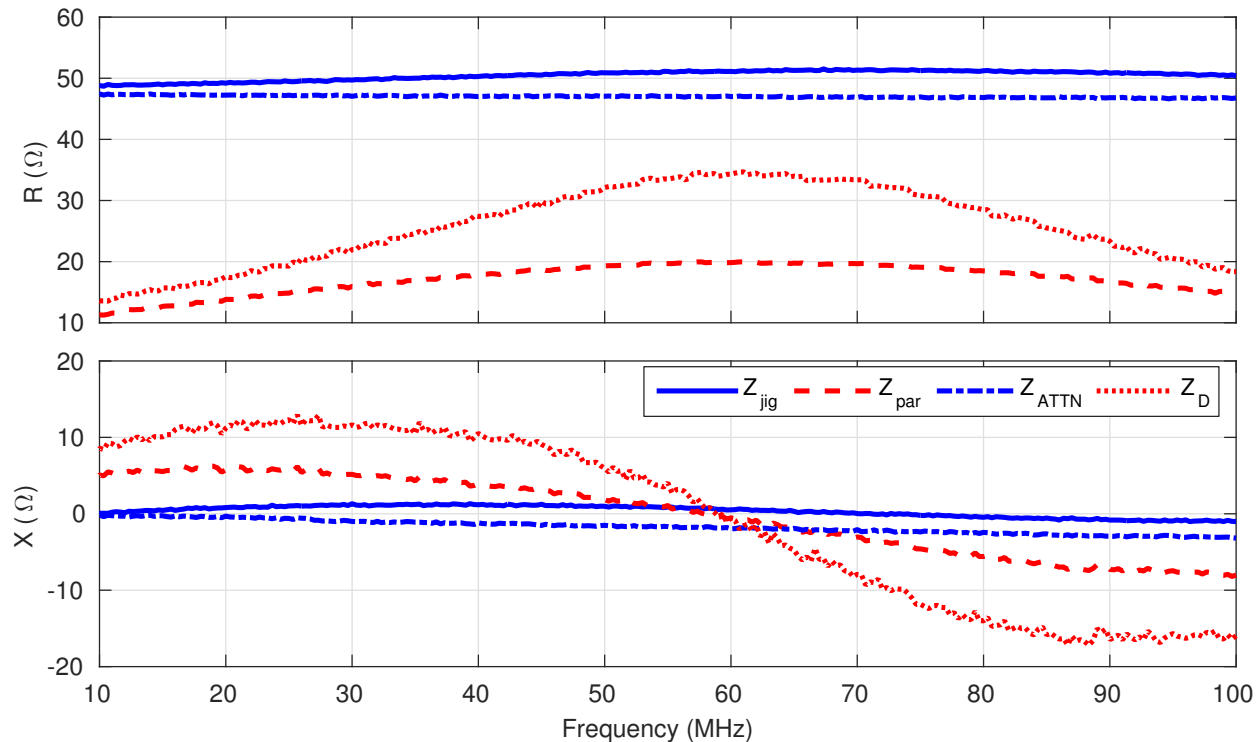


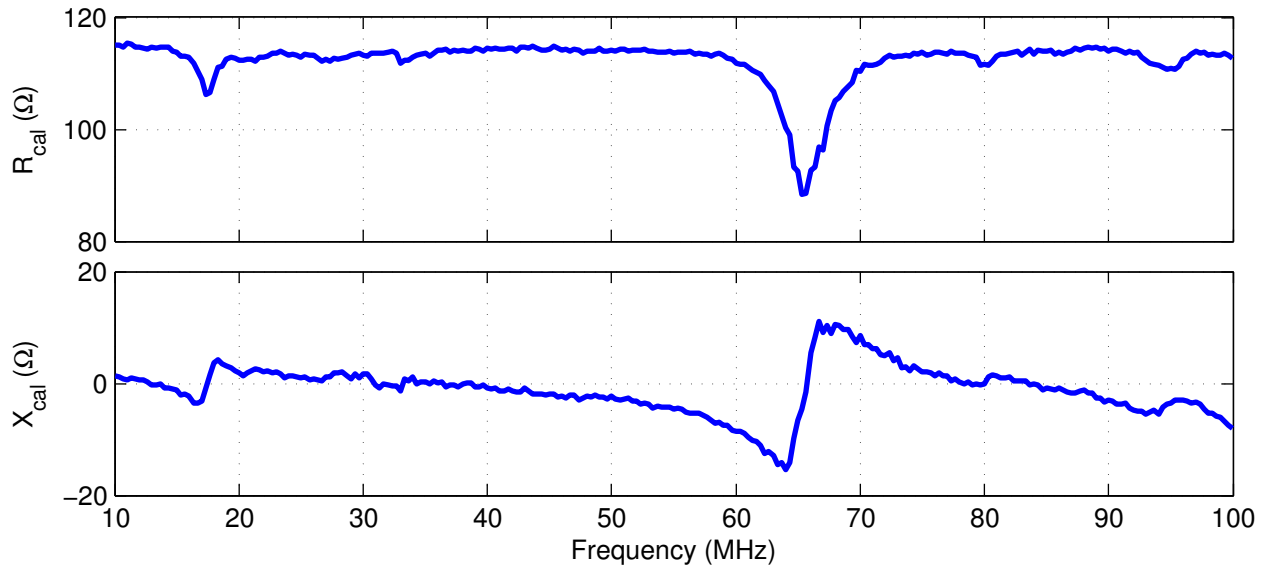
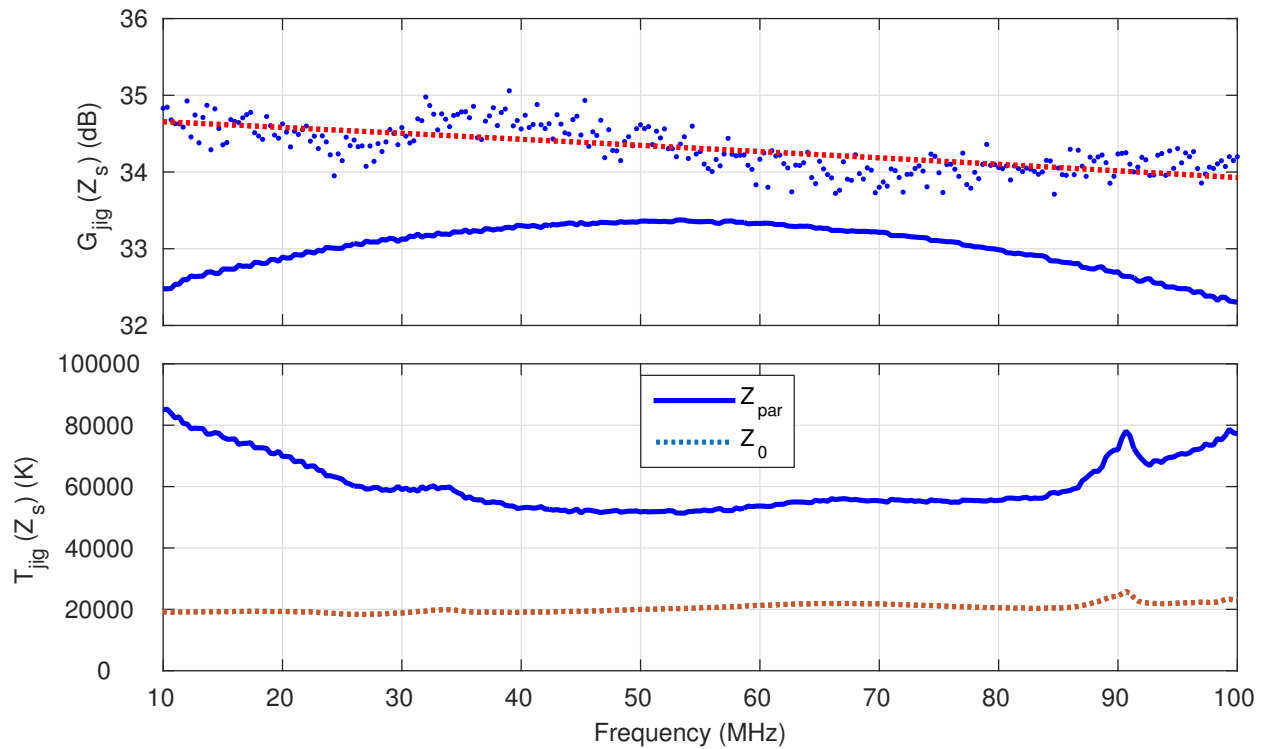
Figure E.4: Measured impedances used in the noise diode calibration measurement procedure.

50  $\Omega$ , as expected.  $Z_D$  is solved for from the measurement of  $Z_{ATTN}$  and  $Z_{par}$ , which is also included in Fig. E.4. Figure E.5 shows the measured  $Z_{cal}$ .

Figure E.6 shows the measured  $G_{jig}(Z_0)$  and  $T_{jig}(Z_0)$ .  $G_{jig}(Z_0)$  is fit to a 1<sup>st</sup>-order polynomial to mitigate the noise in the measurement. Figure E.6 also shows  $G_{jig}(Z_{par})$  and  $T_{jig}(Z_{par})$ , computed using Eqs. (E.6) and (E.8), respectively.

The spectrum analyzer was used to measure  $s^{ATTN}$ . Figure E.7 shows the resulting  $G_{ATTN}$ , computed using Eq. (E.9).

Figure E.8 shows  $S_{out}$  measured by the spectrum analyzer for the two FEEs used in the measurement campaign, identified as FEE7 and FEE8. Figure E.9 shows the estimated  $S_1$  from Eq. (E.11) for  $S_1$ . Figure E.9 also shows  $S_D$  estimated from measurements of  $S_1$  and by solving Eq. (E.5) for  $S_D$ . Finally, Figure E.10 shows the the estimates of  $T_{cal}$  for the two FEEs used in the campaign.

Figure E.5: Measured  $Z_{cal}$ .Figure E.6: Measured gain and input-referred noise temperature of the test jig. The dots show the measured  $G_{jig}(Z_0)$ , while the dashed line is the fit to the measurement.

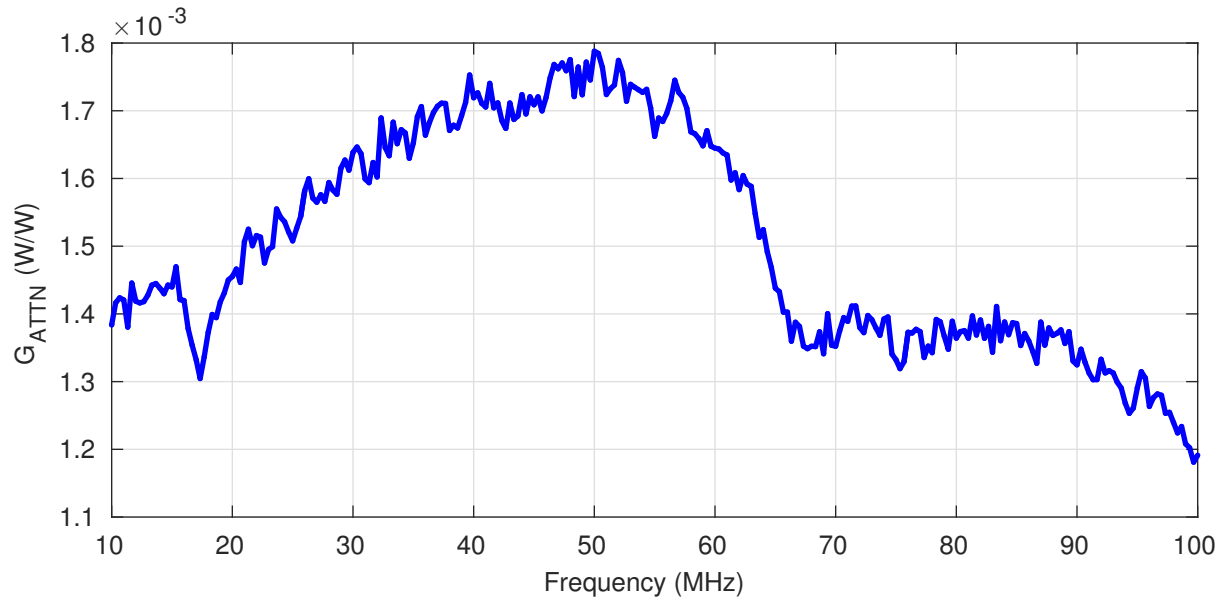
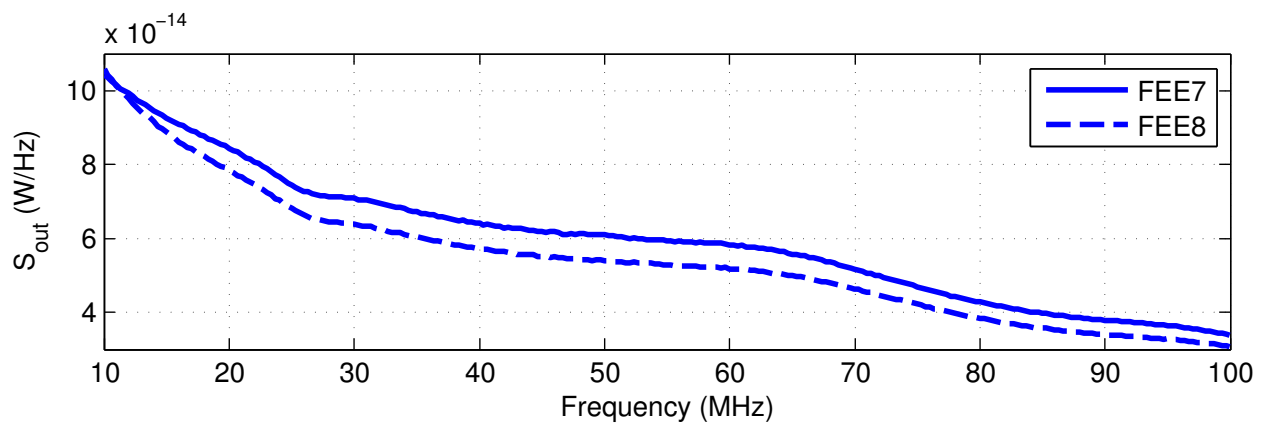
Figure E.7: Measured  $G_{ATTN}$ .

Figure E.8: PSD measured by the spectrum analyzer for the noise diode calibration measurement for the two FEEs.

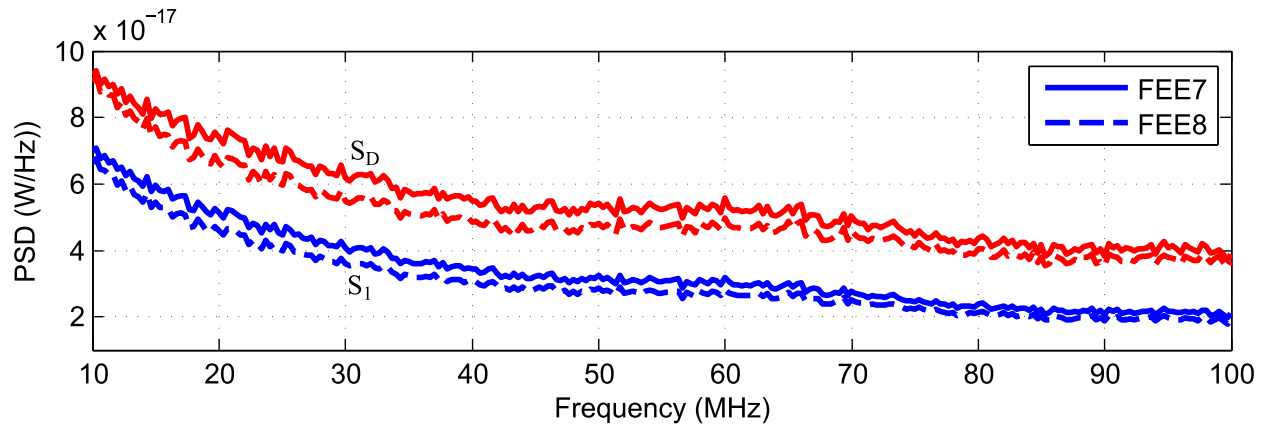


Figure E.9: Estimated PSD available to the test jig ( $S_1$ ) and available from the noise diode ( $S_D$ ).

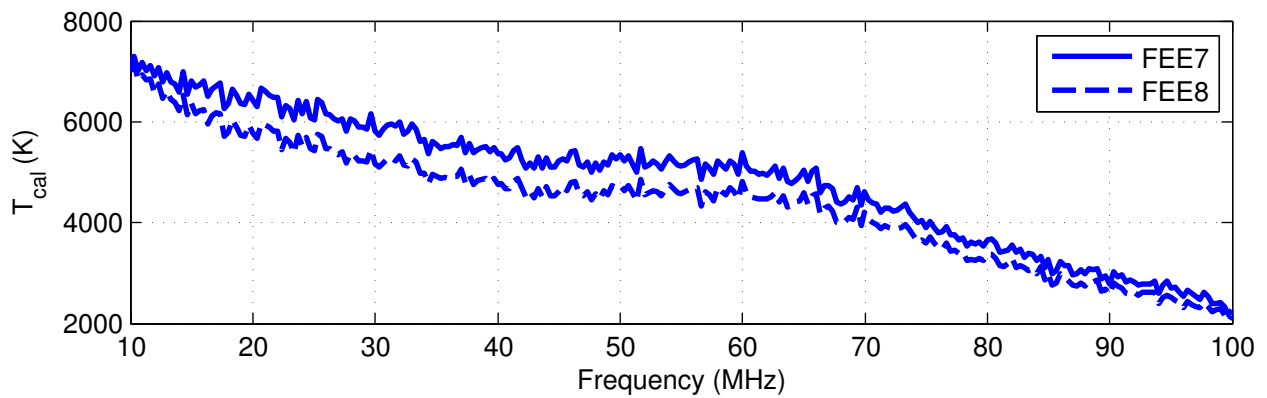


Figure E.10: Estimate of  $T_{cal}$ .

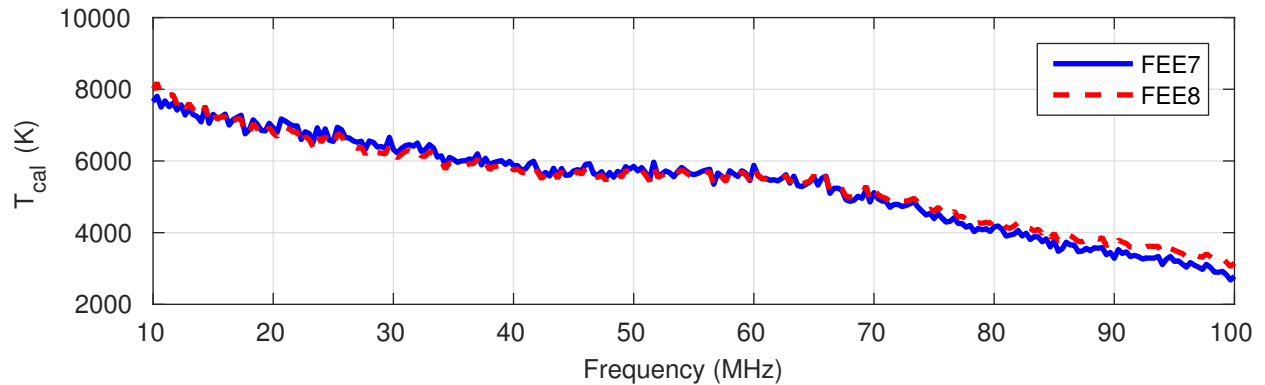


Figure E.11: Same as Fig. E.10, but with the modification  $\Delta T_{cal}$  determined in Section 5.2.

The estimates of  $T_{cal}$  presented in this appendix are obtained after an intricate process. Error is introduced at the various steps in this measurement, and the resulting error in the estimates of  $T_{cal}$  is seen to bias the measurement (see Section 5.1.2). To mitigate this error, a correction term  $\Delta T_{cal}$  is introduced, as discussed in Section 2.6.2. In Section 5.2, we determine that  $\Delta T_{cal}$  is about 500 K and 1,000 K for FEE7 and FEE8, respectively.

Figure E.11 shows  $T_{cal}$  with the  $\Delta T_{cal}$  modifications determined in Section 5.2. This is the estimate of  $T_{cal}$  that is used to obtain the results reported in Chapter 6.

# Appendix F

## The Radiometric Interferometry Model (RIM)

In this Appendix, we compare the Coherent Interferometry Model (CIM) presented in Section 2.7 to the model traditionally used to estimate the flux density of discrete sources (i.e. see Table 1.2). We refer to this model as the “Radiometric Interferometry Model” (RIM). This simpler model operates directly on power-like quantities.<sup>1</sup> In terms of variables defined in Chapter 2, the measurement equation is

$$|\rho_{mn}(t)| = \frac{1}{2} \sqrt{A_e^{(m)} G_p^{(m)} G_R^{(m)}(Z'_A)} \sqrt{A_e^{(n)} G_p^{(n)} G_R^{(n)}(Z'_A)} S_\nu^{src} \quad (\text{F.1})$$

where  $A_e$  is the effective aperture of the antenna in the direction of the source, and the factor of 2 accounts for the fact that a single polarization receives only half of the available flux.

We wish to compare the RIM and the CIM to show they are equivalent, and providing further validation to the CIM. To do so, we must relate  $A_e$  to the projected effective length  $l_e$ .  $A_e$

---

<sup>1</sup>It should also be noted that the earlier work has assumed very good impedance matching throughout, so even Eq. (F.1) is a generalization in this sense.

is defined as

$$A_e \triangleq \frac{S_A}{S_\nu^{src}} \quad (\text{F.2})$$

where  $S_A$  is the power spectral density (PSD) the antenna would deliver to a conjugate-matched load having impedance  $Z_A^*$ . From Eqs. (2.4) and (2.8),  $S_A$  is given by

$$\begin{aligned} S_A &= \frac{\langle |v_{src}|^2 \rangle}{4R_A} \\ &= \frac{|l_e|^2 \eta S_\nu^{src}}{4R_A} \end{aligned} \quad (\text{F.3})$$

By applying Eq. (F.3) to Eq. (F.2):

$$A_e = \frac{\eta}{4R_A} |l_e|^2 \quad (\text{F.4})$$

Now, by applying Eq. (F.4) to Eq. (F.1), and assuming  $l_e$  is the same for the two antennas:

$$|\rho_{mn}(t)| = \frac{\eta}{2} |l_e|^2 \sqrt{\frac{G_p^{(m)} G_R^{(m)}(Z'_A)}{4R_A^{(m)}}} \sqrt{\frac{G_p^{(n)} G_R^{(n)}(Z'_A)}{4R_A^{(n)}}} S_\nu^{src} \quad (\text{F.5})$$

By equating Eq. (F.5) to Eq. (2.63):

$$|H^{(m)} H^{(n)}| = \sqrt{\frac{G_p^{(m)} G_R^{(m)}(Z'_A)}{4R_A^{(m)}}} \sqrt{\frac{G_p^{(n)} G_R^{(n)}(Z'_A)}{4R_A^{(n)}}} \quad (\text{F.6})$$

Therefore,

$$|H^{(m)}| = \sqrt{\frac{G_p^{(m)} G_R^{(m)}(Z'_A)}{4R_A^{(m)}}} \quad (\text{F.7})$$

and similarly for  $H^{(n)}$ . Finally, by applying Eq. (2.48)

$$|H^{(m)}| = \left| \frac{Z_p || (Z'_A)^*}{Z_p || (Z'_A)^* + Z_A} \right| \sqrt{G_R(Z'_A) \frac{R'_A}{|Z'_A|^2}} \quad (\text{F.8})$$

which is identical to Eq. (2.68), providing independent confirmation of the derivation in Section 2.7.2.

While CIM and RIM are in principle equivalent, we prefer CIM since it operates on coherent, voltage-related quantities (effective lengths and voltages) as opposed to incoherent, power-related quantities (effective aperture and TPG). CIM is particularly convenient when large and spectrally-variable mismatches in complex-valued impedances are present. This is the case in our system, which is presented in Chapter 3.

# Appendix G

## Instrumentation Design Details

This appendix presents the design details for the custom-designed system components. The front end electronics (FEE) presented in Section 3.2 are documented in Section G.1. The bias and control circuit presented in Section 3.9 are documented in Section G.3.

### G.1 FEE Design Details

This section documents the design details of the FEE presented in Section 3.2. Figures G.1 and G.2 shows the schematic of the FEE's RF path and bias and control circuit, respectively. The printed circuit board (PCB) layout is shown in Fig. G.3. Table G.1 is a bill of materials for the FEE.

The calibration state is determined by the DC voltage used to power the FEE. Figure G.4 shows a block diagram of the circuit used to set the calibration state. The comparators CPR1 and CPR2, contained in U5 in Fig. G.2, set the state of the mechanical relays RLY1 and RLY2 in Fig. G.1 to the antenna in the antenna state, and to the calibration circuit in the hot and cold states. The comparator CPR3 sets the noise diode (D1 in Fig. G.1) bias voltage to  $\sim 9$  V in the hot state, and  $\sim 0.8$  V in the cold state. The transition voltages

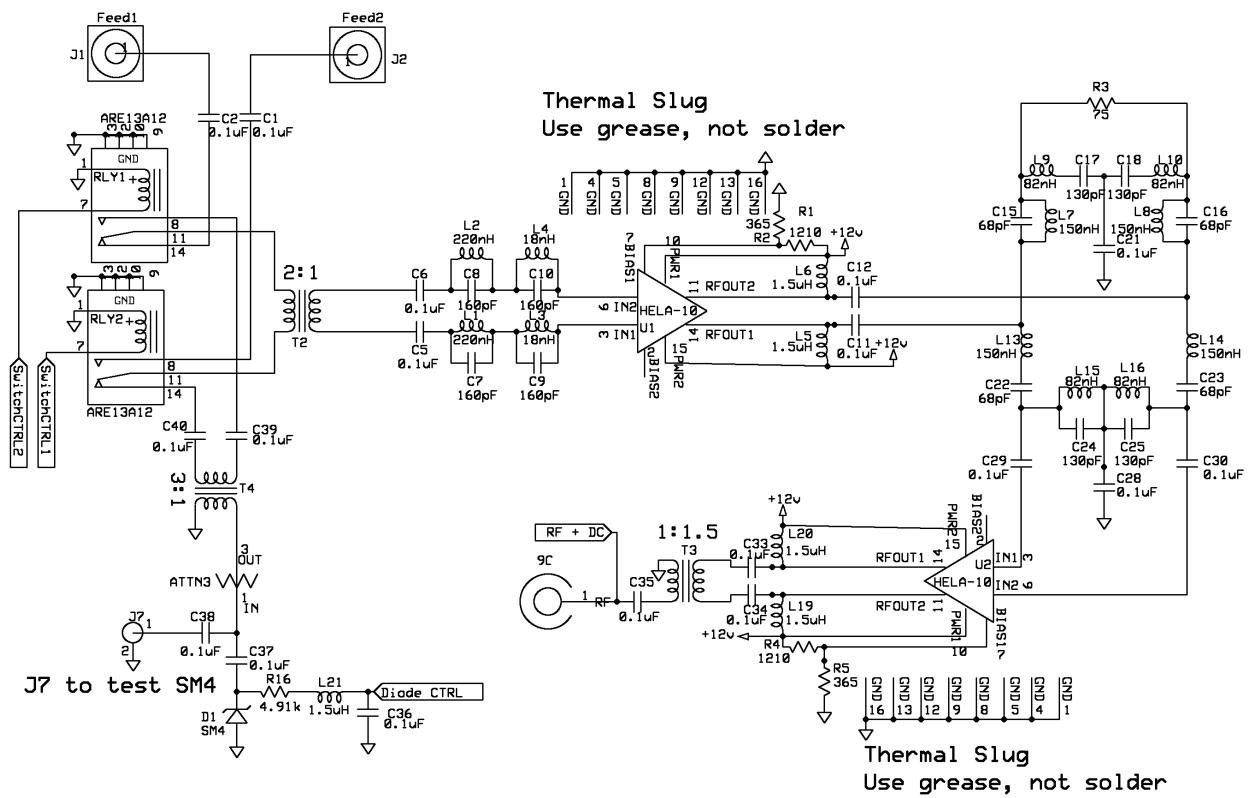


Figure G.1: Schematic of the FEE. “Feed1” and “Feed2” are the antenna terminals.

Table G.1: Bill of materials for the FEE, including the enclosure, mechanical parts, and temperature sensors. The different sections, demarcated by the double lines, indicate parts procured from different distributors; from top to bottom, these distributors are Digikey, Lowe's, Mouser, Mini-Circuits, Mercury, OnSet, and ExpressPCB. Total cost is for 4 FEEs, and includes spare parts.

Part ID	MFG	MFG Part #	Unit Price	Quantity	Total Price
Relays	Panasonic	ARE13A12	\$6.39	10	\$63.90
J3-J5,J8	Sullins	PPTC021LFBN-RC	\$0.26	50	\$13.10
J6,J7	Linx	CON SMA001	\$2.40	25	\$60.00
Bias Inductor	TDK	MLZ2012E4R7M	\$0.09	50	\$4.33
Diplexer/Notch Inductors	Epcos	B82498F3180J	\$0.70	20	\$14.04
"	Epcos	B82498F3680J	\$0.70	20	\$14.04
"	Epcos	B82498F3820J	\$0.70	20	\$14.04
"	Epcos	B82498F3101J	\$0.70	20	\$14.04
"	Epcos	B82498F3151J	\$0.70	20	\$14.04
R1,R4,R6	SEI	RNCF0805BTC1K13	\$0.55	20	\$11.02
R11	SEI	RNCS0805BKE1K00	\$0.52	10	\$5.23
R16	SEI	RNCS0805BKE825R	\$0.52	10	\$5.23
R2,R5	SEI	RNCS0805BKE332R	\$0.52	20	\$10.46
R3	SEI	RNCS0805BKE75R0	\$0.52	10	\$5.23
R7-R10,R12-R15	SEI	RNCS0805BKE10K0	\$0.32	50	\$15.81
U3	TI	LM2940CSX-12/NOPB	\$1.58	10	\$15.78
U5	TI	LP339DR	\$0.54	10	\$5.42
Board-Enclosure Cable	Amphenol	135111-02-M0.25	\$20.82	2	\$41.64
Enclosure	LMB Heeger	J-882 PL/UNPD	\$13.70	4	\$54.80
4-40 Screws	B&F	PMS 440 0025 PH	\$0.03	100	\$2.98
4-40 Nuts	B&F	HNZ 440	\$0.01	100	\$1.49
1/4in x 2.5in Carriage Bolt			\$0.20	20	\$4.00
Bypass Capacitors	AVX	06035C104KAT2A	\$0.04	100	\$3.50
Diplexer/Notch Cs	AVX	08052U560GAT2A	\$0.46	20	\$9.20
"	AVX	8052U680JAT2A	\$0.35	20	\$7.00
"	AVX	08052U101JAT2A	\$0.35	20	\$7.00
"	AVX	08052U131JAT2A	\$0.35	20	\$7.00
"	AVX	08051U161JAT2A	\$0.35	20	\$7.00
U1,U2	Mini-Circuits	HELA-10	\$15.95	10	\$159.50
Impedance Transformers	Mini-Circuits	ADT3-1	\$3.45	20	\$69.00
"	Mini-Circuits	ADT2-1	\$3.45	20	\$69.00
"	Mini-Circuits	ADT1.5-1	\$2.95	20	\$59.00
ATTN3	Mini-Circuits	PAT-30	\$2.95	20	\$59.00
D1	Mercury	SM4	About 35	Requires Quote	
Temperature Sensors Controller	OnSet	BASE-U-1	\$67.00	1	\$67.00
Temperature Sensors Software	OnSet	BHW-PRO-CD	\$99.00	1	\$99.00
Temperature Sensor	OnSet	UA-001-08	\$42.00	4	\$168.00
PCB	ExpressPCB		\$195.00	1	\$195.00
			Totals		\$1375.82

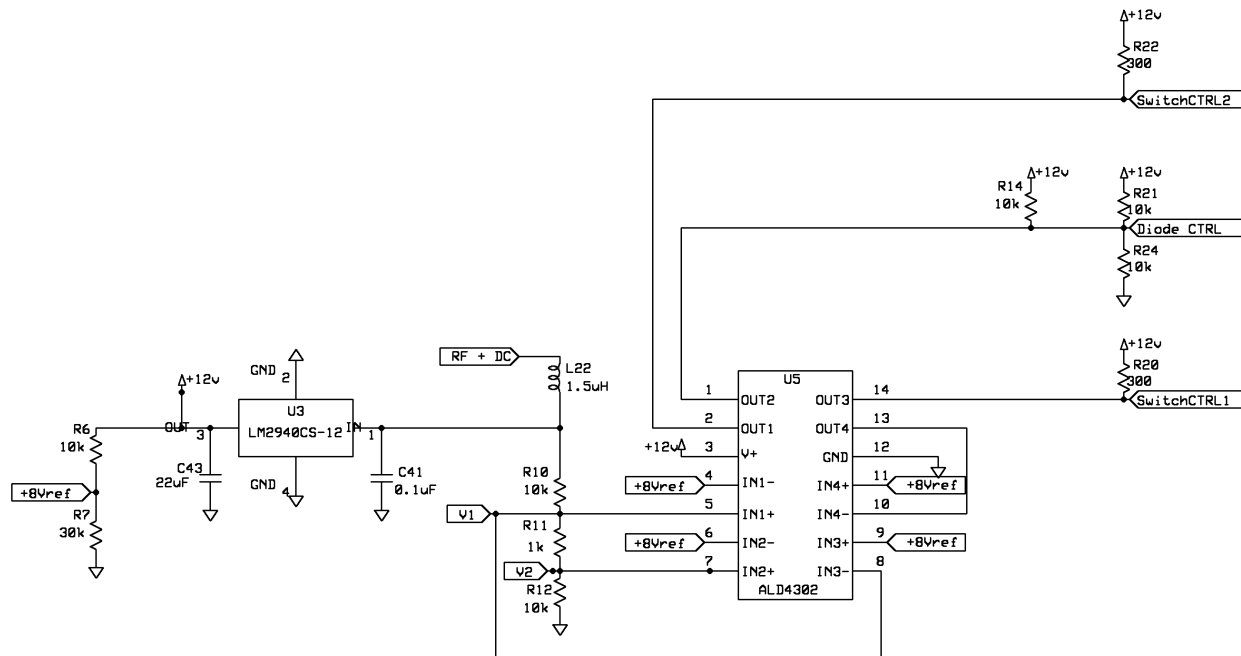


Figure G.2: Bias and control circuit on the FEE PCB.

State	DC Bias	CPR1	CPR2	CPR3	Terminal Connection
1	16 V	High	Low	Low	Antenna
2	18 V	Low	High	Low	Noise Source Off
3	20 V	Low	High	Low	Noise Source On

Table G.2: DC voltages on which the FEE changes its calibration state.

between the three different states are 17.2 and 19 V. Table G.2 shows the specified DC bias voltages and their associated calibration state.

The resistor used to bias the noise diode (R16 in Fig. G.1) was modified from the datasheet recommendations (from 900 k $\Omega$  to 4.91 k $\Omega$ ) to increase the power output from the noise diode. Lab measurements found of diode's noise temperature are shown in Fig. E.10, and a description of the measurement is in Appendix E.

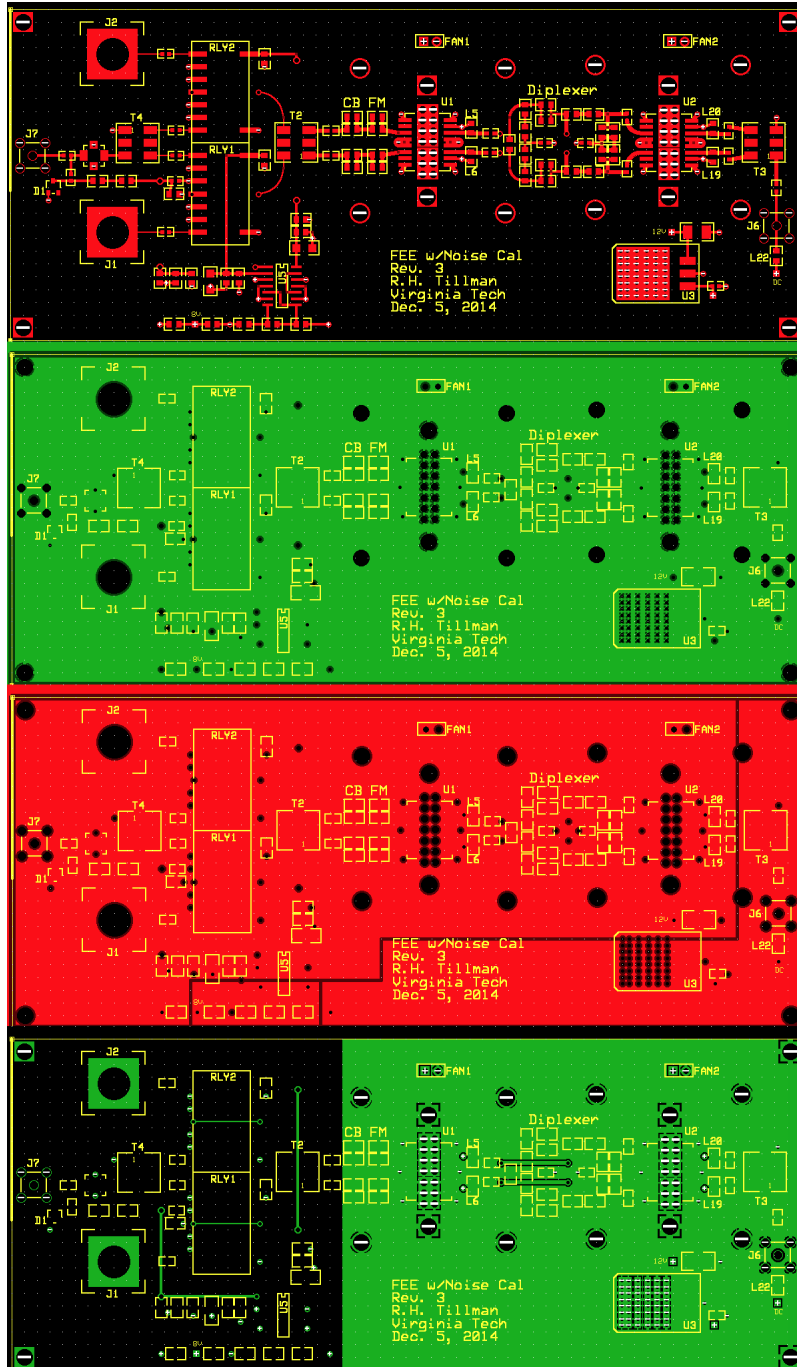


Figure G.3: Layout of FEE. From top to bottom, the layers are top copper, ground plane, power plane, and bottom copper. The top silk screen layer is shown on all layers for reference.

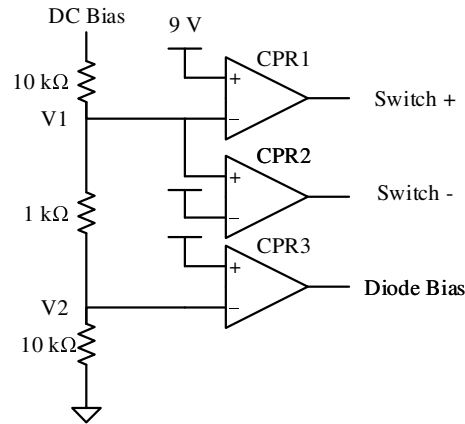


Figure G.4: Block diagram of the control circuit on the FEE PCB.

## G.2 Anti-Aliasing Filter Design Details

Table G.3 shows a bill of materials for each of the three anti-aliasing filters used in the interferometer presented in Chapter 3.5.

## G.3 Bias and Control Design Details

This section documents the design of the bias and control circuit presented in Section 3.9. As discussed in Fig. 3.1 and surrounding text, these boards regulate the power from the power supply to the various voltage levels required by the instrument components.

Figures G.5 and G.6 shows a detailed schematic and PCB layout of the Control board. Figures G.7 and G.8 shows a detailed schematic and PCB layout of the Bias board. Figures G.9, G.10, and G.11 shows a detailed schematic PCB layout, and picture of the I/V Monitor board.

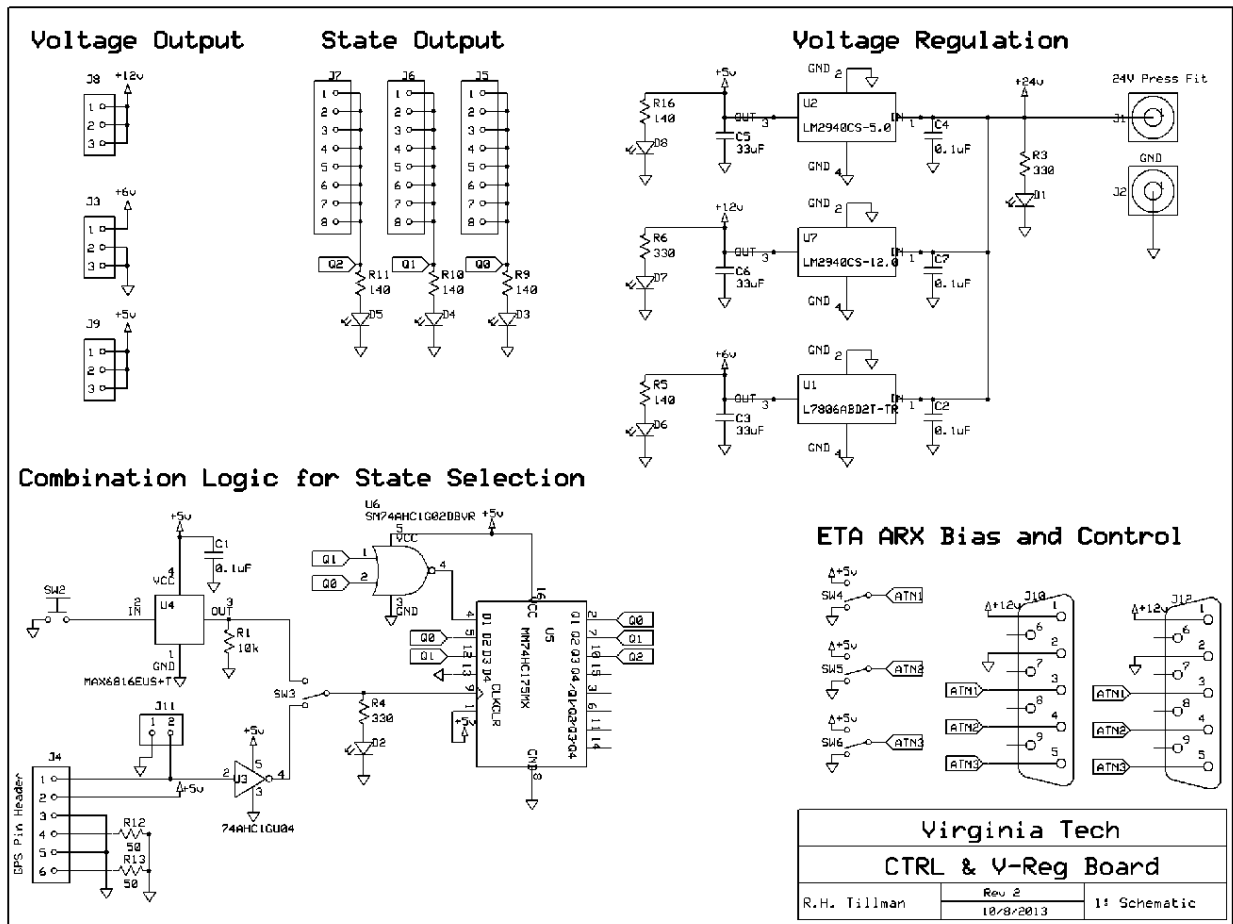


Figure G.5: Schematic of the control board.

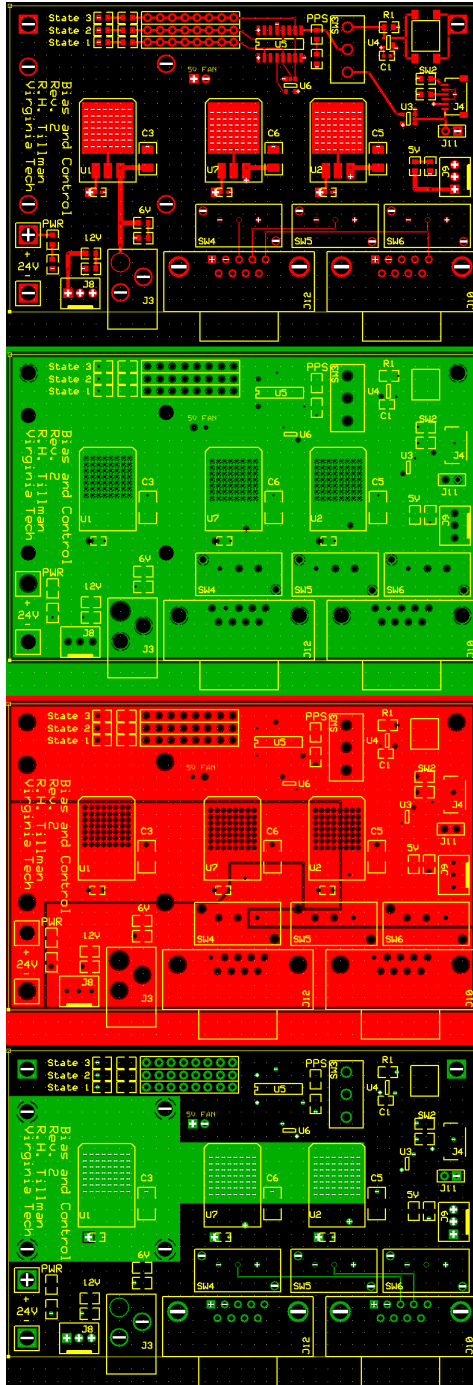


Figure G.6: PCB layout of the control board. From top to bottom, the layers are top copper, ground plane, power plane, and bottom copper.

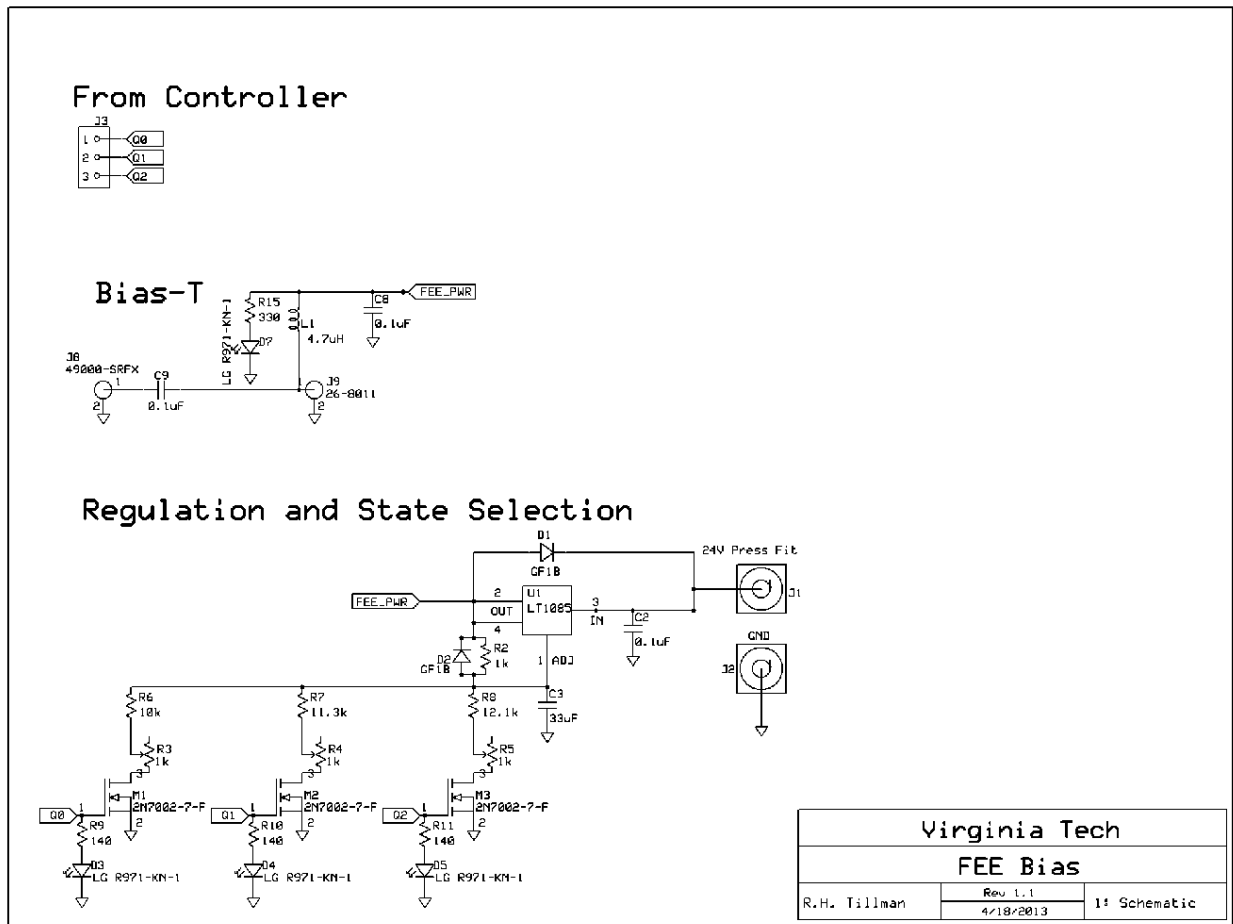


Figure G.7: Schematic of the bias board.

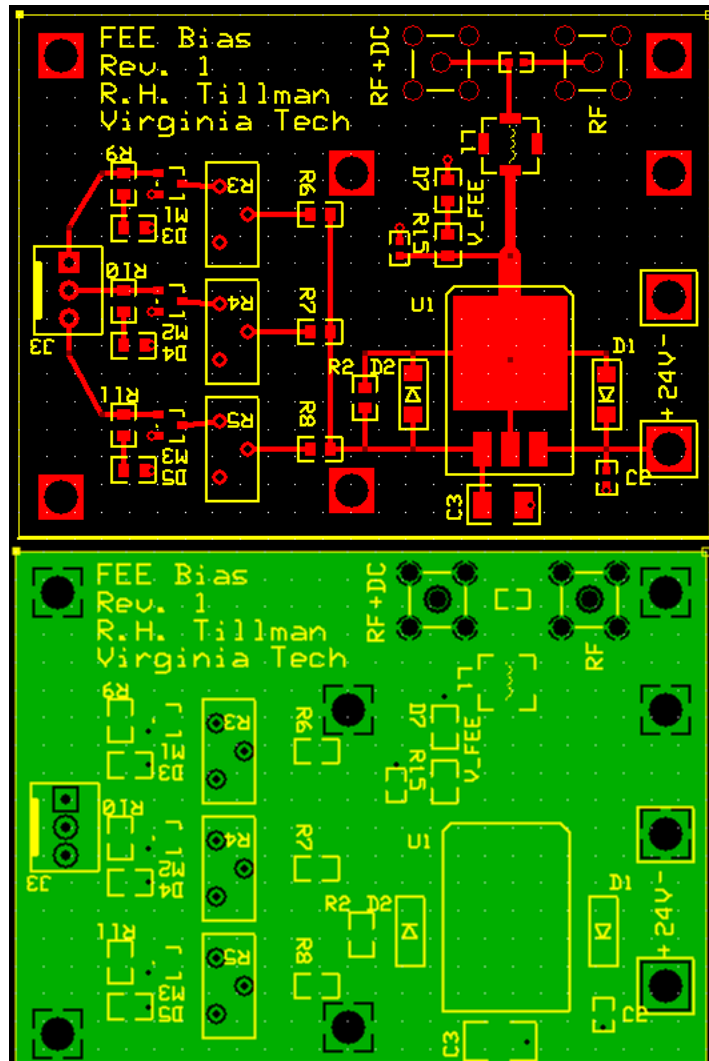


Figure G.8: PCB layout of the bias board. The top and bottom layers are top and bottom copper, respectively.

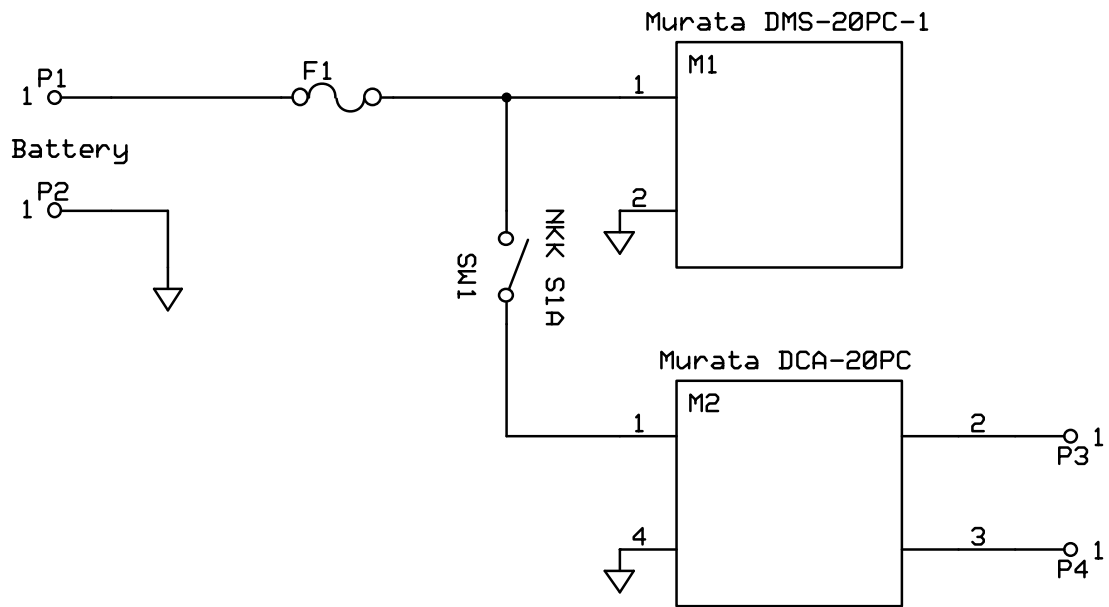


Figure G.9: Schematic of the I/V Monitor board.

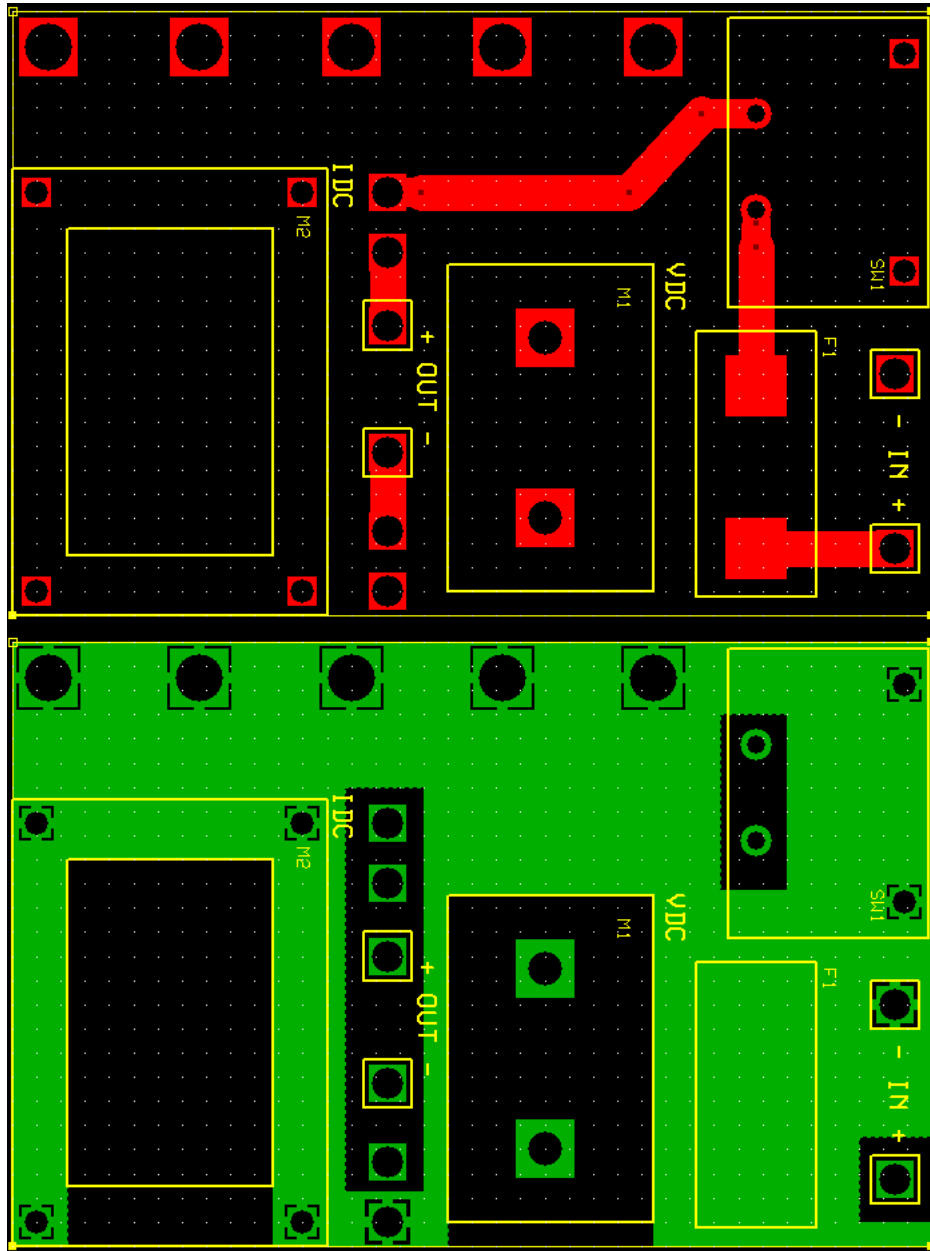


Figure G.10: PCB layout of the I/V Monitor board. The top and bottom layers are top and bottom copper, respectively.

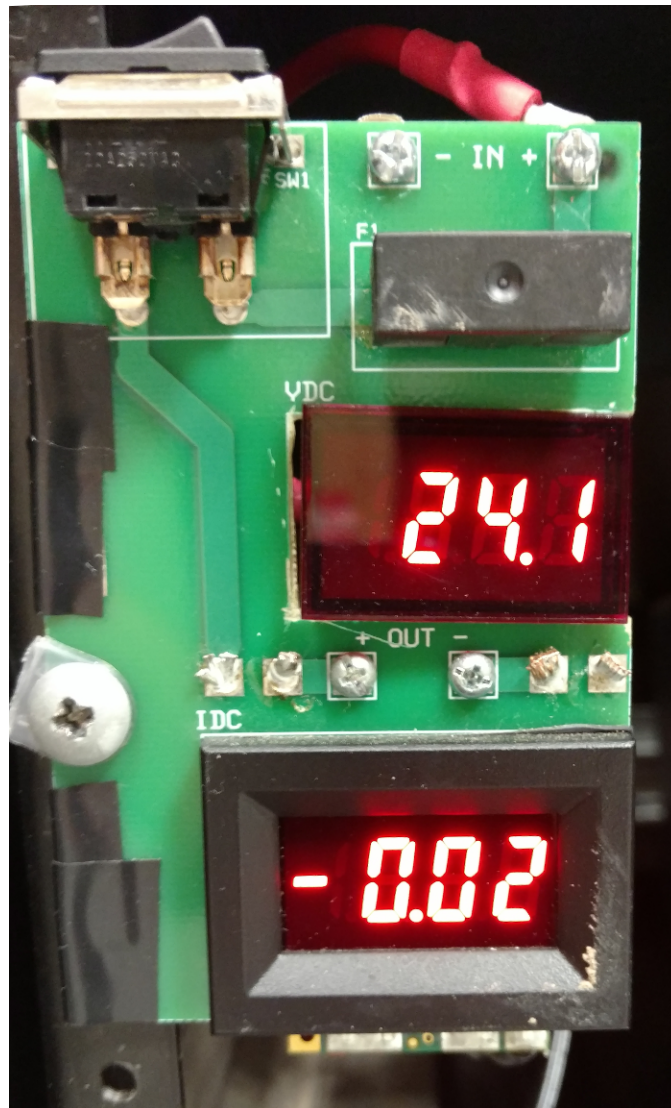


Figure G.11: The fabricated I/V Monitor board.

Table G.3: Bill of materials for each AAF. Nyquist zone and corner frequency ( $\nu_c$ ) are indicated for each filter. Digikey is the distributor for all parts.

Part	MFG	MFG Part #	Distributor Part #	Qty
AAF1: Low Pass Chebyshev, $\nu_c = 48$ MHz				
51 pF	ATC	600S510FT250XT	1284-1228-1-ND	3
560 nH	Abracon	AISC-0805-R56G-T	AISC-0805-R56G-TCT-ND	2
820 nH	Abracon	AISC-0805-R82G-T	AISC-0805-R82G-TCT-ND	2
AAF2: High Pass Chebyshev, $\nu_c = 52$ MHz				
13 pF	Kemet	CBR06C130FAGAC	399-8822-1-ND	2
18 pF	Kemet	CBR06C180FAGAC	399-8842-1-ND	2
200 nH	Murata	LQW18ANR20G00D	490-6929-1-ND	3
AAF3: Low Pass Butterworth, $\nu_c = 50$ MHz				
82 pF	AVAX	08055A820JAT2A	478-1315-1-ND	2
130 pF	AVAX	08051U131JAT2A	08051U131JAT2A-ND	1
160 pF	AVAX	08051U161JAT2A	08051U161JAT2A-ND	2
33 nH	EPCOS	B82498F3330J	495-1852-1-ND	1
47 nH	EPCOS	B82498F3470J	495-1854-1-ND	1
68 nH	EPCOS	B82498F3680J	495-1856-1-ND	2
270 nH	EPCOS	B82498F3271J	B82498F3271J-ND	2

# Appendix H

## GNL Analysis

This appendix derives the gain, noise, and linearity (GNL) analysis used to evaluate a cascade system. This analysis was used in Section 3.6 to evaluate the receiver used in this work.

Figure H.1 shows a block diagram of a receiver.  $G_i$ ,  $T_i$ , and  $P_{1dB}^i$  represent the gain, input-referred equivalent noise temperature, and input-referred 1 dB compression point of stage  $i$ . All values are linear. Each block is assumed to be impedance matched.

The total (cascade) gain is

$$G_{sys} = G_1 G_2 \cdots G_n \quad (\text{H.1})$$

The system temperature is

$$T_{sys} = T_1 + \frac{T_2}{G_1} + \cdots + \frac{T_n}{G_1 G_2 \cdots G_{n-1}} \quad (\text{H.2})$$

The cascade  $P_{1dB}$  is derived from the well-known expression for the cascade input-referred third-order intercept (IIP3) (see e.g. [68]):

$$\text{IIP3} = \left[ \frac{1}{\text{IIP3}^{(1)}} + \frac{G_1}{\text{IIP3}^{(2)}} + \cdots + \frac{G_1 G_2 \cdots G_{n-1}}{\text{IIP3}^{(n)}} \right]^{-1} \quad (\text{H.3})$$

Assuming the common memory-less third-order polynomial linearity model [68, Chapter 2.2],

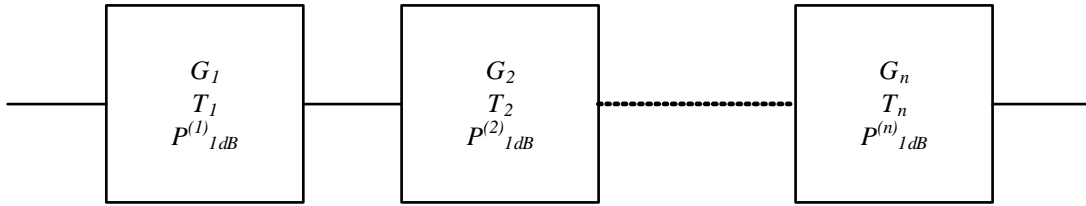


Figure H.1: Block diagram of a general receiver.

$P_{1dB}$  is related to IIP3 by:

$$P_{1dB} \approx 0.11 \times \text{IIP3} \quad (\text{H.4})$$

Applying Eq. (H.4) to Eq. (H.3), we find the cascade  $P_{1dB}$  is:

$$P_{1dB} = \left[ \frac{1}{P_{1dB}^{(1)}} + \frac{G_1}{P_{1dB}^{(2)}} + \dots + \frac{G_1 G_2 \dots G_{n-1}}{P_{1dB}^{(n)}} \right]^{-1} \quad (\text{H.5})$$

# Appendix I

## Measurement of Baselines

The baselines at VLA-NA were estimated using a laser range finder (Nikon Laser 1200 Monarch) to measure the distance of each antenna to the two closest posts of the VLA-NA perimeter fence. The distance between the fence posts is approximately 120 m, measured with a measuring wheel. The fence is oriented approximately north-south by east-west, with a slight rotation of  $2^\circ$ , as measured with a compass.

Figure I.1 shows a diagram of the measurements used to estimate baselines. The fence posts are labeled A, B, C, and D, counter-clockwise starting with the Northwest post. The positions of the antennas are denoted as  $\mathbf{p}_1$ ,  $\mathbf{p}_2$ ,  $\mathbf{p}_3$ ,  $\mathbf{p}_4$ .

Table I.1 lists the laser range finder measurements.

The laser range finder was not available during the Kelly Flats measurement campaign. Instead, the baseline was measured with a hand-held GPS unit (in a personal cell phone). The GPS unit returned the latitude  $\mathcal{L}$  and longitude  $LON$  of each antenna, reported in Table I.2.

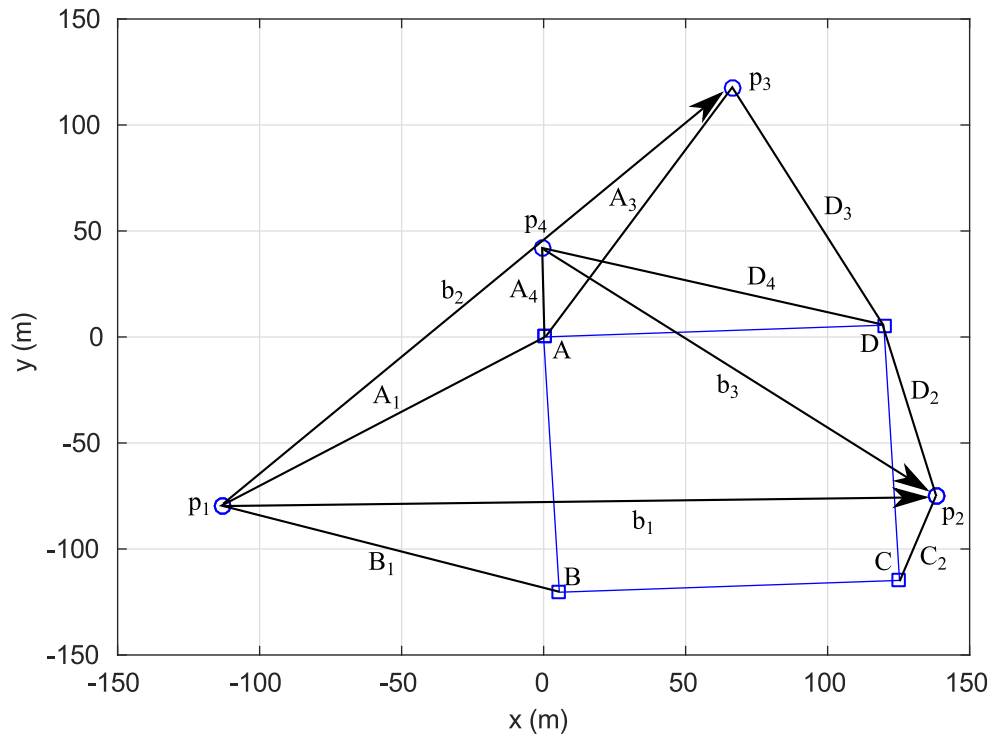


Figure I.1: Coordinate distances and notation used to estimate the baselines used in the VLA-NA campaign.

Table I.1: Measured distance between the antenna locations and the VLA-NA fence posts.

Point	Distance (m)			
	A	B	C	D
$\mathbf{p}_1$	138.5	125.0		
$\mathbf{p}_2$			41.5	82.5
$\mathbf{p}_3$	135.0			124.0
$\mathbf{p}_4$	42.0			125.5
A		120	120	120
B	120		120	120
C	120	120		120
D	120	120	120	

Table I.2: GPS coordinates for the antennas during the Kelly Flats measurement campaign.

	Antenna A	Antenna B
$\mathcal{L}$	$37.425^\circ$	$37.426^\circ$
$LON$	$-80.559^\circ$	$-80.556^\circ$

# List of Symbols

Symbol	Definition	First Appears (p.)
$S_{\nu}^{src}$	Flux density of the source at a frequency $\nu$	4
$\nu$	Frequency	4
$\alpha$	Spectral index	5
$\tau_g$	Geometric delay	6
$\rho$	Cross correlation	6
$\theta$	Zenith angle	16
$\phi$	Azimuth angle	16
$T_{sky}$	Sky noise contribution to antenna temperature	17
$\Omega_A$	Antenna beam solid angle	17
$T(\theta, \phi)$	Sky brightness temperature distribution	17
$P(\theta, \phi)$	Antenna normalized power pattern	17
$d\Omega$	Differential element of solid angle	17
$\mathbf{E}^{src}$	Electric field from the source	19
$\mathbf{r}$	Position in space where $\mathbf{E}^{src}$ is sampled	19
$t$	Time	19
$\hat{\mathbf{s}}$	Direction of the source	19
$\hat{\boldsymbol{\theta}}$	Unit vector pointing in the $+\theta$ direction	19
$\hat{\boldsymbol{\phi}}$	Unit vector pointing in the $+\phi$ direction	19

$c_\theta, c_\phi$	Gaussian random variables	
$E_\nu^{src}$	Amplitude of $\mathbf{E}^{src}$	19
$\beta$	Wavenumber	19
$\eta$	Free space wave impedance	19
$\psi$	Direction ( $\theta, \phi$ ) in the sky	19
$dS^g(\psi)$	Differential element of flux density from a direction $\psi$	19
$k$	Boltzmann's constant	19
$\lambda$	Wavelength	19
$d\mathbf{E}^g(\psi)$	Differential element of electric field from a direction $\psi$	20
$g_\theta, g_\phi$	Gaussian random variables	
$v_A^{(m)}$	Open circuit voltage on the terminals of antenna $m$	20
$\mathbf{l}_e$	Vector effective length of the antenna	20
$\mathbf{b}$	Baseline vector	20
$Z_A$	Antenna impedance	21
$R_{rad}$	Radiation resistance	21
$R_{loss}$	Resistance due to ohmic loss	21
$X_A$	Antenna reactance	21
$T_A$	Antenna temperature	21
$v_{int}$	Noise voltage due to ohmic loss	21
$T_{amb}$	Ambient physical temperature	21
$Z_p$	Parasitic impedance	22
$A_R$	Receiver voltage gain	22
$Z_R$	Receiver input impedance	22
$Z_{in}$	Parallel combination of $Z_R$ and $Z_p$	22
$Z'_A$	Parallel combination of $Z_A$ and $Z_p$	22
$v_n$	Receiver equivalent noise voltage	23
$n$	Gaussian random variable	
$T_R$	Receiver noise temperature	23

$R_n$	Receiver noise resistance	23
$v_{out}^{(m)}$	Voltage output by receiver $m$	23
$H^{(m)}$	Ratio of $v_{out}$ to $v_A$	23
$G^{(m)}$	Ratio of $v_{out}$ to $v_n$	23
$\Delta\nu$	Resolution bandwidth (spectral resolution)	24
$\Delta t$	Integration time (temporal resolution)	25
$\rho_{mn}$	Cross correlation of the outputs from receivers $m$ and $n$	25
$P^{src}$	Contribution to $\rho_{mn}$ from the source	25
$P^g$	Contribution to $\rho_{mn}$ from the background	25
$l_e$	Projected effective length	25
$f_g$	Fringe rate of a source	26
$T$	Observation duration	26
$t_0$	Start time of the observation	26
$c_0, c_1, c_2$	Coefficients of the Taylor series approximation of $f_g$	26
$f_r$	Fringe rate	27
$G_R(Z_s)$	Receiver transducer power gain when the source impedance is $Z_s$	34
$v_{cal}$	Open circuit noise voltage of the calibration circuit	34
$Z_{cal}$	Input impedance of the calibration circuit	34
$R_{cal}$	Real part of $Z_{cal}$	34
$X_{cal}$	Imaginary part of $Z_{cal}$	34
$T_{cal}$	Noise temperature of the calibration circuit	34
$S_{out,i}$	Power spectral density received in state $i$	36
$G_p$	Gain of the parasitic impedance	36
$\Gamma$	Reflection coefficient	37
$s_{ij}$	$s$ -parameters	37
$Z_0$	Reference impedance used to compute $s$ -parameters	37
$\epsilon_A$	Ground loss efficiency	37
$T_{gnd}$	Contribution of the ground to $T_A$	38

$Z_{A,prior}$	Prior estimate of $Z_A$	40
$C_p$	Parallel capacitance used to modify $Z_{A,prior}$	40
$C_s$	Series capacitance used to modify $Z_{A,prior}$	40
$T_{cal,prior}$	Prior estimate of $T_{cal}$	41
$\Delta T_{cal}$	Modification to $T_{cal}$	41
$S_A$	Power spectral density available from a source	43
$I_t$	Test current applied to the antenna terminals	52
$l'$	Arc length along the antenna	52
$I(l')$	Current distribution along the antenna	52
$\hat{\mathbf{l}}_e(l')$	Unit tangent along the antenna	52
$\hat{\mathbf{r}}$	Radial unit vector	52
$\mathbf{r}(l')$	Distance from the origin to $l'$	52
$L$	Total length of the antenna	52
$h$	Height of the antenna above ground	53
$A_e(\theta, \phi)$	Effective aperture of the antenna	54
$G(\theta, \phi)$	Far field gain of the antenna	54
$\rho_{Cu}$	Resistivity of copper	61
$a$	Radius of the antenna	61
$P_{\theta \leq 90^\circ}$	Power radiated into the upper half plane	63
$P_{\theta > 90^\circ}$	Power absorbed by the ground	63
$E$	Electric field amplitude	63
$R$	Distance to the far field	63
$v_t$	Peak voltage across the antenna terminals	63
$P_{in}$	Power delivered to the antenna (in transmit mode NEC4 simulations)	63
$P_{1dB}$	Input-referred 1 dB compression point	66
$G_F$	Gain of the FEE	68
$T_F$	Noise temperature of the FEE	68

$\tau_c$	Cable delay	72
$\tau_0$	Nominal cable delay	72
$\tau_d$	Cable delay due to dispersion	72
$\mu$	Permeability of free space	73
$a_c$	Radius of the inner conductor	73
$b_c$	Radius of the outer conductor	73
$\sigma_a$	Conductivity of the inner conductor	73
$\sigma_b$	Conductivity of the outer conductor	73
$G_c$	Gain of the cable	78
$T_c$	Noise temperature of the cable	78
$G_s$	Gain of the splitter	79
$T_s$	Noise temperature of the splitter	79
$G_{AAF}$	Gain of the anti-aliasing filter	80
$T_{AAF}$	Noise temperature of the anti-aliasing filter	80
$T_{sys}$	System temperature	81
SEFD	System equivalent flux density	81
$\Delta S_{mn}$	Noise in the cross correlation	83
$T_0$	$T(\theta, \phi)$ for a uniform sky	157
$l_{e0}$	Projected effective length	157
$D$	Baseline length	157
$\mathcal{E}$	Elevation	160
$\mathcal{A}$	Azimuth	160
$H$	Hour angle	160
$\alpha$	Right ascension	160
$\delta$	Declination	160
$\mathcal{L}$	Local latitude	160
$S_D$	Power spectral density available from the noise diode	170
$S_R$	Received power spectral density	166

$v_D$	Noise diode voltage	170
$Z_D$	Noise diode impedance	170
$R_D$	Real part of $Z_D$	170
$X_D$	Imaginary part of $Z_D$	170
$S_{cal}$	Power spectral density available from the calibration circuit	171
$G_{ATTN}$	Gain of the attenuator and balun	171
$S_{out}$	Power spectral density measured by the spectrum analyzer	171
$G_{jig}$	Gain of the test jig	171
$T_{jig}$	Noise temperature of the test jig	171
$S_1$	Power spectral density available to the test jig	171

---

# References

- [1] S. W. Ellingson *et al.*, “The LWA1 Radio Telescope,” *IEEE Trans. Antennas Propag.*, vol. 61, no. 5, p. 2540, May 2013.
- [2] M. P. van Haarlem *et al.*, “LOFAR: The LOW-Frequency ARray,” *Astronomy & Astrophysics*, vol. 556, p. A2, Aug. 2013.
- [3] S. J. Tingay *et al.*, “The Murchison Widefield Array: The Square Kilometre Array Precursor at Low Radio Frequencies,” *Publications of the Astronomical Society of the Pacific*, vol. 30, no. e007, p. 7, Jan. 2013.
- [4] J. F. Helmboldt and N. E. Kassim, “The Evolution of Cassiopeia A at Low Radio Frequencies,” *Astronomical Journal*, vol. 138, no. 3, p. 838, July 2009.
- [5] B.W. Stappers *et al.*, “Observing pulsars and fast transients with LOFAR,” *Astronomy & Astrophysics*, vol. 530, p. A80, June 2011.
- [6] K. Stovall *et al.*, “Pulsar Observations Using the First Station of the Long Wavelength Array and the LWA Pulsar Data Archive,” *Astrophysical Journal*, vol. 808, no. 2, p. 156, 2015.
- [7] J.F. Helmboldt *et al.*, “High-Precision Measurements of Ionospheric TEC Gradients with the Very Large Array VHF System,” *Radio Science*, vol. 47, Feb. 2012.

- [8] J.F. Helmboldt, W.M. Lane, and W.D. Cotton, “Climatology of Midlatitude Ionospheric Disturbances from the Very Large Array Low-frequency Sky Survey,” *Radio Science*, vol. 47, 2012.
- [9] J. F. Helmboldt and H. T. Intema, “Advanced Spectral Analysis of Ionospheric Waves Observed with Sparse Arrays,” *Journal of Geophysical Research*, vol. 119, no. 2, p. 1392, 2014.
- [10] H. Falcke *et al.*, “Detection and Imaging of Atmospheric Radio Flashes from Cosmic Ray Air Showers,” *Nature*, vol. 435, May 2005.
- [11] S. Buitink *et al.*, “A Large Light-Mass Component of Cosmic Rays at  $10^{17} - 10^{17.5}$  Electronvolts from Radio Observations,” *Nature*, vol. 531, Mar 2016.
- [12] S. R. Furlanetto, S. P. Oh, and F. H. Briggs, “Cosmology at Low Frequencies: The 21 cm Transition and the High-Redshift Universe,” *Phys. Rep.*, vol. 433, p. 181, Oct. 2006.
- [13] J. W. M. Baars *et al.*, “The Absolute Spectrum of Cas A; An Accurate Flux Density Scale and a Set of Secondary Calibrators,” *Astronomy & Astrophysics*, vol. 61, p. 99, Oct. 1977.
- [14] T. L. Wilson, K. Rohlfs, and S. Hüttemeister, *Tools of Radio Astronomy*, 6th ed. Springer, 2009.
- [15] H. W. Wells, “Flux Measurements of Cassiopeia A and Cygnus A between 18.5 MC and 107 MC,” *Proceedings of the IRE*, vol. 46, no. 1, p. 205, Jan. 1958.
- [16] S. Y. Braude *et al.*, “The Radio Emission Spectrum of Cassiopeia A at Frequencies below 30 Mc,” *Soviet Astronomy*, vol. 6, p. 122, Aug. 1962.
- [17] A. H. Bridle, “Flux Densities of Cassiopeia A and Cygnus A at 10.05 MHz,” *The Observatory*, vol. 87, p. 60, Apr. 1967.

- [18] E. A. Parker and J. R. Shakeshaft, "Precise Measurement of the Flux Densities of the Radio Sources Cas A and Cyg A at Metre Wavelengths," *MNRAS*, vol. 138, no. 4, p. 407, 1968.
- [19] S. Y. Braude *et al.*, "The Spectra of Discrete Radio Sources at Decametric Wavelengths-I," *MNRAS*, vol. 143, p. 289, 1969.
- [20] M. R. Viner, "26.3-MHz Radio Source Survey. I - The Absolute Flux Scale," *Astronomical Journal*, vol. 80, p. 83, Feb. 1975.
- [21] R. S. Roger, C. H. Costain, and J. D. Lacey, "Spectral Flux Densities of Radio Sources at 22.25 MHz. I." *Astronomical Journal*, vol. 74, p. 366, Apr. 1969.
- [22] M. R. Viner and W. C. Erickson, "26.3-MHz Radio Source Survey. II - Radio Source Positions and Fluxes," *Astronomical Journal*, vol. 80, p. 931, Nov. 1975.
- [23] N. E. Kassim, "The Clark Lake 30.9 MHz Galactic Plane Survey," *Astrophysical Journal Supplement Series*, vol. 68, p. 715, Dec. 1988.
- [24] D. C. Jacobs *et al.*, "New 145 MHz Source Measurements by PAPER in the Southern Sky," *Astrophysical Journal Letters*, vol. 734, p. L34, Jun. 2011.
- [25] J. F. Helmboldt *et al.*, "Radio Frequency Spectra of 388 Bright 74 MHz Sources," *Astrophysical Journal Supplement Series*, vol. 174, p. 313, Feb. 2008.
- [26] A. M. M. Scaife and G. H. Heald, "A Broad-Band Flux Scale for Low-Frequency Radio Telescopes," *MNRAS*, vol. 423, p. 30, Jun. 2012.
- [27] D. C. Jacobs *et al.*, "A Flux Scale for Southern Hemisphere 21 cm Epoch of Reionization Experiments," *Astrophysical Journal*, vol. 776, no. 2, p. 108, Oct. 2013.
- [28] A. de Oliveira-Costa *et al.*, "A Model of Diffuse Galactic Radio Emission from 10 MHz to 100 GHz," *MNRAS*, vol. 388, p. 247, Jul. 2008.

- [29] S. W. Ellingson *et al.*, “Observations of Crab Giant Pulses in 20-84 MHz using LWA1,” *Astrophysical Journal*, vol. 768, no. 2, p. 136, 2013.
- [30] J.D. Bowman and A.E.E. Rogers, “A Lower Limit of  $\Delta z > 0.06$  for the Duration of the Reionization Epoch,” *Nature*, vol. 468, Dec. 2010.
- [31] L. J. Greenhill and G. Bernardi, “HI Epoch of Reionization Arrays,” arXiv:1201.1700, Jan. 2012.
- [32] A.E.E. Rogers *et al.*, “Radiometric Measurements of Electron Temperature and Opacity of Ionospheric Perturbations,” *Radio Science*, vol. 50, p. 130, Feb. 2015.
- [33] J. K. Hargreaves and D. L. Detrick, “Application of Polar Cap Absorption Events to the Calibration of Riometer Systems,” *Radio Science*, vol. 37, 2002.
- [34] R. H. Tillman, S. W. Ellingson, and J. Brendler, “Practical Limits in the Sensitivity-Linearity Trade-off for Radio Telescope Front Ends in the HF and VHF-low Bands,” *Journal of Astronomical Instrumentation*, vol. 5, no. 2, 1650004, p. 15, 2016.
- [35] A. E. E. Rogers and J. D. Bowman, “Absolute Calibration of a Wideband Antenna and Spectrometer for Accurate Sky Noise Temperature Measurements,” *Radio Science*, vol. 47, no. 6, Jun. 2012.
- [36] E. N. Viniikin and V. A. Razin, “Secular Decreases in the 927 MHz Emission from the Supernova Remnants Cas A and Tau A,” *Australian Journal of Physics*, vol. 32, p. 93, Mar. 1979.
- [37] W. Stutzman and G. Thiele, *Antenna Theory and Design*, 2nd ed. J. Wiley & Sons, 1997.
- [38] S. Ellingson, “Antennas for the Next Generation of Low-Frequency Radio Telescopes,” *IEEE Trans. Antennas Propag.*, vol. 53, no. 8, p. 2480, Aug. 2005.
- [39] W. Stutzman, *Polarization in Electromagnetic Systems*. Artech House, 1993.

- [40] J. D. Romney, "Cross Correlators," in *Synthesis Imaging in Radio Astronomy II*, G. B. Taylor, C. L. Carilli, and R. A. Perley, Eds. ASP Conference Series, vol. 180, 1999.
- [41] B. A. Munk, *Finite Antenna Arrays and FSS*. J. Wiley & Sons, 2003.
- [42] International Telecommunications Union, "Electrical Characteristics of the Surface of the Earth," *ITU-R Rep.*, pp. 527–3, 1992.
- [43] W. H. Hayt and J. A. Buck, *Engineering Electromagnetics*, 7th ed. McGraw-Hill, 2004.
- [44] P. Harden, NRAO, Personal Communication.
- [45] B. C. Hicks *et al.*, "A Wide-Band, Active Antenna System for Long Wavelength Radio Astronomy," *Publications of the Astronomical Society of the Pacific*, vol. 124, no. 920, p. 1090, 2012.
- [46] S. J. Wijnholds and W. A. Van Cappellen, "In Situ Antenna Performance Evaluation of the LOFAR Phased Array Radio Telescope," *IEEE Trans. Antennas Propag.*, vol. 59, no. 6, p. 1981, Jun. 2011.
- [47] S. W. Ellingson, "Dispersion in Coaxial Cables," LWA Memo 136, June 2008. [Online]. Available: <http://www.ece.vt.edu/swe/lwa/>
- [48] K. Deshpande, "A Dedicated Search for Low Frequency Radio Transient Astrophysical Events using ETA," M.S. Thesis, Virginia Tech, Nov. 2009.
- [49] M. Harun and S. W. Ellingson, "Practical considerations in the design of a bandpass filter for the lwa analog receiver," LWA Memo 63, Nov. 2006. [Online]. Available: <http://www.ece.vt.edu/swe/lwa/>
- [50] M. Harun and S. W. Ellingson, "A Prototype Analog Receiver for LWA," LWA Memo 82, Mar. 2007. [Online]. Available: <http://www.ece.vt.edu/swe/lwa/>

- [51] J. M. Wrobel and R. C. Walker, "Sensitivity," in *Synthesis Imaging in Radio Astronomy II*, G. B. Taylor, C. L. Carilli, and R. A. Perley, Eds. Utah, USA: ASP Conference Series, vol. 180, 1999.
- [52] S. W. Ellingson, Q. Liu, and J. Craig, "The LWA-1 S60 System," LWA Memo 176, Dec. 2010. [Online]. Available: <http://www.ece.vt.edu/swe/lwa/>
- [53] J. H. Reed, *Software Radio: A Modern Approach to Radio Engineering*. Prentice Hall, 2002.
- [54] Q. Liu and S. W. Ellingson, "Coherent Dual-Sampling Direct Conversion Receiver with Continuous Acquisition over Ethernet to a PC," Internal Report, Jun. 2010. [Online]. Available: <http://www.ece.vt.edu/swe/eta/>
- [55] K. Obenburger and J. Dowell, "LWA1 RFI Survey," LWA Memo 183, Dec. 2011. [Online]. Available: <http://www.ece.vt.edu/swe/lwa/>
- [56] G. Bernardi *et al.*, "Bayesian Constraints on the Global 21-cm Signal from the Cosmic Dawn," *MNRAS*, vol. 461, p. 2847, 2016.
- [57] R. H. Tillman and S. W. Ellingson, "Broadband VHF Radiometry with a Notch-Filtered Antenna Exhibiting a Large Impedance Mismatch," in *2015 IEEE Int. Symp. Ant. Prop.*, Jul. 2015, p. 1696.
- [58] G. E. Evans, *Antenna Measurement Techniques*. Artech House, 1990.
- [59] W. J. Pisano, D. A. Lawrence, and S. E. Palo, "Low-Cost UAV Avionics for Autonomous Antenna Calibration," *Proc. AIAA Infotech@Aerospace Conf.*, Sept. 2005.
- [60] G. Virone *et al.*, "Antenna Pattern Verification System Based on a Micro Unmanned Aerial Vehicle (UAV)," *IEEE Antennas and Wireless Propag Lett.*, vol. 13, p. 169, 2014.
- [61] A. Gaber, R.H. Tillman, R.M. Buehrer, and S.W. Ellingson, "Navigation via Discrete Astronomical Radio Sources: Geolocalization Using Fringe Rates," in *2016 IEEE/ION Position, Location, and Navigation Symp. (PLANS)*, Apr. 2016, p. 403.

- [62] N. M. Temme, *Special Functions: An Introduction to the Classical Functions of Mathematical Physics*. J. Wiley & Sons, 1996.
- [63] F.W. Olver *et al.*, *NIST Handbook of Mathematical Functions*, 1st ed. New York, NY, USA: Cambridge University Press, 2010.
- [64] S. W. Ellingson, “Sky Noise-Induced Spacial Correlation,” LWA Memo 142, Oct. 2008. [Online]. Available: <http://www.ece.vt.edu/swe/lwa/>
- [65] A. R. Thompson, J. M. Moran, and G. W. Swenson JR., *Interferometry and Synthesis in Radio Astronomy*, 1st ed. J. Wiley & Sons, 1986.
- [66] S. W. Ellingson, “Suggestions for Experimental Verification of Instrumental Responses,” LWA Memo SLC0003, Oct. 2008. [Online]. Available: <http://www.ece.vt.edu/swe/lwavn/>
- [67] D. Pozar, *Microwave Engineering*, 4th ed. J. Wiley & Sons, 2011.
- [68] B. Razavi, *RF Microelectronics*, 2nd ed. Prentice-Hall, 2012.